DEPARTAMENT DE FÍSICA APLICADA I
ELECTROMAGNETISME

STRUCTURAL, OPTICAL AND MAGNETIC
CHARACTERISATION OF PULSED LASER DEPOSITED
THIN FILMS OF $Zn_{1-x}M_xO$ (M= Mn, Fe, Ni, Cu)
TRANSPARENT MAGNETIC ALLOYS

SAMUEL JOHN GILLILAND

UNIVERSITAT DE VALÈNCIA
Servei de Publicacions
2009

Aquesta Tesi Doctoral va ser presentada a València el dia 2 de abril de 2009 davant un tribunal format per:

- Dr. Vicente Muñoz Sanjosé
- Dr. Fernando Rodríguez González
- Dr. Jesús González Gómez
- Dr. Luis Miguel García Vinuesa
- Dr. Juan Francisco Sánchez Royo

Va ser dirigida per:
Dr. Alfredo Segura García del Río

Structural, Optical and Magnetic Characterisation of Pulsed Laser Deposited Thin Films of $Zn_{1-x}M_xO$ (M = Mn, Fe, Ni, Cu) Transparent Magnetic Alloys.

Samuel John Gilliland
Doctoral Thesis

Director: Prof. Alfredo Segura García del Río

December 2008

Agradecimientos

Supongo que debo escribir esta parte en español, ya que la mayoría de vosotros, a que voy a expresar mi gratitud, sois españoles o, por lo menos, habláis español mejor que yo.

En primer lugar quiero agradecer a Alfredo Segura, mi director, por toda su ayuda y paciencia. La inversión de tiempo que ha dedicado a mi formación sería incalculable si no fuera por mi afán de calcular las cosas (más que 1000 horas). Ha sido un placer trabajar bajo la dirección de alguien tan simpático y con tan amplio conocimiento científico. Quiero extender mi agradecimiento, también, a los otros profesores del grupo de semiconductores que han ayudado y compartido sus conocimientos conmigo. Entre ellos nombro a Juan Francisco Sánchez por su gran esfuerzo con las medidas fotoelectrónicas y la interpretación de los resultados magnéticos y Julio Pellicer por su asistencia en el análisis de los resultados de absorción de rayos X.

He sido afortunado al poder trabajar con científicos de entidades colaboradoras, a los cuales quiero dar las gracias. En el ESRF (Grenoble, Francia) quiero mencionar a Germán Castro, Félix Jiménez y Gema Martínez por su cooperación con las medidas de absorción de rayos X. También quiero dar un agradecimiento especial a Juan Angel Sans quien ha sido, para mí, como un hermano mayor durante estos cuatro años (el cheque está en el correo). En el LNCMP (Toulouse, Francia) reconozco a Jean-Marc Broto, Michael Goiran, Jean Léotin, Marius Millot y Stefan Hansel por la buena introducción que me han dado al mundo de los altos campos magnéticos con sus súper imanes. En el grupo de materia condensada de la Universidad de Zaragoza agradezco a Luis Miguel García y Fernando Bartolomé por darme buenos consejos y dejarme usar su SQUID dos veces (juro que el artículo está casi listo para publicar). Por fin, quiero mencionar a Alicia Mestre y Enrique Navarro de nuestro propio servicio de apoyo a la investigación experimental (SCSIE). Sin su colaboración con la difracción de Rayos X y la microscopía electrónica, esta tesis habría sido mucho más delgada.

Como sabemos, la investigación requiere mucho dinero, así que quiero reconocer las organizaciones que han hecho posible este trabajo: El Ministerio de Ciencia y Tecnología de España (proyectos MAT2002-04539-C02-01/03 y MAT2004-05867-C03-01) y la Generalitat Valenciana (proyecto GV04A-123). También agradezco la Universidad de Valencia por la beca "cinq segles" y la beca de colaboración que evitó que viviera en una caja de cartón durante mi formación (la oferta de invitaros a una copa sigue en pie).

Últimamente quiero dar las gracias (en orden alfabético) a Ana, Antonio(s), Cristian, David, Irma, Jaime, Javi, Jorge, Pere, Raúl, Salva y Vanessa, mis amigos de la universidad, por hacer aún más divertido todo este proceso (incluiría los apodos también pero me quedo sin espacio). Además reconozco el apoyo moral y espiritual de Dios, mi familia, mis pastores y todos mis amigos de la iglesia. Sin vosotros ni siquiera estaría aquí. Seguro que habré olvidado a alguien, pero no lo tomes personalmente, puedes estar seguro que estoy muy agradecido.

Index

1 Introduction

Zinc Oxide (ZnO) is a II-VI wide gap semiconductor, with a room temperature bandgap energy of 3.37 eV [1]. Although undoped bulk crystals normally show low n-type conductivity or resistive behaviour [2], high n-type electrical conductivity may be induced by doping with various group-III elements, such as Al [3], Ga [4] or In [5]. These elements contribute a free electron when they occupy the zinc substitutional position, producing a transparent conducting oxide (TCO). The ISI "Web of knowledge™" alone records over 30,000 papers on ZnO, with publications as early as 1900 [6], making it a relatively well-studied material. This is undoubtedly linked to the numerous industrial applications that have been found in fields as diverse as agriculture, chemicals, glass, ceramics, lubricants, medicines, cosmetics and rubbers. Of particular recent interest have been optoelectronic applications such as ultraviolet LEDs [7], lasers [8] and photoconductive detectors [9], for which ZnO is particularly appropriate. Its bandgap energy is similar to that of GaN, 3.44 eV [1], making it suitable as a possible substitute. Moreover, the higher exciton binding energy of 59 meV [10], compared to 22 meV in GaN [11], in principle leads to enhanced light emitting capabilities.

Undoped ZnO is diamagnetic [12] but its magnetic properties may be altered by forming an alloy with a magnetic element such as Mn [13], Fe [14] or Co [15] to produce a dilute magnetic semiconductor (DMS). Although DMSs have been studied for more than 30 years, they have recently attracted more interest due to the publication of a paper by Dietl et al. [16], which predicts room temperature ferromagnetic behaviour in wide gap DMS alloys, such as $Ga_{1-x}Mn_xN$ and $Zn_{1-x}Co_xO$. Semiconducting and ferromagnetic properties coexist in magnetic semiconductors like Eu and Mn chalcogenides [17, 18] and Cr spinels [19], but the crystal structure of such materials is very different to that of traditional semiconductors, such as Si and GaAs, which are used in industry. Moreover, their Curie temperatures are somewhat low and their crystal growth is difficult. Therefore, magnetic semiconductors based on non-magnetic semiconductors would be more convenient. Such materials could have applications in magnetooptics and spintronics [20], such as non-volatile memory, quantum computing and novel communication devices. For this reason it is of particular interest to study wide gap DMSs based on ZnO alloyed with transition metals (TMs), such as Mn, Fe, Ni and Cu.

There have been many publications on $Zn_{1-x}Mn_xO$, most of which concern its magnetic properties. This has been fuelled by the apparent controversy as to whether or not the material is ferromagnetic, with often contradictory reports finding it to be antiferromagnetic [21], diamagnetic [22] and paramagnetic [23]. Even when ferromagnetism is reported, there is rarely agreement on the Curie temperature, with values ranging from as low as 45K [24] to in excess of 420K [25]. There have been significantly fewer publications on $Zn_{1-x}Fe_xO$, $Zn_{1-x}Cu_xO$ and $Zn_{1-x}Ni_xO$ but the vast majority also focus on magnetic properties, with room temperature ferromagnetism normally reported in all three alloys [26-28], although controversy also exists [29]. Few would disagree that a more comprehensive understanding of the materials is required, making sure that preparation and experimental techniques are correctly applied to avoid erroneous results produced by substrates or clusters of magnetic atoms.

Almost as enigmatic as the magnetic properties themselves is the origin of such properties. In the previously mentioned Deitl paper [16], the mechanism proposed to explain ferromagnetism is an exchange interaction between free holes and localised spins. However, for this to happen in ZnO-based DMSs, they would need to be strongly p-doped. This poses a problem because the materials are normally n-type due to donors from zinc interstitials or oxygen vacancies. Moreover, Zhang et al. [30] showed that intrinsic p-doping in ZnO is theoretically impossible due to the low formation enthalpy of compensating defects. Nevertheless, Kim et al. report that $Zn_{1-x}Mn_xO$ with a certain degree of p-conductivity may still be obtained by doping with the group V elements N [31] and As [32]. In this case, there is a possible explanation for the observed ferromagnetism; however, other groups claim that even n-doped ZnMnO samples are ferromagnetic [33, 34]. In this case another theory would be required, such as the electron mediated exchange in a spin-split impurity band proposed by Coey et al. [35].

With regards to optical properties, some publications already mention the optical absorption of $Zn_{1-x}Mn_xO$ [36, 37], although none report high pressure measurements. This is a particularly appropriate technique for understanding the relationship between structural and electronic properties, as the "chemical pressure" produced as one atomic species is substituted for another of a different size is often analogous to externally applied physical pressure. Moreover, high pressure phases may be attained and characterised. The situation with the other DMSs under investigation is similar, although notably fewer papers have been published. Some optical properties of Fe [38], Cu [39] and Ni [40] ZnO-based DMSs have been reported, but none make use of high pressure techniques. Therefore, this study is of particular interest.

As an introductory background to the materials, the crystal and electronic structures of ZnO and its aforementioned DMSs shall now be presented.

1.1 Crystal Structure

At room temperature and pressure (RTP), it is well known that the ZnO assumes the wurtzite crystal structure. Wurtzite has a hexagonal Bravais lattice as shown in fig 1.1. The primitive lattice vectors in are defined in Euclidean space by the following relationships:

$$\vec{A_1} = \frac{1}{2}a\vec{x} - \frac{\sqrt{3}}{2}a\vec{y}$$

$$\vec{A_2} = \frac{1}{2}a\vec{x} + \frac{\sqrt{3}}{2}a\vec{y} \qquad (1.1)$$

$$\vec{A_3} = c\vec{z}$$
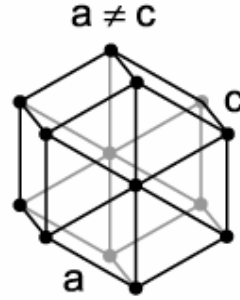
Fig 1.1: Hexagonal Bravais lattice.

Where a and c are lattice constants. In the case of ZnO at RTP, these constants take the values of a = 3.2495 Å and c = 5.2069 Å [41]. At each lattice point the basis, consisting of two zinc and two oxygen atoms is repeated. The position of these atoms may be expressed in terms of the primitive lattice vectors in the following way and the resulting structure is shown in fig 1.2.

$$\vec{Z_1} = \frac{1}{3}\vec{A_1} + \frac{2}{3}\vec{A_2}$$

$$\vec{Z_2} = \frac{2}{3}\vec{A_1} + \frac{1}{3}\vec{A_2} + \frac{1}{2}\vec{A_3}$$

$$\vec{O_1} = \frac{1}{3}\vec{A_1} + \frac{2}{3}\vec{A_2} + u\vec{A_3}$$

$$\vec{O_2} = \frac{2}{3}\vec{A_1} + \frac{1}{3}\vec{A_2} + \left(\frac{1}{2}+u\right)\vec{A_3}$$

$$(1.2) \,[42]$$
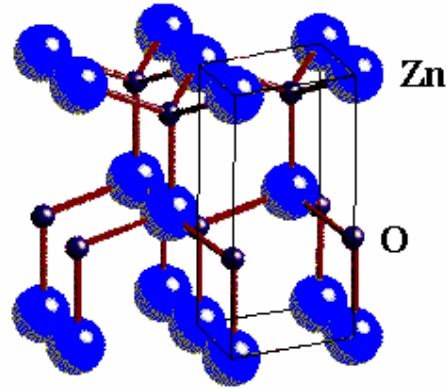
Fig 1.2: ZnO wurtzite structure.

Where $\vec{Z}$ and $\vec{O}$ refer to the respective positions of zinc and oxygen atoms and u is the ratio between the cation-anion distance along the c-axis and the lattice parameter c, which in ZnO at RTP takes the value of 0.380 [43]. Therefore, the structure consists of tetrahedrally coordinated zinc and oxygen atoms stacked in an ABAB pattern. The space group of this structure is $P6_3mc$. In a regular tetrahedron the value of u would be 0.375, meaning that in wurtzite ZnO, there is a small uniaxial compression in the c direction. This is due to the attraction between planes of anions and cations, meaning that the bonding is not entirely sp^3 covalent but also contains an ionic component. The effect that the ionic and covalent nature of the bonding have on the bandgap may be separated using the Philips-Van Vechten model, described in section 3.3.5. However, the principal bonding in wurtzite ZnO remains sp^3 covalent, which is common in tetrahedrally coordinated materials. In this bonding the O $2s^2$ electrons are promoted to the p-shell, changing its configuration to $2p^6$. These electrons then hybridise with the outer Zn $4s^2$ levels to produce two sp^3 covalent bonds.

On forming a DMS, the lattice parameters change according to the concentration and type of TM ion that is substituting zinc. It is important to note that above a certain limit, increasing the TM concentration tends to form secondary phases, at which point the simple description used up to now breaks down. In $Zn_{1-x}Mn_xO$, for example, the Mn solubility limit is normally between 15% [44] and 35% [45], where the highest concentrations are only obtainable when growth occurs in non-equilibrium conditions. Above this concentration extra peaks appear on x-ray diffractograms corresponding to secondary phases, such as $ZnMnO_3$, which intensify progressively with Mn concentration. In the case of other TMs, the solubility limits for growth by molecular beam epitaxy (MBE) have been determined by Ando et al. and are shown in fig 1.3 [46].
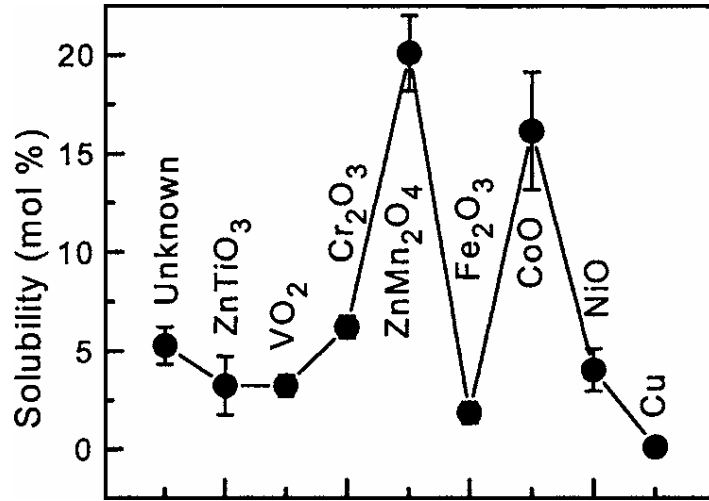
Fig 1.3: Solubility limit of TM ions in ZnO.

Assuming the absence of secondary phases, the factor that has the greatest influence on the change in lattice constant when forming a DMS is the ionic radius of the TM. The ionic radius of Mn^{2+} in tetrahedral coordination is 0.66 Å [44], which is larger than that of Zn^{2+}, 0.60 Å. For this reason, the a and c lattice parameters both increase with Mn concentration, with Tomaszewska et al. reporting changes of $\delta a = 0.007$ and $\delta c = 0.014$ Å with respect to pure ZnO on alloying with 5% Mn [47]. A similar increase in lattice constants is observed on alloying with Fe, which has an ionic radius of 0.63 Å [48]. However, both $Zn_{1-x}Cu_xO$ [39] and $Zn_{1-x}Ni_xO$ [44] show a decrease in lattice constants on increasing the TM content, as the respective ionic radii of Cu^{2+} and Ni^{2+} are 0.57 and 0.55 Å, smaller than that of Zn^{2+}.

The application of hydrostatic pressure to ZnO causes a decrease in the unit cell volume. This is confirmed by the high pressure x-ray diffraction experiments performed by Recio et al. [49]. At a pressure of around 10 GPa, it becomes energetically favourable for ZnO to assume the rocksalt structure, with a corresponding decrease in volume of about 17% [50]. The rocksalt phase has a face-centre-cubic (FCC) Bravais lattice (fig 1.4) with the following primitive lattice vectors:

$$\vec{A}_1 = \frac{a}{2}(\vec{x} + \vec{y})$$

$$\vec{A}_2 = \frac{a}{2}(\vec{y} + \vec{z}) \qquad (1.3)$$

$$\vec{A}_3 = \frac{a}{2}(\vec{z} + \vec{x})$$
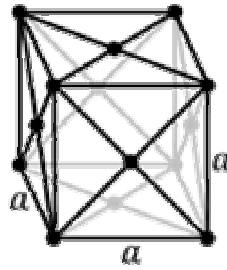
Fig 1.4: FCC Bravias lattice.

The value of lattice constant a at RTP is 4.275 ± 0.004 Å. It is possible to know this because a large hysteresis is observed on decreasing the pressure with a typical transition reversal at around 2 GPa [51], although exceptionally metastable rocksalt ZnO may be recovered [49]. The basis consists of a single zinc and oxygen atom separated by $\vec{A}/2$, where $\vec{A}$ is any primitive lattice vector. Therefore, the structure may be considered as two FCC lattices shifted by $\vec{A}/2$ with respect to each other, as shown in fig 1.5. The coordination of each atom is octahedral and the corresponding space group is Fm3m.
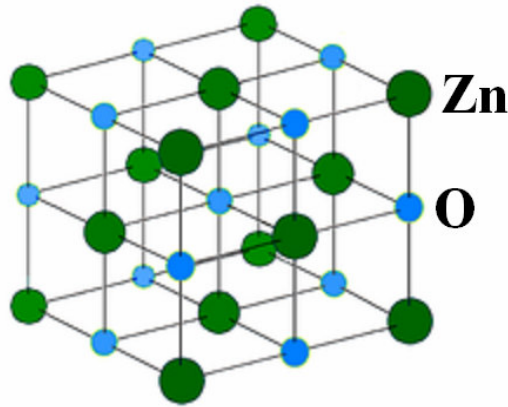
Fig 1.5: ZnO rocksalt structure.

In the next section it is necessary to refer to the wurtzite and rocksalt phases in reciprocal space. Therefore the Brillouin zones corresponding to the hexagonal and FCC Bravais lattices are shown in Fig 1.6 below. High symmetry points have been labelled according to current conventions.
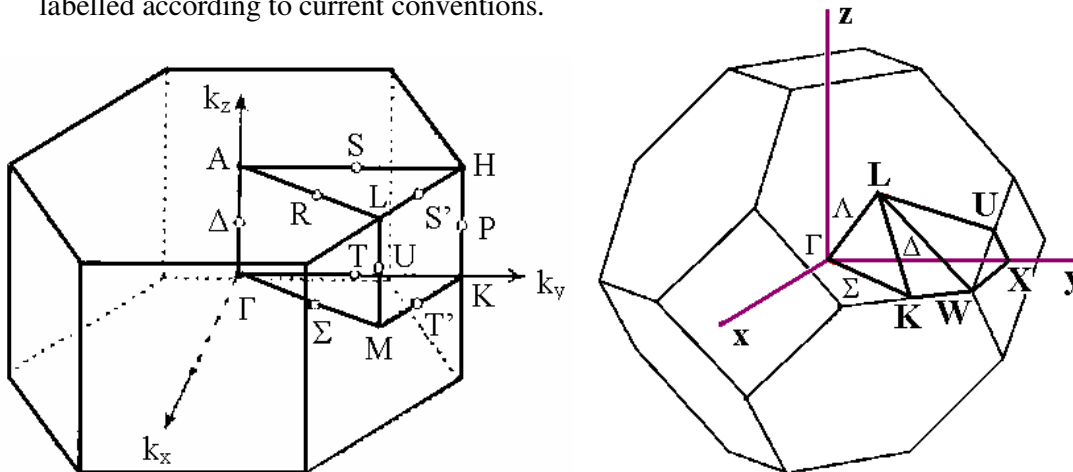
Fig 1.6: Brillouin zones for a) (left) hexagonal Bravais lattice and b) (right) FCC Bravais lattice.

1.2 Electronic structure

Fig 1.7 shows the electronic band structure of wurtzite ZnO at RTP [52] given by ab-initio pseudopotential calculations with a plane wave basis in the framework of the density functionial theory (DFT) in the local-density approximation (LDA). The high symmetry points on the horizontal axis correspond to those shown in the hexagonal Brillouin Zone of fig 1.6a.
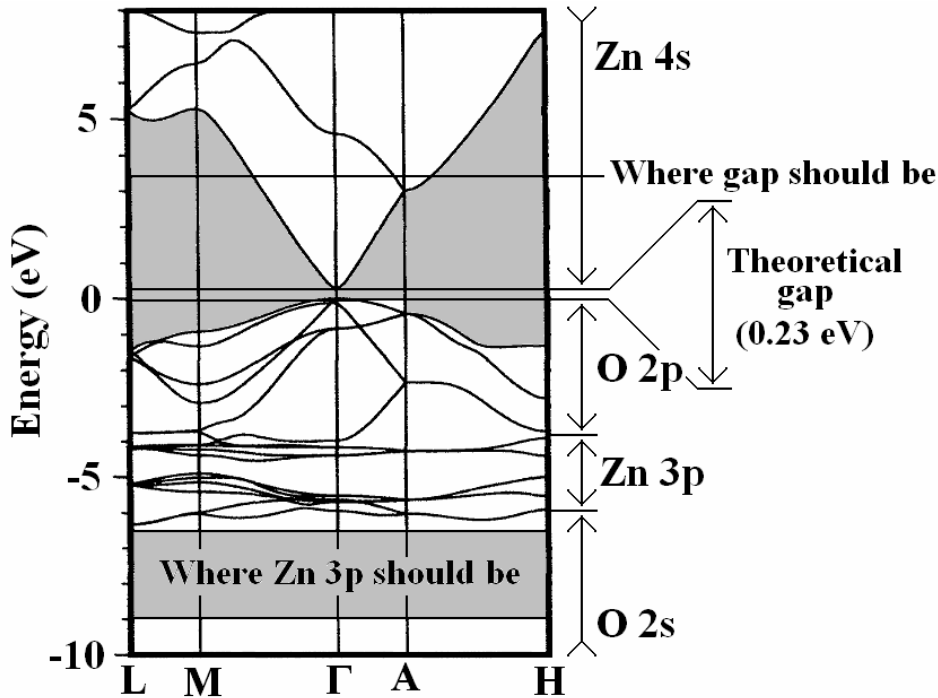
Fig 1.7: Electronic band structure of wurtzite ZnO.

The electronic structure consists of three broad regions with the conduction band comprising of Zn 4s levels, the upper valence band of O 2p levels and the lower valence band of Zn 3d levels. There is significant hybridisation between the O 2p and Zn 3d levels due to their proximity. We note that the bandgap occurs at Γ and it is a direct transition. A typical shortcoming of the LDA is that it frequently underestimates the energy of the gap, which is clearly seen in this case. This is compounded by the closeness of the Zn 3d levels to the gap, making it necessary for these electrons to be included in the valence band [53]. However, the overestimation of their energies, shown in the figure, increases the repulsion from the O 2p levels in an effect known as p-d repulsion, which shall be described in section (3.1.2). This closes the gap and flattens the band dispersion, distancing the theoretical effective electron and hole masses from the respective experimental values of $m_e = 0.19\ m_0$ and $m_h = 1.21\ m_0$ [54].

When a DMS is formed, levels from the dilute cation (Mn, Fe, Cu or Ni) are introduced in the band structure. For practical purposes, the levels that have the greatest influence on the near-gap band structure are the 3d levels, which also need to be considered as valence electrons. As in the case of the Zn 3d levels, the dilute cation 3d levels hybridise with the O 2p levels and produce p-d repulsion. Crystal field theory, which shall be discussed in section 3.1.3, shows that in tetrahedrally

coordinated complexes, such as wurtzite ZnO, where four ligands form a tetrahedron around the metal ion, it is energetically favourable to place a single electron into each of the 5 d orbitals before any pairing occurs. The resulting complex is said to be "high spin", which is especially true in the case of Mn and Fe, whose electron configurations favour a high proportion of unpaired d electrons. Spin produces spin-spin coupling and spin-orbit coupling so these effects also need to be taken into account when calculating the band structure. Chien et al. [55] published the band structure of $Zn_{1-x}Mn_xO$, $Zn_{1-x}Fe_xO$ and $Zn_{1-x}Cu_xO$ in spin up and spin down configurations. Fig 1.8 shows the result of their calculations for spin up $Zn_{1-x}Mn_xO$.
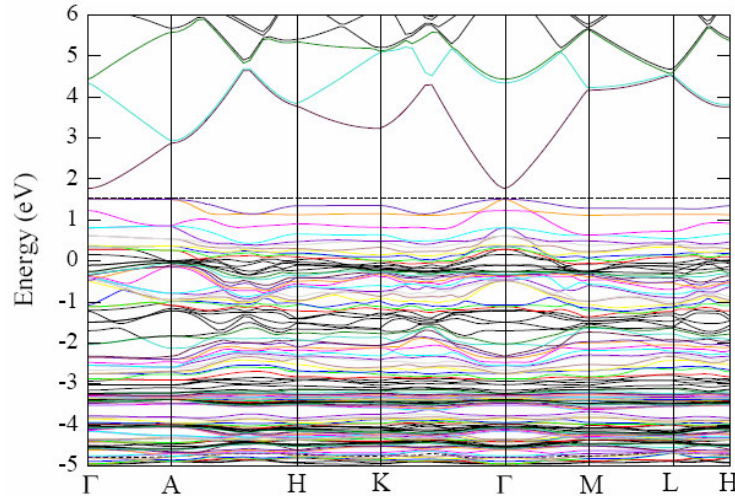
Fig 1.8: Band structure of spin up $Zn_{1-x}Mn_xO$.

By direct comparison with fig 1.7 it is clear to see that the inclusion of Mn 3d levels produces large changes to the upper valence band. Another way to appreciate the effect that these levels have on the electronic structure is by considering the density of states (DOS), defined in section 3.2.1. In pure wurtzite ZnO the LDA DOS [55] is shown in fig 1.9, which shall be compared to the DOS of the DMSs in fig 1.10. Toyoda et al. [56] calculated the DOS for Mn, Fe and Ni DMSs and Xiong et al [57] did likewise for the Cu DMS. Bands corresponding to dilute cation 3d levels are shown in grey and the DOS is shown for majority and minority spin configurations.
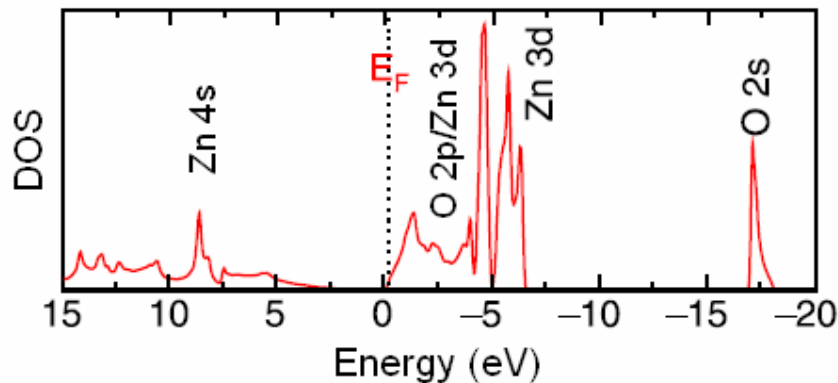
Fig 1.9: Theoretical DOS of wurtzite ZnO.
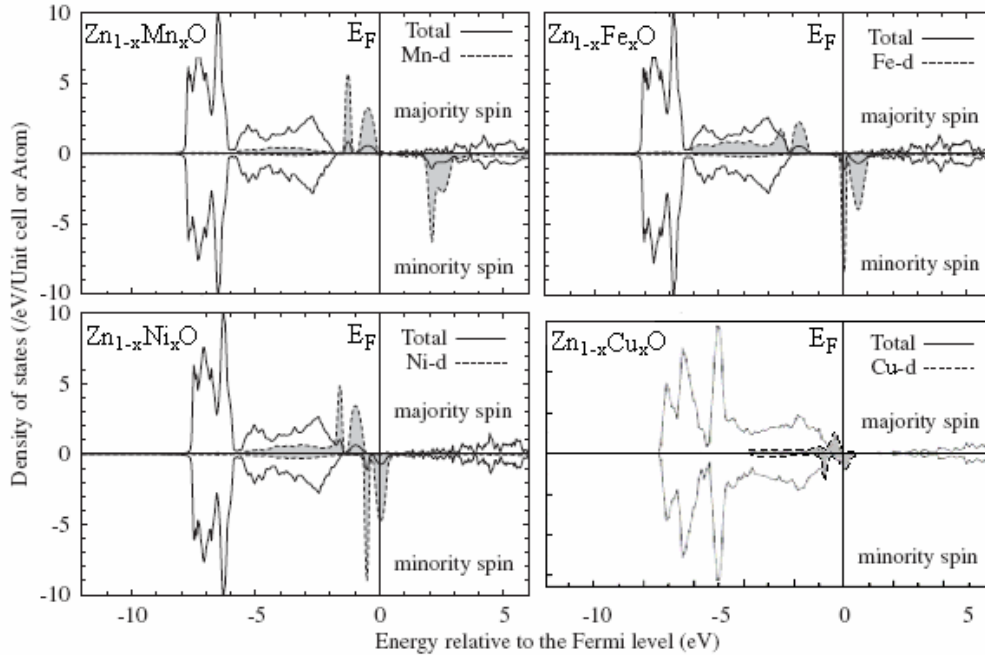
Fig 1.10: Theoretical DOS of ZnO DMSs.

In $Zn_{1-x}Mn_xO$ (majority spin) we note that the Mn 3d levels fall mainly within the top 2eV of the valence band, therefore one would expect the inclusion of Mn in the lattice to strongly affect the near edge optical properties of the material, including the bandgap energy. The large role that spin plays in the DOS would also suggest strong magnetic properties. In $Zn_{1-x}Fe_xO$, the Fe 3d levels are slightly further from the gap, in an energy range of around -1.5 to -6 eV, whereas the Ni 3d levels in $Zn_{1-x}Ni_xO$ fall between Mn and Fe, at an energy of around -1 to -5 eV. Finally, the Cu 3d levels in $Zn_{1-x}Cu_xO$ are very close to the valence band maximum, as in $Zn_{1-x}Mn_xO$, with the majority of the levels within just 1eV of the Fermi energy (E_F). However, theoretical calculations are only an approximation of reality which may be determined experimentally by photoelectronic measurements, the theory of which is described in section 3.2.1.

On applying hydrostatic pressure to wurtzite ZnO, the evolution of the DOS, calculated by Jaffe et al. [58], is shown in fig 1.11. While still in the wurtzite phase, the three major changes that pressure produces are a splitting in the Zn 3d levels, a slight broadening of the O 2s and Zn 3d levels and a reduction in the intensity and energy of the first peak below E_F. On reaching the transition to the rocksalt phase at pressure p_t, we observe a sudden decrease in the intensity of the first peak below E_F accompanied by a narrowing of the Zn 3d peaks and a reduction of the energy of the O 2s states. The band structure of the rocksalt phase at p_t is shown in fig 1.12. We note that the lowest energy interband transition is no longer a direct gap at Γ but an indirect gap between L and Γ, with reference to the FCC Brillouin Zone (fig 1.6b). The calculated energy of the gap is just below the experimentally determined value of $E_{gi} = 2.45 \pm 0.15$ eV [59]. The reason for the transition from a direct to indirect semiconductor is based on the change in coordination from tetrahedral to octahedral. In tetrahedral coordination p and d orbitals may mix at Γ but in octahedral coordination there is inversion symmetry at that point so the Laporte selection rules prevent mixing from happening there. However, mixing may occur away from Γ so

the lack of p-d repulsion at Γ reduces the energy at that point while its presence increases the energy at L, forming the new gap.
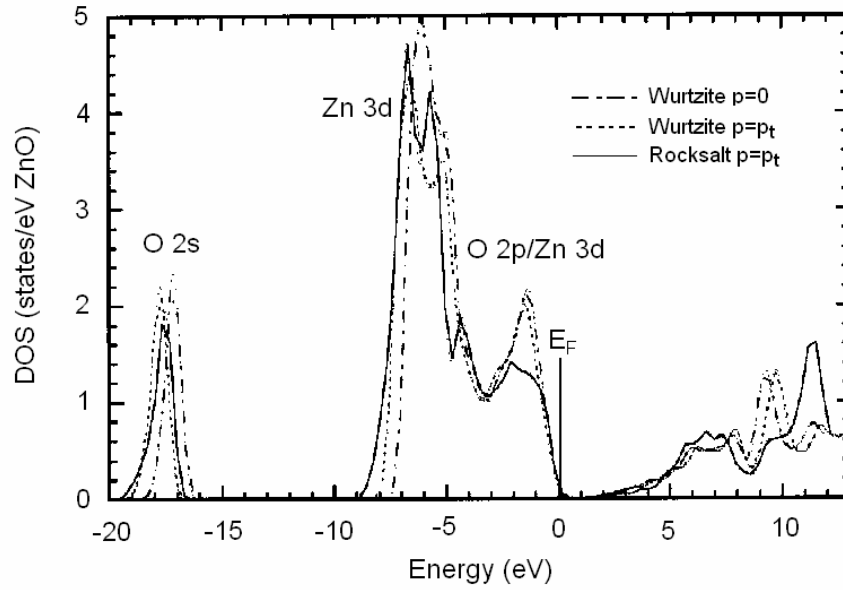
Fig 1.11: High pressure evolution of ZnO DOS.
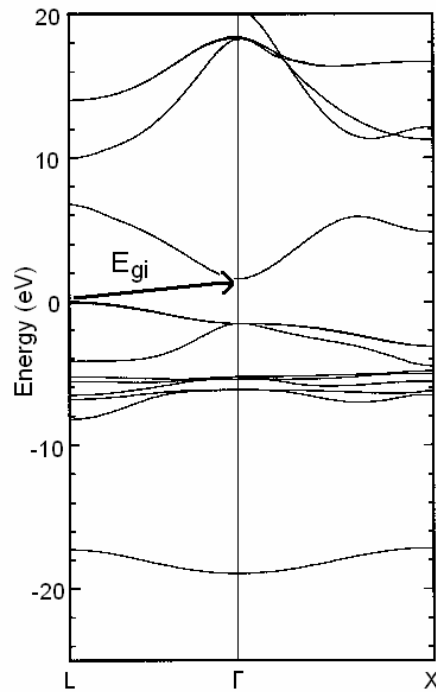
Fig 1.12: Band structure of rocksalt ZnO at p_t.

Samuel John Gilliland

1.3 Bibliography

[1] Yu and Cardona "Fundamentals of Semiconductors", Springer (2001).

[2] A. Polyakov, N. Smirnov, A. Govorkov and E. Kozhukhova. J. Electron. Mater. **35**, 4, 663 (2006).

[3] Y. Igasaki and H. Saito. J. Appl. Phys. **70**, 3613 (1991).

[4] M. Miyazaki, K. Sato, A. Mitsui and H. Nishimura. Microelectron. J. **36**, 928 (2005).

[5] K. Zhang, F. Zhu, C. Huan, A. Wee and T. Osipowicz. Surf. Interface Anal. **28**, 271 (1999).

[6] http://portal.isiknowledge.com/

[7] H. Ohta, K. Kawamura, M. Orita, N. Sarukura, M. Hirano and H. Hosono. Electron. Lett. **36**, 984 (2000).

[8] C. Czekalla, J. Lenzner, A. Rahm, T. Nobis and M. Grundmann. Superlattices Microstruct. **41,** 347 (2007).

[9] L. Mandalapu, F. Xiu, Z. Yang and J. Liu. Solid-State Electron. **51**, 1014 (2007).

[10] T. Pedersen. Phys. Status Solidi C **2**, 4026 (2005).

[11] J. Muth, J. Lee, I. Shmagin, R. Kolbas, H. Casey, B. Keller, U. Mishra and S. DenBaars. Appl. Phys. Lett. **71**, 2572 (1997).

[12] J. Blasco, F. Bartolomé, L. García and J. García. J. Mater. Chem. **16**, 2282 (2006).

[13] A. Mofor, A. El-Shaer, A. Bakin, A. Waag, H. Ahlers, U. Siegner, S. Sievers, M. Albrecht, W. Schoch, N. Izyumskaya, V. Avrutin, S. Sorokin, S. Ivanov and J. Stoimenos. Appl. Phys. Lett. **87**, 062501 (2005).

[14] S.D. Yoon, Y. Chen, D. Heiman, A. Yang, N. Sun, C. Vittoria and V. Harris. J. Appl. Phys. **99**, 08M109 (2006).

[15] S. Han, B. Lee, J. Ku, Y. Kim and Y. Jeong. J. Magn. Magn. Mater. **272**, 2008 (2004).

[16] T. Dietl, H. Ohno, F. Matasukura, J. Cibert and D. Ferrand. Science **287**, 1019 (2000).

[17] A. Comment, J. Ansermet, C. Slichter, H. Rho C. Snow and S. Cooper. Phys. Rev. B **72**, 014428 (2005).

[18] C. Gumus, A. Bayri, C. Ulutas M. Karakaplan and Y. Ufuktepe. J. Optoelectron. Adv. Mater. **8**, 261 (2006).

[19] T. Suzuyama, J. Awaka, H. Yamamoto, S. Ebisu, M. Ito, T. Suzuki, T. Nakama, K. Yagasaki and S. Nagata. J. Solid State Chem. **179**, 140 (2006).

[20] T. Fukumura, Y. Yamada, H. Toyosaki, T. Hasegawa, H. Koinuma and M. Kawasaki. Appl. Surf. Sci. **223** 62 (2004).

[21] T. Fukumura, Z. Jin, M. Kawasaki, T. Shono, T. Hasegawa and Koinuma. Appl. Phys. Lett. **78**, 958 (2001).

[22] X.M. Cheng and C.L. Chien. J. Appl. Phys. **93**, 7876 (2003).

[23] A. Che Mofor, A. El-Shaer, A. Bakin, H. Wehmann, H. Ahlers, U. Siegner, S. Sievers, M. Albrecht, W. Schoch, N. Izyumskaya, V. Avrutin, J. Stoemenos and A. Waag. Superlattices Microstruct. **39**, 381 (2006).

[24] S. Jung, S. An, G. Yi, C. Jung, S. Lee and S. Cho. Appl. Phys. Lett. **80**, 4561 (2002).

[25] P. Sharma, A. Gupta, K.V. Rao, F.J. Owens, R. Verma, R. Ahuja, J.M.O. Guillen, B. Johansson and G.A. Gehring. Nat. Mater. **2**, 673 (2003).

[26] X. Wei, C. Song, K. Geng, F. Zeng, B. He and F. Pan. J. Phys.: Condens. Matter **18**, 7471 (2006).

[27] D. Buchholz, R. Chang, J. Song and B. Ketterson. Mater. Sci. Semicond. Process. **9**, 141 (2006).

[28] P. Guangqing, X. Changtai, C. Shixun, Z. Jungang, W. Feng and X. Jun. J. Magn. Magn. Mater. **302**, 340 (2006).

[29] K. Ando, H. Saito, V. Zayets and M. C. Debnath. J. Phys.: Condens. Matter **16**, S5541 (2004).

[30] S. Zhang, S. Wei and A. Zunger. Phys. Rev. B **63**, 075205 (2001).

[31] S. Lee, H. Lee, S. Hwnag, Y. Shon, T. Kang D. Kim and E. Kim. Mater. Sci. Eng. B **126**, 300 (2006).

[32] S. Lee, S. W. Lee, Y. Shon and D. Kim. Mater. Sci. Eng. B **137**, 40 (2007).

[33] C. Liu, F. Yun and H. Morkoc. J. Mater. Sci.: Mater. Electron. **16**, 555 (2005).

[34] Ü. Özgür, Ya. I. Alivov, C. Liu, A. Teke, M. Reshchikov, S. Dogan, V.Avrutin, S. J. Cho and H. Morkoc. J. Appl. Phys. **98**, 041301 (2005).

[35] J. Coey, M. Venkatesan and C. Fitzgerald. Nat. Mater. **4**, 173 (2005).

[36] V. Avrutina, N. Izyumskaya, Ü. Özgür, A. El-Shaer, H. Lee, W. Schoch, F. Reuss, V.G. Beshenkov, A.N. Pustovit, A. CheMofor, A. Bakin, H.Morkoç and A. Waag. Superlattices Microstruct. **39**, 291 (2006).

[37] A.I. Savchuk, V.I. Fediv, S.A. Savchuk and A. Perrone. Superlattices Microstruct. **38**, 421 (2005).

[38] Y. Wang, P. John Thomas and P. O'Brien. J. Phys. Chem. Lett. B **2006**, 21412 (2006).

[39] S.A. Nasser, H.H. Afify, S.A. El-Hakim and M.K. Zayed. Thin Solid Films **315**, 327 (1998).

[40] H. Weakliem. J. Chem. Phys. **36**, 2117 (1962).

[41] R. Heller, J. McGannon and A. Weber. J. Appl. Phys. **21**, 1283 (1950).

[42] E. Kisi and M. Elcombe. Acta Crystallogr. C **45**, 1867 (1989).

[43] F. Decremps, F. Datchi, A. Saitta and A. Polian. Phys. Rev. B **68**, 104101 (2003).

[44] S. Thota, T. Dutta and J. Kumar. J. Phys.: Condens. Matter **18**, 2473 (2006).

[45] T. Fukumura, Z. Jin, A. Ohtomo, H. Koinuma, and M. Kawasaki. Appl. Phys. Lett. **75**, 3366 (1999).

[46] K. Ando, H. Saito, T. Sekiguchi, Y. Zoo, M. Murakami, Y. Matsumoto, T. Hasegawa and H. Koinuma. Appl. Phys. Lett. **78**, 3824 (2001).

[47] A. Tomaszewska, A. Opalinska, E. Grzanka, W. Lojkowski, A. Gedanken, M. Godlewski, S. Yatunenko, V. Osinniy and T. Story. Appl. Phys. Lett. **89**, 242102 (2006).

[48] S. Seo, C. Kwak, Y. Lee, S. Kim, S. Park and S. Han. J. Korean Phys. Soc. **52**, 805 (2008).

[49] J. Recio, M. Blanco, V. Luaña, R. Pandey, L. Gerward and J. Staun Olsen. Phys. Rev. B **58**, 8949 (1998).

[50] S. Desgreniers. Phys. Rev. B **58**, 14102 (1998).

[51] C. H. Bates, W. B. White, and R. Roy. Science **137**, 993 (1962).

[52] D. Vogel, P. Krüger and J. Pollmann. Phys. Rev. B **52**, R14316 (1995).

[53] U. Rössler. Phys. Rev. **184**, 733 (1969).

[54] S.Z. Sze "Physics of Semiconductor Devices", Wiley (1981).

[55] B. Amrani, I. Chiboub, S. Hiadsi, T. Benmessabih and N. Hamdadou. Solid State Commun. **137**, 395 (2006).

[56] M. Toyoda, H. Akai, K. Sato and H. Katayama. Physica B **376**, 647 (2006).

[57] Z. Xiong, S. Shi, Q. Wan and F. Jiang. Phys. Scr. **T129**, 358 (2007).

[58] J. Jaffe, J. Snyder, Z. Lin and A. Hess. Phys. Rev. B **62**, 1660 (2000).

[59] A. Segura, J. Sans, F. Manjon, A. Muñoz and J. Herrera. Appl. Phys. Lett. **83**, 278 (2003).

2 Objectives

There are five main objectives in this investigation, which shall be briefly introduced in this section:

1) **Crystal growth**

To use the process of pulsed laser deposition to produce optimal quality thin films of $Zn_{1-x}M_xO$ (M=Mn, Fe, Cu, Ni) over sapphire and mica substrates. The range of concentration values must be sufficiently wide to cover the whole solubility range of each cation and adequately spaced to appreciate any trends that occur.

2) **Structural characterisation**

To verify the correct deposition of the DMS in each film. This will firstly involve a determination of the stoichiometry by x-ray fluorescence and x-ray photoelectron spectroscopy. However, it is also necessary to confirm the correct positioning of the dilute magnetic cations within the ZnO host and the absence of secondary phases. This will be done by x-ray absorption near edge structure, x-ray diffraction, electron microscopy and microanalysis measurements.

3) **Electronic characterisation**

To determine the energies and distribution of core and valence band electronic states in the films and quantify how they change on forming a DMS. This will be done using x-ray photoelectron spectroscopy, in the case of the core states, and ultraviolet photoelectron spectroscopy for the valence band.

4) **Optical characterisation**

To investigate the absorption edge in the region around the optical gap in the wurtzite DMS by ultraviolet-visible spectroscopy at low temperature and high pressure. This will allow several effects produced by changing the dilute magnetic cation and its concentration to be identified and explained, such as bandgap energy, phonon frequencies and pressure coefficients. High pressure will also used to produce the transition to the rocksalt phase, which will also be investigated by absorption spectroscopy.

5) **Magnetic characterisation**

To determine the magnetic moment of the various DMS films and interpret these results in light of the structural characterisation, hence helping to resolve the controversy about ferromagnetism. This will be done by taking magnetisation measurements in function of applied field and temperature.

3 Theory

3.1 Alloy formation

3.1.1 Common anion-cation rule

It is often observed that in materials with a common cation, the direct bandgap at Γ increases as the proton number of the anion decreases. Likewise in materials with a common anion, the direct bandgap at Γ also increases as the proton number of the cation decreases. This is known as the common anion-cation rule. On a simple level, the reasoning on which this rule is based is that in covalently bonded materials, the smaller the atom, the shorter the bond distance and the stronger the resulting bond. This increases the energy difference between the bonding and antibonding orbitals and, hence, the gap. For example, in the III-VI common anion series from InAs to AlAs, the bandgaps increase steadily, in accordance to the rule. Similarly, in the III-VI common cation series from GaSb to GaN the bandgaps also shows a steady increase [1]. Of course, this is a very simplistic description and many breakdowns exist, especially when there is an ionic character to the bonding. For example, when going from ZnS to ZnO the bandgap decreases by 0.46 eV. There is a similar decrease of 0.60 eV between InP and InN [2]. All these trends are shown on fig 3.1.
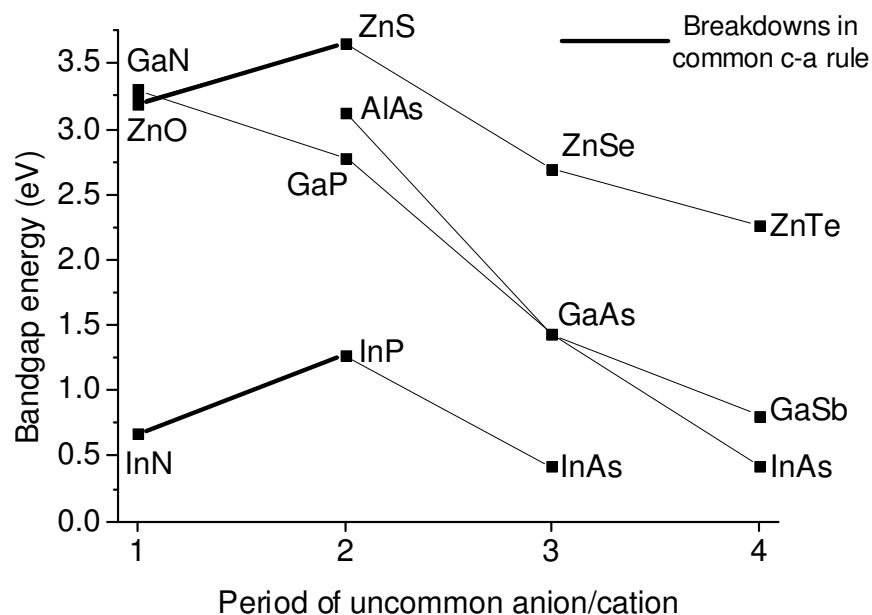
Fig 3.1: Successes and failures of the common anion-cation rule.

The main problem with the common anion-cation rule is that it does not consider the specific orbitals involved or the nature of the bonding between those orbitals. Tetrahedrally coordinated materials normally have sp^3 covalent bonding so any rigorous theoretical model would need to take this into account. Hall [3] was the first to do this in 1952 with diamond, using a model based on tight-binding combinations of bonding hybrid orbitals. Later Thorpe [4] extended his work to any tetrahedrally coordinated solid with a single atomic species and Harrison [5]

introduced a second atomic species into the theory. Following a similar reasoning, we start by considering the orbitals involved in the bonding: $|s\rangle$ and $|p\rangle$. The hybridised sp^3 state $|h\rangle$ on the anion (a) is:

$$|h^a\rangle = \frac{1}{2}\left(|s^a\rangle + \sqrt{3}|p^a\rangle\right) \qquad (3.1)$$

The expectation value of the energy of the hybridised state is:

$$\varepsilon^a = \langle h^a|H|h^a\rangle = \frac{1}{4}\left(\varepsilon_s^a + 3\varepsilon_p^a\right) \qquad (3.2)$$

where

$$\varepsilon_s^a = \langle s^a|H|s^a\rangle \text{ and } \varepsilon_p^a = \langle p^a|H|p^a\rangle \qquad (3.3 \text{ a, b})$$

By following the same process with the hybridised state on the cation (c), we define a fundamental parameter for the system:

$$V_3 = \frac{1}{2}\left(\varepsilon^c - \varepsilon^a\right) \qquad (3.4)$$

The other fundamental parameters for the system are:

$$V_1^a = -\langle h^a|H|h^{a'}\rangle = \frac{1}{4}\left(\varepsilon_p^a - \varepsilon_s^a\right) \qquad (3.5)$$

and

$$V_2 = -\langle h^c|H|h^a\rangle \qquad (3.6)$$

where V_1^a is related to the expectation energy of two different sp^3 hybrids on the anion and may be formulated for a similar interaction on the cation to give V_1^c. V_2 is related to the expectation energy of two sp^3 hybrids in the same bond. For bonding states (i.e. the valence band) we look for a linear combination of sp^3 hybrids with the lowest expectation energy:

$$|b\rangle = u_a|h^a\rangle + u_c|h^c\rangle \qquad (3.7)$$

where

$$u_a^2 + u_b^2 = 1 \qquad (3.8)$$

The expectation energy of this bond orbital is:

$$\langle b|H|b\rangle = \frac{1}{2}\left(\varepsilon^a + \varepsilon^c\right) - \sqrt{\left(V_2^2 + V_3^2\right)} \qquad (3.9)$$

Now the valence states are constructed using a linear combination of these bond orbitals. Using (3.5), the matrix element between two bonds sharing an anion is:

$$A = -\langle b|H|b'\rangle^a = \frac{1}{2}\left(1 + \frac{V_3}{\sqrt{(V_2^2 + V_3^2)}}\right)V_1^a \qquad (3.10)$$

and a similar expression can be found for when two bonds share a cation. In a tetrahedral structure there are four possible bond orientations so it is necessary to express the bond orbital wavefunctions in terms of Block functions for each orientation (α):

$$|\alpha, \vec{k}\rangle = \frac{1}{\sqrt{N}} \sum_j e^{i\vec{k}\cdot\vec{r}_j} |b_\alpha(\vec{r} - \vec{r}_j)\rangle \qquad (3.11)$$

Where N is the number of primitive unit cells in the crystal, $\vec{k}$ is the wavevector and $\vec{r}_j$ is the position of the midpoint of the bond in orientation α. Finally the matrix elements are evaluated and the resulting 4×4 matrix is diagonalised to determine the equations of the valence energy bands. To determine the conduction energy bands, the whole process is repeated for the antibonding orbitals. The bandgap can then be identified and its energy found from the band structure. Hence, the bandgaps of tetrahedrally coordinated common anion and common cation materials may be compared.

In practice, using the simple model described here for ZnO gives more inaccurate results than the common anion-cation rule itself. This is because of the large number of assumptions made, which include:

- The Hamiltonian is symmetric around each atom.
- The two hybrids in the same bond are orthogonal.
- The energy expectation values of the initial s and p orbitals are the same as their atomic values.
- Spin-orbit coupling is negligible.
- Orbitals only interact with those of their nearest neighbours.
- The crystal structure is perfectly tetrahedral.

Perhaps the most significant reason for the breakdown of this model and, indeed, the common anion-cation rule is the assumption that the cation d orbitals do not affect the bandgap energy. This shall be the subject of the next section.

3.1.2 p-d repulsion

As mentioned in the introduction, the interaction between p and d orbitals is permitted at Γ when the crystal structure is not centrosymmetric. As this is the case in tetrahedrally coordinated materials, this interaction needs to be taken into account when cation d and anion p orbitals are energetically close enough to overlap. The p and d orbitals hybridise to produce a bonding state with lower energy than the original d orbital and an antibonding state with higher energy than the original p orbital. Therefore, the overall effect may be described as an effective repulsion between the p and d orbitals, as shown in fig 3.2.
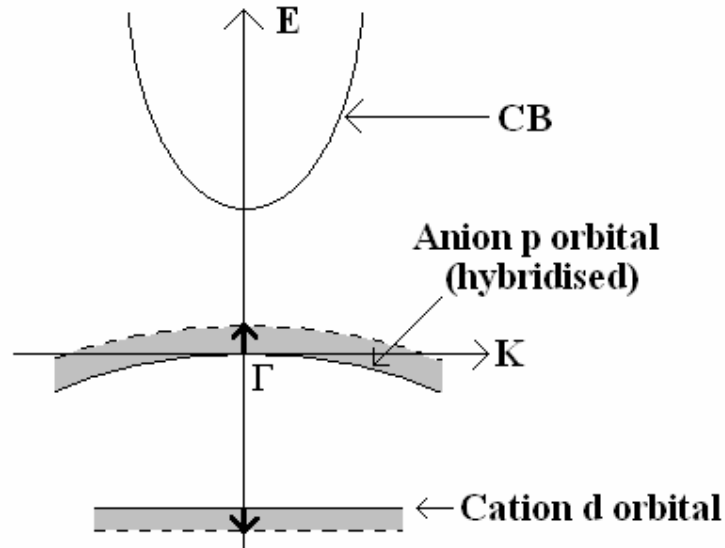
Fig 3.2: The effect of p-d repulsion.

If the cation p states can be ignored then this problem simplifies to a two level system regarding the anion p orbitals $|p\rangle$ and the cation d orbitals $|d\rangle$. The wavefunction for the system is:

$$\Psi = a|p\rangle + b|d\rangle \qquad (3.12)$$

where a and b are coefficients related to the occupation probabilities of the p and d orbitals, respectively. The total energy of the system (E) is determined through the Hamiltonian operator (H):

$$H\Psi = E\Psi \qquad (3.13)$$

On operating with the Hamiltonian and separating the orthogonal contributions, the following two equations are obtained:

$$aE_p + bV_{pd} = Ea \qquad (3.14a)$$
$$aV_{pd} + bE_d = Eb \qquad (3.14b)$$

where E_p is the energy of the anion p orbital, E_d is the energy of the cation d orbital and V_{pd} is the p-d coupling matrix element. The equations may be solved simultaneously to find the total energy of the system by calculating the determinant of the 2×2 matrix:

$$\begin{vmatrix} a(E_p - E) & bV_{pd} \\ aV_{pd} & b(E_d - E) \end{vmatrix} = 0 \qquad (3.15)$$

which gives the following quadratic equation:

$$E^2 - E(E_p + E_d) + E_p E_d - |V_{pd}|^2 = 0 \qquad (3.16)$$

On applying the quadratic formula, this relationship is obtained:

$$E = \frac{E_p + E_d}{2} \pm \frac{E_p + E_d}{2} \sqrt{1 + \frac{4|V_{pd}|^2}{(E_p - E_d)^2}} \qquad (3.17)$$

which may be simplified by performing a Taylor expansion on the square root expression. Terms corresponding to the second power and greater have been ignored.

$$E = \frac{E_p + E_d}{2} \pm \frac{E_p + E_d}{2} \left(1 + \frac{2|V_{pd}|^2}{(E_p - E_d)^2} - \ldots \right) \qquad (3.18)$$

By taking the positive and negative roots, two energies are obtained, which correspond physically to the energies of the antibonding (E_{AB}) and bonding (E_B) orbitals after p-d coupling has taken place.

$$E_{AB} = E_p + \frac{|V_{pd}|^2}{E_p - E_d} \qquad (3.19a)$$

$$E_B = E_d - \frac{|V_{pd}|^2}{E_p - E_d} \qquad (3.19b)$$

The energy difference between the orbitals is:

$$\Delta E = E_{AB} - E_B = E_p - E_d + \frac{2|V_{pd}|^2}{E_p - E_d} \qquad (3.20)$$

In the absence of p-d repulsion, the energy difference is simply E_p-E_d, so the effect of p-d repulsion may be found by subtracting this term. It is customary to express this as an energy change per orbital so the result is divided by two:

Samuel John Gilliland

$$\Delta E_{pd} = \frac{\left|V_{pd}\right|^2}{E_p - E_d} \qquad (3.21)$$

Wie and Zunger [6] combined a similar model with numerical data from band structure calculations using all-electron self-consistent electronic-structure techniques to investigate p-d repulsion in II-VI semiconductors. It was found that the following physical effects are usually produced:

- Reduction in bandgap energy.
- Reduction in cohesive energy.
- Increase in equilibrium lattice parameters.
- Reduction in spin-orbit splitting.
- Sign change in crystal splitting.
- Modification to charge distributions.

Moreover, by using this model to calculate the valence band offsets caused by p-d repulsion, the two breakdowns in the common anion-cation rule mentioned in the previous section may be resolved. The difference in offset between ZnS and ZnO is 1.00 eV, which more then compensates for the 0.46 eV between their bandgap energies. Similarly, the 0.6 eV between the bandgap energies of InP and InN is countered by the 1.56 eV difference in their offsets. Therefore, in the absence of p-d repulsion, the common anion-cation rule would be correct in these cases [7].

In the investigated DMSs, there are two cations that need to be taken into account: Zn and the dilute TM cation, which substitutes for Zn in a certain fraction, x, of the cation sites. The expression for the energy shift produced by p-d repulsion is:

$$\Delta E_{pd} = x\frac{\left|V_{pd}^{TM}\right|^2}{E_{2p}^O - E_{3d}^{TM}} + (1-x)\frac{\left|V_{pd}^{Zn}\right|}{E_{2p}^O - E_{3d}^{Zn}} \qquad (3.22)$$

As the electronic states at the valence band maximum (VBM) comprise of the hybridised anion 2p and cation 3d orbitals, this energy corresponds to the shift in the VBM in function of the dilute cation concentration. Moreover, it also corresponds to the shift in bandgap energy, since the energy of the conduction band minimum (CBM) is unaffected by p-d repulsion, due to its Zn 4s nature. By taking the derivative with respect to x, the rate of change of bandgap energy may be determined:

$$\frac{dE_g}{dx} = \frac{\left|V_{pd}^{TM}\right|^2}{E_{2p}^O - E_{3d}^{TM}} - \frac{\left|V_{pd}^{Zn}\right|^2}{E_{2p}^O - E_{3d}^{Zn}} \qquad (3.23)$$

Hence, there are two factors that affect the bandgap shift as dilute cation concentration increases. The first term corresponds to the effect of the dilute cation. It is interesting to note that this term could be positive or negative, depending on the sign of $E_{2p}^O - E_{3d}^{TM}$. If the TM 3d levels are more weakly bound than the O 2p levels, the sign is positive and vice versa. The second term corresponds to the effect of the reduction in Zn content. The Zn 3d levels are more strongly bound than the O 2p

levels, so $E^O_{2p} - E^{Zn}_{3d}$ is negative, making the sign of the term positive. Therefore, for the bandgap energy to decrease with x it is not only necessary for the dilute cation 3d levels to be more strongly bound than the O 2p levels, but the shift they produce must be large enough to compensate for the effect of the reduction in Zn concentration. In all other cases the bandgap energy will increase with x. The effect of the energy of the TM 3d orbital is shown diagrammatically in fig 3.3.
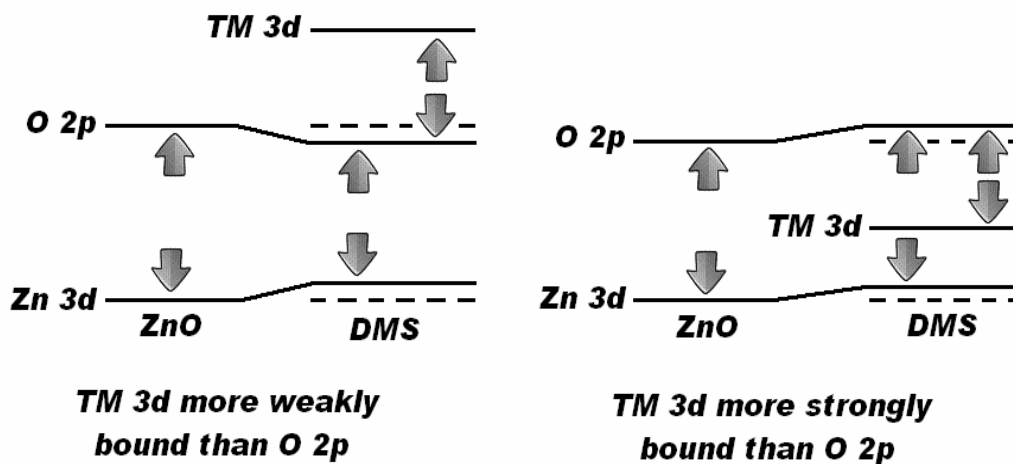
Fig 3.3: The effect of TM 3d level energy on p-d repulsion.

Although theoretical values were not readily available for the bandgap shift in the investigated DMSs, a value of a few meV per percentage increase in x would be expected, by comparison with other common anion series in [6].

3.1.3 Crystal field theory

Crystal field theory (CFT) [8] is a model that describes the electronic properties of TM complexes. It was developed in the 1930s by Hans Bethe and John Hasbrouck van Vleck and has been successfully used to explain various magnetic [9], structural [10] and optical properties [11]. It also forms a key part of ligand field theory (LFT), which may be used to explain the bonding in many of these materials [12]. The objective of the model is to calculate the change in energy in the five degenerate d orbitals of the TM cation when surrounded by ligands, which are modelled as point charges. There is an attraction between the cation and the unbonded ligand electrons but there is also a repulsion between the cation d orbitals and the ligand electrons, which becomes stronger the closer they are to each other. As not all the d orbitals are the same distance from the ligands, a splitting occurs in the d orbital energies. This splitting depends on various factors, such as the particular cation and ligands in question, the coordination of the cation and its oxidation state.

Octahedral   **Tetrahedral**
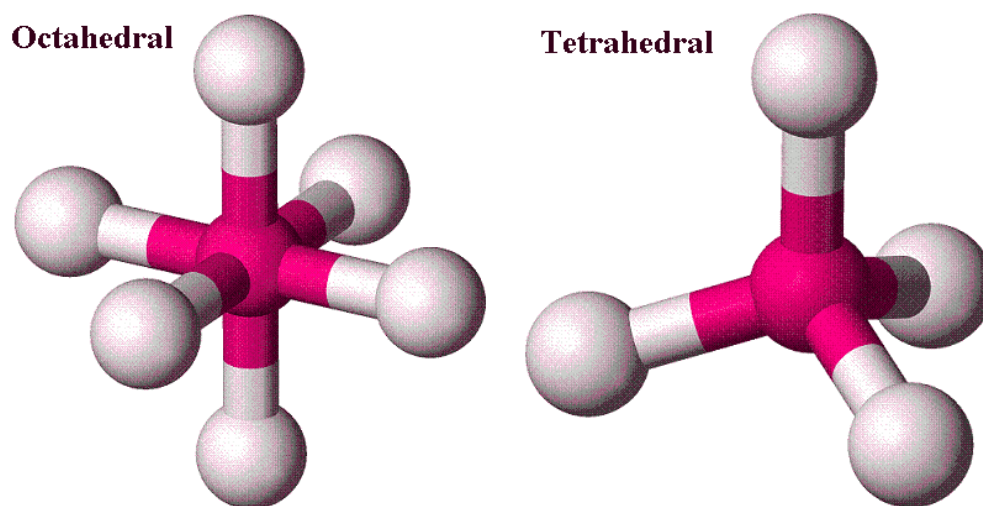
Fig 3.4: Arrangement of cation and ligands in different coordinations.

In octahedral coordination (fig 3.4 left), six ligands form an octahedron around the cation. By direct comparison with the family of 3d orbitals in fig 3.5, we note that the d_{xy}, d_{yz} and d_{zx} orbitals are further away from the ligands than the $d_{x^2y^2}$ and d_{z^2} orbitals. Therefore, the former set of orbitals will have a lower energy than the latter because they experience less repulsion. Hence, the d orbitals split into two distinct sets with an energy difference Δ_{oct} between them, as shown at the top of fig 3.6. In tetrahedral coordination (fig 3.4 right), four ligands form a tetrahedron around the cation. By similar comparison with fig 3.5, we note that the d_{xy}, d_{yz} and d_{zx} orbitals are now closer to the ligands than the $d_{x^2y^2}$ and d_{z^2} orbitals. Therefore, the former set will have a higher energy than the latter. The energy difference caused by the splitting, Δ_{tet}, is shown in the lower part of fig 3.6. We also note that $\Delta_{oct} > \Delta_{tet}$ because the d orbitals are oriented directly towards the ligands in octahedral coordination but this is not the case in tetrahedral coordination.
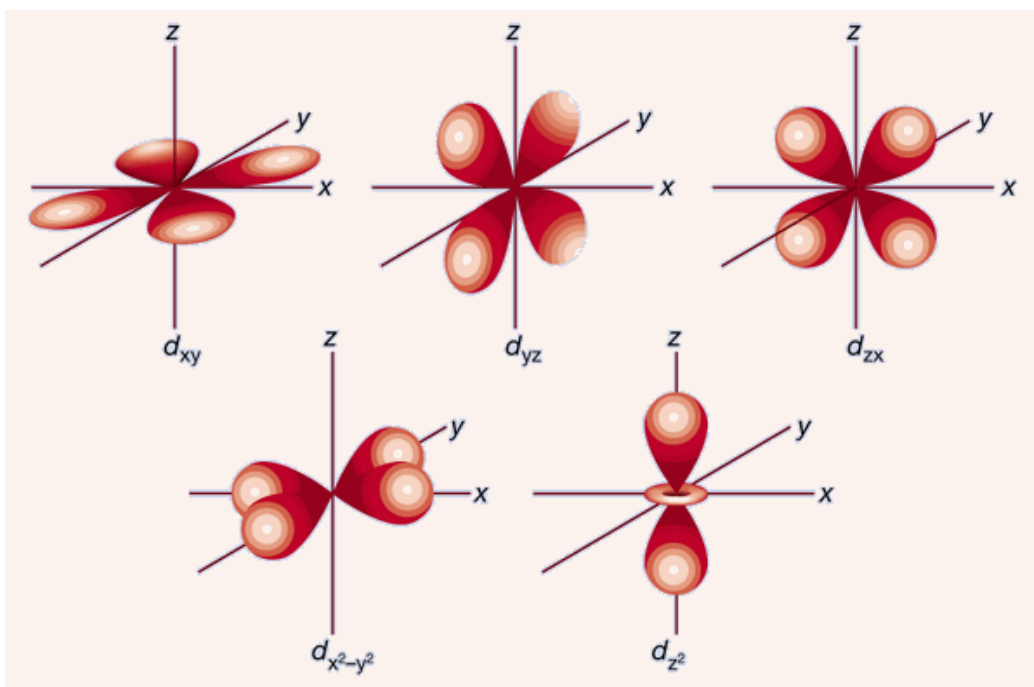
Fig 3.5: The family of 3d orbitals [13].
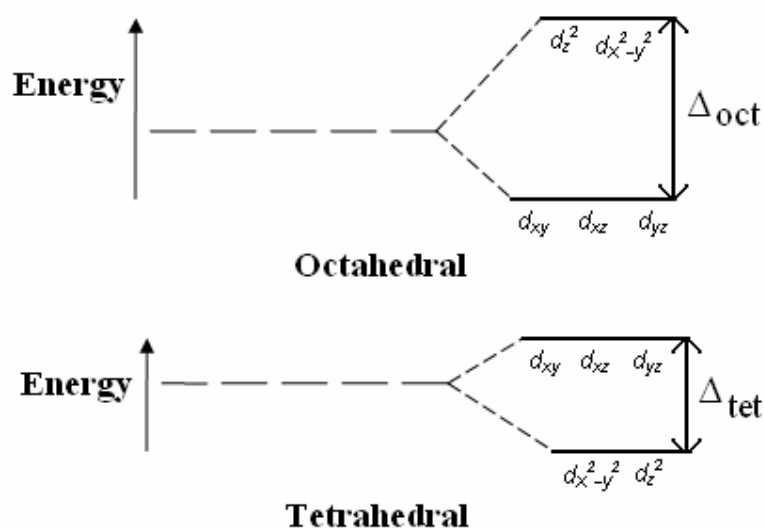
Fig 3.6: d orbital crystal field splitting in different coordinations.

The oxidation state of the cation affects the size of the crystal field splitting (Δ). In general, the higher the oxidation state, the higher the splitting. This is because the change in charge density that occurs when going from, say, a TM^{2+} to a TM^{3+} state, allows the ligands to draw closer to the cation, increasing the repulsive potential. Another factor that influences Δ is the chemical composition of the ligand. Certain ligands, such as CN^- and CO produce a large splitting and are referred to as strong-field ligands. Other ligands, such as I^- and Br^- produce small splitting and are referred to as weak-field ligands. The reason why ligands produce different field

strengths is explained by LFT and is related to the nature of the bonding between the cation and ligands. In complexes with strong-field ligands, it is energetically unfavourable to put electrons into the high energy (e_g) levels produced by the splitting so the lower energy (t_{2g}) levels are filled first, in accordance to the Aufbau principle. Such complexes are referred to as "low spin", as they tend to have a high proportion of paired d electrons. An example of a low spin complex is the octahedral ion $[Fe(NO_2)_6]^{3-}$, that has all 5 of its d electrons in the t_{2g} level. The reverse is true in the case of weak-field ligands, where it is energetically favourable to place an electron into an unoccupied e_g level rather than overcoming the repulsion caused by pairing it with another electron in a t_{2g} level. Therefore, one electron would be placed in each of the five d orbitals before the occurrence of pairing, in accordance with Hund's rule. The resulting complexes are referred to as "high spin", as they tend to have a high proportion of unpaired d electrons. For example, the ion $[FeBr_6]^{3-}$ has all five of its d electrons in different levels. The concepts of low and high spin are illustrated in fig 3.7.
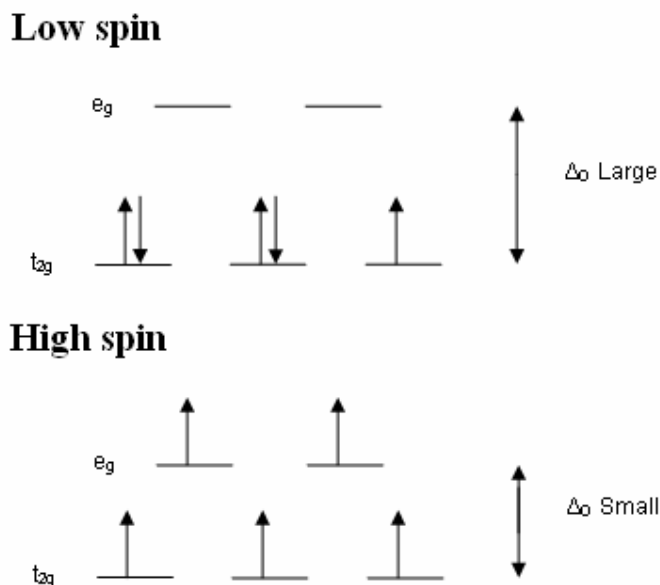
Fig 3.7: d electron allocation in low spin and high spin complexes.

In tetrahedral TM complexes, $\Delta_{tet} \approx 4/9\ \Delta_{oct}$ so the energy required to pair two t_{2g} electrons would normally be higher then the energy required to place an electron in an unoccupied e_g level. Therefore tetrahedral complexes are usually high spin.

3.2 Ionising radiation

3.2.1 Photoelectric effect

Hertz discovered the photoelectric effect in 1887 but the physical theory behind it did not come until 1905 when Einstein explained the effect making reference to the quantum nature of light [14]. In this effect (fig 3.8), light incident on a material gives rise to the emission of photoelectrons from its surface which have a kinetic energy (KE) given by the following equation:

$$KE = \hbar\omega - \Phi - E_B \qquad (3.24)$$
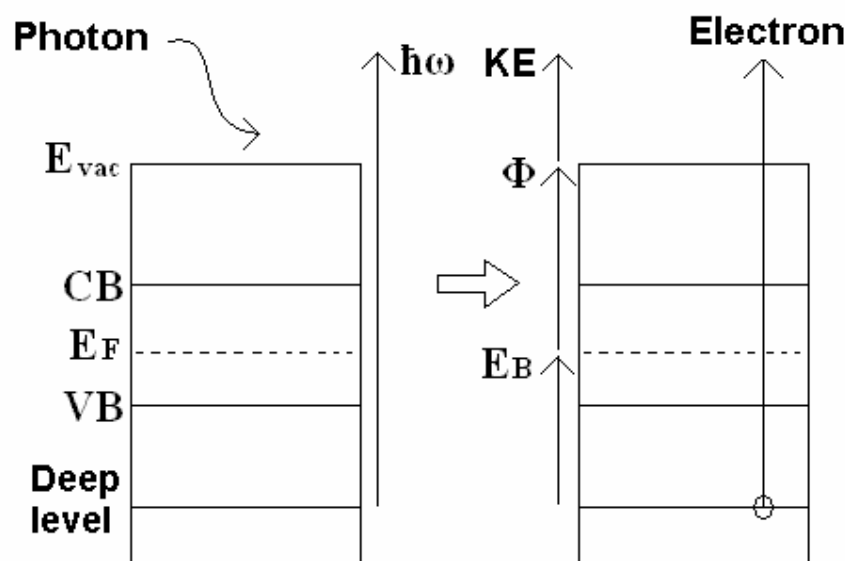
Fig 3.8: The photoelectric effect.

Where $\hbar\omega$ is the energy of the incident photons, Φ is the work function of the material (the energy between E_F and the vacuum energy, E_{vac}) and E_B is the binding energy of the electron (relative to E_F) that has been released by the photon. Clearly it is necessary for the photon to have at least the work function energy for an electron to be released. Therefore, if the incident light energy and work function are known then, by measuring the KE of the photoelectrons, it is possible to determine the values of E_B for the electronic states of the material. This is the theoretical basis for the experimental method of photoelectron spectroscopy. As this method is also able to determine the relative number of photoelectrons released in a certain KE interval, the results share many similarities with the DOS, mentioned in the introduction.

The DOS is defined as the number of permitted states per unit energy in the energy range between E and δE [15]. If the energy levels of a system have values E_k, then the DOS is:

$$n(E) = \sum_k \delta(E - E_k) \qquad (3.25)$$

In the case of a deep level, electronically isolated from the other levels, a simple peak appears in the DOS at the energy of the level. However, in the case of electronic bands the situation is more complex and it is convenient to define a joint density of states (JDOS) for the conduction and valence bands [15]:

$$D_j(E_{cv}) = \frac{1}{4\pi^3} \int \frac{dS_k}{|\nabla_k(E_{cv})|} \qquad (3.26)$$

Where E_{cv} is the difference between the energy of the conduction and valence bands at a certain value of k. As the bands have a continuous range of energies, it is necessary to change the summation in (3.25) to an integral over the constant energy surface, S_k, which is defined by $E_{cv}(k) = $ constant.

The photoelectric effect may be considered as a three step process:

1) Photoionisation.
2) The ionised electron moves through the material to the surface.
3) The electron escapes from the surface to the vacuum.

With regards to the first step, Fermi's Golden Rule makes use of quantum mechanics and the DOS in (3.25) to calculate the probability of photoionisation at a particular energy (P_{if}):

$$P_{if} = \frac{2\pi}{\hbar} \sum \left|\langle \psi_f | H_{int} | \psi_i \rangle\right|^2 \delta(KE - E_B - \hbar\omega) \qquad (3.27)\ [16]$$

Where ψ_i and ψ_f are the initial and final states in the process and H_{int} is the interaction Hamiltonian. The larger the matrix element is, the greater the probability of photoionisation. In the second step, during the electron's journey to the surface, it may be scattered inelastically. Some examples of inelastic scattering could be plasmon excitation or interband transitions within the material. This causes a background of secondary electrons. In the final step, the electron needs to overcome the potential barrier at the surface (V_b) to escape to the vacuum. Energy conservation must be satisfied at the surface so:

$$\frac{\hbar^2 k_{\perp mat}^2}{2m} = \frac{\hbar^2 k_{\perp vac}^2}{2m} + V_b \qquad (3.28)\ [16]$$

Where $k_{\perp mat}$ and $k_{\perp vac}$ are the momenta perpendicular to the surface in the material and the vacuum, respectively. Moreover, if momentum is conserved at the surface then the following relationship is true, as it is periodic:

$$k_\perp^2 = \frac{2m}{\hbar^2} E_{vac} \cos^2(\varsigma) + \frac{2m}{\hbar^2} V_b \qquad (3.29)$$

Where ς is the angle between the electron momentum and the c axis.

The three step model is normally sufficiently precise to be able to describe most results but there are limitations and physical effects that are not considered, such as:

- The final state has a hole, whose positive charge changes the electronic properties of the material.

- Conservation of momentum only holds to a certain extent.

- The matrix element cannot always be calculated exactly.

- The electromagnetic field of the incident photon changes inside the material.

3.2.2 X-ray absorption

When an x-ray beam passes through a material, its field interacts with electrons in its path, which either scatter the radiation or are ionised by absorbing it due to the photoelectric effect, described in the previous section. Absorption causes the intensity of a narrow parallel monochromatic x-ray beam of intensity I_0 passing through a sample of thickness x to be reduced according to the following expression:

$$I = I_0 e^{-\mu d} \qquad (3.30)$$

Where μ is the linear absorption coefficient, which depends principally on the energy of the beam (E) and the density (ρ), proton number (Z) and mass number (A) of the material:

$$\mu \approx \frac{\rho Z^4}{A E^3} \qquad (3.31)$$

An absorption edge occurs at energies which are just sufficient to cause the ionisation of a core electron, which correspond to the binding energies of electrons in the K, L, M etc. shells of the absorbing elements, as shown in fig 3.9.
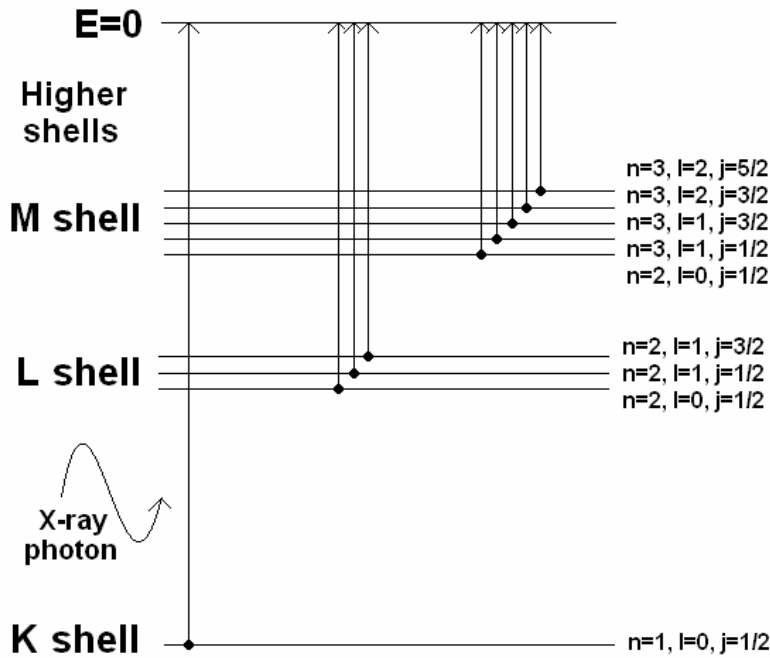
Fig 3.9: Energy level diagram for x-ray absorption

Before the edge, absorption is low but any minor features that may be observed are usually due to the electron transitions from the core level to the higher unfilled or half-filled orbitals. In the case of ionisation, the photoelectron leaving the atom is backscattered by neighbouring atoms. Both the outgoing and backscattered photoelectrons may be considered as waves, which superpose. This produces oscillations after the absorption edge due to the resulting constructive and destructive

interference (fig 3.10). The region from the onset of the edge up to about 50 eV above it is referred to as the x-ray absorption near edge structure (XANES). In this region core electron transitions occur to non-bound levels that are energetically close. The ejected photoelectrons have low kinetic energy and, therefore, experience strong multiple scattering by the first and higher coordinating shells. Therefore, XANES is dependent on the spatial arrangement of atoms neighbouring the absorbing atom, their radial distances and their orientations relative to each other. In practice, extracting all this information directly from an XANES spectrum is very difficult, since multiple scattering complicates the calculations. Therefore, simulations are often used.
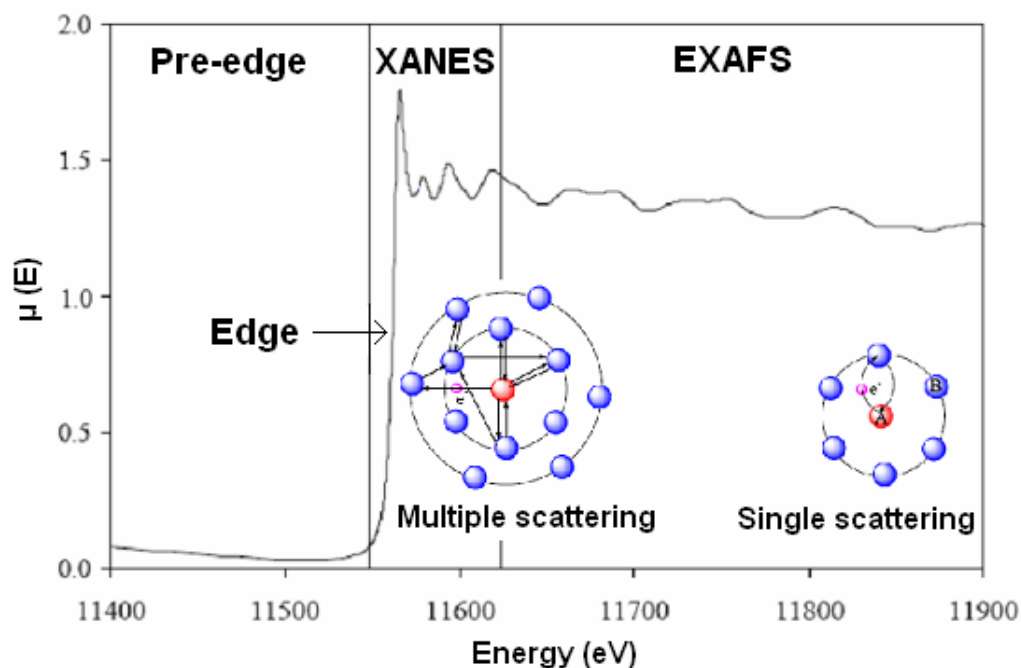
Fig 3.10: Typical XAS spectrum showing different regions.

The extended x-ray absorption fine structure (EXAFS) starts approximately from 50 eV and continues up to 1 keV above the edge. In this region, the photoelectrons have high kinetic energies and single scattering by the nearest neighbouring atoms normally dominates. For this reason, it is theoretically much easier to extract information about the surroundings of the absorbing atoms from EXAFS oscillations than XANES. One of the most fundamental steps during this analysis is the Fourier transform, which separates the neighbouring atoms according to their distances from the absorbing atom. The EXAFS oscillations are described by the following equation [17]:

$$\chi(k) = \frac{\mu(k) - \mu_0(k)}{\mu_0(k)} = \sum_j \frac{N_j F_j(k)}{k R_j^2} e^{-2k^2\sigma_j^2} e^{\frac{-2R_j}{\lambda}} \sin\left[2kR_j + \delta_j(k)\right] \quad (3.32)$$

On the left hand side is the normalised EXAFS, which is corrected for the background signal (μ_0). The right hand side corresponds to the summation of contributions from all the coordination spheres (j), each one with N_j atoms situated at distance R_j from the absorbing atom. k is the wave number of the incident photon and $F_j(k)$ is the

backscattering amplitude. The term $e^{-2k^2\sigma_j^2}$ is obtained after averaging the EXAFS formula when there is a slight Gaussian disorder or when thermal vibrations are taken into account. σ_j is the standard deviation of the position of an atom in sphere j. The factor $e^{-\frac{2R_j}{\lambda}}$ is introduced empirically and represents the probability that the photoelectron will reach the backscattering atom and return without being scattered and without the hole in the absorbing atom being filled, as these two processes tend to break the coherence. The sin function takes into account the interference between the outgoing and backscattered wave, with $2kR_i$ being the phase difference of the backscattered wave due to its outward and return paths. λ is the mean free path of the electron and δ_j is the phase difference introduced by the atomic potentials.

The ionisation of a photoelectron from a material leaves behind a hole in a core level which is filled by an electron from a higher core level, emitting either x-ray fluorescence or an Auger electron, as shown in fig 3.11. In the case of fluorescence, the energy depends on the internal levels of the atoms producing the fluorescence and the intensity depends on the number of these atoms.
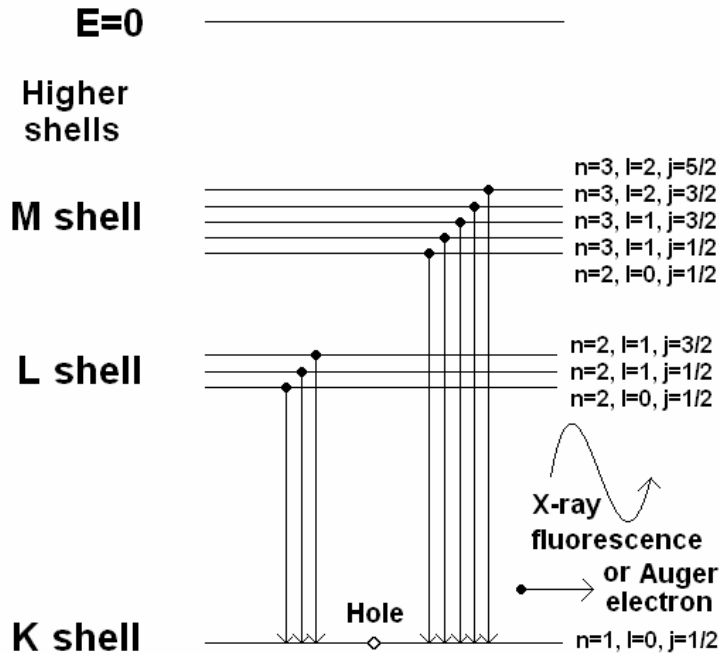
Fig 3.11: Energy level diagram for x-ray fluorescence.

When self-absorption is taken into account the expression for the measured fluorescence intensity is given by [18]:

$$I_f = I_0 \frac{\varepsilon \Delta\Omega}{4\pi} \frac{\mu_x(E)}{\mu_{tot}(E) + \mu_{tot}(E_f)} \left[1 - e^{-[\mu_{tot}(E) + \mu_{tot}(E_f)]d} \right] \quad (3.33)$$

where ε is the fluorescence efficiency, $\Delta\Omega$ is the solid angle range of the detector, $\mu_\chi(E)$ is the absorption for the element of interest, μ_{tot} is the total absorption of the sample for all elements, E_f is the energy of the x-ray fluorescence and d is the sample

thickness. We note that the higher the absorption at the fluorescence energy, the lower the intensity of the detected fluorescence. Finally, the measurement cross section is given by:

$$\sigma_{K\alpha\kappa\beta} = \sigma_K(E)\omega_K F_{K\alpha,\beta} \qquad (3.34)$$

where σ_K and ω_K are the respective cross section and fluorescence yield of the K shell and $F_{K\alpha,\beta}$ is the fractional emission rate of recombination to the K level from the L and M levels ($F_{\alpha,\beta} = I_{K\alpha} + I_{K\beta}$).

3.3 Optical absorption

The response of a material in the presence of an electromagnetic field can be described completely by its complex dielectric function (ε) which has the form:

$$\varepsilon = \varepsilon_1 + i\varepsilon_2 \qquad (3.35)$$

The dielectric function is also defined in the following way:

$$\varepsilon = (n + i\kappa)^2 = \tilde{n}^2 \qquad (3.36)$$

Where n is the real part of the refractive index, κ is the extinction coefficient and ñ is the complex refractive index. Multiplying out the bracket and equating with real and imaginary parts of (3.35) implies:

$$\varepsilon_1 = n^2 - \kappa^2 \qquad (3.37a)$$
$$\varepsilon_2 = 2n\kappa \qquad (3.37b)$$

Supposing that the electromagnetic field is composed of plane waves, incident in the z-direction, normal to the surface of the sample, the electric field ($\vec{E}$) and the magnetic field ($\vec{H}$) would have the form:

$$E_z = E_{z0} e^{i(k_z - \omega t)} \qquad (3.38a)$$
$$H_z = H_{z0} e^{i(k_z z - \omega t)} \qquad (3.38b)$$

Where $\vec{k}$ is the wave vector of the radiation incident on the material. If the wave vector in vacuum is $\vec{k}_0$:

$$\vec{k} = \tilde{n}\vec{k}_0 \qquad (3.39)$$

Substituting into (3.38a) and using (3.36) shows that:

$$E_z = E_{z0} e^{i(\tilde{n}k_{z0}z - \omega t)} = E_{z0} e^{-\kappa z} e^{i(nk_{z0}z - \omega t)} \qquad (3.40)$$

Using Poynting's Theorem, the electromagnetic flux intensity (Φ) may be calculated:

$$\Phi = \left| \vec{E} \times \vec{H}^* \right| = E_{z0} H_{z0} e^{-2\kappa k_{z0}z} = \Phi_0 e^{-2\kappa k_{z0}z} \qquad (3.41)$$

Assuming that this expression describes a transmitted wave within a homogeneous, isotropic and linear (HIL) medium that is semi-infinite (starting at z = 0):

$$2\kappa k_{z0} = \alpha = \frac{4\pi\kappa}{\lambda_0} \qquad (3.42)$$

where α is the absorption coefficient, by direct comparison with:

$$\Phi_T = \Phi_{T0}e^{-\alpha z} \qquad (3.43)$$

In order to remove the constant, it is necessary to normalise the equation. Starting with the intensity of the radiation incident on the material (Φ_0), the transmittance (T) is:

$$T = \frac{\Phi_T}{\Phi_0} = e^{-\alpha z} \qquad (3.44)$$

This expression ignores the effect of reflection. Since materials are not semi-infinite, nor do they absorb perfectly, there is reflection of radiation at the two surfaces, like a Fabry-Perot cavity (fig 3.12). The intensity of this reflection depends on the indices of refraction of the materials at the interfaces (n_1 and n_2).

$$R = \left(\frac{n_2 - n_1}{n_2 + n_1}\right)^2 \qquad (3.45)$$
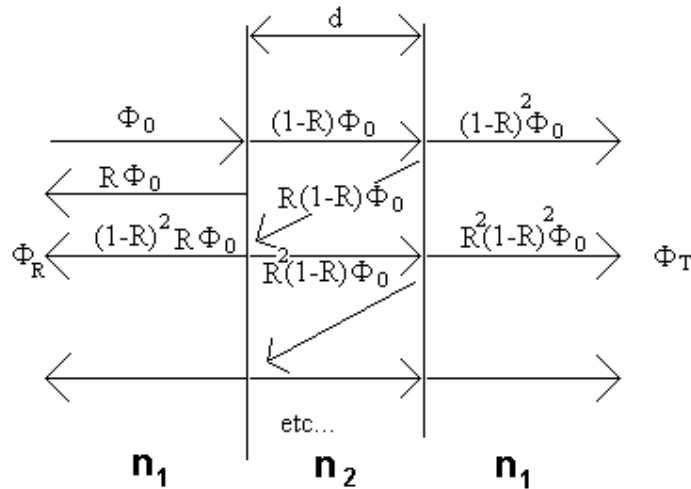
Fig 3.12: Fabry-Perot cavity.

The transmission is the sum of all components that pass through the material, including the rays which are internally reflected m times, where m is an even integer. The sum of the intensities of these rays creates a geometric progression which, on summing to infinity, gives:

$$T = \frac{(1-R)^2 e^{-\alpha d}}{1 - R^2 e^{-2\alpha d}} \qquad (3.46)$$

Where d is the thickness of the material. Using the substitution $x = e^{\alpha d}$, one can rewrite this equation in terms of α to calculate the absorption coefficient from the transmittance, which forms part of the spectral analysis in section (5.4).

$$\alpha = \frac{1}{d} \ln \left(\frac{(1-R)^2}{2T} + \sqrt{\left(\frac{1-R^2}{2T} \right)^2 + R^2} \right) \qquad (3.47)$$

The optical properties of materials are determined by their electronic structure. In the case of semiconductors, it is relatively simple to obtain the absorption coefficient from basic quantum mechanical considerations. We will firstly recall the expressions for direct and indirect transitions without considering the electron-hole electrostatic interaction. Then on we will consider how this interaction leads to the formation of excitons and modifies the absorption edge.

3.3.1 Direct absorption
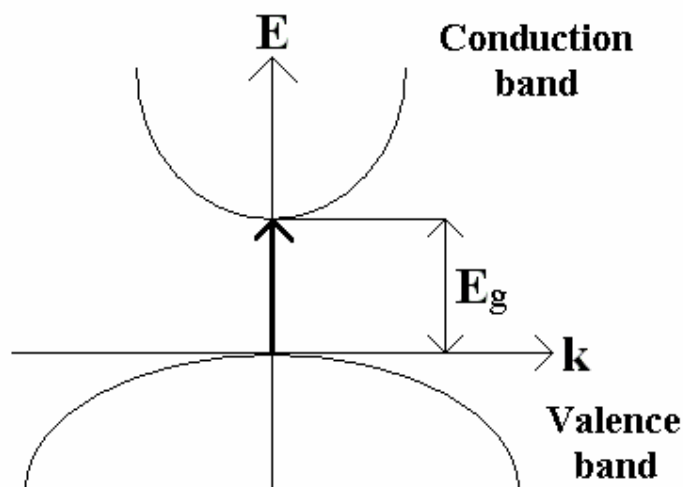
Fig 3.13: Direct absorption.

In a direct semiconductor the VBM and CBM occur at the same value of k. Assuming a parabolic form for the valence and conduction bands (fig 3.13), the energy difference between the two is:

$$E_{cv} = E_g + \frac{\hbar^2 k^2}{2\mu} \qquad (3.48)$$

where μ is the reduced effective mass of the bands. It will also be assumed that the electric dipole approximation is applicable. Sometimes electric dipole transitions are not permitted by the selection rules. In this case, higher orders such as the electric quadrupole would be needed. As in the case of ionising radiation, Fermi's Golden Rule (3.27) gives the absorption probability per unit time of an photon with energy ℏω:

$$P = \frac{2\pi}{\hbar} \left(\frac{e}{m\omega} \right)^2 \left| \frac{E(\omega)}{2} \right| \sum_k |P_{cv}|^2 \delta(E_{cv}(k) - \hbar\omega) \qquad (3.49)$$

where P_{cv} is the transition matrix element [15]. By considering the power loss of the field passing through the medium, P may be related to the absorption coefficient:

$$\alpha(\hbar\omega) = \frac{\pi e^2}{\varepsilon_0 m^2 cn\hbar\omega} \sum_k |P_{cv}|^2 \delta(E_{cv}(k) - \hbar\omega) \qquad (3.50)$$

As previously seen, within a band there is a continuous range of transition energies, so it is necessary to use the JDOS, defined in (3.26). In the case of electric dipole direct absorption:

$$D_j(E_{cv}) = \left[\frac{2^{1/2}\mu^{3/2}}{\pi^2\hbar^3}\right]\sqrt{E_{cv} - E_g} \qquad \text{when } E_{cv} > E_g \qquad (3.51)$$

When $E_{cv} < E_g$ the JDOS is zero. On substituting 3.45 in 3.44, it is found that close to E_d, the absorption coefficient has the following form:

$$\alpha(\hbar\omega) = A\sqrt{(\hbar\omega - E_g)} \qquad \text{when } \hbar\omega > E_g \qquad (3.52)$$

where A is a constant. When $\hbar\omega < E_g$ there is no absorption. Therefore, if a graph of α^2 against $\hbar\omega$ is drawn, a direct gap would fit to a straight line, crossing the energy axis at E_g.

3.3.2 Indirect absorption
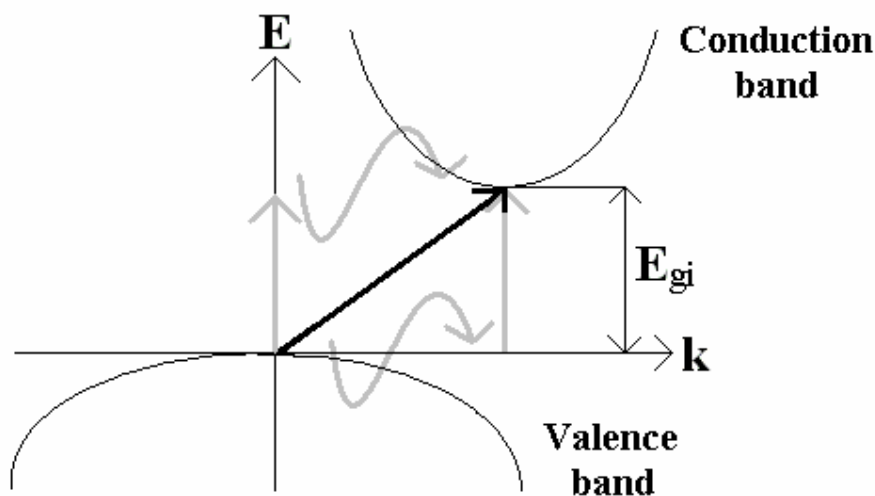
Fig 3.14: Indirect absorption.

At an indirect gap (fig 3.14) a photon can excite an electron from the valence band to the conduction band by interacting with a phonon to satisfy momentum conservation, since the phonon supplies the required difference in wave vector. There are two possible ways that this can be done, as the electron can absorb or emit phonons. Therefore, conservation of energy and momentum demand that:

$$\hbar\omega = E_{cv} \pm E_f \qquad (3.53a)$$

$$\vec{k}_v - \vec{k}_c = \pm\vec{Q} \qquad (3.53b)$$

where E_f is the phonon energy, $\vec{Q}$ is its wave vector and $\vec{k}_v$ and $\vec{k}_c$ are the respective wave vectors of the VBM and the CBM. Indirect absorption is a second order process and, therefore, Fermi's Golden Rule needs to be taken to the second order by using perturbation theory to express the probability of indirect absorption in unit time:

$$P_{ind} = \frac{2\pi}{\hbar} \sum_{\vec{k}_c, \vec{k}_v} \left| \sum_i \frac{\langle f|H_{ef}|i\rangle\langle i|H_{eR}|0\rangle}{E_{i0} - \hbar\omega} \right|^2 \delta(E_c(\vec{k}_c) - E_v(\vec{k}_v) - \hbar\omega \pm E_f) \quad (3.54) \ [15]$$

where H_{ef} and H_{eR} are the respective Hamiltonians for the electron-phonon and electron-radiation interactions. E_{i0} is the energy of the initial state. Since the VBM and the CBM do not occur at the same wave vector, separate densities of states need to be used for the two bands, rather than the joint one. Assuming parabolic bands in three dimensions:

Samuel John Gilliland

$$D_v \propto \sqrt{-E_v} \qquad \text{when } E_v < 0 \qquad (3.55)$$

where D_v is the DOS of the valence band (which is zero when $E_v > 0$) and

$$D_c \propto \sqrt{E_c - E_{gi}} \qquad \text{when } E_c > E_{gi} \qquad (3.56)$$

where D_c is the DOS of the conduction band (which is zero when $E_c < E_{gi}$). Substituting into 3.22 and integrating over the valence band states, followed by the conduction band, the following form of the absorption coefficient is obtained:

$$\alpha(\hbar\omega) = B\left[n(\hbar\omega + E_f - E_{gi})^2 + (n+1)(\hbar\omega - E_f - E_{gi})^2\right] \qquad \text{when } \hbar\omega > E_{gi} \pm E_f \quad (3.57)$$

where B is another constant. The first term corresponds to the phonon absorption contribution (threshold at $\hbar\omega = E_{gi} - E_f$) and the second term corresponds to the phonon emission contribution (threshold at $\hbar\omega = E_{gi} + E_f$). When $\hbar\omega < E_{gi} \pm E_f$ there is no absorption. Therefore, on a graph of $\alpha^{1/2}$ against $\hbar\omega$, an indirect gap would fit to a straight line crossing the energy axis at a value of $E_{gi} \pm E_f$.

3.3.3 Excitonic absorption

An exciton is a bound state between a free electron and a free hole which attract each other by the Coulomb force. It has less energy than the sum of the energies of the two separate particles, is electrically neutral and is free to move through a crystal until disassociated. Elliot [19] expressed the wave function of an exciton at a direct gap in three dimensions as a linear combination of Bloch functions (ψ) of the electron (e) and hole (h):

$$\Psi(\vec{r}_e, \vec{r}_h) = \sum_{\vec{k}_e, \vec{k}_h} C(\vec{k}_e \vec{k}_h) \varphi_{\vec{k}_h}(\vec{r}_e) \varphi_{\vec{k}_e}(\vec{r}_h) \quad (3.58)$$

where $\vec{r}$ is the position and C is a constant. By considering an exciton as a particle with reduced mass μ at the position of its centre of mass, the Schrödinger equation may be solved to show that the electronic states of an exciton are like those of a hydrogen atom (1s, 2s, etc.) with energies of:

$$E_r(n) = E_d - \frac{R^*}{n^2} \qquad (3.59)$$

where n is an integer and R^* is the effective Rydberg constant of the exciton (as opposed to the Rydberg constant, R) which is defined as:

$$R^* = \frac{\mu e^4}{2\hbar^2 \varepsilon^2} \times \frac{1}{(4\pi\varepsilon_0)^2} = R \frac{\mu}{m_0} \left(\frac{\varepsilon_0}{\varepsilon} \right)^2 \qquad (3.60)$$

where ε is the low frequency dielectric constant. It may also be shown that the exciton has an effective Bohr radius (as opposed to Bohr radius, a_0) of:

$$a^* = \frac{\varepsilon \hbar^2}{\mu e^2} \times 4\pi\varepsilon_0 = a_0 \frac{\varepsilon \mu_0}{\varepsilon_0 \mu} \qquad (3.61)$$

Finally, by using Fermi's Golden Rule for excitonic absorption:

$$P_X = \frac{2\pi}{\hbar} \sum_f \left| \left\langle f | H_{XR} | 0 \right\rangle \right|^2 \delta(E_f(\vec{K}) - E_d - \hbar\omega) \qquad (3.62)$$

where H_{XR} is the Hamiltonian for the exciton-radiation interaction, an expression for the absorption coefficient of the exciton may be obtained. Toyozawa [20] extended this expression by taking into account the exciton-phonon interaction, which causes a broadening of the exciton, giving it the form of a Lotentzian profile by means of a convolution. Goñi et al. [21] then formed an analytical expression in which the absorption is split into two parts:

- The discrete excitonic states (a summation) which may be evaluated directly.

Samuel John Gilliland

- The contribution from the band-to-band absorption continuum (an integral) which may be evaluated in the complex plane.

The final expression which was found for the absorption coefficient of an excitonic absorption edge was:

$$\alpha(\hbar\omega) = \frac{C_0\Re^{1/2}}{\hbar\omega}\left\{\sum_{n=1}^{\infty}\frac{2\Re}{m^3}\frac{\Gamma_m}{(\hbar\omega-E_m)^2+\Gamma_m^2}+\frac{1}{2}\left[\frac{\pi}{2}+\arctan\left[\frac{\hbar\omega-E_d}{\Gamma_C}\right]\right]\right.$$

$$\left.-\sum_{m=1}^{\infty}\frac{\Re}{m^3}\frac{\Gamma_c}{(\hbar\omega-E_m)^2+\Gamma_C^2}+\frac{\pi}{2}\frac{\sinh(2u^+)}{\cosh(2u^+)-\cos(2u^-)}\right\} \qquad (3.63)\ [21]$$

where

$$u^{\pm}=\pi(\frac{\Re}{2})^{1/2}\left[\frac{\left[(\hbar\omega-E_d)^2+\Gamma_C^2\right]^{1/2}\pm(\hbar\omega-E_d)}{(\hbar\omega-E_d)^2+\Gamma_C^2}\right]^{1/2} \qquad (3.64)$$

3.3.4 Low temperature effects

The vibrational properties of a solid are strongly related to the temperature, as phonons are bosons and their energy distribution obeys a Bose-Einstein relationship:

$$f(\hbar\omega_p) = \frac{1}{e^{\frac{\hbar\omega_p}{kT}} - 1} \qquad (3.65)$$

where k is the Boltzmann constant and f is the probability that a phonon of energy $\hbar\omega_p$ will be excited at temperature T. There are four types of phonons which cover a wide range in energy and wave vector, since they can be longitudinal acoustic (LA), longitudinal optical (LO), transverse acoustic (TA) or transverse optical (TO). Phonon dispersion curves at the Γ point may be determined experimentally by Raman scattering.

The electron-phonon interaction may be described by a Hamiltonian with the following form:

$$H_{e-p}(\vec{r}_i, \delta\vec{R}_j) = \sum_j \left(\frac{\partial H_e(\vec{r}_i, \vec{R}_j)}{\partial \vec{R}_j} \right)\bigg|_{\vec{R}_{j0}} \cdot \delta\vec{R}_j + ... \qquad (3.66) \ [15]$$

where $\vec{r}_i$ are the positions of the electrons, $\delta\vec{R}_j$ are the changes in the ion positions and H_e is the electronic Hamiltonian. The energy change in a non-degenerate electronic band in the presence of a phonon may be approximated by a change in the electronic Hamiltonian so:

$$\left(\partial H_e / \partial \vec{R}_j \right)\bigg|_{\vec{R}_{j0}} \cdot \delta\vec{R}_j \approx \left(\partial E_{n\vec{k}} / \partial \vec{R}_j \right)\bigg|_{\vec{R}_{j0}} \cdot \delta\vec{R}_j \qquad (3.67)$$

where n is the band index and k is the wave vector. Therefore, when a phonon propagates through a crystal, the displacement of the atoms can provoke a lattice deformation which changes the electronic energies at different points of the Brillouin zone. The change may be quantified using deformation potentials, which are related to the value of $\left(\partial E_{n\vec{k}} / \partial \vec{R}_j \right)\big|_{\vec{R}_{j0}}$. In general, the deformation caused by phonons reduces the bandgap energy. Therefore, when the temperature decreases, the energy of the gap increases, as there are less phonons. There are various models to describe this behaviour. One, which is purely empirical, is called Varshni's law [22]:

$$E = a - \frac{\alpha T^2}{\beta + T} \qquad (3.68)$$

where E is the energy of the gap and α and β are adjustable parameters. A more rigorous model is based on the Bose-Einstein distribution (3.65). If the number of phonons emitted by the lattice at a certain temperature is proportional to f($\hbar\omega_p$) and the reduction in the gap is proportional to the number of phonons, one could say:

$$\Delta E_{emission} = -Af(\hbar\omega_p) \qquad (3.69)$$

However, the lattice can also absorb phonons. At high temperature it is supposed that the number of phonons absorbed would be balanced with the number of phonons emitted but in the limit T→0, (3.69) also tends to 0 and the lattice can only absorb phonons, since it does not have sufficient thermal energy to emit them. Therefore, it is necessary to introduce the "+1" term in the following expression:

$$\Delta E_{absorption} = -A(f(\hbar\omega_p) + 1) \qquad (3.70)$$

The total change in energy is obtained by adding the contributions from (3.69) and (3.70):

$$\Delta E = -A(2f(\hbar\omega_p) + 1) \qquad (3.71)$$

A phonon can also interact with an exciton and, if the energy of the phonon is greater than the Rydberg energy of the exciton (3.59), the interaction will cause the thermal disassociation of the exciton. Therefore, at low temperature, where this is less likely, one would expect excitons to have a higher average lifetime. A Bose model derived in a similar way to (3.70) describes the width of the exciton, which is inversely proportional to the lifetime:

$$\Delta\Gamma = B(2f(\hbar\omega_p) + 1) \qquad (3.72) \; [22]$$

where $\Delta\Gamma$ is the broadening of the exciton which occurs when the temperature increases. It is not necessary for the same type of phonon to be responsible for the change in gap position and the broadening of the exciton because they are related to different electronic transitions, so they may need photons with different energies or wave vectors. In the case of the gap position, interband transitions are involved, whereas with the exciton broadening they are intraband transitions.

3.3.5 High pressure effects

On forming a crystal, the orbitals in the atoms of the isolated molecules begin to overlap with other orbitals in the same quantum state, causing interference between the wave functions, which produces hybridised orbitals with different energies. Half of these correspond to constructive interference between the original orbitals and they form bonding orbitals. The other half corresponds to destructive interference and they form antibonding orbitals. In a semiconductor, the set of bonding and antibonding orbitals often forms the valence and conduction bands, respectively. Between both bands is the gap, with energy E_g, as shown in fig 3.15.
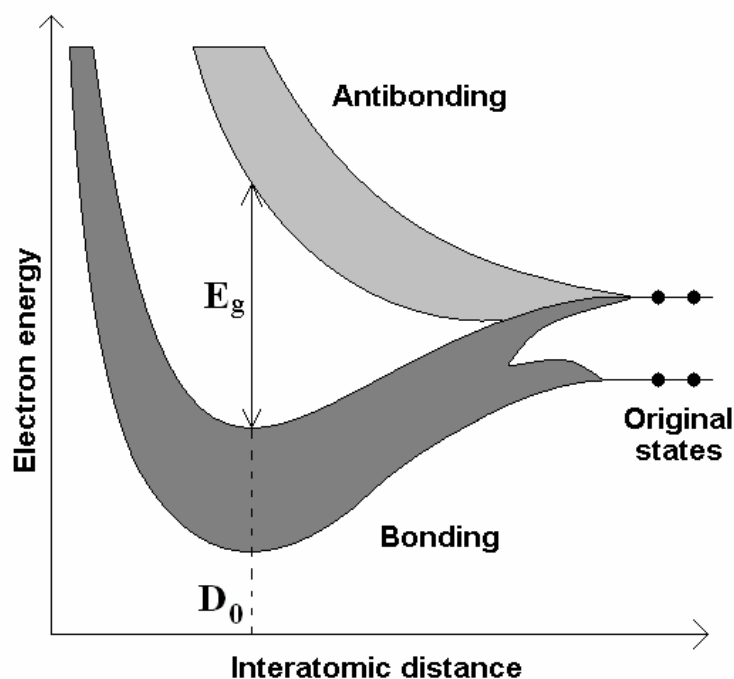
Fig 3.15: The formation of electronic bands.

On applying hydrostatic pressure to a material, the interatomic distance is reduced, which normally produces an increase in the gap because the energy separation between the bonding and antibonding orbitals increases, as seen in fig 3.15. The physical origin of this increase is the repulsive potential between the nuclei, provided it increases at a greater rate than the attractive potential between the nuclei and electrons. This is particularly true in covalently bonded materials, for reasons that shall be described shortly. As the principal bonding in ZnO is sp^3 covalent, this would be the expected behaviour in both the pure material and its DMSs. To express quantitatively the effect that hydrostatic pressure has on the gap, we shall firstly define the bandgap pressure coefficient:

$$a_P = \frac{dE_g}{dP} \qquad (3.73)$$

Samuel John Gilliland

As pressure causes a volume change, high pressure effects may also be described in terms of a volume deformation potential:

$$a_V = \frac{dE_g}{d \ln V} \qquad (3.74)$$

These two quantities are related by the equation:

$$a_P = -\frac{a_V}{B} \qquad (3.75)$$

Where B is the bulk modulus:

$$B = -\frac{dP}{d \ln V} \qquad (3.76)$$

Paul found an empirical rule to estimate the bandgap pressure coefficient for tetrahedral semiconductors based on the points in the Brillouin Zone between which the fundamental transition occurs. For a direct gap at the Γ point, as in wurtzite ZnO, the rule estimates a coefficient of the order of 100 meV/GPa [23]. However, this rule frequently breaks down because it cannot explain the variation in bandgap pressure coefficient observed in many common cation systems, such as GaN (~40 meV/GPa) to GaP (~100 meV/GPa) to GaSb (~140 meV/GPa) [24]. Therefore Wei and Zunger developed a model based on LDA calculations, using the relativistic linearised augmented plane-wave (LAPW) method [25], with specific details of the calculations given in their paper [24]. Although these calculations were only applied to semiconductors with cubic diamond and zincblende crystal structures, they are also applicable to wurtzite structures, such as ZnO. This is because the tetrahedral coordination environment in zincblende and wurtzite are very similar. The only differences are that in wurtzite, the ratio of lattice parameters $c/a = \eta$ may vary and there is also the u factor to take into account (the ratio between the cation-anion distance along the c-axis and the lattice parameter c). Therefore, a rigorous model would start by defining the volume deformation potential in the following way:

$$\frac{dE_g}{d \ln V} = \frac{\partial E_g}{\partial \ln V} + \frac{\partial E_g}{\partial \eta} \frac{\partial \eta}{\partial \ln V} + \frac{\partial E_g}{\partial u} \frac{\partial u}{\partial \ln V} \qquad (3.77)$$

Naturally, this would complicate the calculation considerably. However, in most cases the additional terms are unnecessary because they are very small. For example, in wurtzite InN, $\partial \eta / \partial \ln v = -0.001$ and $\partial u / \partial \ln v = 0.030$ [24].

In the calculations, the contributions to the volume deformation potential from the conduction band and valence band are found separately and then combined through the relationship:

$$a_V = \frac{dE^{CVM}}{d \ln V} - \frac{dE^{VBM}}{d \ln V} \qquad (3.78)$$

In cubic diamond and zincblende semiconductors, the pressure coefficient of the CBM is always positive for two main reasons. Firstly, there is an increase in kinetic energy on applying high pressure, which is inversely proportional to the square of the anion-cation bond length (l). Secondly, there is often an accompanying increase in s-s repulsion between the antibonding orbitals at the CBM. The energy of the CBM is described by the following equation, obtainable from the simple tight-binding model [26]:

$$E^{CBM} = \left(\frac{\varepsilon_s^c + \varepsilon_s^a}{2} \right) + \sqrt{\left(\frac{\varepsilon_s^c - \varepsilon_s^a}{2} \right)^2 + V_{ss}^2} \qquad (3.79)$$

where ε_s^c and ε_s^a are the s orbital energies of the cation and anion, respectively, and V_{ss} is the coupling potential between the two states. V_{ss} is inversely proportional to l^2, so by taking the derivative with respect to volume (proportional to l^3), the contribution to the volume deformation potential produced by s-s repulsion is:

$$a_V^{CBM}(ss) = \frac{-4b_{ss}^2}{3l^2 \sqrt{\left(\varepsilon_s^c - \varepsilon_s^a \right)^2 l^4 + 4b_{ss}^2}} \qquad (3.80)$$

Where b_{ss} is a compound-dependent constant. The magnitude of $a^{CBM}v(ss)$ is mainly affected by the type of bonding in the material, whether it be ionic or covalent. The covalent and ionic contributions to the gap energy may be separated by means of the Philips-Van Vechten model [27-29]. Starting with the Fourier transform of the crystal potential, we note that it has symmetric (S) and antisymmetric (AS) parts depending on how the charge in the bond is distributed.

$$V(\vec{G}) = V_S(\vec{G})e^{i\vec{G}\cdot R_S} + V_{AS}(\vec{G})e^{i\vec{G}\cdot \vec{R}_{AS}} \qquad (3.81)$$

where $\vec{G}$ is a reciprocal lattice vector. It can be shown that:

$$V(\vec{G}) = \left(V_S(\vec{G}) + V_{AS}(\vec{G}) \right)\cos \vec{G}\cdot \vec{\tau} + i\left(V_S(\vec{G}) - V_{AS}(\vec{G}) \right)\sin \vec{G}\cdot \vec{\tau} \qquad (3.82)$$

where

$$2\vec{\tau} = \vec{R}_S - \vec{R}_{AS} \qquad (3.83)$$

Therefore, the gap (E_g) has two parts: one which comes from the covalent character, related to the symmetric (homopolar) part of the potential (E_h), and the other which comes from the ionic character, related to the antisymmetric (heteropolar) part of the potential (C).

$$E_g = 2\left| V(\vec{K}_M) \right| = \left| E_h + iC \right| = \sqrt{E_h^2 + C^2} \qquad (3.84)$$

In (3.84) the Philips-Van Vechten model is used to separate the gap into its covalent (homopolar) and ionic (heteropolar) components. Returning to (3.80), in the covalent limit, $\epsilon_s^c = \epsilon_s^a$. Therefore the expression simplifies to:

$$a_V^{CBM}(ss) = \frac{2b_{ss}}{3l^2} \qquad (3.85)$$

Hence, as l decreases, the volume deformation potential typically increases by a relatively large amount. However, in the ionic limit the behaviour is not as clear as (3.80) simplifies to:

$$a_V^{CBM}(ss) = \frac{-4b_{ss}}{3l^4\left(\varepsilon_s^c - \varepsilon_s^a\right)} \qquad (3.86)$$

The volume deformation potential is inversely proportional to the energy difference between the s orbitals of the cation and anion. As a result, ionic bonds are often insensitive to pressure.

In cubic diamond and zincblende semiconductors, the pressure coefficient of the VBM is usually also affected by two main factors. Firstly there is the kinetic energy increase on applying high pressure, which increases its energy in a similar way to the CBM. Secondly there is the accompanying increase in p-p coupling between the bonding states at the VBM, which decreases its energy. The energy of the VBM in the simple tight binding model is given by:

$$E^{VBM} = \left(\frac{\varepsilon_p^c + \varepsilon_p^a}{2}\right) + \sqrt{\left(\frac{\varepsilon_p^c - \varepsilon_p^a}{2}\right)^2 + V_{pp}^2} \qquad (3.87)$$

where ε_p^c and ε_p^a are the p orbital energies of the cation and anion, respectively, and V_{pp} is the coupling potential between the two states. By following a similar procedure to that used with s-s repulsion, it may be shown that p-p coupling also increases on decreasing l and the energy difference between the cation and anion p orbitals. As the effects of the kinetic energy and p-p coupling partially cancel, the pressure coefficient of the VBM, although usually positive, is much smaller than that of the CBM. However, in the ZnO DMSs, it is also necessary to take into account the pressure effect on p-d repulsion, which was introduced in section 3.1.2. The shift in the VBM produced by the coupling is given in (3.22) so, by taking the derivative with respect to volume, we once again find that the repulsion increases with decreasing l and the energy difference between anion p and cation d orbitals (ϵ_p^a - ϵ_d^c). If the cation d orbitals are more tightly bound than the anion p orbitals, the sign of the energy difference and, hence, the change in volume deformation potential is positive and vice versa. Therefore, p-d repulsion could cause the pressure coefficient of the VBM to increase or decrease, depending on the position of the cation 3d levels.

Once the combined conduction band and valence band volume deformation potentials are determined, the bulk modulus may be calculated by fitting the total energy, found in the calculations, to Murnaghan's equation of state:

$$B(P) = B(O) + B'P \qquad (3.88) [30]$$

where B' is the the pressure derivative of the bulk modulus. The pressure coefficient may then be obtained by applying (3.75). As only cubic diamond and zincblende

semiconductors were considered in Wei and Zunger's calculations, the closest material to ZnO for which a pressure coefficient is given is ZnS, with a predicted value of 47 meV/GPa. However, we note that the predicted pressure coefficients decrease in the series ZnTe to Zn Se to ZnS by 37 meV/GPa so, following this trend, the expected coefficient for ZnO would be considerably lower. Zhang et al. [31] used a different theoretical approach, the ab-initio pseudopotential plane-wave method, to calculate the pressure coefficient of wurtzite ZnO directly and a value of 21 meV/GPa was obtained.

This theory could potentially have a significant effect on the pressure coefficient of ZnO based DMSs. This is because substituting Zn for another TM changes the strength of the s-s interaction that determines the pressure dependence of the CBM via equation (3.80). This is the principal contribution to the bandgap pressure coefficient because the pressure dependence of the VBM energy is small. On substituting Zn for any of the investigated dilute cations, the decrease in the TM 4s binding energy is approximately constant with an average value of 1.7 eV [32]. Assuming that the anion s orbitals do not alter their energy considerably, it is clear that the value of $\left(\varepsilon_s^c - \varepsilon_s^a\right)$ increases, resulting in a decrease in the corresponding volume deformation potential. For this reason, increasing the dilute cation concentration would be expected to cause a decrease in the bandgap pressure coefficient. The physical explanation behind this trend is that as the dilute cation concentration increases, the bandgap increases, showing the material to be more compact and, therefore, more difficult to compress further. As the dilute cation is changed, the pressure dependence of the p-d repulsion can not be ignored. However, it is thought that this factor would be much smaller than the effect of s-s coupling, in agreement with the theory presented in section 3.1.2.

Samuel John Gilliland

3.4 Magnetic properties

3.4.1 Fundamentals

When a magnetic field ($\vec{H}$) is applied to a material, a different magnetic moment ($\vec{m}$) is induced in every atom of the material. The average value of $\vec{m}$ per unit volume of the material is called the magnetisation ($\vec{M}$). The magnetic susceptibility (χ) quantifies the degree of magnetization of a material in response to an applied magnetic field:

$$\vec{M} = \chi\vec{H} \qquad (3.89)$$

Magnetic permeability (μ) is the degree of magnetization of a material that responds linearly to an applied magnetic field and it is defined by the following equation:

$$\vec{B} = \mu\vec{H} \qquad (3.90)$$

where $\vec{B}$ is the magnetic induction, defined by:

$$\vec{B} = \mu_0\left(\vec{H} + \vec{M}\right) \qquad (3.91)$$

where μ_0 is the permeability of free space. If μ_r is the relative permeability of the material then:

$$\mu = \mu_0\mu_r \qquad (3.92)$$

and

$$\chi = \mu_r - 1 \qquad (3.93)$$

At least fourteen different kinds of magnetic behaviour have been observed in solids [33]. However, on an atomic level only two basic effects exist: paramagnetism and diamagnetism. Diamagnetism, on one hand, is the repulsion of an atom out of an applied magnetic field as a result of the interaction between the field and orbitals containing paired electrons. Therefore, it is observed in all elements apart from hydrogen. It is independent of temperature and roughly proportional to the molecular mass. Paramagnetism, on the other hand, is the attraction of an atom into an applied magnetic field, as a result of the interaction between the field and orbitals containing unpaired electrons. It is normally temperature dependent. In a solid, the interaction between the magnetic moments of the constituent atoms determines the overall magnetic properties of the material. This introduces new properties that go beyond simple diamagnetism and paramagnetism, especially when taking into account that the magnetic behaviour of a material can be different along different axes. The five principle bulk magnetic behaviours are diamagnetism, paramagnetism, ferromagnetism, antiferromagnetism and ferrimagnetism and fig 3.16 shows how the magnetic moments are aligned in these different systems. They shall be briefly described here before focussing in more detail on paramagnetism and ferromagnetism.
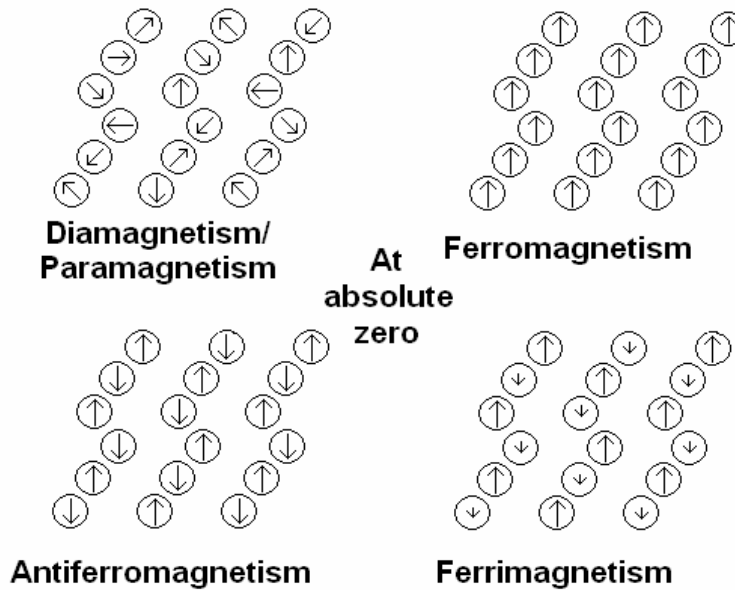
Fig 3.16: Alignment of magnetic moments with no applied field at absolute zero for different magnetic behaviours.

Diamagnetism: In the absence of an applied magnetic field, the magnetic moments have no particular orientation. However, when a field is applied, the magnetic moments tend to align in such a way as to oppose it. All materials show diamagnetism but, as it is a relatively weak effect (except for in superconductors), if the material also shows another behaviour, the latter will probably dominate. The magnetic susceptibility of diamagnetic materials is small and negative.

Paramagnetism: Like diamagnetic materials, the magnetic moments have no particular orientation in the absence of an applied magnetic field but when one is applied, the magnetic moments will tend to align themselves in its direction. However, this alignment is weak and, once the field is removed, the moments return to a random distribution. Pure paramagnetism is rare, as materials normally show other behaviours at low temperature. However, as we shall see, all materials that are not diamagnetic become paramagnetic beyond a certain critical temperature. The magnetic susceptibility of paramagnetic materials is small and positive.

Ferromagnetism: As in paramagnetic materials, an applied field will cause the magnetic moments to align with the field. However, when the field is removed, the magnetic moments remain aligned in the same direction, an effect known as spontaneous magnetisation. This is possible because there is no quantum mechanical overlap between the orbitals containing electrons with the same spin states so it is energetically favourable to remain in the aligned state, as this minimises electron-electron repulsion. At high temperature, the thermal energy becomes large enough to destroy the macroscopic magnetic ordering and the material becomes paramagnetic. The critical temperature at which this transition occurs is called the Curie temperature. The magnetic susceptibility of ferromagnetic materials is large and positive.

Antiferromagnetism: The behaviour of an antiferromagnetic material is similar to that of a ferromagnetic material; however, spontaneous magnetisation causes adjacent

magnetic moments to become anti-parallel, resulting in no overall magnetic moment. Therefore, at low temperature, only diamagnetism is observed but as the temperature increases there comes a point, as in ferromagnetic materials, where paramagnetic behaviour takes over. The critical temperature at which this transition occurs is called the Néel temperature. Therefore, the curves corresponding to antiferromagnetic susceptibility in fig 3.17 are a cross between diamagnetic and paramagnetic behaviour.
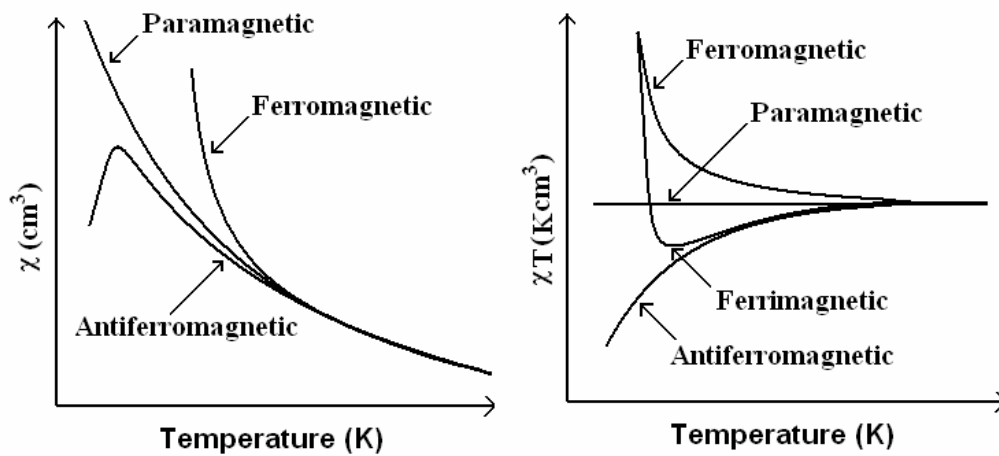
Fig 3.17: Typical magnetic susceptibility of different types of magnetic materials.

Ferrimagnetism: If the magnitudes of opposing magnetic moments in an antiferromagnetic material are not equal then the material may be referred to as ferrimagnetic. As the uncompensated part of the magnetisation remains at low temperatures, the behaviour of the material is Ferromagnetic until the critical temperature where paramagnetic behaviour, once again, takes over. Therefore, its magnetic susceptibility, shown on the right hand side of fig 3.17, is a cross between ferromagnetic and paramagnetic behaviour.

3.4.2 Paramagnetism

The magnetic properties of materials are usually characterised by the temperature and applied field dependence of the magnetic susceptibility. Most paramagnetic materials show temperature dependent magnetic susceptibility; however, this is not always the case, as coupling between the magnetic ground state and non-thermally populated excited states can cause temperature independent paramagnetism in certain materials [34]. Nevertheless, in an ideal paramagnetic material, the temperature dependence of the magnetic susceptibility is described by Curie's law:

$$\chi_m = \frac{Ng^2\mu_B^2}{3k_B T} J(J+1) \qquad (3.94)$$

where χ_m is the molar magnetic susceptibility, N is Avagadro's number, g is the Landé g factor, μ_B is the Bohr magneton, k_B is the Boltzmann constant and J is the total angular momentum of the paramagnetic molecule or atom. By grouping all constant terms and replacing them by the Curie constant (C), (3.94) is simplified to:

$$\chi_m = \frac{C}{T} \qquad (3.95)$$

Curie's law only holds when H/kT is small; however, the field dependence of an ideal paramagnetic material may be described by the Brillouin function at any value of H/kT [35]:

$$M = Ng\mu_B J \cdot B_J(y) \quad (3.96)$$

where

$$B_J(y) = \frac{2J+1}{2J}\coth\left(\frac{2J+1}{2J}y\right) - \frac{1}{2J}\coth\left(\frac{1}{2J}y\right) \qquad (3.97)$$

and

$$y = \frac{g\mu_B JH}{kT} \quad (3.98)$$

This function makes it possible to determine the spin state of a paramagnet even when the chemical composition of the material is unknown.

3.4.3 Ferromagnetism

An important feature of ferromagnetic materials and, indeed, all materials that remain magnetised after the applied field is removed is the domain strucutre. The unmagnetised material consists of a series of magnetic domains, where the magnetisation of each domain is in a particular direction but, as these directions are randomly oriented, there is no overall magnetisation. As a field is applied and increased, the domains oriented in the direction of the field grow and the other domains diminish until all the magnetic moments are aligned and the material is said to be magnetically saturated, as shown in fig 3.18.
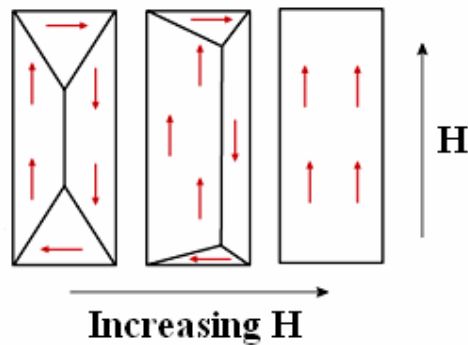
Fig 3.18: Magnetisation and the domain structure.

Another feature of ferromagnetic materials is the hysteresis observed on reversing the direction of the applied field (see fig 3.19). This occurs because energy is required to rearrange the domain walls within the material. The hysteresis loop is characterised by two points: the remnant magnetisation (M_r) and the coercive field (H_c).
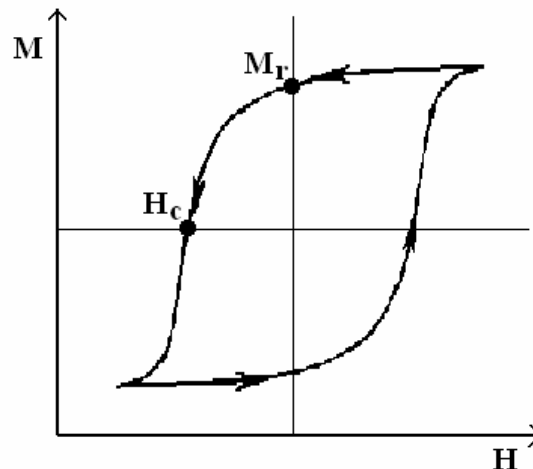
Fig 3.19: Ferromagnetic hysteresis.

Curie's law (3.95) describes the temperature dependence of the magnetic susceptibility for paramagnets. However, ferromagnetic behaviour deviates from this law, as shown in fig 3.20. To take into account this deviation, a constant that is

proportional to the strength of Ferromagnetic interactions, the Weiss constant (Θ), also known as the Curie-Weiss temperature, is included:

$$\chi_m = \frac{C}{T - \Theta} \quad (3.99)$$

This equation also applies to antiferromagnetic interactions, which have a negative Weiss constant, whereas ferromagnetic interactions have a positive value.
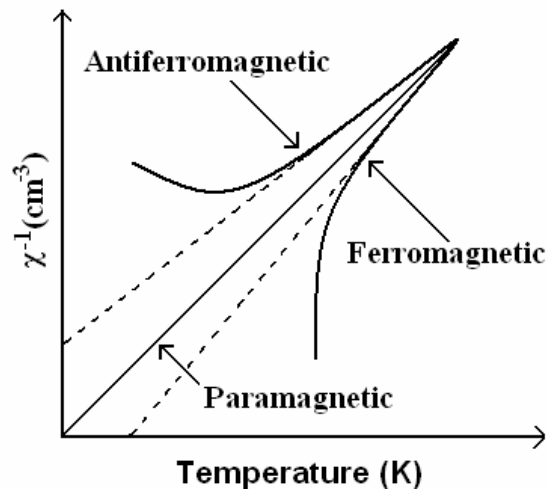
Fig 3.20: Deviation of ferromagnetic behaviour from the Curie law.

When considering a ferromagnetic DMS it is necessary to take into account the effect of the dilute cation proportion (x). Assuming that the deviation from Curie's law varies linearly with x and that the magnetic properties of the host material are negligible:

$$\chi_m = \frac{C_0 x}{T - \Theta_0 x} \quad (3.100)$$

Where C_0 and Θ_0 are the respective Curie and Weiss constants when x=1.

Although the behaviour of ferromagnetic materials has been described, the physical explanation as to why it occurs has still not been discussed. Exchange interactions between electronic spins are the origin of spontaneous magnetisation, so this shall be the subject of the final theory section. The procedure followed is similar to that of Hernando [36].

4.3.4 Exchange Interactions

Direct exchange:

The description of all magnetic exchange interactions is based on coulomb repulsion and the Pauli Exclusion Principle (PEP). We shall consider an isolated atom with two electrons (1 and 2), which occupy the same atomic orbital but with different values of l_z so their spins may be aligned (symmetric) or anti-aligned (antisymmetric). As electrons are fermions the total wavefunction must be antisymmetric. Therefore if the spin is symmetric, the orbital wavefunction is antisymmetric and vice versa. Hence, in the absence of electron-electron repulsion, the total orbital wavefunction for aligned spins is:

$$\Psi_A = [\psi_a(1)\psi_b(2) - \psi_a(2)\psi_b(1)] \qquad (3.101)$$

and in the case of anti-aligned spins:

$$\Psi_S = [\psi_a(1)\psi_b(2) + \psi_a(2)\psi_b(1)] \qquad (3.102)$$

where ψ_a and ψ_b are the wavefunctions of the individual electrons. On including the Coulomb interaction, the energies associated with the wavefunctions are:

$$E_A = \left\langle \Psi_A \left| \frac{e^2}{(4\pi\varepsilon_0|\vec{r}_1 - \vec{r}_2|)} \right| \Psi_A \right\rangle \text{ and } E_S = \left\langle \Psi_S \left| \frac{e^2}{(4\pi\varepsilon_0|\vec{r}_1 - \vec{r}_2|)} \right| \Psi_S \right\rangle \qquad (3.103\text{a, b})$$

in the case of aligned and anti-aligned spins, respectively. $\vec{r}_1$ and $\vec{r}_2$ are the positions of the two electrons. The difference between the two energies is:

$$2J = E_S - E_A = 2\left\langle \psi_a(1)\psi_b(2) \left| \frac{e^2}{(4\pi\varepsilon_0|\vec{r}_1 - \vec{r}_2|)} \right| \psi_a(2)\psi_b(1) \right\rangle \qquad (3.104)$$

where J is called the exchange integral, which quantifies the strength of the magnetic interaction. In an isolated atom, J is always positive, provided the electrons are in the same orbital. Therefore, the coulomb interaction makes it energetically favourable for the spins of electrons in the same atomic orbital to align parallelly, provided this is permitted by the PEP. Hence, atomic orbitals are filled according to Hund's rule, mentioned in section 3.1.3.

Once an atomic orbital is half full, any additional electrons that need to be included in the orbital must pair up with the existing electrons, assuming anti-parallel spin, in agreement with the PEP. In certain cases the energy required to overcome the resulting increase in Coulomb repulsion (δV) is greater than the energy difference needed to place the electron in a higher orbital (δE). In this case it is energetically favourable to occupy the higher orbital and, if the overall spin is unpaired, the atom will be ferromagnetic. In more complicated systems, the energy difference between the orbitals is determined by the DOS, n(E), mentioned in section 3.2.1, such that:

$$\delta E = \frac{1}{n(E)} \qquad (3.105)$$

Therefore, the condition for ferromagnetism, known as the Stoner Criterion, is:

$$\delta V n(E) > 1 \qquad (3.106)$$

In order to extend this model to molecules and then to solids it is necessary to generalise the ideas introduced thus far. When atoms bond the atomic orbitals of the constituent atoms hybridise to form bonding and antibonding orbitals with different energies. These orbitals may be described by a linear combination of the original atomic orbitals. Once their energies are known, the electrons can be placed in the lowest energy configuration permitted by the PEP. Electron-electron coulomb repulsion may be included as a perturbation of the orbitals. The effect of bonding is normally to reduce spin. For example, in the H_2 molecule, the constituent H atoms each have a spin of ½. When bonding occurs, the two 1s atomic orbitals hybridise to form a bonding and antibonding orbital but the energy between the orbitals is greater than the energy needed to overcome the coulomb repulsion caused by placing both of the electrons in the bonding orbital with anti-parallel spins. Therefore, the Stoner Criterion is not obeyed and the resulting spin of the H_2 molecule is zero. However, other molecules, such as O_2 have a resultant spin after bonding. Metallic solids often also have this property but, unlike in a gas, many electrons with unpaired spins are close enough to be able to interact with each other via Coulomb repulsion, leading to the possibility of magnetic ordering. If the interaction occurs directly between the metal electrons without making use of an intermediary, it is known as a direct exchange.

In the rare earth metals, the unpaired spins are in relatively deep electronic levels. Therefore, the bonding does not cause the energy of their associated electronic orbitals to vary considerably from their atomic values. Hence, the direct exchange integral for the system may be determined by simply integrating over all the atomic exchange integrals given by (3.104):

$$J = \int \psi_a^*(1)\psi_b^*(2)\left|\frac{e^2}{\left(4\pi\varepsilon_0\left|\vec{r}_1 - \vec{r}_2\right|\right)}\right|\psi_a(2)\psi_b(1)d\vec{r}_1 d\vec{r}_2 \qquad (3.107)$$

However, unlike the atomic orbitals, the specific positions of the interacting electrons could give rise to a ferromagnetic or antiferromagnetic exchange, indicated by a positive or negative value of J, respectively. Evaluation of the integral is not straightforward but Stuart et al. [37] showed that when it is done, the value of J obtained for a typical ferromagnet is about two orders of magnitude smaller than the experimentally determined value. For this reason, direct exchange between localised magnetic moments is not sufficient to explain spontaneous magnetism, and even less in DMSs, where the distance between unpaired electrons is much greater than in typical ferromagnets.

It is important to note that the 3d levels of the dilute cations used in this study are not as deep as the levels containing the unpaired electrons in the rare earth metals.

Samuel John Gilliland

Therefore, another possibility for direct exchange, which may be more suitable for the DMSs, would be between itinerant electrons which are delocalised so they can be transferred from atom to atom in the crystal. In this case it is more appropriate to use Bloch functions rather than a linear combination of atomic orbitals. Moreover, the exchange takes place between electrons in a band rather than localised orbitals. Despite these differences, the fundamental mechanism is the same because the Coulomb repulsion between itinerant electrons with spins that are aligned is less than that of electrons with anti-aligned spins. This situation may be described theoretically by the tight-binding model to obtain an expression, $\varepsilon(k)$, for the single-electron band dispersion. This is related to the k-dependence of the probability of finding the electron between two atoms. After obtaining $\varepsilon(k)$, the electronic states may be filled up to the Fermi energy and the effect of Coulomb repulsion is introduced. The effect of this interaction is to minimise the total energy of the electrons in the band by changing the proportion with majority spin. When an electron changes from minority to majority spin, its energy within the band increases but this may be more than compensated for by the reduction in Coulomb repulsion caused by aligning its spin with the majority of the other electrons, leading to a decrease in the total energy. In order for ferromagnetism to result, there must be a large density of states at the Fermi level, $n(E_F)$, and a large exchange integral. It may be shown that the Stoner Criterion in this system is:

$$\frac{2Jn(E_F)}{n} > 1 \quad (3.108)$$

where n is the electron density in the band. Using typical values found in ferromagnetic materials, the Stoner Criterion is a long way from being met. Therefore, direct exchange between itinerant electrons is also insufficient to explain spontaneous magnetisation.

Indirect exchange:

If the exchange interaction between the localised magnetic moments in a metal is mediated via conduction electrons, it is known as an indirect exchange. The localised magnetic moments are distributed periodically throughout the crystal so they may be considered as a sum of Fourier components. They create a molecular field ($\vec{h}$) which spatially polarises the conduction band electrons, which may be modelled as a free electron gas. The effect of this polarisation is to minimise the total energy of the system. The resulting spatial distribution of the magnetism, $\vec{M}(\vec{r})$, has two contributions: one from the localised magnetic moments and the other from that of the conduction band electrons.

$$\vec{M}(\vec{r}) = V^{-1} \int \chi(\vec{r} - \vec{r}')h(\vec{r}')d\vec{r}' \quad (3.109)$$

where $\chi(\vec{r} - \vec{r}')$ is a non-local susceptibility related to the magnetic response of a free electron gas (the conduction electrons) and V is the volume of the system. The related exchange energy is:

$$E = -\mu_0 \int \vec{M}(\vec{r}).\vec{h}(\vec{r})d\vec{r} \quad (3.110)$$

which is minimised by the spatial polarisation. In order to evaluate the integral it is necessary to perform a Fourier transform. The Fourier components of $\vec{h}$ can be determined directly from those of the localised magnetic moments and the Fourier components of the conduction band susceptibility may be determined by quantum mechanical considerations, treating the molecular field as a perturbation. It may be shown that the molecular field produces a partial localisation of the conduction band electrons, since conduction electrons with the same spin orientation will tend to accumulate in corresponding regions of the molecular field in order to reduce the Coulomb repulsion. The probability of finding the electrons at different positions is related to the spatial density of the magnetic moment which, when integrated over all the electrons situated within the Fermi sphere, gives the total spatial distribution of the magnetisation.

If the conduction band is polarised by a single localised magnetic moment at the origin, as in the case of a ferromagnetic impurity in a paramagnetic or diamagnetic metal, the procedure described above may be followed to find the spatial variation of the magnetisation. It is found to decrease with r^{-3}, oscillating between positive (ferromagnetic) and negative (antiferromagnetic) values. Moreover, the period of the oscillations is a few Å, comparable to typical bond lengths. Therefore, two localised magnetic moments could interact ferromagnetically or antiferromagnetically depending on the distance between them. This is known as the RKKY interaction, developed by Ruderman, Kittel, Kasuya and Yosida [38-40]. Although it is responsible for spontaneous magnetisation in the rare earth metals, it is unlikely that the RKKY interaction could produce this type of long-range magnetism in DMSs due to the relatively large distances between localised magnetic moments, low electrical conductivity and lack of periodicity.

In a DMS, the dilute cations, with their localised magnetic moments, occupy random substitutional positions throughout the host material. Therefore, if the RKKY interaction occurs, the electronic spin of each dilute cation will be influenced by the ferromagnetic and antiferromagnetic indirect exchanges with the other dilute cations, according to the distance between them. As the distribution of dilute cations is random, no particular spin orientation will be favoured and, as a result, the localised magnetic moments of the material will be locked in different directions. Such a material is called a spin glass because the spin disorder is similar to the structural disorder that exists in amorphous materials like glass. When the temperature becomes great enough to overcome the indirect exchange, the spins are no longer locked and the material becomes paramagnetic. By applying a magnetic field to the paramagnetic material and cooling below the spin glass transition temperature, the spins may be locked parallel to the field. The resultant magnetic moment remains even when the field is removed.

Superexchange:

Direct exchange can only happen between localised magnetic moments with a high degree of overlap and indirect exchange is only possible when there are itinerant electrons. However, spontaneous magnetism is occasionally found in electrical insulators where the cations are separated by a non-magnetic anion, such as certain perovskites. In this case different exchange mechanisms exist, of which the main two

are superexchange and double exchange. In these mechanisms, the magnetic exchange is mediated by the anion. The superexchange interaction was proposed by Kramers in 1934 [41] and refined by Anderson [42]. It is a second order process because the interaction, which usually results in strongly antiferromagnetic ordering, occurs in two stages. It is important to note that the interaction occurs between two cations of the same oxidation state. In the case of a DMS, the superexchange would be between the 3d electrons of the dilute cation, mediated by the O 2p electrons, as shown in fig 3.21.
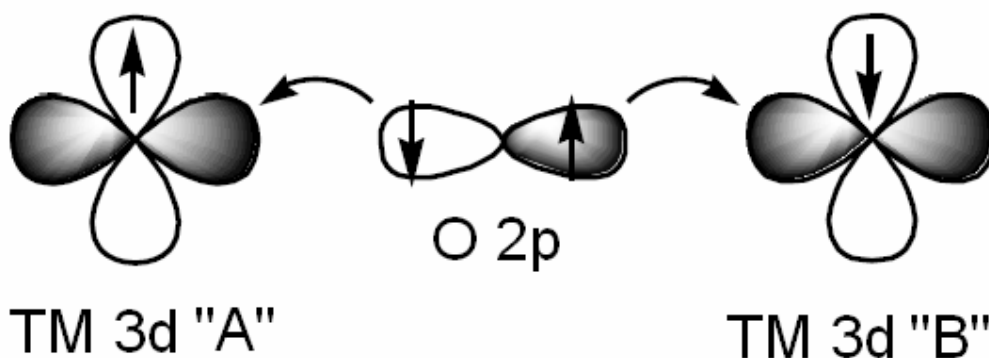
Fig 3.21: Magnetic superexchange interaction (antiferromagnetic).

Assuming that each TM-O bond contains a single electron from the TM 3d and O 2p orbitals, the fundamental state of the bonding may be written as $(pd_A)(pd_B)$, where A and B refer to the two dilute cations between which the superexchange occurs. In the first stage, the O 2p electron in the bond with dilute cation "A" is also excited to the TM 3d level, with the resulting bonding configuration $(2d_A)(pd_B)$. For the antiferromagnetic superexchange to function, it is necessary for there to be an unoccupied sub-level within the TM 3d orbital so that the excited electron can assume a spin orientation parallel to that of the other "A" cation 3d levels, to minimise Coulomb repulsion, in agreement with Hund's rule. In order for the O ion to have neutral spin, the TM 3d electron in the other bond (d_B) must assume anti-parallel spin to the excited electron. The other 3d electrons in the "B" dilute cation then align their spins with that of d_B to minimise Coulomb repulsion. Hence, the spins in the "A" cation are anti-aligned with those of the "B" cation and, when the whole material is considered, the resulting behaviour is antiferromagnetic. Ferromagnetic superexchange is also possible, but it requires certain TM 3d sublevels to be filled.

Double exchange:

The double exchange interaction was proposed by Zener in 1951 [43] and refined by de Gennes [44]. For it to be possible, it is necessary to have a mixed valence system where one cation has an additional electron with respect to the other, for example Mn^{3+} and Mn^{4+} in the perovskite $La_{1-x}Ca_xMnO_3$, shown in fig 3.22. Unlike the superexchange, it is a first order process and usually results in ferromagnetic behaviour. In the case of $La_{1-x}Ca_xMnO_3$, the Mn^{3+}-O^{2-}-Mn^{4+} and Mn^{4+}-O^{2-}-Mn^{3+} configurations are degenerate. The double exchange is made by the simultaneous transfer of an electron from the Mn^{3+} ion to the O along with another from the O to the Mn^{4+} ion. However, as the two transferred electrons have the same spin, the exchange is only energetically favourable if the spins of the two cations are

aligned, in agreement with Hund's rule. If the cation spins are anti-aligned then the transfer is forbidden. The double exchange causes a certain proportion of the electrons in the material to become delocalised and, in the absence of an applied electric field, these electrons just oscillate between Mn^{3+} and Mn^{4+} cations. However, when an electric field is applied, the electron drift is in the direction of the field, leading to electrical conductivity. Above the Curie temperature, the thermal energy of the electrons is greater than the decrease in energy caused by the double exchange. Therefore, the ferromagnetic ordering is lost and the electrical conductivity disappears.
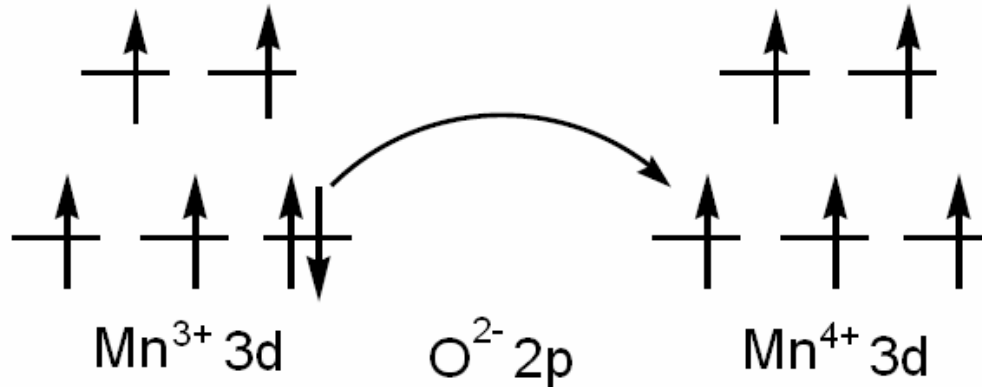
Fig 3.22: Double exchange in $La_{1-x}Ca_xMnO_3$.

Other mechanisms:

According to Coey et al. [45], conventional superexchange and double exchange theory is not able to explain long-range magnetic order in DMSs with dilute cation concentrations of just a few percent. The reasons given are that superexchange is a short-range interaction, which would need a large dilute cation concentration to function and double exchange requires mixed valence, which DMSs appear not to have. For this reason, several other theoretical models have been proposed to describe alternative mechanisms to explain the alleged spontaneous magnetisation. Coey attributes ferromagnetism in DMSs to bound magnetic polarons formed by the alignment of dilute cation spins with that of weakly bound carriers. The holes left by the polarons interact with the surrounding TM impurities, producing a localised magnetic field which aligns all the spins. As the temperature decreases, the interaction distance of each polaron grows until they overlap, resulting in them becoming correlated. When the effect of the correlation spreads to the whole material, spontaneous magnetisation is observed, which could be antiferromagnetic or ferromagnetic.

Other possible mechanisms include the original model proposed by Dietl et al. [46] that initiated much of the research into DMSs. This model relies on the strong coupling that exists between the localised dilute cation spins and holes on the anion. The holes mediate long-range interactions between the localised spins producing ferromagnetism in the material. As mentioned in the introduction, this mechanism would require strong p-type conductivity, with all the associated complications of producing it. Another model which also would require p-doping is that of Sato et al. [47], which suggests that, with the presence of holes, a ferromagnetic double

exchange and an antiferromagnetic superexchange exist simultaneously in certain ZnO based DMSs. Finally, there is the theory of Wang et al. [48] which predicts an antiferromagnetic behaviour in $Zn_{1-x}Mn_xO$ due to the clustering of Mn ions around O anions.

3.5 Bibliography

[1] S. Wei, X. Nie, I. Batyrev, G. Batyrev and S. Zhang. Phys. Rev. B **67**, 165209 (2003).

[2] J. Wu and W. Walukiewicz. Superlattices Microstruct. **34**, 63 (2003).

[3] G. Hall. Philos. Mag. **43**, 338 (1952).

[4] D. Weaire and M. Thorpe. Phys. Rev B **4**, 2508 (1971).

[5] W. Harrison. Phys. Rev. B **8**, 4487 (1973).

[6] S. Wei and A. Zunger. Phys. Rev. B **37**, 8958 (1988).

[7] S. Wei and A. Zunger. Appl. Phys. Lett **72**, 2011 (1998).

[8] S. Zumdahl. "Chemical Principles", Houghton Mifflin (2005).

[9] L. Soderholm, C. Loong, G. Goodman and B. Dabrowski. Phys. Rev. B **43**, 7923.

[10] S. Asbrink, A. Waskowska, L. Gerward, J. Staun Olsen and E. Talik. Phys. Rev. B **60**, 12651 (1999).

[11] D. Reinen, W. Rauw, U. Kesper, M. Atanasov, H. Güdel, M. Hazenkamp and U. Oetliker. J. Alloys Compd. **246**, 193 (1997).

[12] H. Schläfer and G. Gliemann. "Basic principles of ligand field theory", Wiley (1969).

[13] C. Humphreys. Nature **401**, 21 (1999).

[14] S. Hüfner. "Photoelectron Spectroscopy", Springer (2003).

[15] P. Yu and M. Cardona. "Fundamentals of Semiconductors", Springer (2001).

[16] J. F. Sánchez Royo, doctoral thesis: "Preparación y caracterización de capas delgadas de InSe/GaSe crecidas por epitaxia van der Waals". Universitat de València (1998).

[17] E. Stern. "Principles, applications, techniques of EXAFS, SEXAFS and XANES", Wiley (1988).

[18] A. Brunetti, M. Sanchez del Rio, B. Golosio, A. Simionovici and A. Somogyi. Spectrochim. Acta B **59**, 1725 (2004).

[19] R. Elliot. Phys. Rev. **108**, 1384 (1957).

[20] Y. Toyozawa. Progr. Theor. Phys. **20**, 53 (1958).

[21] A.R.Goñi, A.Cantarero, K.Syassen and M.Cardona. Phys. Rev. B **41**, 10111 (1989).

[22] L. Viña, S. Logothetidis and M. Cardona. Phys. Rev. B **30**, 1979 (1984).

[23] W. Paul. "High Pressure in Semiconductor Physics", Academic (1998).

[24] S. Wei and A. Zunger. Phys. Rev. B **60**, 5404 (1999).

[25] S. Wei and H. Krakauer. Phys. Rev. Lett. **55**, 1200 (1985).

[26] W. Harrison. "Electronic Structure and Properties of Solids", Freeman (1980).

[27] J. Phillips. Rev. Mod. Phys. **42**, 317 (1980).

[28] J. Van Vechten. Phys. Rev. **182**, 891 (1969).

[29] J. Van Vechten. Phys. Rev. **187**, 1007 (1969).

[30] F. Murnaghan. Proc. Natl. Acad. Sci. USA **30**, 244 (1944).

[31] X. Zhang, Z. Chen, Y. Qi, Y. Feng, L. Zhao, M. Ma, R. Liu and W. Wang. Chin. Phys. Lett. **24**, 1032 (2007).

[32] F. Cotton, G. Wilkinson and P. Gaus. "Basic Inorganic Chemistry", Wiley (1994).

[33] C. Hurd. J. Contemp. Phys. **23**, 469 (1982).

[34] S. Mishra. Phys. Status Solidi A **24**, K153 (2006).

[35] R.L. Carlin. "Magnetochemistry", Springer (1986).

[36] A. Hernando and J. Rojo. "Física de los materiales magnéticos", Síntesis (2001).

[37] R. Stuart and W. Marshall. Phys. Rev. **120**, 353 (1960).

[38] M. Ruderman and C. Kittel. Phys. Rev. **96**, 99 (1954).

[39] T. Kasuya. Prog. Theor. Phys. **16**, 45 (1956).

[40] K. Yosida. Phys. Rev. **106**, 893 (1957).

[41] H. A. Kramers. Physica **1**, 182 (1934).

[42] P. Anderson. Phys. Rev. **79**, 350 (1950).

[43] C. Zener. Phys. Rev. **82**, 403 (1951).

[44] P. de Gennes. Phys. Rev. **118**, 141 (1960).

[45] J. Coey, M. Venkatesan and C. Fitzgerald. Nat. Mater. **4**, 173 (2005).

[46] T. Dietl, H. Ohno, F. Matsukura, J. Cibert and D. Ferrand. Science **287**, 1019 (2000).

[47] K. Sato and H. Katayama-Yoshida. Jpn. J. Appl. Phys., Part 2 **39**, L555 (2000).

[48] Q. Wang and P. Jena. Appl. Phys. Lett. **84**, 4170 (2004).

4 Method

4.1 Crystal Growth

Three-dimensional crystals can be grown in bulk form or as thin films. The reason why thin films were chosen was that they allow optical measurements to be performed up to absorption coefficients in excess of 10^5 cm^{-1}, much greater than those attainable in thicker bulk samples. Even within the field of thin film deposition, there are a wide range of techniques that are used to deposit ZnO-based compounds, including sputtering [1], metal-organic chemical vapour deposition (MOCVD) [2] and molecular beam epitaxy (MBE) [3]. In this study, pulsed laser deposition (PLD) was used, as it provides a convenient trade-off between crystal quality, deposition time and cost.

The process of PLD is conceptually simple and may be divided into the following four steps: ablation, expansion, deposition and nucleation. In the first step, a target is ablated by a laser to produce a plasma plume. This plume expands through the chamber in such a way as to reach a substrate, on which it is deposited. The deposited material then nucleates to form the thin film on the surface of the substrate, which builds up over time. All of these steps need to be carefully controlled to ensure that the desired composition, uniformity and crystallinity of the film are achieved. The way in which this was done will be explained in more detail in section 4.1.2.

From a historical perspective, PLD first became possible after the invention of the ruby laser by Maiman in 1960 [4]. Five years later, Turner and Smith used this type of laser to create the first pulsed laser deposited films [5]. Initially PLD was not a very popular technique because other growth processes produced superior quality films but, as the method was developed, film quality improved until, in some cases, it even exceeded that of the established techniques. An example of this would be the deposition of the high temperature superconductor $YBa_2Cu_3O_7$ by Dijkkamp et al. in 1987 [6]. Since then, PLD technology has improved further with the introduction of new short pulse high repetition lasers, making it possible to deposit a wide range of materials and superlattices [7].

The following sections focus on target production, the system used to deposit the films, the deposition of heterojunctions for photoelectron spectroscopy and measurements taken during the growth process.

4.1.1 Target production

Targets used in the PLD system were made in a similar way to the description in [8]. Firstly, stoichiometric masses of powders fabricated by CERAC with a purity of 99.999% (5N) were dispersed in ethanol and finely ground in a mortar and pestle to ensure that they were thoroughly mixed. The specific powders used were ZnO, MnO, Fe_2O_3, Cu_2O and NiO and the mass of ZnO was set at 3.000g so that the volume of the targets would be suitable for the deposition system. Taking into account the molecular masses of each element, the masses (in g) of the other powders required for a stoichiometric mix were calculated using the following equations:

$$m_{MnO} = \frac{x}{1-x} \times 2.615 \quad (4.1a)$$

$$m_{Cu_2O} = \frac{x}{1-x} \times 2.637 \quad (4.1c)$$

$$m_{Fe_2O_3} = \frac{x}{1-x} \times 2.943 \quad (4.1b)$$

$$m_{NiO} = \frac{x}{1-x} \times 2.753 \quad (4.1d)$$

where x is the fraction of dilute cation with respect to total cation content. PLD is a highly non-equilibrium growth process so one would expect that the solubility limits in the introduction (fig 1.3) could be reached and even exceeded by a small margin without producing a phase separation. For this reason, the range of x chosen was 0.01 to 0.25 for MnO, 0.005 to 0.10 for Fe_2O_3, 0.01 to 0.10 for Cu_2O and 0.005 to 0.05 for NiO. After drying, the mixtures of powders were compressed at 10 MPa for 10 minutes in a pellet press. The resulting pellets were thermally treated in a Nabertherm L3 oven with an air atmosphere to produce the targets. The profile of the thermal treatment is shown in fig 4.1. The purpose of the hour-long plateau below 100°C was to allow any water that was still in the pellets to evaporate, reducing the chance of subsequent deformation of the targets.
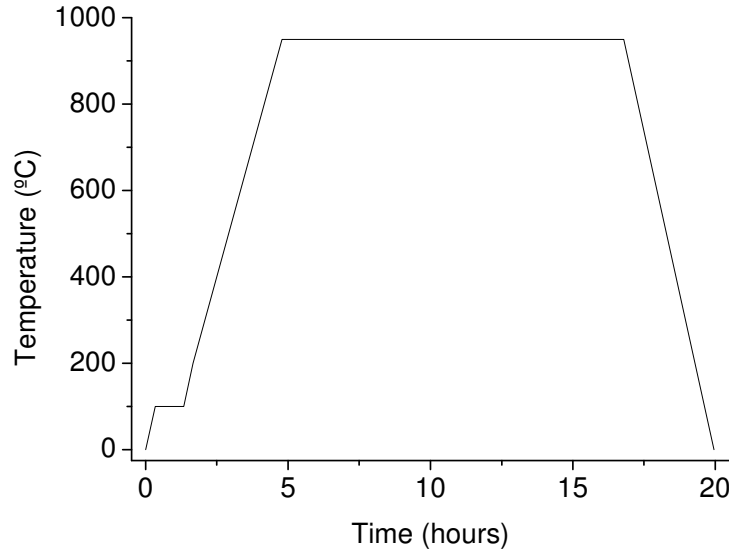
Fig 4.1: Profile of the thermal treatment of the pellets.

4.1.2 Pulsed laser deposition

The vacuum chamber in which the films characterised in this work were deposited, shown in fig 4.2, is made from stainless steel. It has a T-shaped form with different openings for the sample holder, vacuum pumps, sensors, laser radiation and oxygen. It has a height of 500mm and an interior diameter of 250mm to make it sufficiently large to avoid overheating. The vacuum is maintained by a rotary pump and a turbomolecular pump which reduce the pressure to around 10^{-7} mbar after several hours of operation. A high vacuum was required to reduce the contamination of the film by unwanted impurities.
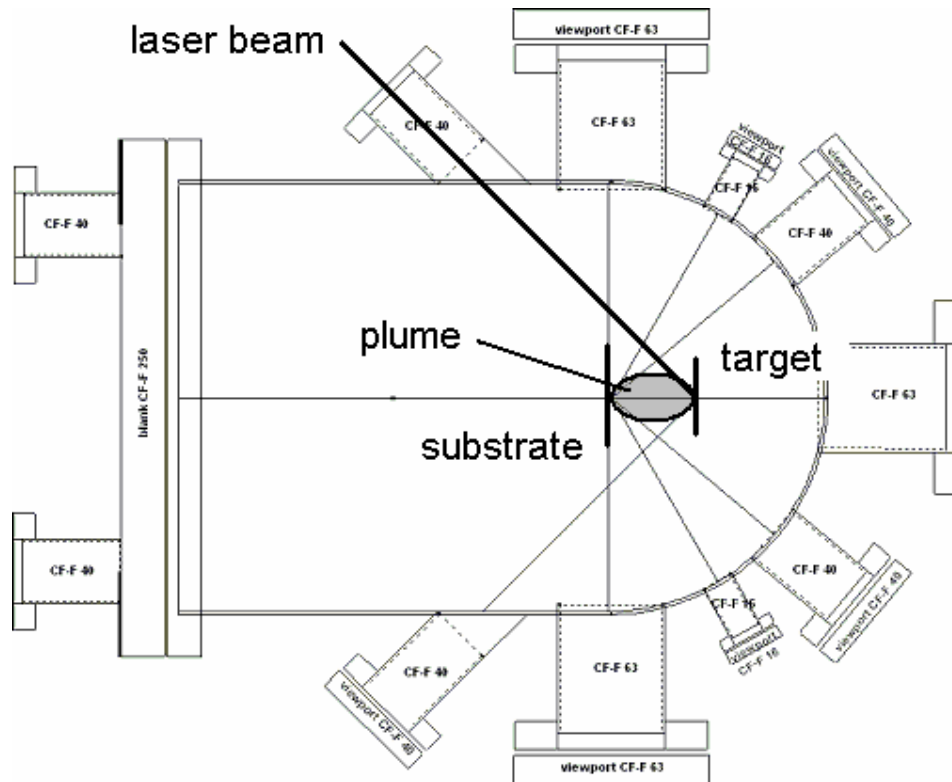
Fig 4.2: Horizontal cross-section of the sample deposition chamber.

The targets, prepared by the method described in the previous section, were mounted in a holder, shown in fig 4.3, which could be displaced vertically to allow the ablation of up to five targets. In this way superlattices could be deposited without breaking the vacuum. To produce the ablation, pulsed radiation from a quadrupled Nd:YAG laser was used with wavelength 266nm and energy 12-15 mJ at a repetition frequency of 10 Hz. This allowed time for relaxation between pulses to improve sample quality. To achieve a uniform ablation, the targets were rotated by a magnetic system.
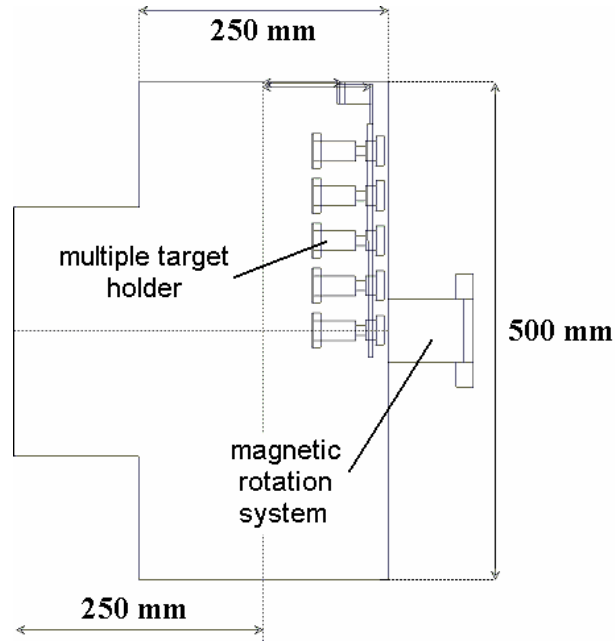
Fig 4.3: Vertical cross-section of the sample deposition chamber.

The radiation, which enters the chamber through a quartz window, has an instantaneous flux of greater than 10^8 W/cm^2, causing evaporation from the surface of the target. Moreover, the target had an absorption coefficient of the order of 10^5 cm^{-1} for this laser wavelength so the evaporation process was very effective. The evaporated atoms produce a plasma plume which expands towards the substrate positioned parallel to the target at a distance of 4cm. During the expansion, the atoms interact with the oxygen within the chamber which had a controlled pressure of 2×10^{-5} mbar. This reduces their velocity so that they can be deposited as a layer over the substrate with sufficiently low kinetic energy to avoid pulverisation or modifications to the material already deposited. Vacuum is a reducing atmosphere because oxygen atoms in the plasma tend to form molecules, which are removed by the vacuum pumps. Therefore, it was necessary to introduce a relatively high O_2 partial pressure to compensate for the loss. During the growth process, the chemical equations for the interaction of the initial mix of materials to form the DMS films are given below. Note that there is an oxygen excess in the case of $Zn_{1-x}Fe_xO$ and a deficiency in the case of $Zn_{1-x}Cu_xO$. This was compensated by oxygen absorption or release in the deposition chamber and oven, during the baking of the targets.

$$(1-x)ZnO + xMnO \rightarrow Zn_{1-x}Mn_xO \qquad\qquad (4.2a)$$

$$4(1-x)ZnO + 2xFe_2O_3 \rightarrow 4Zn_{1-x}Fe_xO + xO_2 \qquad (4.2b)$$

$$4(1-x)ZnO + 2xCu_2O + xO_2 \rightarrow 4Zn_{1-x}Cu_xO \qquad (4.2c)$$

$$(1-x)ZnO + xNiO \rightarrow Zn_{1-x}Ni_xO \qquad\qquad (4.2d)$$
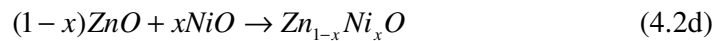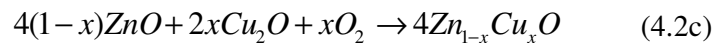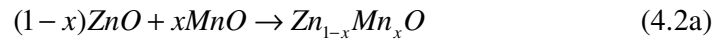
A suitable substrate for laser ablation must be flat, clean, free from defects and chemically unreactive with the material to be deposited. Also the lattice parameters and coefficient of thermal expansion should adapt well to those of the film without causing strain. C-oriented sapphire (Al_2O_3) and mica ($KMg_3(AlSi_3O_{10})F^2$ [9]) substrates were used because sapphire has a high transparency in the ultraviolet, the range in which the optical measurements were taken. Mica was used because it could be exfoliated to almost completely separate the film from the substrate to produce samples that could be used for high pressure measurements in the diamond anvil cell (DAC). The substrate was heated to 600°C by means of a MgO resistance in thermal contact with the substrate holder. This is the optimum temperature for ZnO nucleation because it facilitates the crystallisation of atoms over the substrate surface without producing reevaporation. The temperature was calibrated in function of the power supplied to the resistance using the known dependence of the bandgap of GaAs in function of temperature [10], a K-type thermocouple and a platinum resistance thermometer. Fig 4.4 shows the calibration curves. The methods produced slightly different results due to non-uniform heating. Thin films with thickness of the order of tens or hundreds of nanometers were obtained, depending on the deposition time. These times typically varied between 4 and 12 hours, depending on x.
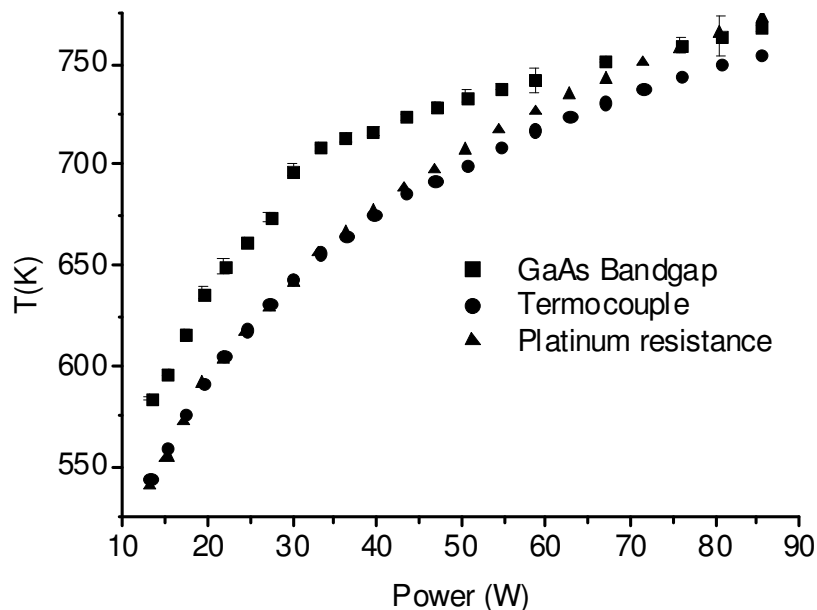
Fig 4.4: Substrate temperature calibration.

Samuel John Gilliland

4.1.3 Heterojunctions
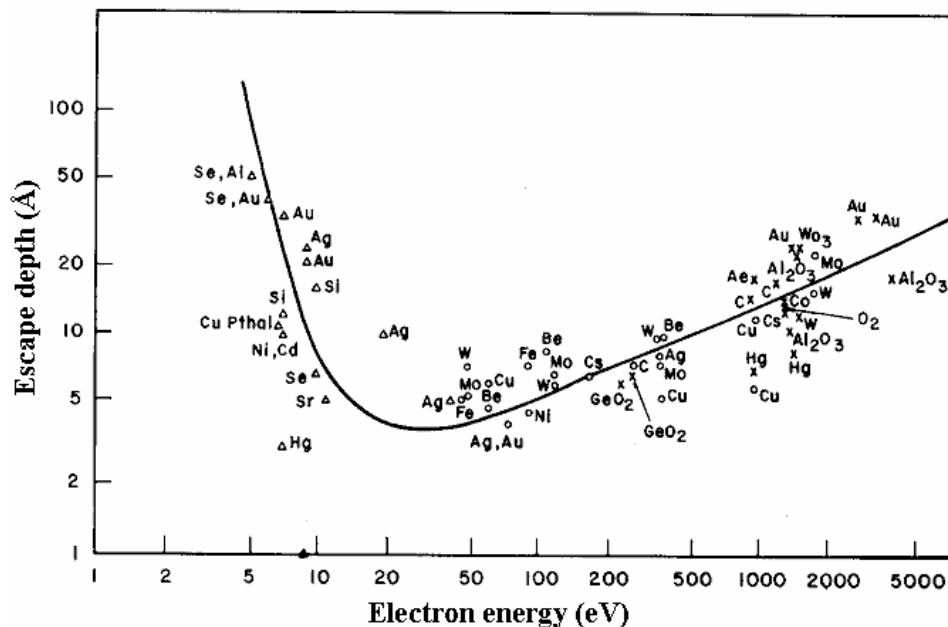
Fig 4.5: Photoelectron mean free path [11].

A common difficulty in photoelectron spectroscopy (described in section 4.2.4) is maintaining a constant Fermi energy for all samples. The energy shift caused by even small variations could lead to complications in the analysis or even erroneous results so a reference is required to correct for any differences. The reference used in this study was the photoelectron spectrum of pure ZnO. Firstly a layer of ZnO was deposited over a c-oriented sapphire substrate. As photoelectron spectroscopy is a surface technique, it was necessary to ensure that sufficient ZnO was deposited to avoid detecting a signal from the substrate. Fig 4.5 shows the photoelectron mean free path in function of energy. In the energy range of interest, it appears that the average escape depth does not exceed 20 Å but to air on the side of caution, a film of at least 50 nm was deposited. Secondly, half of the ZnO layer was covered by mica and the DMS was deposited over the exposed half to produce a heterojunction, as shown in fig 4.6. The thickness of the DMS layer was also at least 50 nm. Heterojunctions were produced for all DMSs.
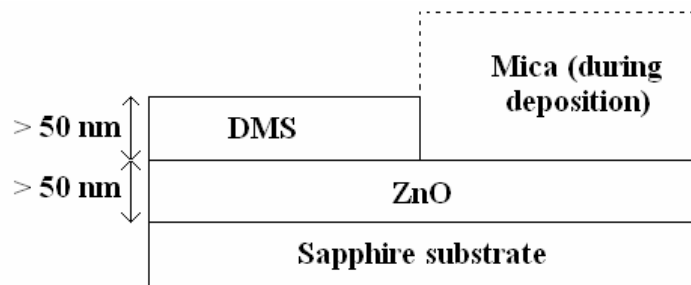
Fig 4.6: ZnO/DMS heterojunction.

4.1.4 In-situ measurements

The growth process could be monitored and controlled by means of in-situ measurements. The method described here is for plume analysis. The plume consists of neutral and ionised species, along with electrons. It produces an intense white light, due to Bremsstrahlung, caused mainly by electrons decelerated by the electrostatic field of the positive ions. It also emits luminescence at energies corresponding to electronic transitions in the neutral and ionised species. Therefore, in order to monitor the composition of the material ejected from the target and verify its constancy throughout the deposition, light from the plume leaving the chamber by the window indicated in fig 4.7 was focussed into a fibre optic guide and measured in the wavelength range 250-700 nm by an Ocean Optics HR2000 spectrometer. The plume spectrum was recorded at the start of the deposition and after 6 hours for all the DMSs.
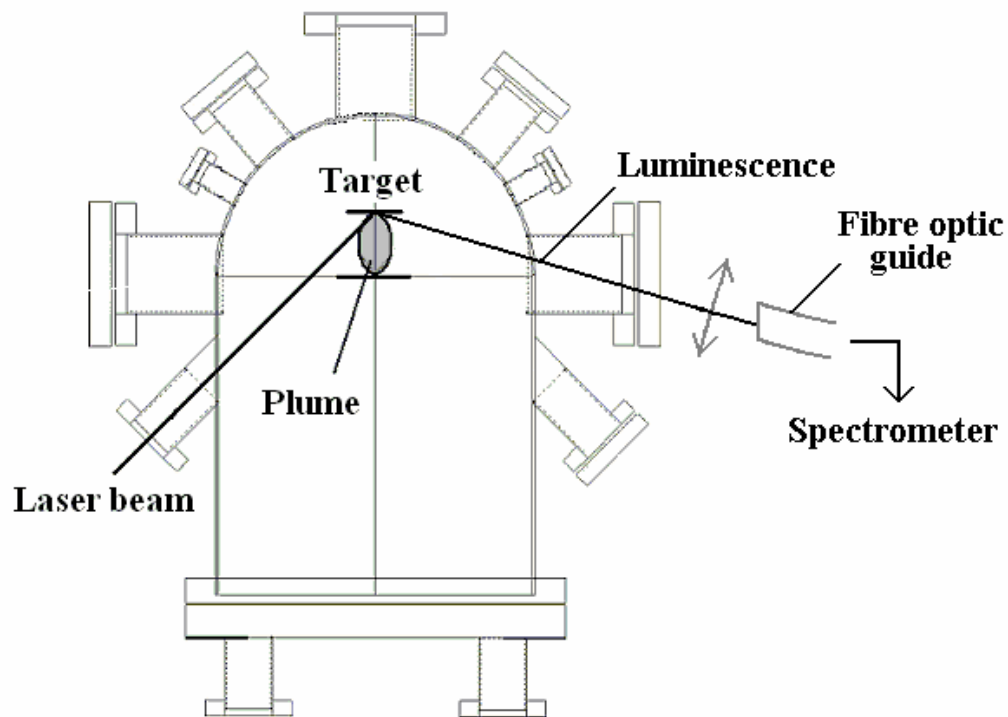
Fig 4.7: Optical setup for plume analysis.

4.2 Structural and Electronic Characterisation

Due to the controversy mentioned in the introduction, particularly over the magnetic properties of these DMSs, it was of particular importance to undertake a detailed structural characterisation of the films. This was done by the following five methods:

- X-ray diffraction (XRD) to confirm the crystal structure of the films and check for secondary phases.
- X-ray absorption spectroscopy (XAS), in particular XANES and EXAFS, to determine the coordination environment of the dilute cations, and X-ray fluorescence to quantify the atomic content of the films.
- Electron microscopy to study the morphology of the surfaces and obtain information about the crystallite sizes.
- Microanalysis to produce element maps of the samples to identify surface structures and large metallic clusters.
- Photoelectron spectroscopy to verify the stoichiometry of the films and investigate their valence band and core level electronic properties.

4.2.1 X-ray diffraction

XRD measurements were taken at the Servicio central de Soporte a la Investigación Experimental (SCSIE) at the Universitat de València using a Bruker AXS D5005 with a copper anode. A 30A current source was used to produce 40meV X-rays at a 2θ angle range of 20-80º. A diffracted ray is only detected when it meets the Bragg condition:

$$2d \sin \theta = n\lambda \quad (4.3)$$

where d is the separation between crystallographic planes, n is an integer, the angle θ is as shown in fig 4.8 and λ is the X-ray wavelength. The incident radiation was a doublet formed by the lines $K_{\alpha 1}$ ($\lambda = 0.1540$ nm) and $K_{\alpha 2}$ ($\lambda = 0.1544$ nm). The two lines had the same spectral width but the intensity of $K_{\alpha 1}$ was twice that of $K_{\alpha 2}$, so $K_{\alpha 1}$ dominated.
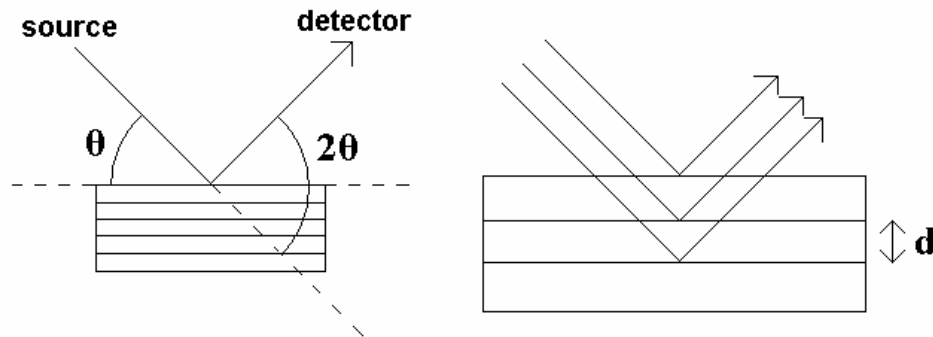
Fig 4.8: The Bragg condition.

As the thin films were polycrystalline, they were rotated in the plane perpendicular to the incident radiation in order to detect diffraction from many crystals at each angle, independently of their orientation. The diffractograms of all DMSs were compared with Joint Committee for Powder Diffraction (JCPD) references to identify the crystallographic phases present in the films.

4.2.2 X-ray absorption spectroscopy

XAS measurements were taken at the Spanish CGR beamline (BM25A) at the European Synchrotron Radiation Facility (ESRF). A generalised synchrotron is shown in fig 4.9. The ESRF storage ring contains the 6 GeV electron beam injected from the booster and has a length of 844.4 m. The maximum electron beam current is 200 mA and a typical horizontal emittance would be 4 nm with 0.6% coupling. The electron revolution frequency is 355 kHz and the beam lifetime is around 24 hours. Synchrotron radiation over an angle of 9 mrad is produced as the beam passes through the 0.85T bending magnet that feeds the line. The beam is split into two branches, each with a constant critical energy and an angular acceptance of 2 mrad. Branch A, which was used in these measurements, has a critical energy of 9.6 keV. The brightness of the beam is shown in fig 4.10 and, from the definition of the critical energy, the shaded area corresponds to half the radiated power.
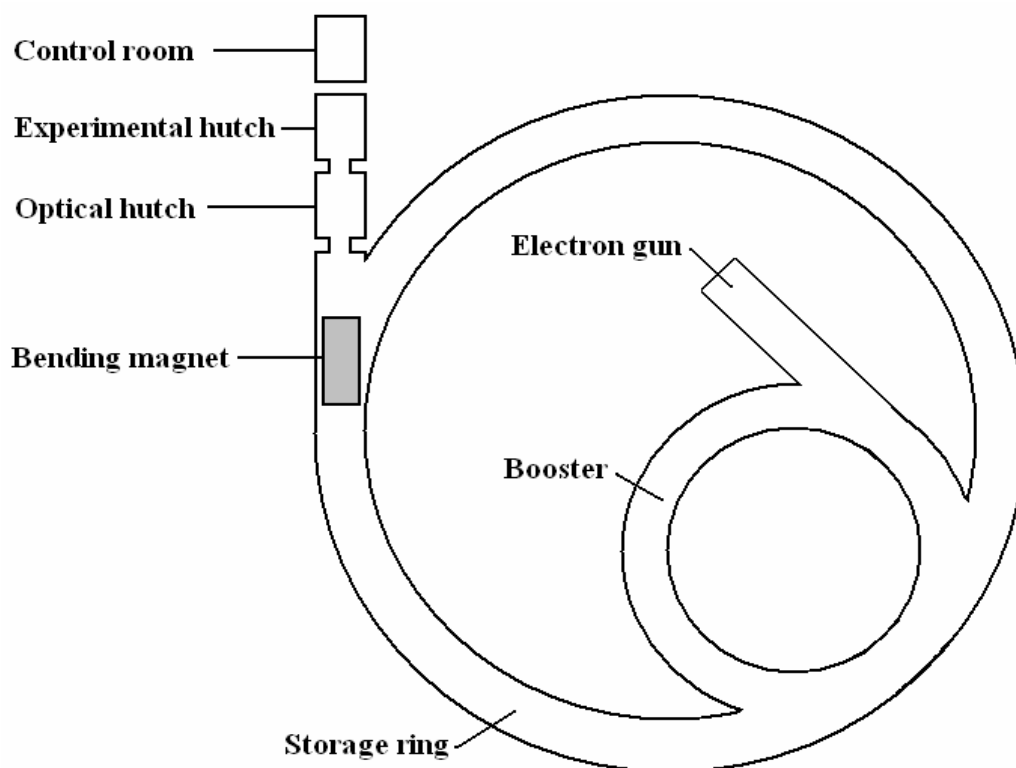
Fig 4.9 A generalised synchrotron.

The beam then passes into the optical hutch, shown in fig 4.11, in which it is collimated and focussed. The first mirror is a cylindrical bent mirror with a length of 1m and a focal length of 26.6 m. This mirror collimates the beam in the vertical plane. The monochromator is of the pseudo channel-cut type with two fixed Si (111) crystals moved together by a goniometer. The pitch of the second crystal may be adjusted to reduce the harmonic content of the beam and it is slightly bent so that the beam is focussed in the horizontal plane, with a focal length of 28.3 m. The second mirror, which is vertically bendable and has a focal length of around 33 m, allows the beam to be focussed at the different sample positions in the experimental hutch.
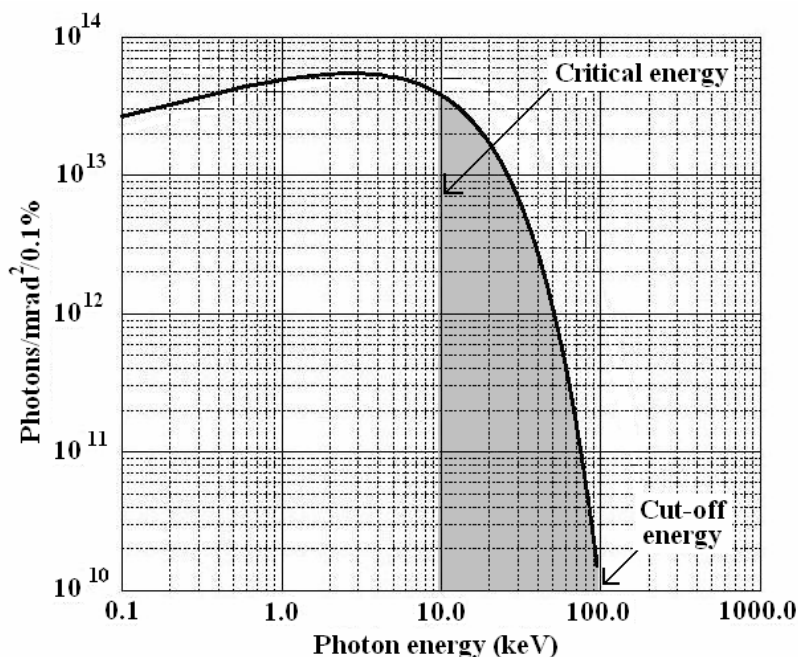
Fig 4.10: Brightness of synchrotron radiation from BM25A.
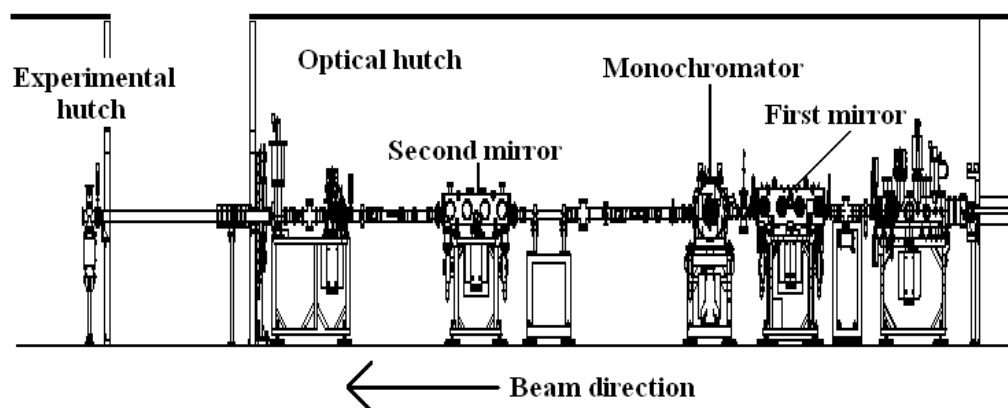
Fig 4.11: The optical hutch.

In the experimental hutch, the beam leaves vacuum conditions via a beryllium window and passes through two ionisation chambers which were used to optimise the energy distribution. The sample was mounted on a holder in the focus at an angle of 45° to the beam. An energy resolving single-element Ge detector at right angles to the beam was used to measure XANES, EXAFS and X-ray fluorescence. XANES and EXAFS spectra were taken for all DMS samples at the K-edge of the dilute cation, which occurs at an energy of 6539 eV in Mn, 7112 eV in Fe, 8333 eV in Ni and 8979 eV in Cu [12]. Results were compared to theoretical simulations to determine the dilute cation coordination environment. X-ray fluorescence (XRF) was also measured at 9.7 keV, just above the Zn K-edge (9659 eV), for all DMS samples and results were analysed to quantify the atomic content of the films and, hence, verify stoichiometry.

4.2.3 Electron Microscopy and Microanalysis

A Hitachi S-4100 scanning electron microscope (SEM) from the SCSIE, shown schematically in fig 4.12, was used to study the morphology of the surface of the films. Samples were fixed to holders using silver paint, which also provided an earth connection to prevent excessive sample charging. The principal beam, which had an energy of 20kV, made a scan over a defined region of the surface, with dimensions of between 3×3 μm^2 (magnification of 40 000) and 600×600 nm^2 (magnification of 130 000). The maximum magnification used with each sample was limited by the effectiveness of charge removal. On interacting with the sample, the beam produced secondary electron emission with energies of the order of 10 eV. The detected secondary electron current depends on the angle at which the primary beam meets the surface, which is determined by the surface morphology. Therefore, by detecting and amplifying this current, an image could be formed of the surface by varying the brightness of the trace from a cathode ray tube (CRT) scanning at the same rate as the principal beam. Images of all DMS samples were recorded, surface structures were identified and the sizes of the crystallites were determined.
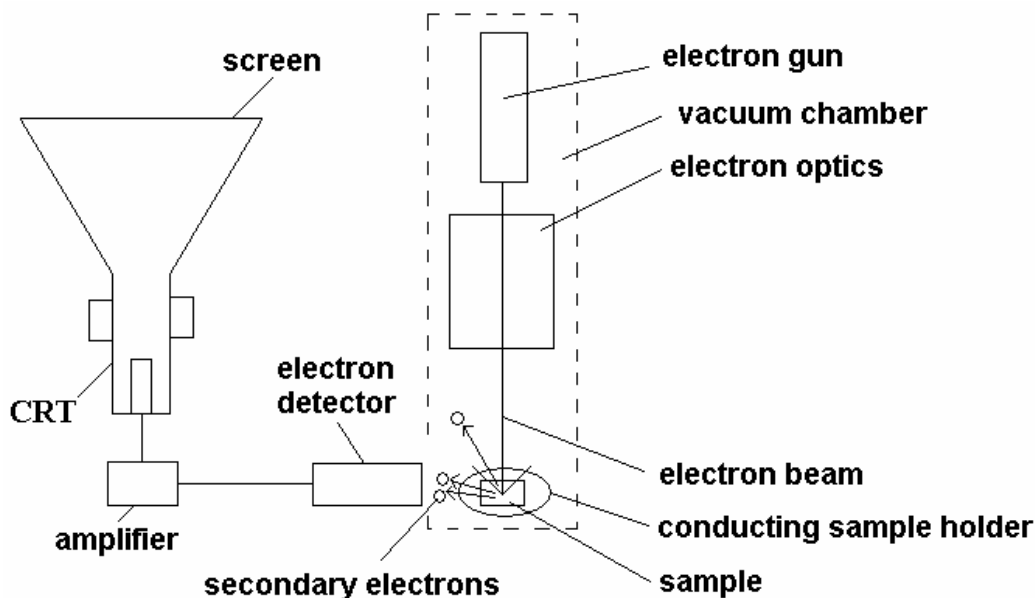
Fig 4.12: A generalised SEM.

In microanalysis, an electron beam is used to produce X-ray photon emission from a sample. As every chemical element emits X-rays with different characteristic energies, the elements that are present and their relative proportions may be determined. If the electron beam is scanned over the sample in two dimensions, a map showing the surface distribution of the chemical elements may be created. This is the basis of the experimental technique of element mapping. The measurements were taken with the electron probe micro-analyser (EPMA) of the SCSIE, shown schematically in fig 4.13. It consists of the aforementioned Hitachi S-4100 SEM connected to an X-ray analyser containing an energy dispersive spectrometer (EDS). The electron beam energy was 20 kV and emitted X-ray photons were detected up to this energy. As before, it was necessary to electrically earth the samples through the

sample holder by means of silver paint to prevent excessive charging. At the highest resolution the system offered a spatial resolution of 5 nm, although element maps were also taken at an intermediate resolution of 15nm. For technical reasons, only the DMS samples containing the greatest and least dilute cation concentrations were mapped. Results were analysed to help identify surface structures and large metallic clusters.
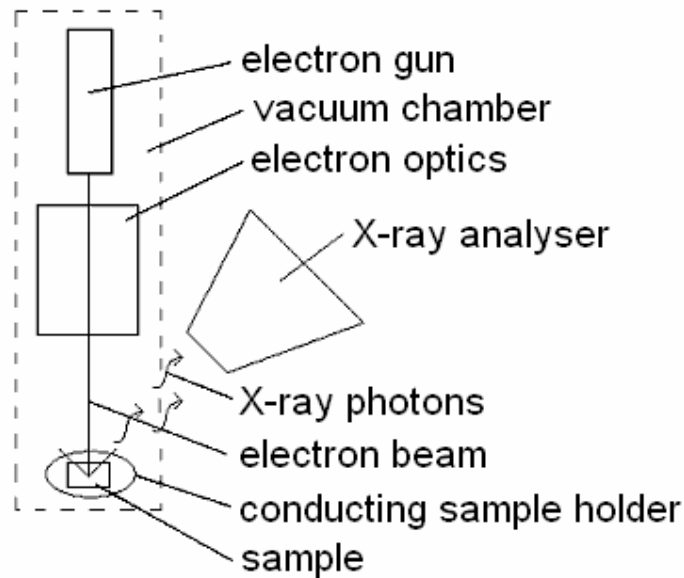
Fig 4.13: A generalised EPMA.

4.2.4 Photoelectron Spectroscopy

Section (3.2.1) explained the theoretical background to photoelectron spectroscopy. From a practical point of view, photoelectrons may be excited by ultraviolet light (UPS) or x-rays (XPS). UPS provides detailed information about the valence band whereas XPS concerns deeper levels. Both measurements were done in the same chamber (fig 4.14), changing only the excitation source and the detector settings.
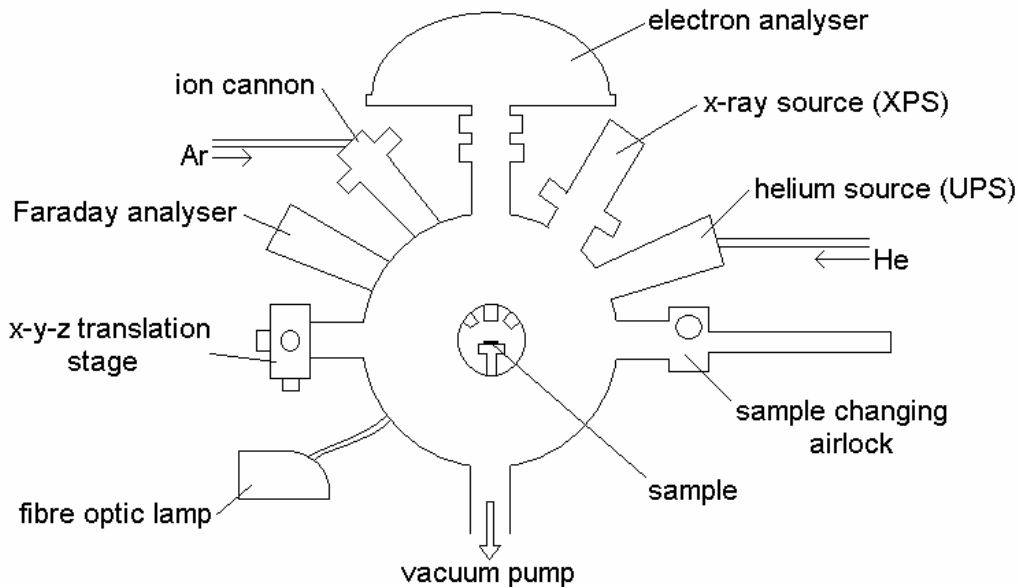
Fig 4.14: Setup for photoelectron spectroscopy measurements.

The growth process for the heterojunction films characterised by this method is described in section 4.1.4. For each film it was firstly necessary to fix the sample to a holder using silver paint to create a short-circuit to prevent the sample from becoming excessively charged while emitting electrons. The film was then introduced by means of an airlock to maintain a high vacuum in the main chamber. The airlock vacuum was produced by rotary and turbomolecular pumps, whereas in the main chamber there was an ionic pump to increase the vacuum to around 10^{-10} mbar. Inside the main chamber there was a fibre optic lamp to illuminate the sample. A Faraday analyser with a video camera connected to a television helped with the sample alignment, done with an x-y-z translation stage. Before taking measurements, the surface of each sample was cleaned for 25 minutes using an ion cannon. A short-circuit was made between the sample holder and the cannon and the cannon was charged with argon at a pressure of 0.5 bar. The bombardment current was 0.44 mA and the argon pressure in the main chamber was around 10^{-6} mbar, regulated by a valve. The Faraday analyser generated a magnetic field to create an image of the electrons leaving the film in order to align it in the ion flux.
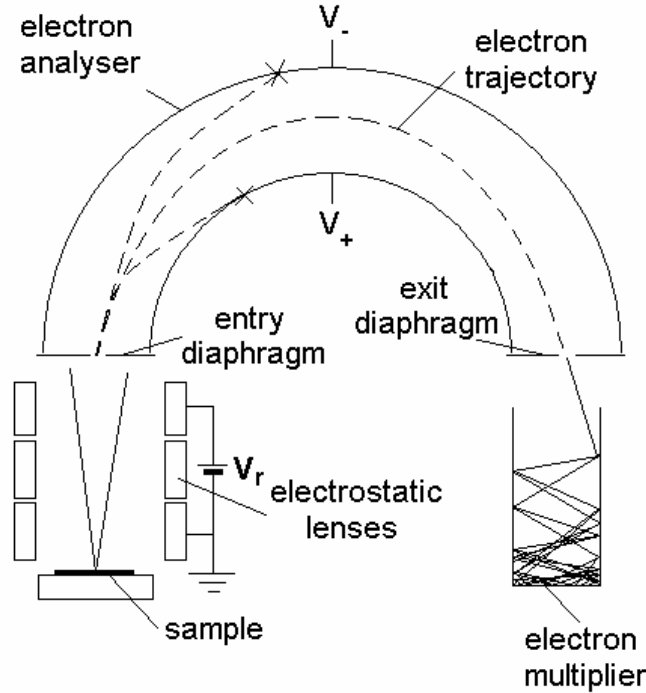
Fig 4.15: Photoelectron spectroscopy electron analyser.

Photoelectrons were excited using a helium lamp in the case of UPS and an X-ray source in the case of XPS. The photoelectrons pass through the high vacuum without being scattered and enter the electron analyser (fig 4.15). The analyser was of the spherical deflection type which permitted both the number and energy of the photoelectrons to be measured. On entering, the photoelectrons pass through electrostatic lenses which focus their trajectories onto the entry diaphragm. There is a variable retarding voltage (V_r) which removes part of the kinetic energy, allowing a highly sensitive analysis. The spherical part consists of a pair of metal plates at potentials of V_+ and V_-. For a photoelectron with energy E_0 to be transmitted to the exit diaphragm, it is necessary for it to pass down the central path marked in fig 4.15. This path is semicircular and the radius is:

$$R_0 = \frac{R_+ + R_-}{2} \qquad (4.4)$$

Where R_+ and R_- are the radii of the interior and exterior plates, respectively. Therefore, the potentials on the plates would be [11]:

$$V_+ = E_0 \left[3 - 2(\frac{R_0}{R_+}) \right] \qquad (4.5a)$$

$$\text{and} \quad V_- = E_0 \left[3 - 2(\frac{R_0}{R_-}) \right] \quad (4.5b)$$

The analyser was connected to a computer by an interface that allowed the system settings to be controlled and data to be acquired. The scan parameters depended on the type of measurement, be it UPS or XPS.

In UPS the excitation source was a helium lamp, shown in fig 4.15. The entry of helium is at a pressure of 0.2 bar. A voltage of 1500 V is applied to the lamp and a valve is opened which increases the helium pressure until a blue discharge is seen at a pressure of $\sim 5\times 10^{-8}$ mbar. A low pressure is preferable because the increase in discharge at higher pressure broadens the spectral peaks. Almost all the helium is singly ionised (He-I) so by using it to excite photoelectrons, the range of kinetic energies produced is between 0 and 16 eV. He-I spectra were measured for all heterojunction samples both in the ZnO and the DMS. On decreasing the helium pressure to 10^{-8} mbar, the high voltage produces an increasing number of double ionisations (He-II) and the proportion of He-II compared to He-I increases, indicated by a more whitish appearance to the discharge. He-II, which is more energetic than He-I, excites photoelectrons with kinetic energies up to 40 eV. However, there is still He-I present, so it is not possible to know if a low energy photoelectron has come from a deep level that has been excited by He-II or a less energetic level excited by He-I. Due to this ambiguity it is only possible to use He-II results up to a binding energy of around 20eV, which corresponds to the highest kinetic energy where there is no contribution from He-I. Therefore, He-II measurements were only done in the energy range from -1 to 18 eV.

In XPS Al-K_α (1486.70 eV [12]) radiation was used to irradiate the samples. It was necessary to cool the source with water to avoid overheating of the target, as the electron flux develops a power of 75 kW. Compared to UPS, the energy resolution is about an order of magnitude lower. The first measurement, a wide scan in the binding energy range 0 - 1350 eV, had 3000 points. Then, on identifying the principal electronic peaks of the constituent elements of each film, more detailed measurements were taken in the region of these peaks both in the ZnO and the DMS halves of the heterojunction samples. In the case of Mn, this was a 300 point scan in the binding energy range 635 – 665 eV. The other scans had 400 points in the energy ranges 700 – 735 eV, 925 – 965 eV and 1015 – 1055 eV for Fe, Cu and Zn respectively.

In a photoelectron spectrum, peaks appear that correspond to the electronic states of the different elements that the sample contains. The number of ionisations of each element is proportional to the integral of the peak that is produced. The relative proportions of elements may be compared in order to verify the stoichiometry of the samples by dividing the integral of the peak by the corresponding subshell photoionisation cross section given in table 4.1.

Element	1s	2s	2p	3s	3p	3d	4s
Mn		0.060	0.18	0.009	0.020	0.0016	0.00060
Fe		0.062	0.23	0.010	0.023	0.0023	0.00070
Ni		0.070	0.29	0.013	0.030	0.0060	0.00085
Cu		0.075	0.34	0.014	0.032	0.014	0.00028
Zn		0.080	0.38	0.016	0.038	0.014	0.00078
O	0.040	0.0019	0.00024				

Table 4.1: Atomic subshell photoionisation cross sections in Mb [13].

4.3 Optical Characterisation

In light of the structural characterisation, the optical properties of the samples were determined by absorption spectroscopy at low temperature and high pressure. Low temperature measurements were taken because the features of the absorption edge are more clearly visible when thermal vibrations are reduced. Moreover, certain vibrational properties of the samples may be determined from the temperature variation of the absorption edge through the Bose model (3.71). High pressure measurements were taken for the reasons described in the introduction; namely to study high pressure phases and investigate the relationship between physical pressure and the "chemical pressure" produced by changing the type and concentration of the dilute cation.

4.3.1 Low temperature

Low temperature absorption spectra were taken for all DMS samples in the spectral range 250-700 nm at temperatures from 20 to 290K using the apparatus shown in fig 4.16.
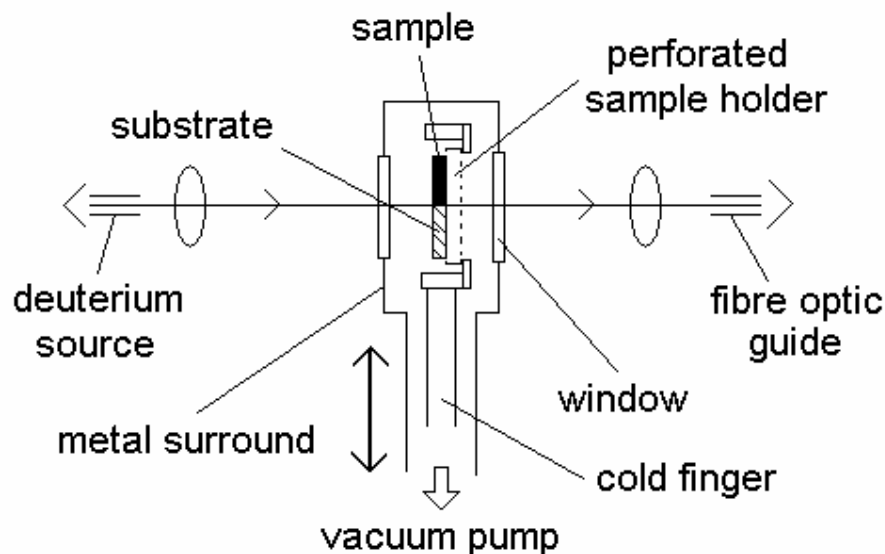
Fig 4.16: Optical setup for low temperature transmission measurements.

The deuterium source used was a Micropack DH-2000, which provided illumination over the whole spectral region of interest. Light transmitted by the sample was focused into the fibre optic guide and measured by an Ocean Optics HR2000 spectrometer. The cold finger, in thermal contact with the perforated sample holder, was cooled using an APD HC-2 closed circuit helium system by Cryogenics Inc. The sample and a sapphire substrate were mounted on the holder to enable the respective measurements of the sample spectra and direct light spectra, required for normalisation purposes. An x-y-z translation stage was used to change the position the focus between the sample and the substrate. To avoid convection heating from the atmosphere, the exterior part of the system was enclosed by a metal surround, inside which a vacuum of 10^{-3} mbar was produced by a rotary pump. On reaching the minimum temperature, the temperature was increased using a heating resistance in thermal contact with the sample holder. The heating power was controlled by a proportional, integral, differential (PID) system whose input signal came from a K-type thermocouple in the sample holder. The absorbance and transmittance was measured in the temperature range 20-290K. The transmittance was converted to the absorption coefficient using (3.47) and spectra were analysed to determine the behaviour of the optical gap of the films in function of temperature.

4.3.2 High Pressure

A diamond anvil cell (DAC) of the membrane type, shown in fig 4.17, was used to apply high pressure to all DMSs. The sample was contained in a hydrostatic medium in a hole in the centre of an Inconel gasket. The gasket was placed between the diamonds and a membrane was inflated with helium to increase the pressure. The membrane transmits the pressure to the gasket through the piston, support and diamond anvils. The anvils have a diameter of 500 μm and a surface area of 0.2 mm^2. However, the membrane has a surface area of several cm^2, therefore there is a large multiplying factor which allows typical pressures of the order of tens of GPa to be reached.
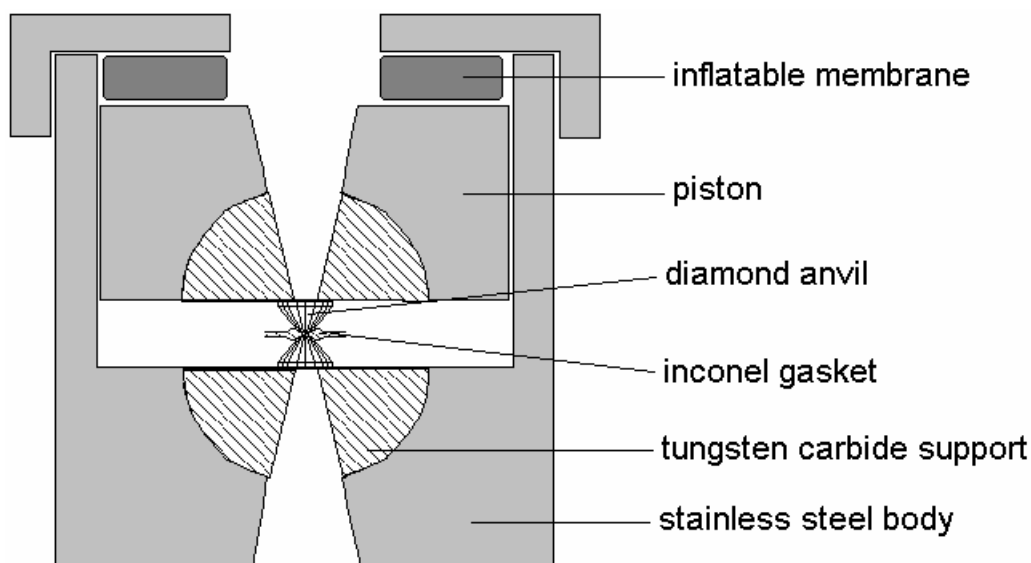
Fig 4.17: Vertical cross-section of the membrane DAC.

To charge the cell (fig 4.18), it was firstly necessary to create the hole in the gasket. To make sure that the hole was well centred, the mark of the diamonds at a pressure of 10 GPa was made. Then, centring the mark of the diamonds under a microscope, an electric discharge from a fine tungsten needle was used to vapourise the hole by the process of electro-erosion. The discharge occurs at a voltage of 100-140 V when there is a separation of the order of 100μm between the tip of the needle and the gasket. The diameter of the final hole was around 200-300μm to leave sufficient space to charge the sample without introducing too much weakness in the gasket by removing material. From the samples grown over mica, a small quantity with dimensions of around 150×150μm was exfoliated using ethanol and a razor blade and charged in the hole. Several ruby grains with a Cr^{3+} concentration of 3000 ppm were also charged with a mounted needle. Finally, a drop of pressure transmitting medium, a mixture of methanol, ethanol and water in the proportions 16:3:1, was added with a syringe before closing the cell. The liquid serves to transmit the pressure hydrostatically from the diamond anvils to the sample. To prevent it from escaping, a small pressure of around 0.5 GPa was applied immediately.
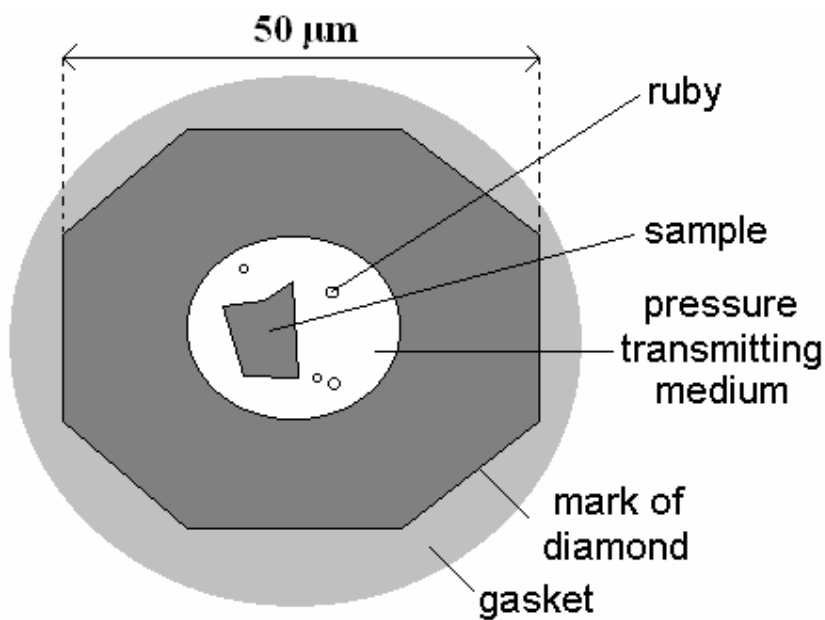
Fig 4.18: Appearance of the charged cell.
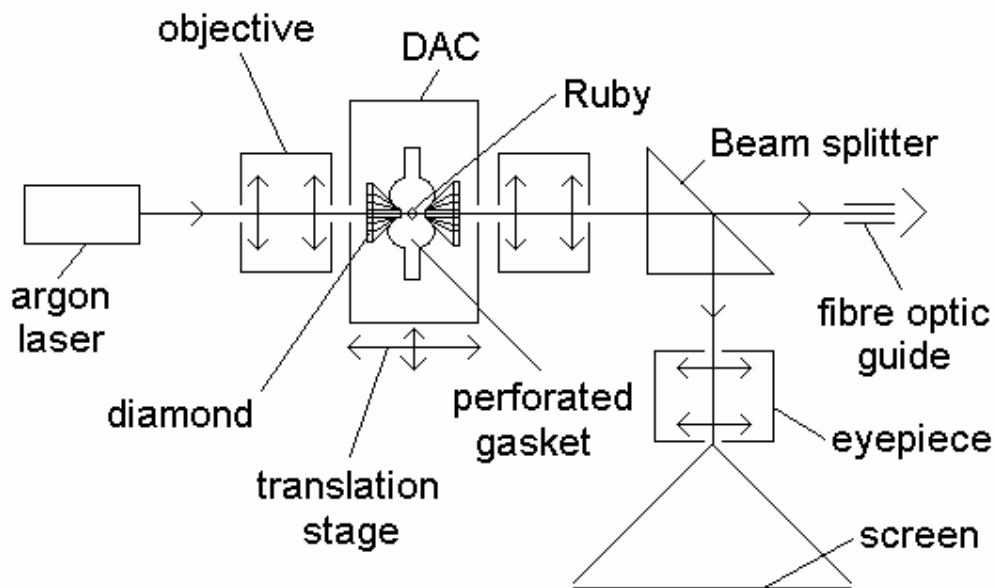
Fig 4.19: Setup to measure ruby photoluminescence.

To measure the pressure within the cell, the ruby luminescence scale was used [14]. The DAC is designed so that light can pass from one side to the other through the diamonds and the hole in the gasket. With the setup in fig 4.19, the beam from the argon laser was focussed in a ruby with the help of the image formed on the screen. The green laser excites electrons in the Cr^{3+} ions from the ground state to the $^4T_{2g}$ level. They then pass to the $^2T_{1g}$ or ^2E_g levels by means of the emission of a phonon and they recombine with the $^4A_{2g}$ level by the emission of a red photon [15]. This gives rise to two Gaussian peaks in the emission spectrum and the electron returns to the ground state by the emission of another phonon, shown in fig 4.20a. The

84

luminescence peaks from the $^2T_{1g}$ and ^2E_g levels are historically known as the R_1 and R_2 lines, respectively, and they give ruby its characteristic red colour. It is known that the position of these peaks (in nm) varies linearly in function of pressure (in GPa) according to the following relationships [14]:

$$\lambda_{R1} = 692.8 + 0.364P \qquad (4.6a)$$
$$\lambda_{R2} = 694.3 + 0.364P \qquad (4.6b)$$

These equations were used to convert the positions of the luminescence lines into the corresponding pressures. Fig 4.20b shows the displacement graphically.
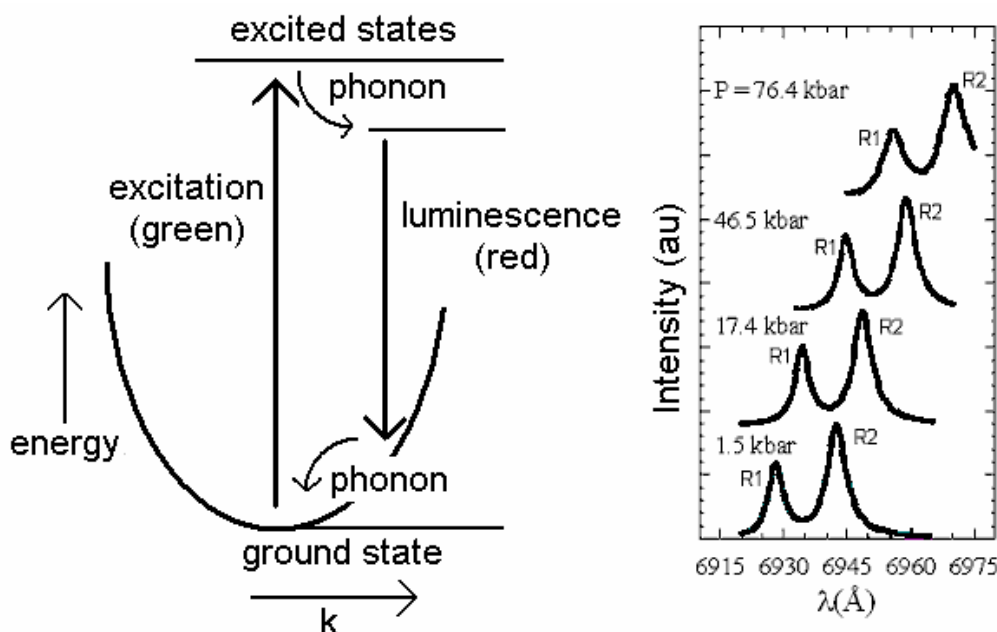
Fig 4.20a (left): Ruby photoluminescence process.
4.20b (right): Linear shift of R1 and R2 peaks in function of pressure [15].

The setup in fig 4.21 was used to take absorbance and transmittance measurements at high pressure with an Ocean Optics HR2000 spectrometer. The wavelength range was 250-700nm and the pressure was varied between 0 and 12 GPa in a closed cycle. The pressure between each point was roughly 1 GPa, although this was lower in the region of phase transitions so that their pressures could be more precisely defined. Transmittance was converted into absorption coefficient using (3.47) and the spectra were analysed to determine the behaviour of the optical gap of the films in function of pressure.
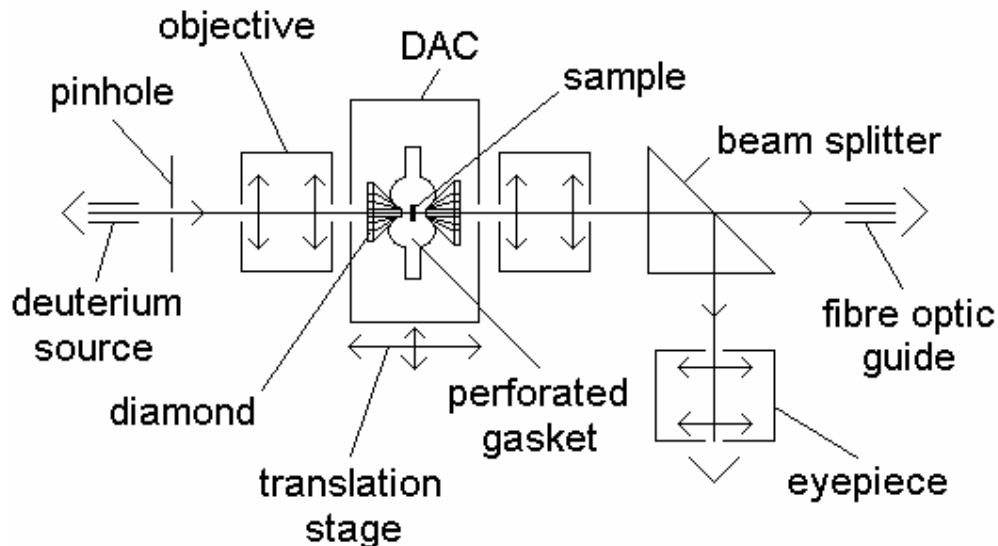
Fig 4.21: Optical setup to measure high pressure transmission.

Fig 4.22 shows the typical variation of the pressure in the cell in function of the membrane pressure, determined from the ruby luminescence scale. The increase in pressure in the chamber is due to the plastic deformation of the gasket, therefore the large hysteresis is due to the plasticity of the gasket. It was necessary to measure the membrane pressure because when a large increase in pressure only produces a small increase in pressure, the gasket is arriving at the limit where increasing the pressure further could cause it to break.
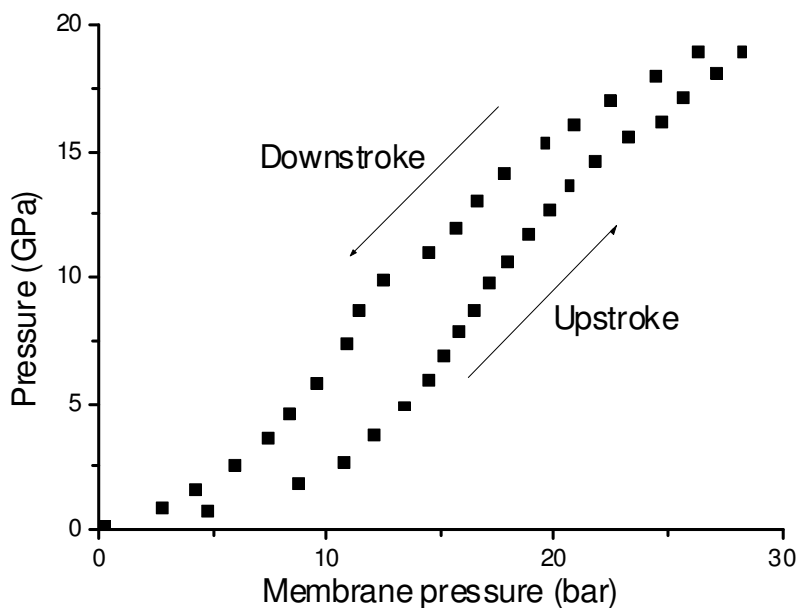
Fig 4.22: Typical dependence of the sample pressure in function of the membrane pressure.

4.4 Magnetic characterisation

To complete the characterisation of the samples and go some way towards resolving the controversies described in the introduction, magnetisation measurements were taken in function of temperature and applied magnetic field. These measurements were taken at the Instituto de Materiales de Aragón at the Universidad de Zaragoza using a semiconductor quantum interference device (SQUID) magnetometer.
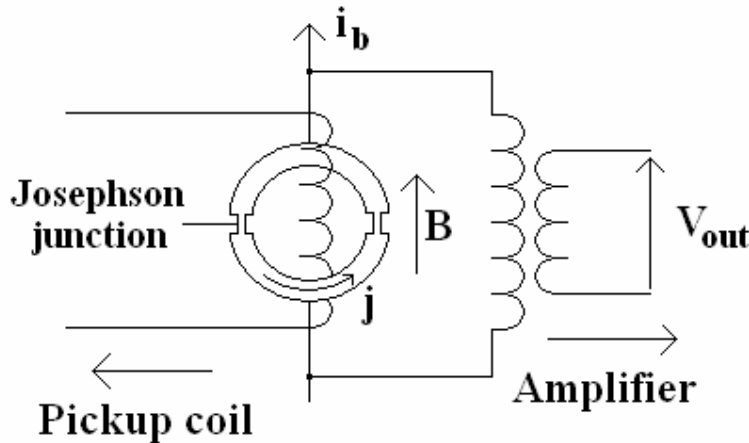
Fig 4.23: A DC SQUID.

A SQUID, shown in fig 4.23, is a very sensitive magnetometer based on a superconducting ring containing at least one Josephson junction, a very thin insulating barrier between two weakly coupled superconductors. The only way that current can pass from one side of a junction to the other is by quantum tunnelling, which produces a phase difference (δ) between the two sides. A DC SQUID, like the one used to take these measurements, has two such junctions, with phase differences δ_1 and δ_2. The ring is biased by current i_b, while current j circulates in the ring. As the SQUID is in series with a resistor, there is no potential difference across the junctions, provided the current passing through both is below the critical value (i_c). Therefore, the maximum supercurrent that can flow through the ring is limited to the sum of the critical currents of the two junctions. The sample is positioned within a pickup coil, which detects its magnetisation field. In order to reduce background magnetic field fluctuations, a second pickup coil, like the first but counter wound, is connected to the first to form an astatic pair. Moreover, the apparatus is contained in a long cylindrical superconducting shield. The pickups are connected to a further coil passing through the centre of the superconducting ring to produce a magnetic field (B) proportional to the magnetic susceptibility of the sample. Assuming that the two junctions are identical, by applying Ampere's law to the two halves of the ring, it may be shown that the following relationship is true [16]:

$$\delta_2 - \delta_1 = \frac{2\pi}{\Phi_0}\left(BA + LJ\right) = \frac{2\pi}{\Phi_0}\Phi_T \qquad (4.7)$$

where A is the effective area of the loop and L is its inductance. Φ_0 denotes the magnetic flux quantum of 2×10^{-15} Tm^2 and Φ_T is the total flux. The currents through the two junctions (i_1 and i_2) are related to their respective phase differences:

$$i_{1,2} = I_c \sin \delta_{1,2} \qquad (4.8)$$

By applying Kirchhoff's Current Law at the top and bottom of the ring, the following relationship is also obtained:

$$i_b = i_2 - i_1 \qquad (4.9)$$

Combining (4.7), (4.8) and (4.9), the maximum bias current is:

$$i_{b\max} = \sqrt{2} i_c \sqrt{1 + \cos\left(\frac{2\pi}{\Phi_0}\Phi_T\right)} \qquad (4.10)$$

The applied magnetic field causes the bias current to be modulated with period Φ_0 and amplitude I_c. Hence, the magnetisation of the sample may be determined by measuring the oscillations of the bias current. I_c can be found directly by increasing the bias current at fixed magnetic field until a potential difference is detected across the junctions.
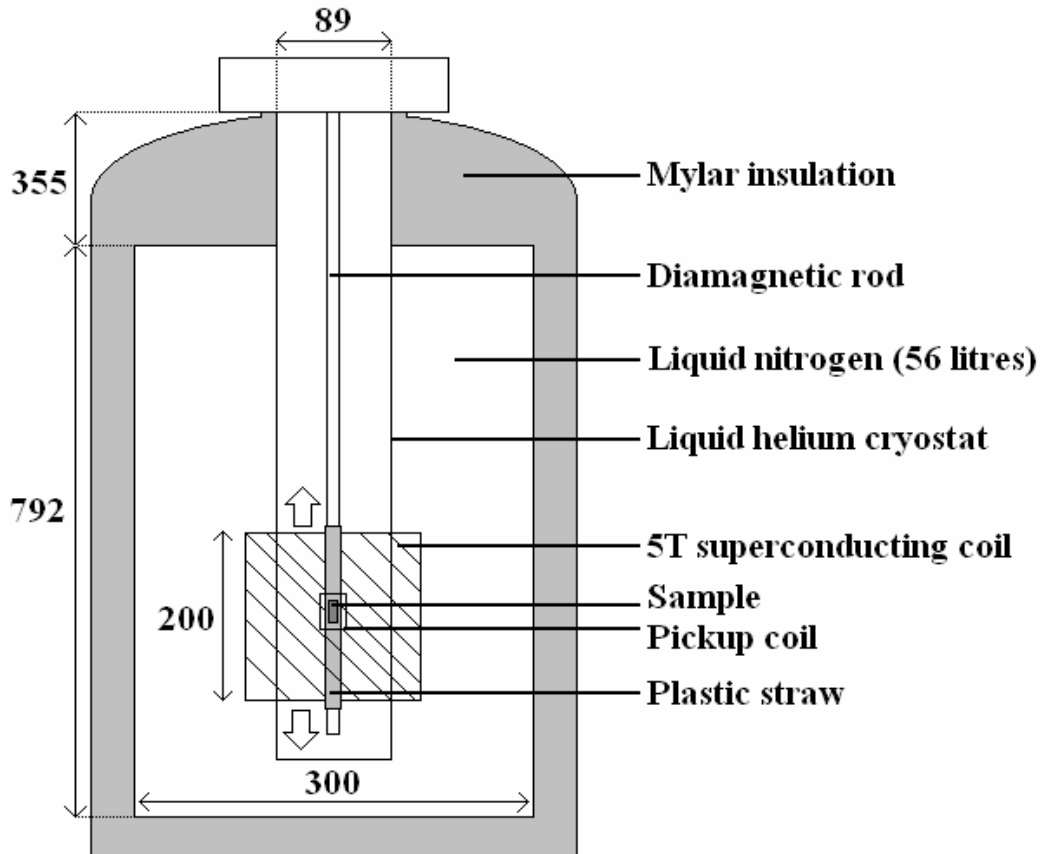
Fig 4.24: The magnetic property measuring system.

The SQUID magnetometer used in this investigation was a Quantum Design XL Magnetic Property Measuring System (MPMS), shown in fig 4.24. Measurements were taken with DMS films deposited over sapphire and mica. Firstly the masses of the samples were measured and their surface areas were estimated from enlarged digital photographs of the samples placed on squared paper. It was necessary to fix each sample to the inside of a plastic straw using Kapton tape so, due to size limitations, the average surface area of the films over sapphire was 20 mm^2. However, films over mica with larger surface areas of the order of 1 cm^2 could be used by cutting the samples into smaller pieces which could then be stacked between layers of Kapton tape. The straw was connected to a diamagnetic rod, which was inserted into the cryostat of the magnetometer. Sample magnetisation was measured in function of temperature in the range 1.8 – 300 K and in function of field in a closed loop from 5 to -5 T at 1.8 and 300 K. Results were corrected for the substrate response by scaling and subtracting the magnetic response of sapphire and mica substrates over which no films had been deposited. In light of structural characterisation results and limited time, these measurements were only taken with $Zn_{1-x}Mn_xO$ and certain $Zn_{1-x}Fe_xO$ samples.

Samuel John Gilliland

4.5 Bibliography

[1] H. Li, X. J. Pan, M. Qiao, Y. Z. Zhang, T. Wang and E.Q. Xie. Vacuum **82**, 459 (2008).

[2] P. F. Zhang, H. Y. Wei, G. W. Cong, W. G. Hu, H. B. Fan, J. J. Wu, Q. S. Zhu and X. L. Liu. Thin Solid Films **516**, 925 (2008).

[3] A. Bakin, A. El-Shaer, A.C. Mofor, M. Kreye, A. Waag, F. Bertram, J. Christen, M. Heuken and J. Stoimenos. J. Cryst. Growth **287**, 7 (2006).

[4] T. H. Maiman. Nature **187**, 493 (1960).

[5] A. F. Turner and H. M. Smith. Appl. Opt. **4**, 147 (1965).

[6] D. Dijkkamp, T. Venkatesan, X. Wu, S. Shaheen, N. Jisrawi, Y. Minlee, W. Mclean and M. Croft. Appl. Phys. Lett. **51**, 619 (1987).

[7] D. Chrisey and G. Hubler. "Pulsed Laser Deposition of Thin Films", Wiley (1994).

[8] J. Sans, A. Segura, J. Sánchez-Royo, C. Ferrer-Roca and E. Guillotel. Phys. Stat. Sol. b **244**, 407 (2007).

[9] F. Tsiu, P. Han and C. Flynn. Phys. Rev. B **47**, 20 (1993).

[10] M. Allali, C. Sorensen and E. Veje. Phys. Rev. B **48**, 4398 (1993).

[11] Stefan Hüfner. "Photoelectron Spectroscopy", Springer (2003).

[12] J.A. Bearden, "X-Ray Wavelengths," Rev. Mod. Phys. **39**, 78 (1967).

[13] J. Yeh and I. Lindau. At. Data Nucl. Data Tables **32**, 1 (1985).

[14] J. Barnett, S. Block and G. Piermarini. Rev. Sci. Inst. **44**,1 (1973).

[15] F. Rodríguez. "Espectroscopia bajo altas presiones". I Escuela de Altas Presiones, Valencia (2002).

[16] J. Clarke and A. Braginski. "SQUID Handbook", Wiley (2004).

5 Results

5.1 Crystal growth

The plume emission spectra obtained by the method described in section 4.1.4 were analysed to confirm that the growth conditions were constant during the film deposition. The spectrum for pure ZnO is shown in fig 5.1 at the start of the process and after 6 hours. The spectra are vertically shifted relative to each other to allow comparison. The most intense line was always the 2nd harmonic of the Nd:YAG laser (523nm) so the spectra were normalised so that this peak would have an intensity of one. In this way, results were corrected for intensity changes not related to the deposition process. By comparison with literature [1, 2], it was possible to index the main peaks, all of which corresponded to optical emissions from Zn. The wavelengths of the emissions have been shown in the figure, along with the Zn ionisation state responsible for the peak. The index * denotes an emission from neutral Zn, while +* is produced by singly ionised Zn. There is also emission from oxygen atoms, but it is found at lower energies in the 750-850 nm range [1]. Clearly the two spectra are very similar, as the intensities of the Zn peaks remain practically constant. Therefore we conclude that the chemical composition of the plasma and, consequently, the growth conditions do not change over time.
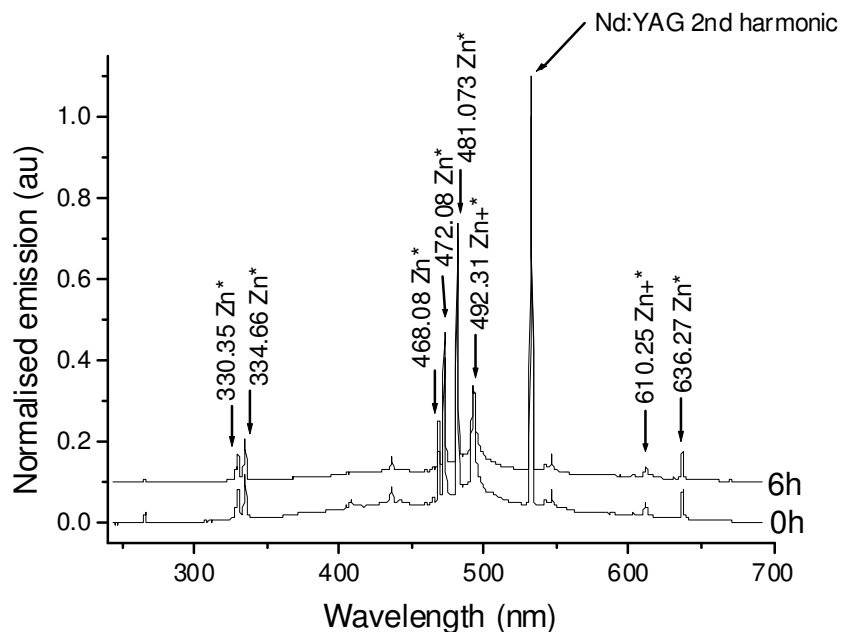
Fig 5.1: Emission spectrum of the ZnO plume.

While depositing $Zn_{1-x}Mn_xO$ films, the plume emission from the targets containing 5% and 25% Mn was also measured initially and after 6 hours. The results are shown in fig. 5.2. In order to appreciate the effect of Mn, it is necessary to zoom in on the highlighted area, which is shown in fig 5.3. The Mn emission is much less intense than that of Zn because there is a lower proportion of Mn in the targets. Moreover, the vapour pressure of Mn is significantly lower, as the graph in fig 5.4 shows. Returning to fig 5.3 there seems to be three major regions where the presence

of Mn in the targets changes the form of the emission spectrum, with respect to that of pure ZnO. The cluster of peaks around 300 nm is due to emission from singly ionised Mn [3], whereas the peaks close to 475 nm correspond to emission from neutral Mn [4]. The particular energies of the peaks are given in the cited publications. However, further peaks, which appear to be unreported, are also observed in the wavelength range 350 – 400 nm. These have been simply marked by "Mn", as the ionisation state that produces them is unclear. As expected, the intensity of the Mn emission is proportional to the Mn concentration in the target and the growth conditions are constant over time.
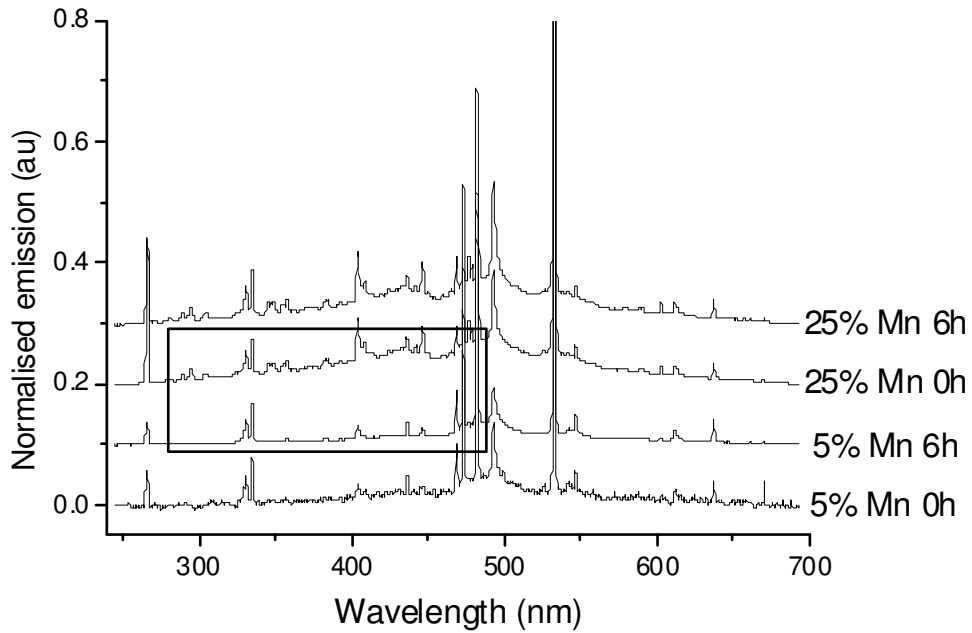
Fig 5.2: Emission spectrum of $Zn_{1-x}Mn_xO$ plume.
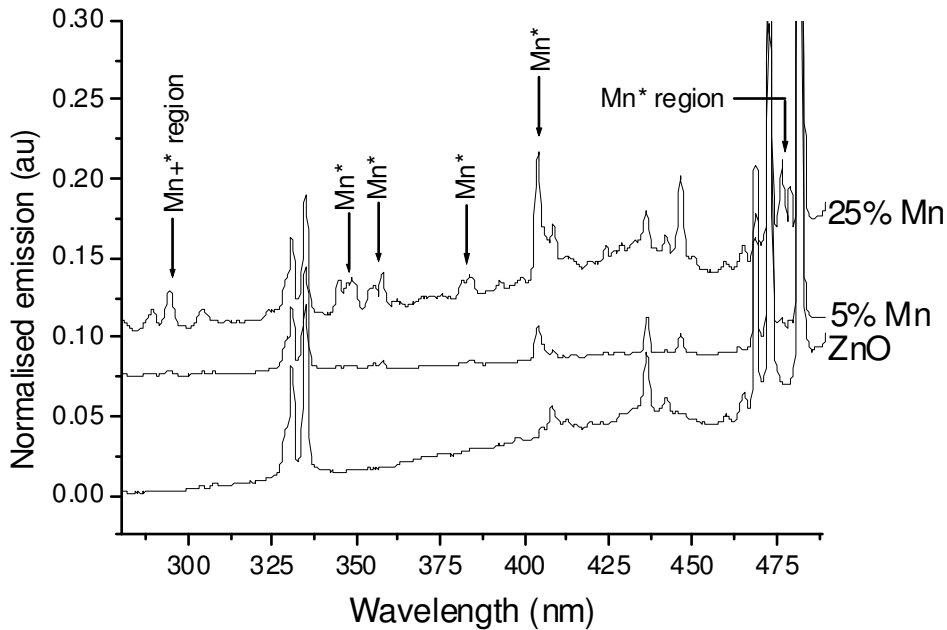
Fig 5.3: Enlarged region of $Zn_{1-x}Mn_xO$ plume spectrum.
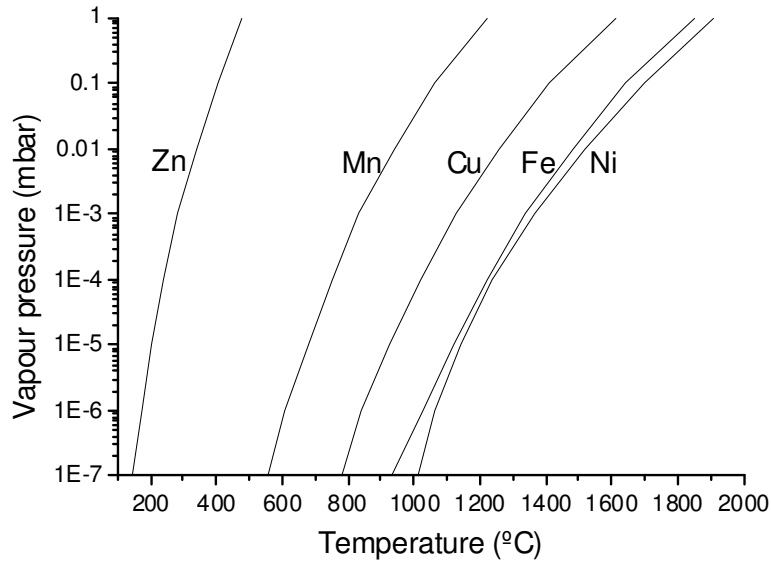
Fig 5.4 Vapour pressure of deposited TMs [5].

In the case of $Zn_{1-x}Fe_xO$ films, the plume spectra from the ablation of the target containing 5% Fe are shown in fig 5.5. American Vacuum Society (AVS) online optical emission tables [6] identify 360 – 380 nm as the major region of Fe emission, so the zoom was done there and is shown in the inset to the figure, along with the spectrum of pure ZnO for comparison purposes. Peaks are observed at the energies given in the AVS tables, which correspond to emission from neutral Fe atoms. The peaks are even less intense than those of Mn, in agreement with fig 5.4 which shows that Fe has a lower vapour pressure. As before, the growth conditions appear to be constant over time.
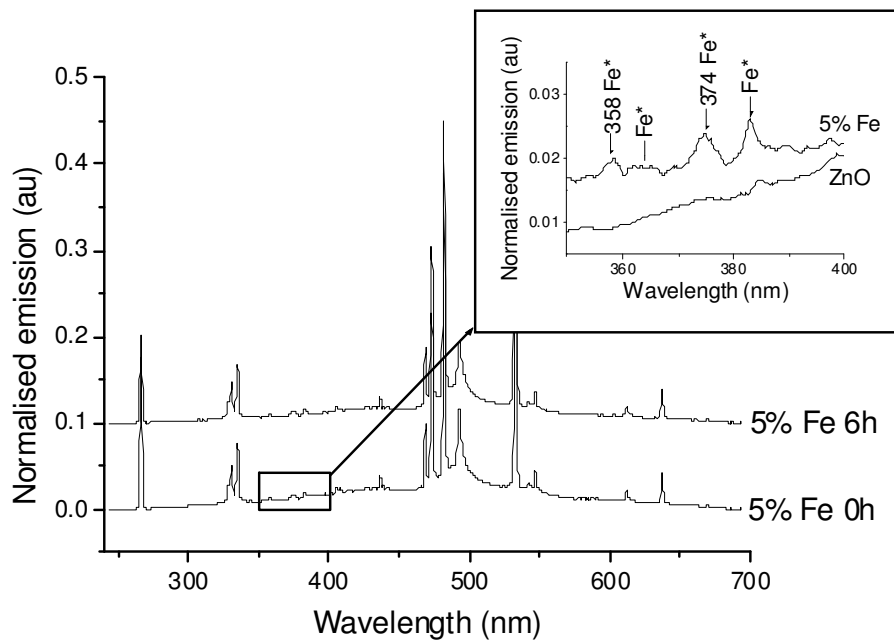
Fig 5.5: Emission spectrum of $Zn_{1-x}Fe_xO$ plume.

93

A similar process was applied to the plume spectra of the target containing 5% Cu, while depositing $Zn_{0.95}Cu_{0.05}O$, as shown in fig 5.6. Only one main peak was listed in the AVS tables and its energy was 325 nm, corresponding to emission from neutral Cu. On performing the zoom around this energy, shown in the inset to the figure, this peak is clearly observed when a comparison is made with the pure ZnO spectrum. Fig 5.4 places the vapour pressure of Cu between that of Mn and Fe. Therefore, an emission peak of intermediate intensity would be expected, in agreement with results. Again, no change in growth conditions is detected over time.
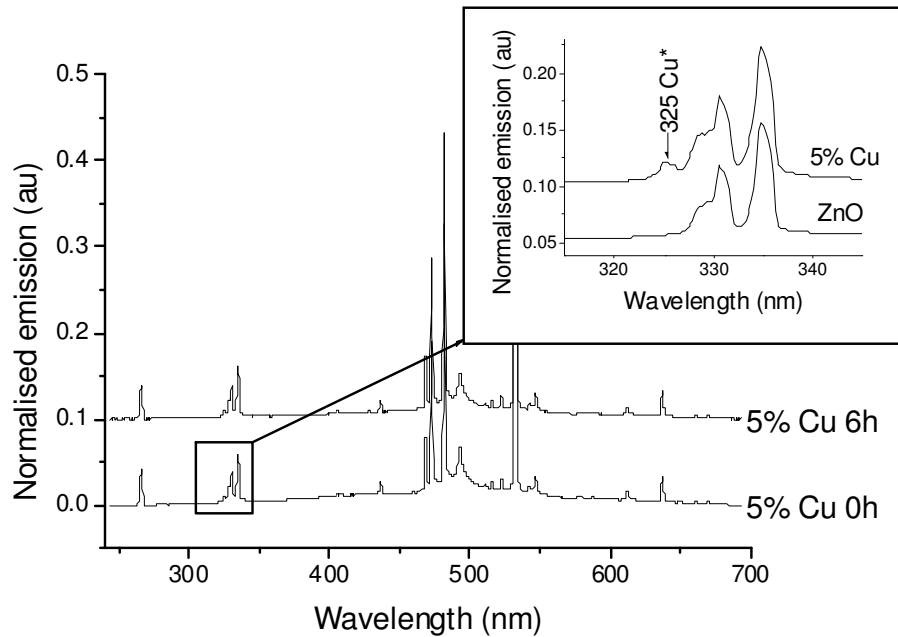
Fig 5.6: Emission spectrum of $Zn_{1-x}Cu_xO$ plume.

Finally, in the case of $Zn_{1-x}Ni_xO$, the plume spectra of the target containing 5% Ni was also measured and is shown in fig 5.7. The AVS tables listed several emissions due to neutral Ni, mainly in the wavelength region 300 – 360 nm. On performing the zoom in that region, shown in the inset to the figure, some but not all of the peaks could be identified. For example the peak at 346 nm clearly appears but at 301 nm there is no appreciable difference between the 5% Ni spectrum and that of pure ZnO. This is hardly surprising, as fig 5.4 shows that Ni has the lowest vapour pressure of all the deposited TMs so very low peak intensities would be expected. As in the previous cases, the growth conditions are constant over time so, at this stage, there is no reason to doubt that the films have been correctly deposited.
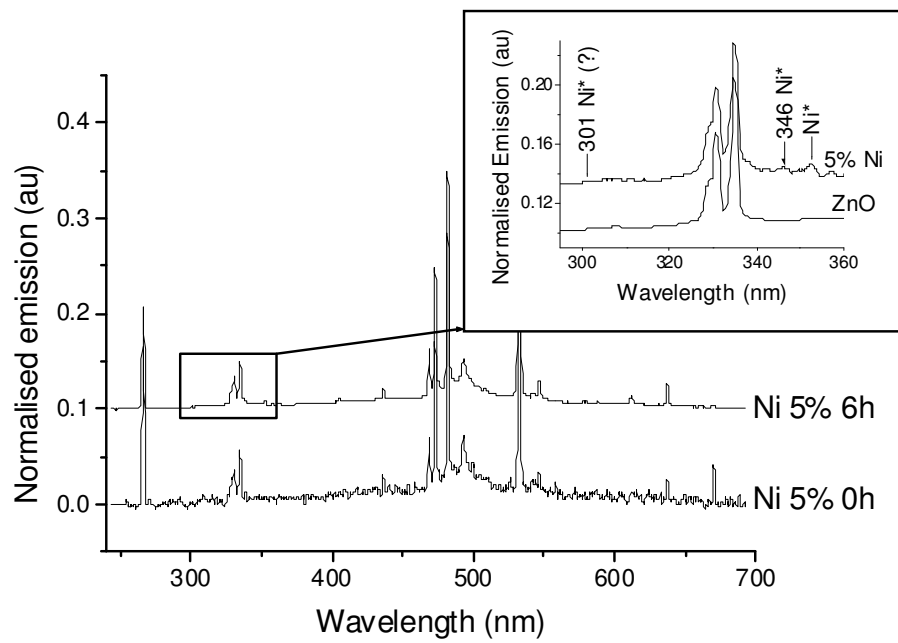
Fig 5.7: Emission spectrum of $Zn_{1-x}Ni_xO$ plume.

5.2 Structural characterisation

5.2.1 XRD
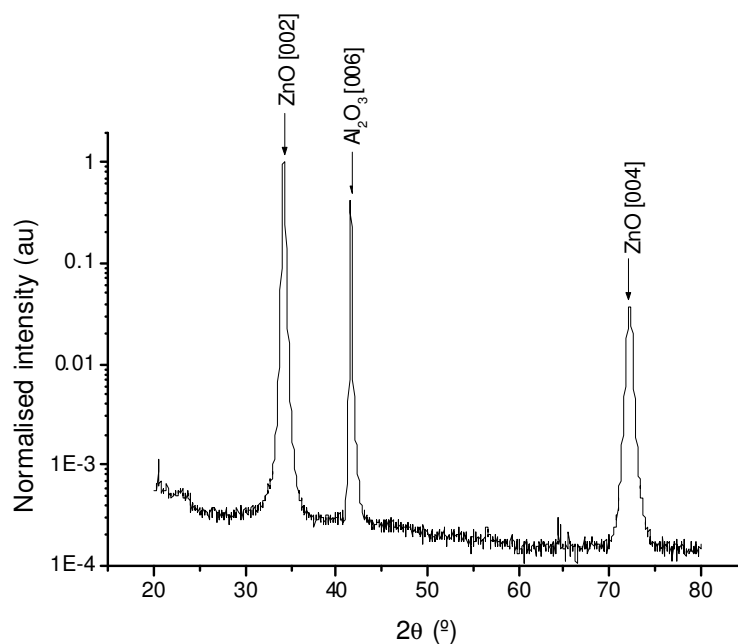
Fig 5.8: X-ray diffractogram of a ZnO film.

Fig 5.8 shows the X-ray diffractogram of a pure ZnO film deposited over a sapphire substrate. Three clear peaks appear and their positions were determined by fitting to Gaussian profiles. As the film had a thickness of only 100nm, it was expected that peaks from the substrate would be detected. By comparison with the JCPD standard for Al_2O_3 [7], the middle peak could be identified as the [006] diffraction, confirming the c-orientation of the substrate. As it is known that this peak should appear at an angle of $2\theta = 41.685°$, the results were always shifted so that this would be the case. Hence, the diffractograms were corrected for minor errors produced by failure to align the sample with the top of the holder. The remaining two peaks were compared with the standard for ZnO [8] and identified as the [002] and [004] diffractions. Therefore, the films were also c-oriented. The reason for the preferred orientation is that the c lattice parameter of sapphire divided by 6 (2.17) is similar to that of ZnO divided by 2 (2.61). Therefore, by assuming this orientation, stress produced by lattice mismatch may be minimised. The Bragg condition (4.3) was used to calculate the c lattice constant and a value of 5.22 ± 0.01 Å was obtained, in agreement with literature [9].

On alloying with Mn, the progressive evolution of the x-ray diffractogram in function of concentration is shown in fig 5.9. Results are shifted vertically with respect to each other to allow comparison. The same three main peaks appear but, in addition, a small contribution from ZnO [110] is occasionally seen, particularly in the sample containing 5% Mn. The intensity of this peak is low because the lattice mismatch in this orientation is greater than in the c-orientation. In the sample containing 20% Mn, two other peaks are observed, one on either side of the ZnO

[002] peak. There are two possible explanations, the first being the presence of secondary phases. In the introduction, the maximum solubility of Mn in ZnO given by Ando et al. [10] is around 20%, although one would expect a non-equilibrium growth process such as PLD to be able to go beyond this limit. Nevertheless, the peak before ZnO [002] corresponds well with body-centred tetragonal $ZnMn_2O_4$ [200] [11] and the peak after could be face-centred cubic $ZnMnO_3$ [311]. Both these peaks are the most intense diffractions that occur when the corresponding materials are grown without a preferred orientation. The other explanation is that the film is becoming more polycrystalline, which broadens and occasionally shifts the energy of the peak. The diffractogram of the sample containing 25% Mn adds weight to this argument because its ZnO [200] and [400] peaks are considerably broadened and shifted. The broadening may be described by the Scherrer formula, which relates the average crystallite size (D) to the FWHM of the diffraction peak (w), in terms of 2θ:

$$D = \frac{K\lambda}{w\cos\theta} \quad (5.1) \ [12]$$

where K is the Scherrer constant, which normally takes a value of 1 or just below, λ is the wavelength of the x-rays and θ is the diffraction angle in radians. This idea will be explored further in the electron microscopy results, section 5.2.4.
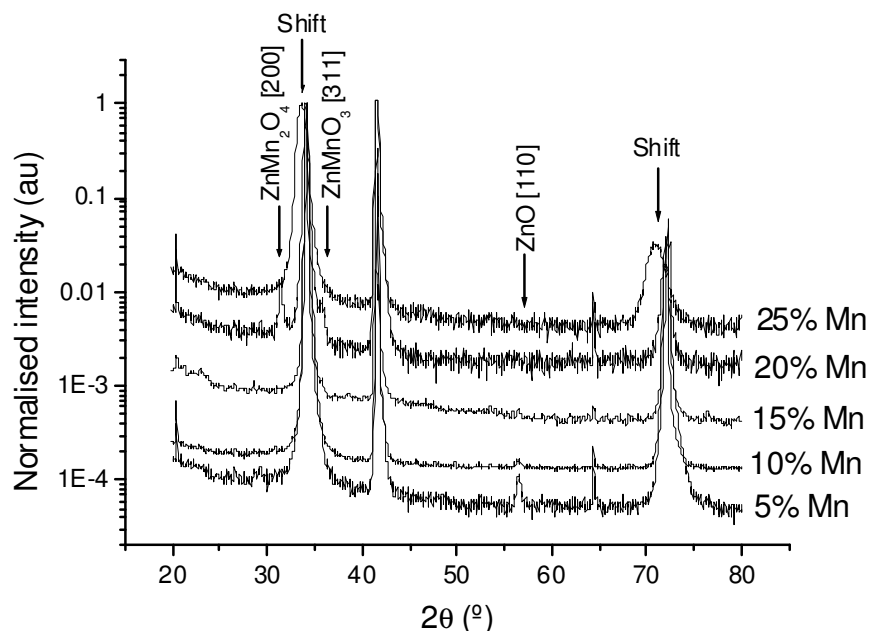
Fig 5.9: X-ray diffractogram of $Zn_{1-x}Mn_xO$ films.

Fig 5.10 shows an enlarged region around the ZnO [002] peak. A shift toward lower angles is observed as the concentration of Mn increases. This occurs because, in tetrahedral coordination, the electrostatic attraction between the nucleus and outer (3d) electrons in Mn is lower than in Zn. Therefore, the Mn ionic radius is larger, increasing the c lattice parameter. Fig 5.11 shows this parameter in function of Mn concentration. Up to a concentration of 15%, the increase appears to be linear with a coefficient of $1.69 \pm 0.04 \times 10^{-3}$ Å%$_{Mn}^{-1}$. Beyond this concentration, the model is not obeyed, possibly for the reasons discussed earlier. At a Mn concentration of 25%, the

value of c is 5.30 ± 0.01 Å, which is so far removed from the other points that it is not shown on the graph. This adds further support to the film being highly polycrystalline in nature. In conclusion, it seems that the substitution of Mn for Zn is effective, at least up to a concentration of 15%. This will be discussed further in the XAS results, section 5.2.2.
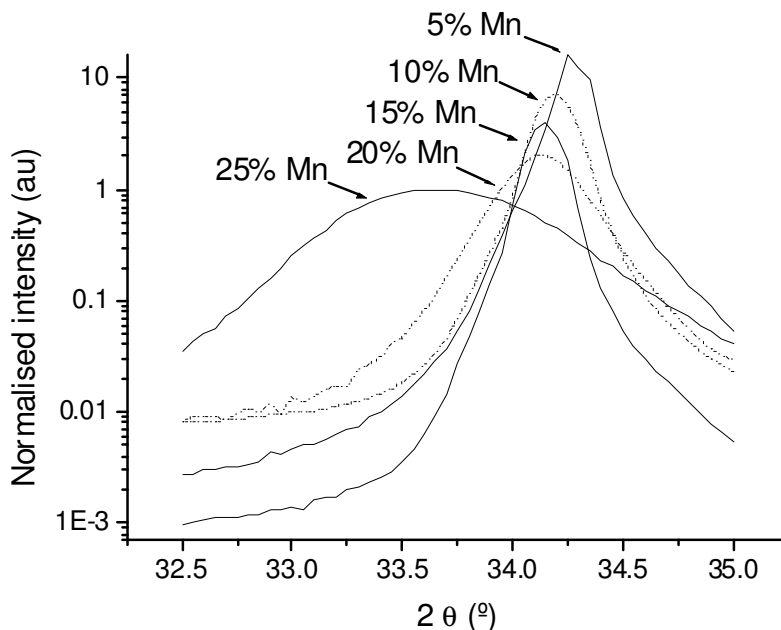
Fig 5.10: Enlarged region of $Zn_{1-x}Mn_xO$ diffractogram at ZnO [002] peak.
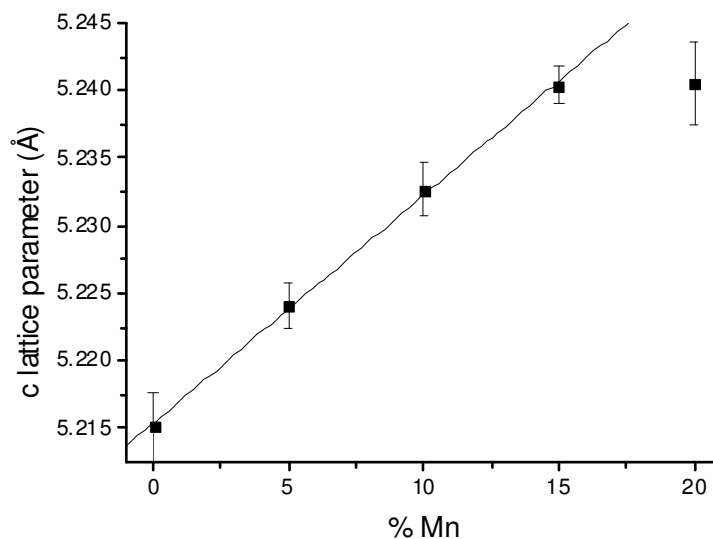
Fig 5.11: Variation of the c lattice parameter with Mn content.

In the case of $Zn_{1-x}Fe_xO$, fig 5.12 shows the x-ray diffractograms at various Fe concentrations. The general form is similar to that of the films containing Mn. However, the reported maximum solubility of Fe in ZnO is much lower than that of Mn, only 2-3 %. For this reason the secondary phase, tetragonal γ-Fe_2O_3, is detected in the films containing 5 and 10% Fe, with the [119] peak occurring just after the ZnO

[002] diffraction. This is the most intense diffraction that occurs in Fe_2O_3 with no preferred orientation [13]. Its measured intensity increases with Fe concentration, corresponding to a decrease in the proportion of Fe ions occupying the Zn substitutional position.
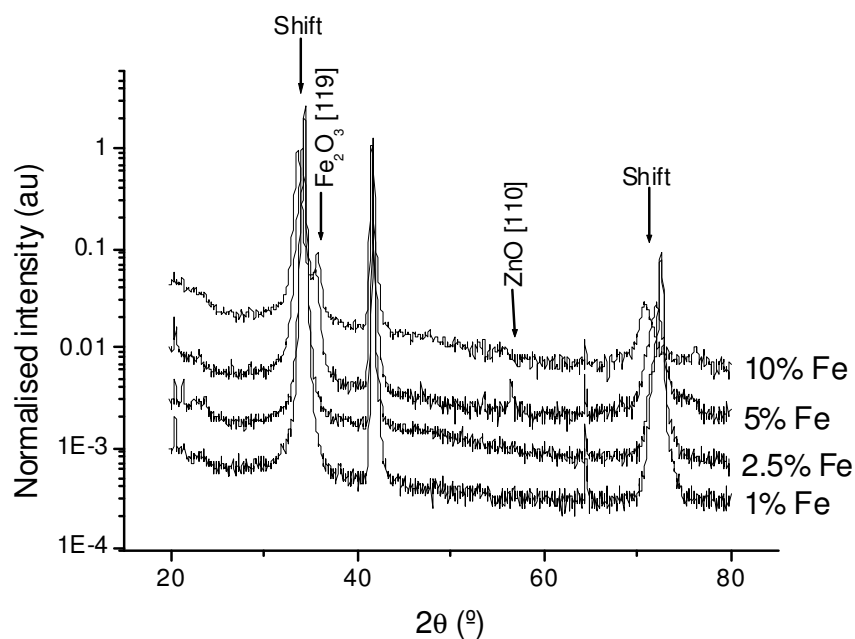
Fig 5.12: X-ray diffractogram of $Zn_{1-x}Fe_xO$ films.
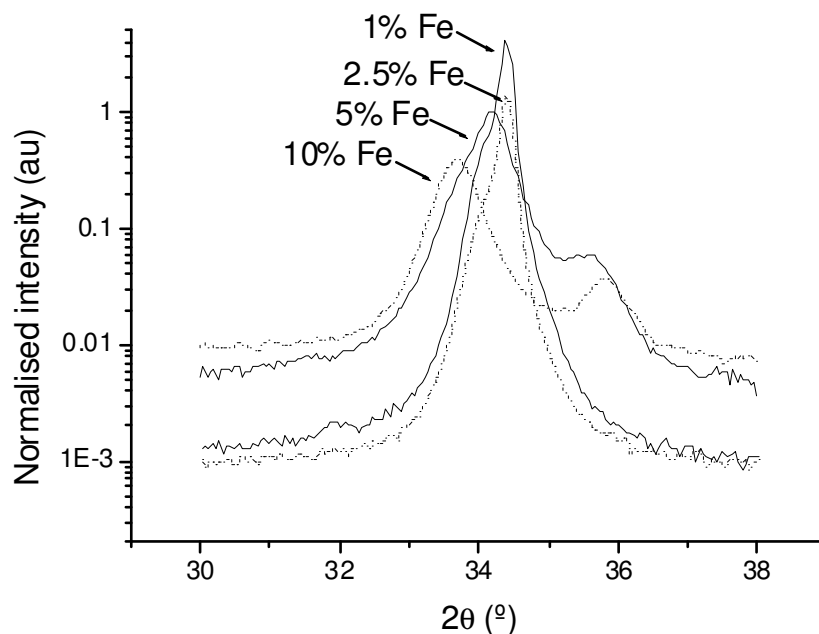
Fig 5.13: Enlarged region of $Zn_{1-x}Fe_xO$ diffractogram at ZnO [002] peak.

As in $Zn_{1-x}Mn_xO$, the ZnO peaks shift to lower angles as the dilute cation concentration increases, as shown in fig 5.13. The corresponding average increase in the c lattice parameter on increasing the Fe concentration from 0 to 2.5 % is $5.2 \pm 0.2 \times 10^{-4}$ Å%$_{Fe}^{-1}$, about a third that of $Zn_{1-x}Mn_xO$. This is because, in tetrahedral

coordination, the ionic radius of Fe is between that of Zn and Mn. However, from 2.5 to 10%, the average increase rises to $0.0134 \pm 0.0006 \, \text{Å}\%_{Fe}^{-1}$, which seems high when compared to the previously calculated values. As before, a possible explanation could be the reduction in crystallite size, which is evident from the broadening of the diffraction peak as the Fe concentration increases.
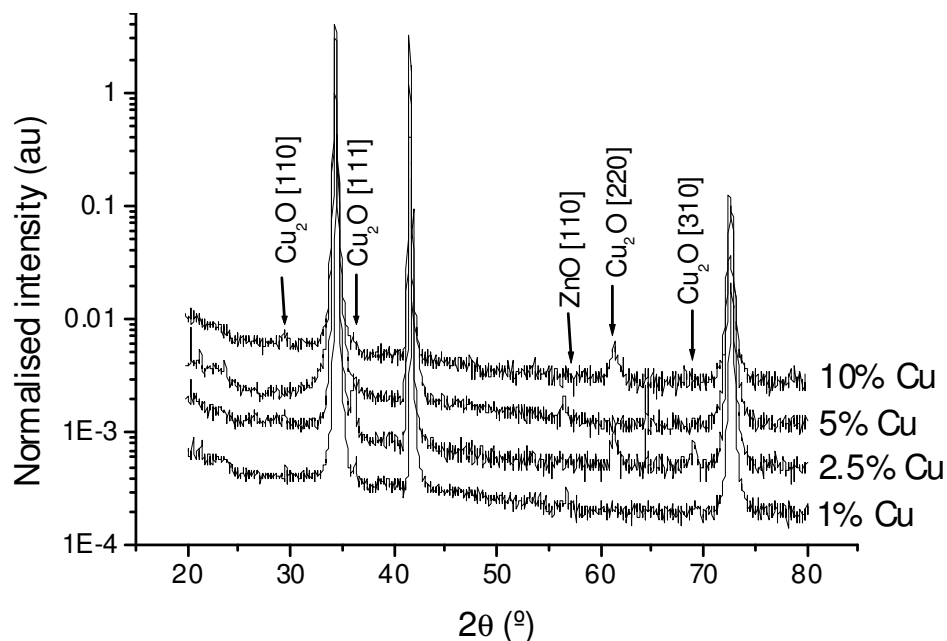
Fig 5.14: X-ray diffractogram of $Zn_{1-x}Cu_xO$ films.

On alloying ZnO with Cu, Fig 5.14 shows the evolution of the X-ray diffraction with Cu concentration. The general form is similar to the previous films, however the maximum reported solubility of Cu in ZnO is about 1 %, even lower than that of Fe. This is confirmed by cubic Cu_2O secondary peaks from several crystallographic orientations [14], which are particularly visible in the diffractograms at 2.5 and 10%. It is possible that these peaks are not visible at a concentration of 5% because the film was significantly thinner than the others and the secondary phase may have also been oriented differently. At 1% Cu this could also be true or the secondary phase may not occur, therefore the XAS results are needed to clarify the situation. In tetrahedral coordination the ionic radius of Cu is smaller than that of Zn. This is reflected by a small positive shift in the angles at which the ZnO peaks occur, with respect to their positions in pure ZnO. There is a corresponding average decrease in the c lattice parameter of $2.13 \pm 0.08 \times 10^{-4} \, \text{Å}\%_{Cu}^{-1}$ between concentrations of 1 and 10%. Although the proportion of secondary phases appears to increase with Cu concentration, the size of the crystallites does not, as the width of the diffraction peaks remains constant.

Finally, in the case of $Zn_{1-x}Ni_xO$, fig 5.15 shows the x-ray diffraction of several films. Once again, the general form is similar to that of the previous diffractograms. The maximum reported solubility of Ni in Zn is around 5 %, nevertheless it appears that the secondary phase NiO could be present at this concentration. The [012] and [101] diffractions are the most intense peaks in rhombohedral NiO with no preferred orientation [15], however they are partially

hidden by the AlO_3 [006] and ZnO [002] peaks so it is not clear whether they really occur. In tetrahedral coordination, the ionic radius of Ni is significantly smaller than that of Cu. However, the observed shift in the position of the ZnO peaks and the consequent effect on the c lattice parameter are negligible, suggesting that Ni may not be effectively occupying the Zn substitutional position. This hypothesis will be discussed further in the next section.
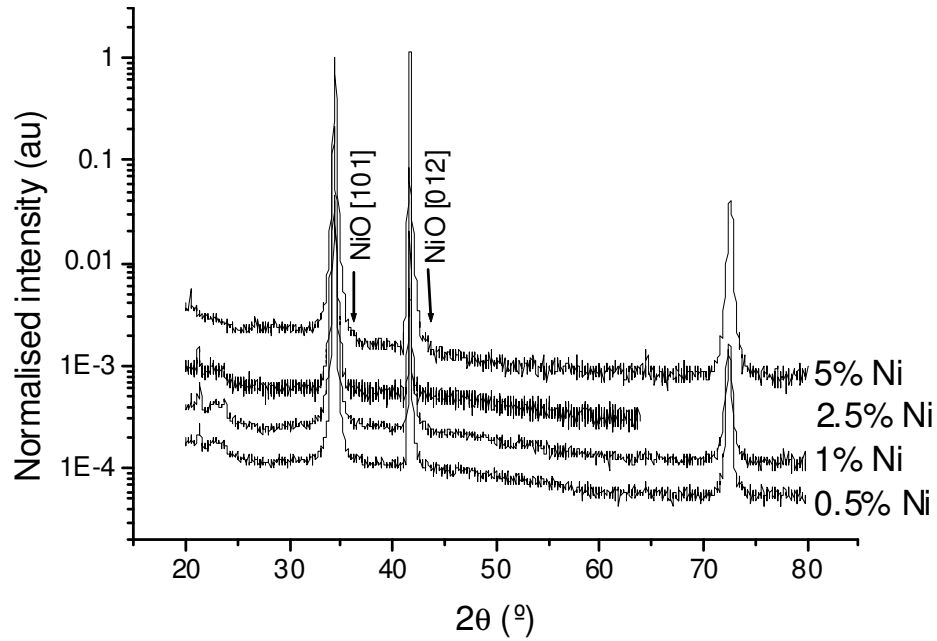
Fig 5.15: X-ray diffractogram of $Zn_{1-x}Ni_xO$ film.

5.2.2 XAS

Fig 5.16 shows the XAS spectra obtained for the $Zn_{1-x}Mn_xO$ films. They have been scaled and shifted vertically with respect to each other to simplify comparison. The XANES region may be clearly identified; however in the EXAFS region it is not possible to observe the characteristic oscillations. This is because, in order to reduce noise, it was necessary to maintain the monochromator crystals at a constant pitch. Therefore, the beam intensity beyond the XANES region was too low to be able to appreciate any oscillations in the signal. Despite this, conclusions of a qualitative nature could still be drawn from the XANES data. In this case, as the Mn concentration increases, the form of the XANES remains roughly constant, suggesting that the Mn in the film remains in the same coordination environment throughout.
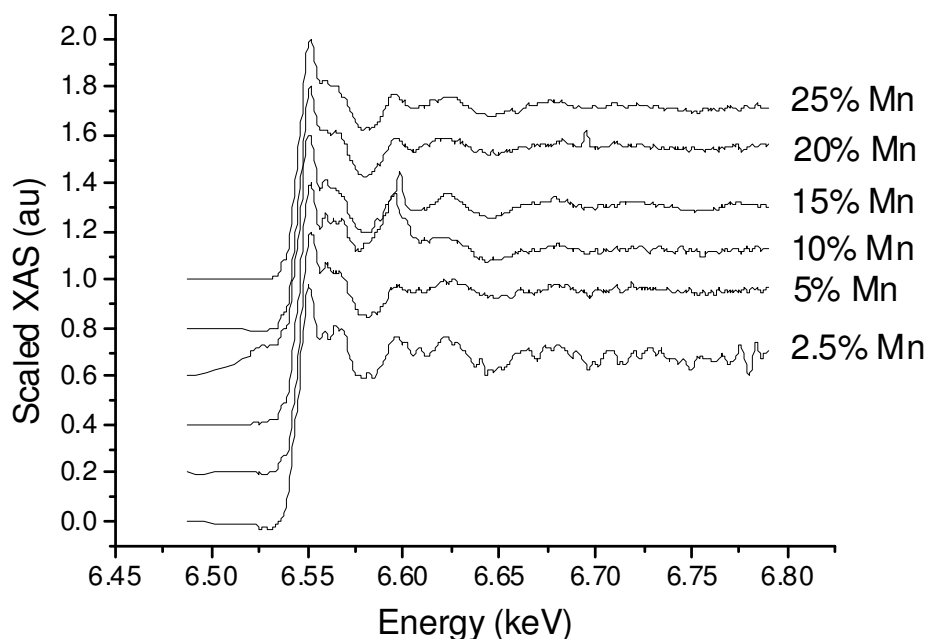
Fig 5.16: Scaled $Zn_{1-x}Mn_xO$ XAS at the Mn K-edge.

To investigate this further, a simulation was run to determine the theoretical form that the XANES would assume if the Mn atoms were in the Zn substitutional position. All simulations were done using FEFF 8, an ab initio self-consistent real space multiple-scattering code for simultaneous calculations of x-ray-absorption spectra and electronic structure [16]. Initial atomic positions were generated by the ATOMS code [17]. Results of the simulation compared with the XANES of the highest and lowest concentration films are shown in fig 5.17. Bearing in mind that the peak intensities and energies produced by simulations of this type are only approximate, the agreement with results is good, particularly in the sample with 5% Mn. At 25%, a slight decrease in the intensity of the peak labelled "C" and a flattening of the "D" and "E" peaks could be signs of a secondary phase but the concentration would probably be small. This is in agreement with the results of Pellicer-Porres et al [18].
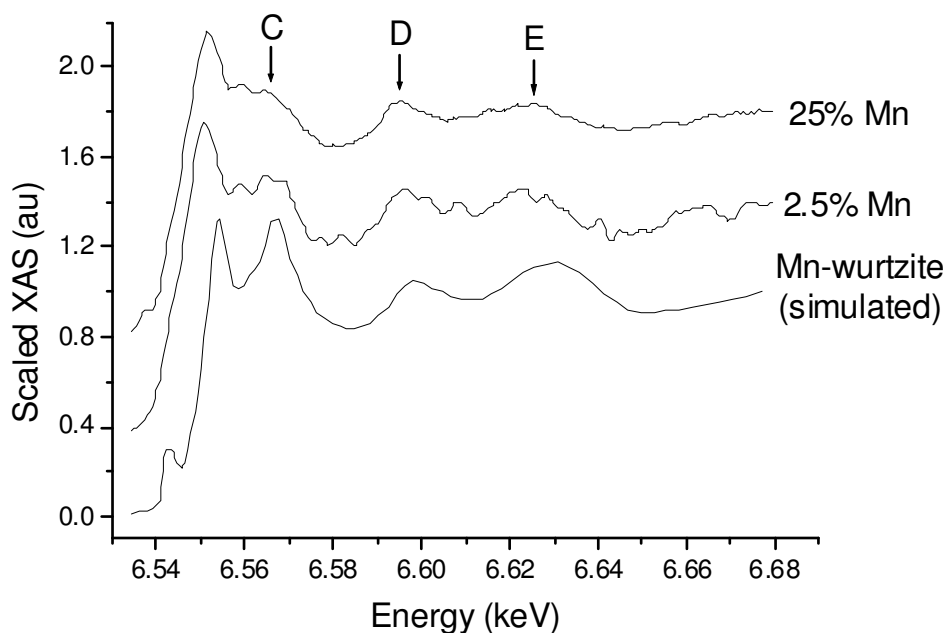
Fig 5.17: Comparison of $Zn_{1-x}Mn_xO$ XANES results with simulation.

The XAS spectra of the $Zn_{1-x}Fe_xO$ films are shown in fig 5.18. At the time of writing, additional results taken on ESRF line BM-29 by Segura et al. were also available. These results have been labelled with an asterisk (*) when shown in figures. At a first glance, the spectra seem similar to those of $Zn_{1-x}Mn_xO$ shifted in energy. This suggests that the Fe atoms are also in the wurtzite coordination. To test this hypothesis, simulations were done of Fe in this coordination. As the concentration increases, the form of the spectra does not remain constant, as it did in $Zn_{1-x}Mn_xO$, indicating that at least one secondary phase is also present. Possible secondary phases could be FeO, Fe_2O_3 or Fe_3O_4 so simulations were done on Fe in these configurations too. The results of all simulations are shown in fig 5.19.
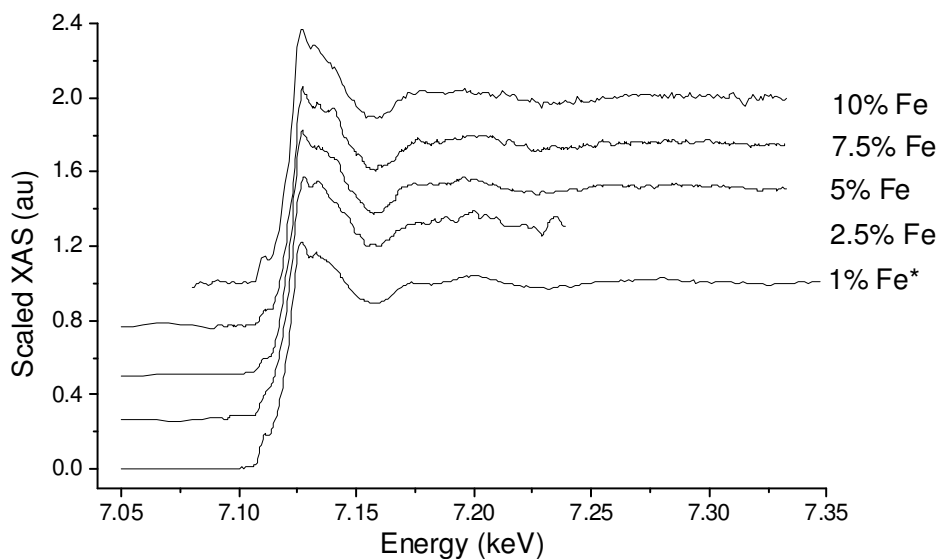
Fig 5.18: Scaled $Zn_{1-x}Fe_xO$ XAS at the Fe K-edge.
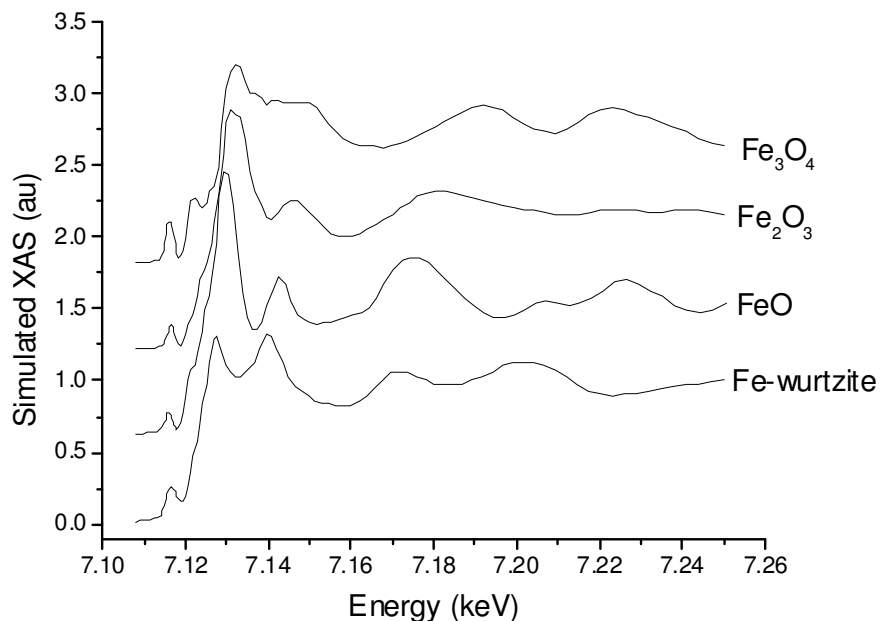
Fig 5.19: Simulations of Fe XANES in different coordination environments.

Fig 5.20 shows standard references for the secondary phases [19]. These spectra were preferable to the simulations because they correspond to real experimental results. It was also realized that atomic Fe could exist in the films in the form of clusters so the reference for Fe foil was also included. On comparing the experimental results to the references, especially at the higher concentrations, it was found their form was similar to that of Fe_2O_3, although other secondary phases could not be ruled out. This is in agreement with the XRD results which found diffraction peaks corresponding to Fe_2O_3 at Fe concentrations of 5% and above.
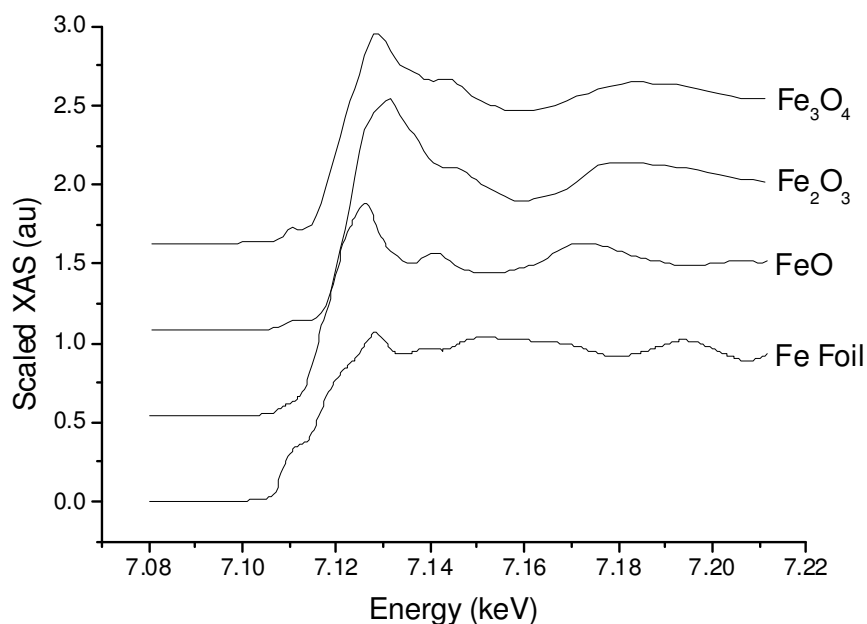
Fig 5.20: References of potential Fe-based secondary phases.

Fig 5.21 shows the comparison of the experimental results with the wurtzite simulation and the Fe_2O_3 standard. Although the changes are very subtle, it appears that there is a mixture of the two phases, with the proportion of Fe_2O_3 increasing with the Fe concentration. This is particularly apparent in the decrease in the intensity of the "C" peak, relative to the white line, and the merging and flattening of the "D" and "E" peaks as Fe concentration increases.
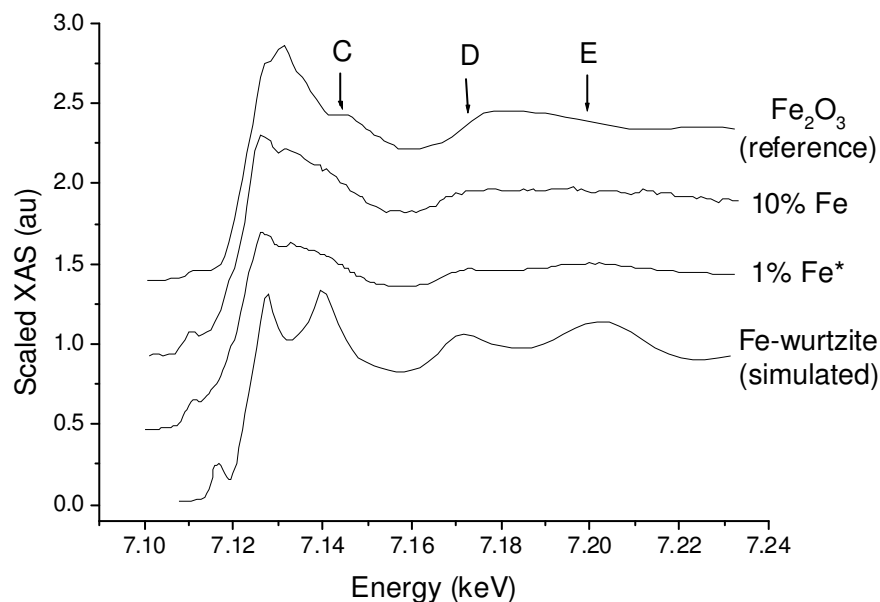
Fig 5.21: Comparison of $Zn_{1-x}Fe_xO$ XANES results with supplementary results.
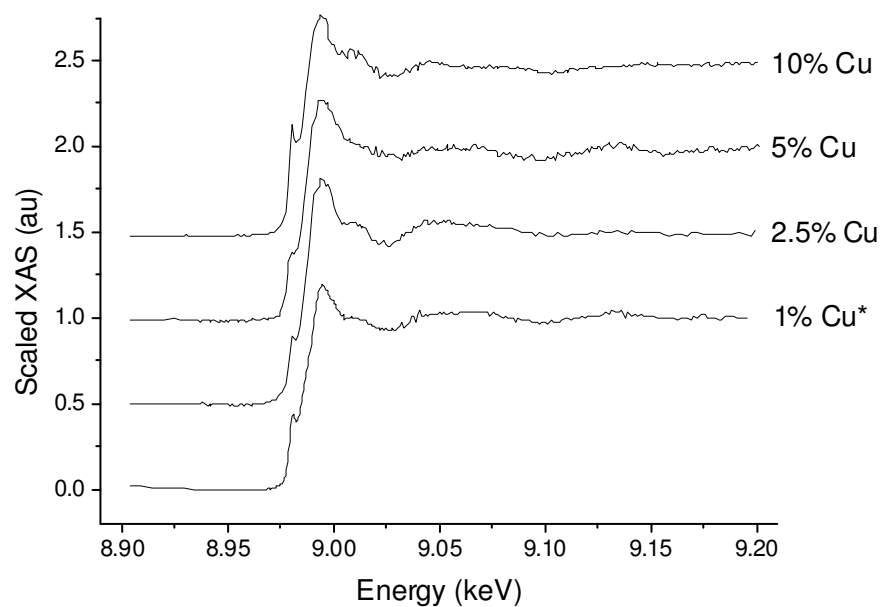
Fig 5.22: Scaled $Zn_{1-x}Cu_xO$ XAS at the Cu K-edge.

In the case of $Zn_{1-x}Cu_xO$, the XAS spectra in function of Cu proportion are shown in fig 5.22. Once again, the general form is similar to that of previous DMSs.

However, differences can be seen between the spectra as the Cu concentration increases. As secondary phase peaks for Cu_2O were visible in XRD, simulations were done for Cu in wurtzite and Cu_2O configurations. Moreover, the XAS of a Cu_2O powder pellet was also measured so that a more accurate comparison could be made. In order to reduce the absorption of the pellet without changing the form of the XANES, the Cu_2O powder was mixed with BN. The results to be compared are shown in fig 5.23. Firstly we note that Cu_2O is, indeed, the secondary phase, as the form of the XANES at 10% Cu is very similar to the spectrum from the Cu_2O powder. The gradual transformation from wurtzite to the cubic Cu_2O configuration is much more marked than in $Zn_{1-x}Fe_xO$, with five main features that change as the concentration of Cu in the film increases: the pre-peak "A" intensifies, the white line "B" becomes broader, the peak "C" is blue-shifted and broadened and peaks "D" and "E" become flatter.
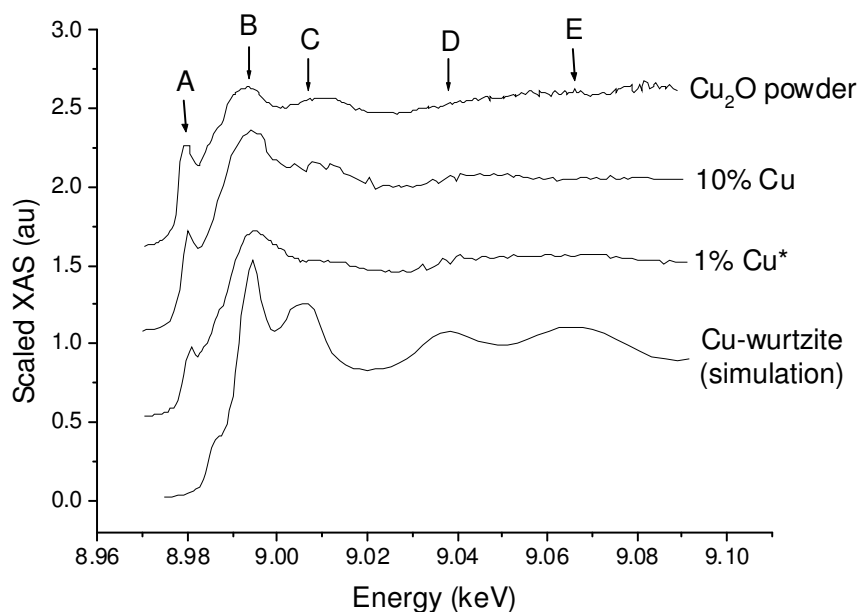
Fig 5.23: *Comparison of $Zn_{1-x}Cu_xO$ XANES with supplementary results.*

Finally, in $Zn_{1-x}Ni_xO$, the evolution of the XAS in function of Ni concentration is shown in fig 5.24. Clear changes are also visible in these spectra so simulations were done of Ni in wurtzite and NiO configurations, since the XRD results suggested that NiO was present. As in the Cu DMS, supplementary measurements were made with a NiO powder pellet and the comparison of the results obtained is shown in fig 5.25. We note that the agreement between the film containing 5% Ni and the NiO powder is very good showing almost all the Ni to be in NiO rather than the Zn substitutional position. As the concentration of Ni increases, the relative intensity between the white line "B" and peak "C" increases, while peak "D" intensifies and "E" diminishes and blue-shifts. Both Li et al. [20] and Pei et al [21] obtain similar results but, despite this, conclude that the Ni remains in the Zn substitutional position, even at concentrations of 5%. This is clearly not the case. NiO is a very stable compound; it is so stable, in fact, that no structural phase transition is observed at hydrostatic pressures up to 141 GPa [22]. For this reason it is more energetically favourable for Ni to occupy NiO than the Zn substitutional position. Probably the only reason why the substitutional phase is still detected at low concentrations is that there

is such a large separation between Ni atoms that they are not able to diffuse far enough to be able to form the secondary phase. This will be investigated in more detail by electron microscopy in section 5.2.4.
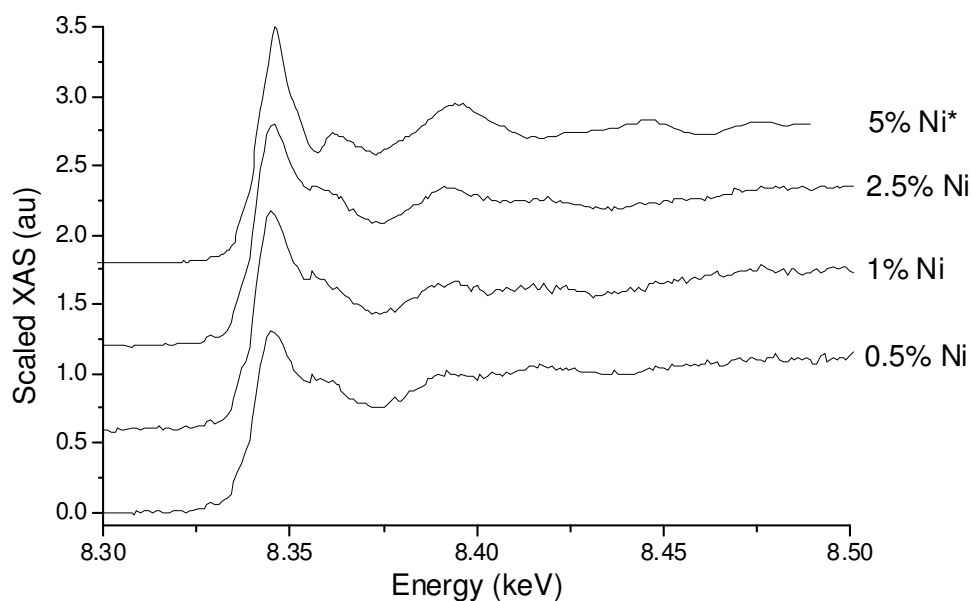
Fig 5.24: Scaled $Zn_{1-x}Ni_xO$ XAS at the Ni K-edge.
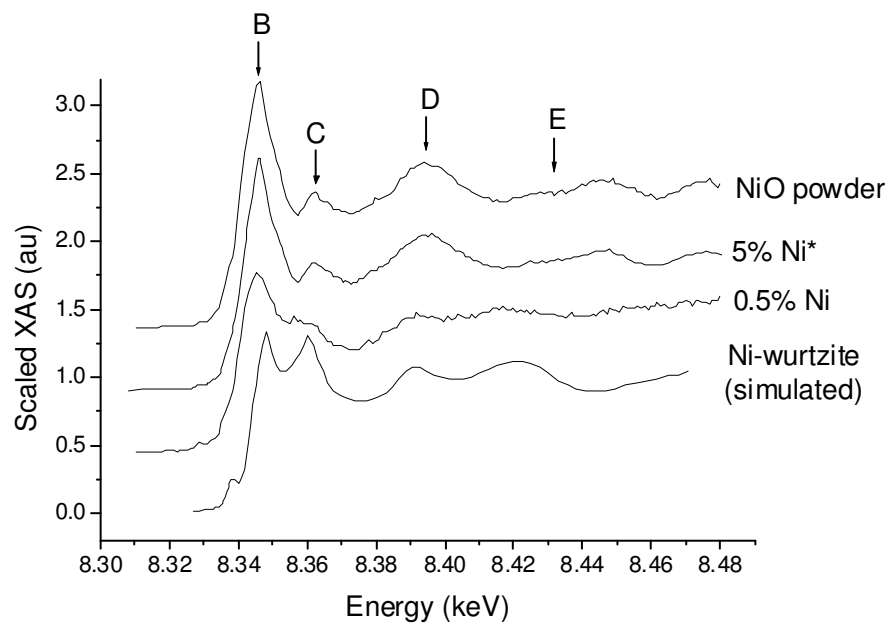
Fig 5.25: Comparison of $Zn_{1-x}Ni_xO$ XANES with supplementary results.

5.2.3. XRF

XRF spectra from the $Zn_{1-x}Mn_xO$ films are shown in fig 5.26. Although films of all available Mn concentrations were measured, only the results corresponding to the least (1%) and greatest (25%) concentrations are shown so that the main differences may be highlighted. Although many fluorescence peaks occur, the only ones of interest in this study are those corresponding to the emission lines K_α and K_β of Mn and Zn. Other peaks occur because the films grown over mica were used (except with $Zn_{1-x}Fe_xO$). This was so that several layers, in this case 6, could be stacked to increase the signal to noise ratio. However, it also had the side effect of introducing fluorescence peaks from the mix of chemical elements present in the mica. It is clear that the Mn peaks intensify significantly on increasing the concentration from 1% to 25%, although for analysis purposes it is not the absolute intensity but the relative integrated intensity between the Mn and Zn peaks that determines the stoichiometry. To obtain the integrated intensities, the baseline was removed and peaks were fitted to Gaussian profiles. The resulting intensities were converted into concentrations using a calculation based on (3.33). A particularly significant factor in this calculation is the K-shell fluorescence yield for the different transition metals, which was found in [23].
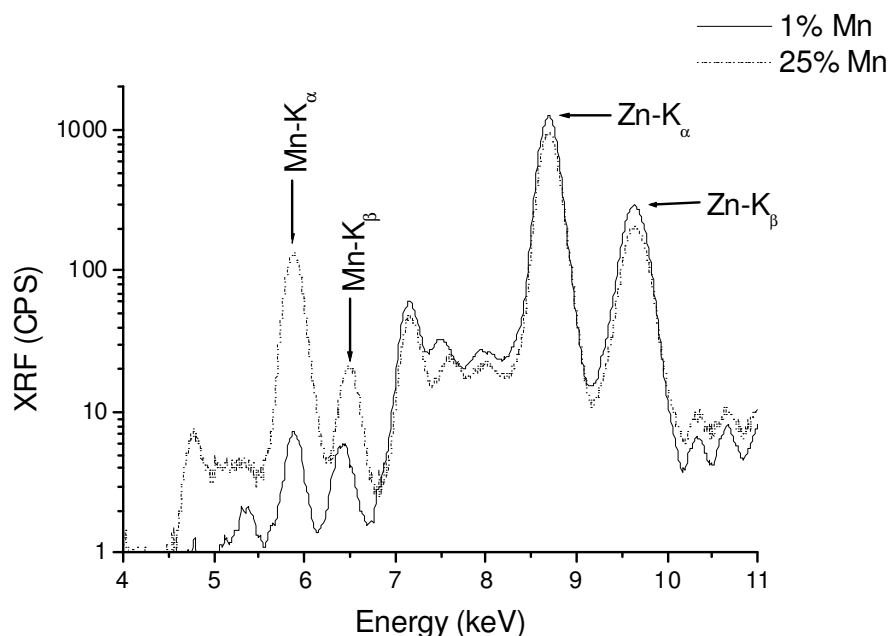
Fig 5.26: XRF of $Zn_{1-x}Mn_xO$ films (excitation energy 9.7 keV).

The XRF spectra from the other DMSs are shown in figs 5.27 to 5.29. In general, an increase in the dilute cation concentration results in an increase in the relative integrated intensity of its fluorescence peaks. The previously described analysis method was used in each case, although the Fe-K_β and Cu-K_β peaks were not separable from the background. Therefore, the analysis for $Zn_{1-x}Fe_xO$ and $Zn_{1-x}Cu_xO$ was based entirely on the integrated intensity of the K_α peaks.
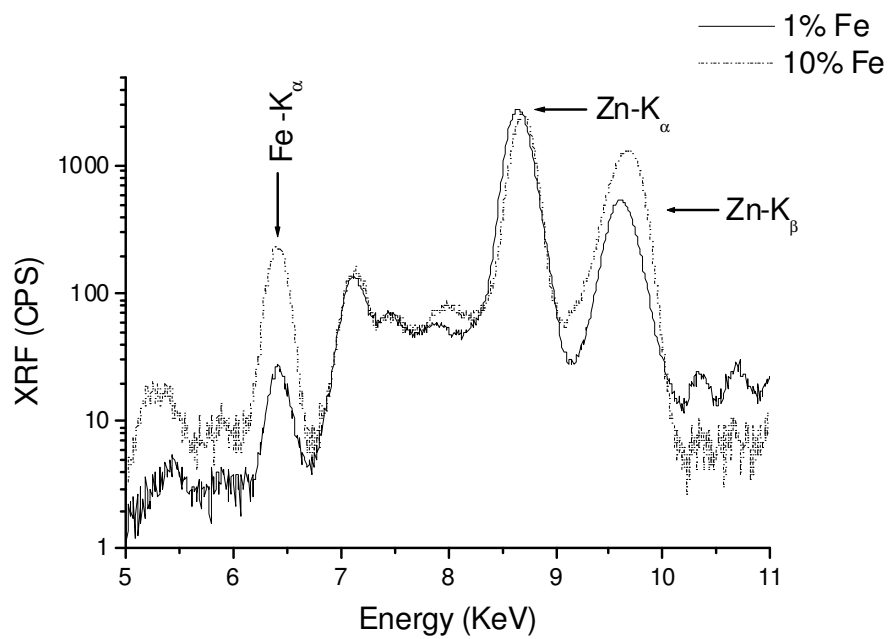
Fig 5.27: XRF of Zn$_{1-x}$Fe$_x$O films (excitation energy 9.7 keV).
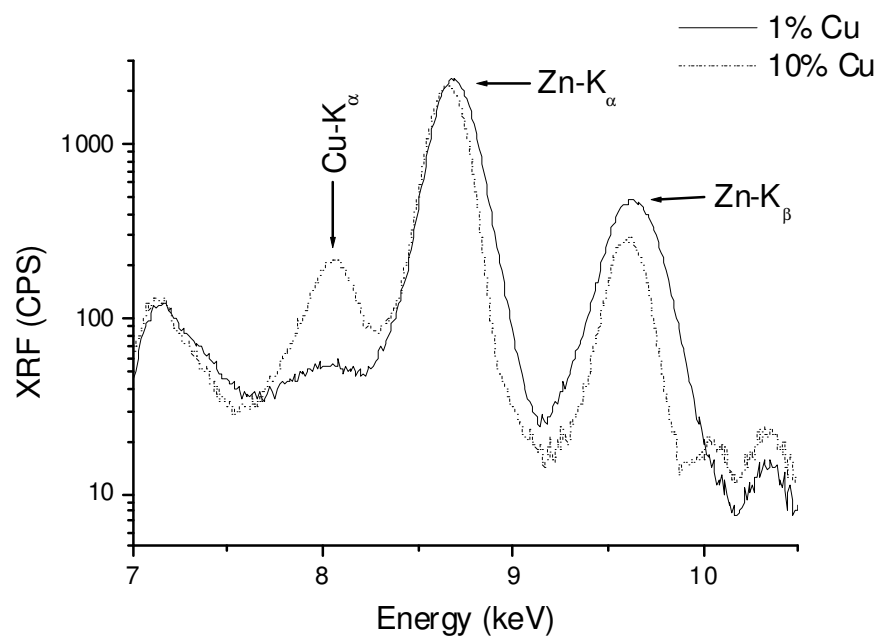
Fig 5.28: XRF of Zn$_{1-x}$Cu$_x$O films (excitation energy 9.7 keV).
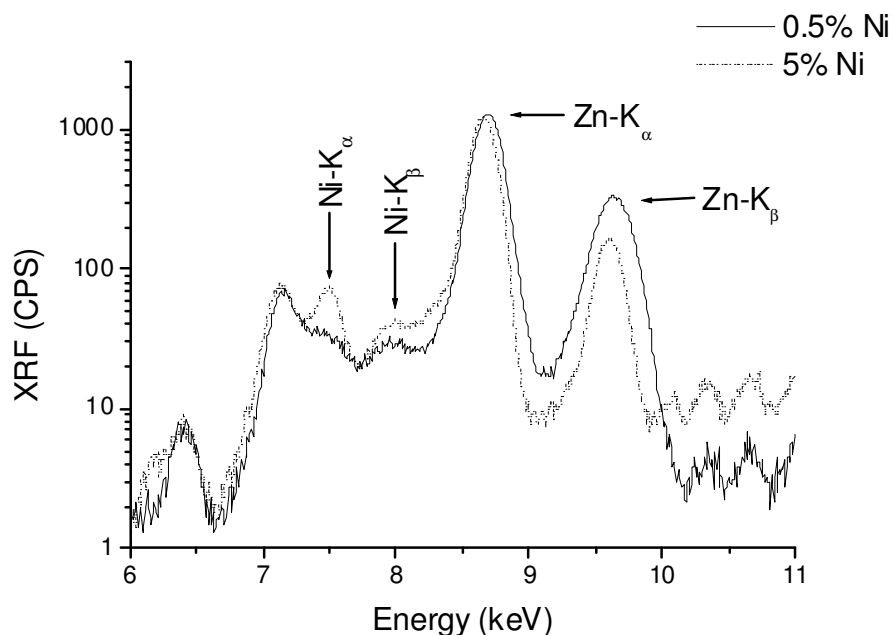
Fig 5.29: XRF of $Zn_{1-x}Ni_{x}O$ films (excitation energy 9.7 keV).

Table 5.1 compares the DMS concentrations determined by XRF with the nominal concentrations, i.e. the dilute cation concentrations in the powder mixes used to produce the ablation targets. The agreement is strong, especially in the case of $Zn_{1-x}Mn_{x}O$. However, in the other DMSs, the relative differences are sometimes large, especially at low concentrations. There are many possible explanations for this, such as inhomogeneity in the targets and films or the accumulation of minor differences in the growth conditions. To follow the already established convention, nominal concentrations will still be used to label figures, but the true concentrations will be referred to when required by the analysis.

Nominal Mn (%)	XRF Mn (%)	Nominal Fe (%)	XRF Fe (%)	Nominal Cu (%)	XRF Cu (%)	Nominal Ni (%)	XRF Ni (%)
1	1.2 ± 0.6	1	1.2 ± 0.5	1	0.6 ± 0.3	0.5	0.4 ± 0.2
2.5	2.6 ± 0.4	2.5	1.6	2.5	3.9 ± 1.4	1	0.9 ± 0.3
5	5.7 ± 0.2	5	3.2 ± 0.2	5	3.3 ± 1.7	2.5	4.2 ± 1.1
10	11 ± 0.8	7.5	8.1 ± 3.2	7.5	8.3 ± 2.9	5	6 ± 0.9
15	15.7 ± 1.7	10	12 ± 3.9	10	9.5 ± 3.1		
20	22.5 ± 3.6						
25	28.2 ± 5.1						

Table 5.1: DMS concentrations determined by XRF.

5.2.4 Electron microscopy and Microanalysis

In order to appreciate the differences in surface morphology produced by the formation of a DMS, the SEM image of a pure ZnO film was firstly taken (fig 5.30). The surface is clearly polycrystalline, with some of the crystallites assuming the commonly observed hexagonal form [24]. Bearing in mind that the magnification was 4×10^4, the average crystallite dimensions could be estimated at 300 ± 100 nm.
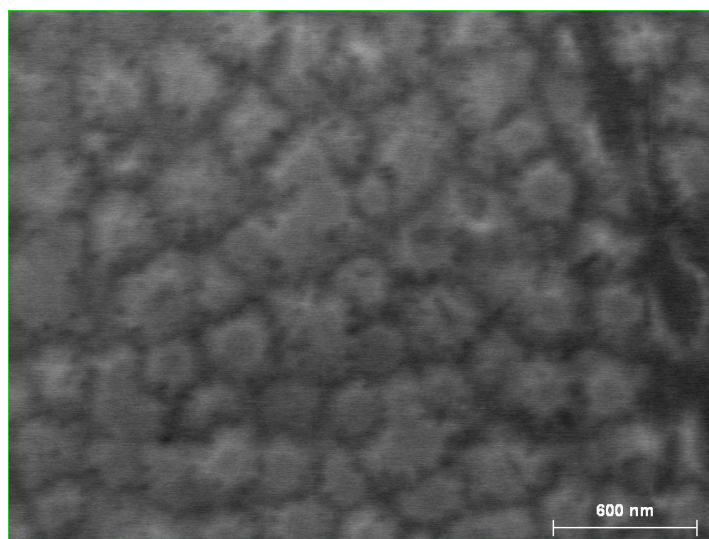
Fig 5.30: SEM image of pure ZnO film surface.
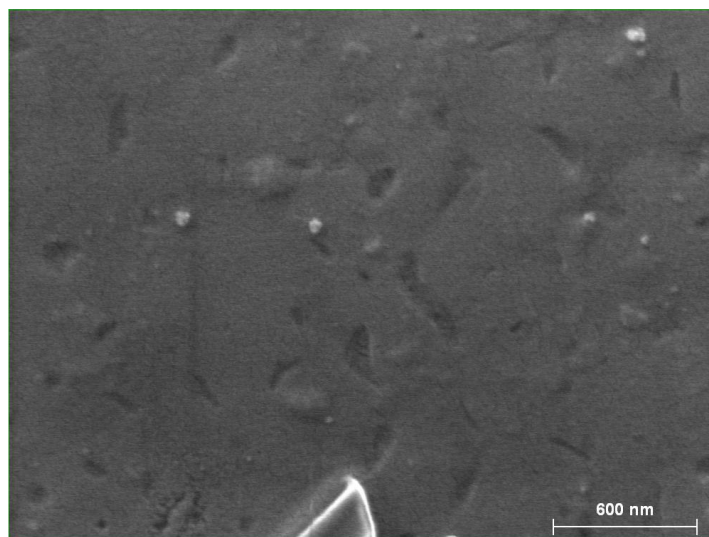
Fig 5.31: SEM image of metalised $Zn_{0.95}Mn_{0.05}O$ film surface.

As the $Zn_{1-x}Mn_xO$ films were electrically insulating, it was not possible to drain the beam current from those samples using silver paint. Therefore, they were metallised by a 7 nm thick layer of Au-Pd, which was deposited over the surfaces. It was hoped that metallisation would not affect the surface features; however, this was

not the case, as fig 5.31 shows. Almost all of the surface detail was removed, showing the films to be very flat. Therefore, no images could be taken of the $Zn_{1-x}Mn_xO$ surfaces, although they have been reported by other groups [24]. Fortunately, images could be taken with the other DMS films, as they were electrically conducting, with resistances of the order of 10 kΩ from corner to corner. The reason for this is that as-grown ZnO is usually a weak n-type conductor, as mentioned in the introduction [25]. XAS results have confirmed that the solubility of Cu and Ni in the ZnO host is low, so the conductivity of $Zn_{1-x}Cu_xO$ and $Zn_{1-x}Ni_xO$ would be expected to be similar to that of ZnO. However, the solubility of Mn and Fe are considerably greater and their introduction decreases the crystallite size in the films, which shall be seen in this section. Electrical conduction across crystallite boundaries is difficult, so $Zn_{1-x}Mn_xO$ films are insulating. The same would be true for $Zn_{1-x}Fe_xO$ samples were it not for the small proportion of Fe (III) present in the films, which shall be confirmed by the XPS measurements (section 5.3.2). Each atom of Fe (III) supplies a free conduction electron, which is sufficient to overcome the effects of the disorder and allow the film to conduct.
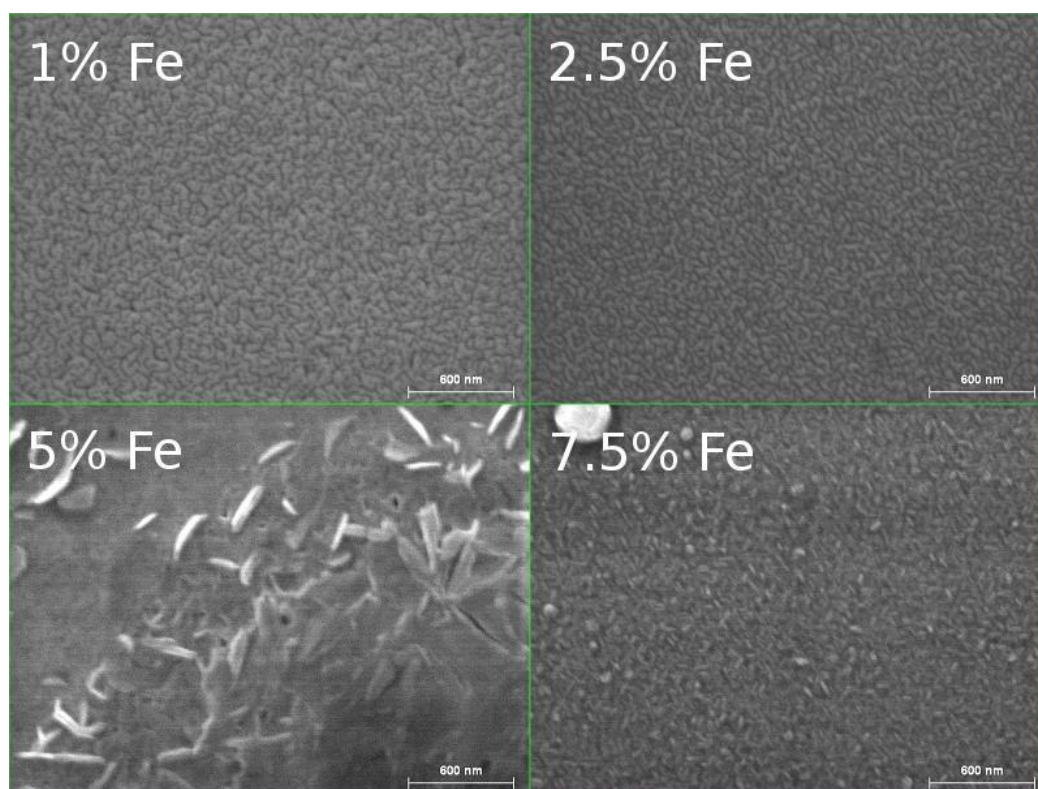
Fig 5.32: SEM images of $Zn_{1-x}Fe_xO$ film surfaces.

Fig 5.32 shows a selection of images from the $Zn_{1-x}Fe_xO$ films, all at a magnification of 4×10^4. In the sample containing 1% Fe (1.2% by XRF), we note that the crystallites are much smaller than that of pure ZnO, with typical dimensions of 50 ± 20 nm. This is indicative of the disorder introduced in the crystal lattice on introducing Fe. The situation is similar in the case of 2.5% Fe, as the XRF value is 1.6%, so only a small change would be expected. The average crystallite dimensions reduce slightly to 40 ± 10 nm establishing a trend of increasing polycrystallinity and

disorder as the Fe concentration increases. Up to this point there is no evidence of secondary phases, in agreement with the XRD results. However, on reaching 5% Fe (3.2% by XRF), the appearance of the surface is significantly altered by the presence of edge-like encrustations. These features have been noted by other authors [26, 27] and it has been suggested that they are due to the Fe_2O_3 secondary phase. The average length of the encrustations is 300 ± 100 nm. On moving to 7.5% Fe (8.1% by XRF), the encrustations are still visible but much smaller, at around 80 ± 30 nm, showing a further increase in disorder. This is in agreement with the Scherrer formula (5.1) which predicted a decrease in the crystallite size with increasing Fe concentration, reflected in the broadening of the XRD peaks.

Element maps for $Zn_{0.99}Fe_{0.01}O$ and $Zn_{0.95}Fe_{0.05}O$ are shown in figures 5.33 and 5.34 respectively. Even at the highest magnification, the resolution is only about 5 nm, which is 10 times larger than the lattice parameters. Therefore, this method could not be used to reveal the presence of small clusters of Fe atoms. However, larger clusters or the concentration of Fe within certain structures could potentially be detected. It would also be possible to analyse the results using atomic number absorption fluorescence (ZAF) algorithms to determine the stoichiometry of the films. In practice this was not done because two other methods had already been used to determine the stoichiometry (XRF and XPS). At a Fe concentration of 1%, both the Zn and Fe counts appear to be evenly distributed within the film. The same is true at 5%, even within the regions corresponding to the encrustations. There are two possible explanations for this: Either the encrustations contain a similar distribution of metal atoms to the rest of the film or they really are Fe_2O_3 and the Zn counts come from the material below. An estimation of the electron beam penetration depth based on the extrapolation of figure 4.5 would be about 50Å. Therefore, for the second explanation to be true, the encrustations would have to be thinner than this, which is certainly possible. Therefore the composition of the encrustations remains inconclusive.
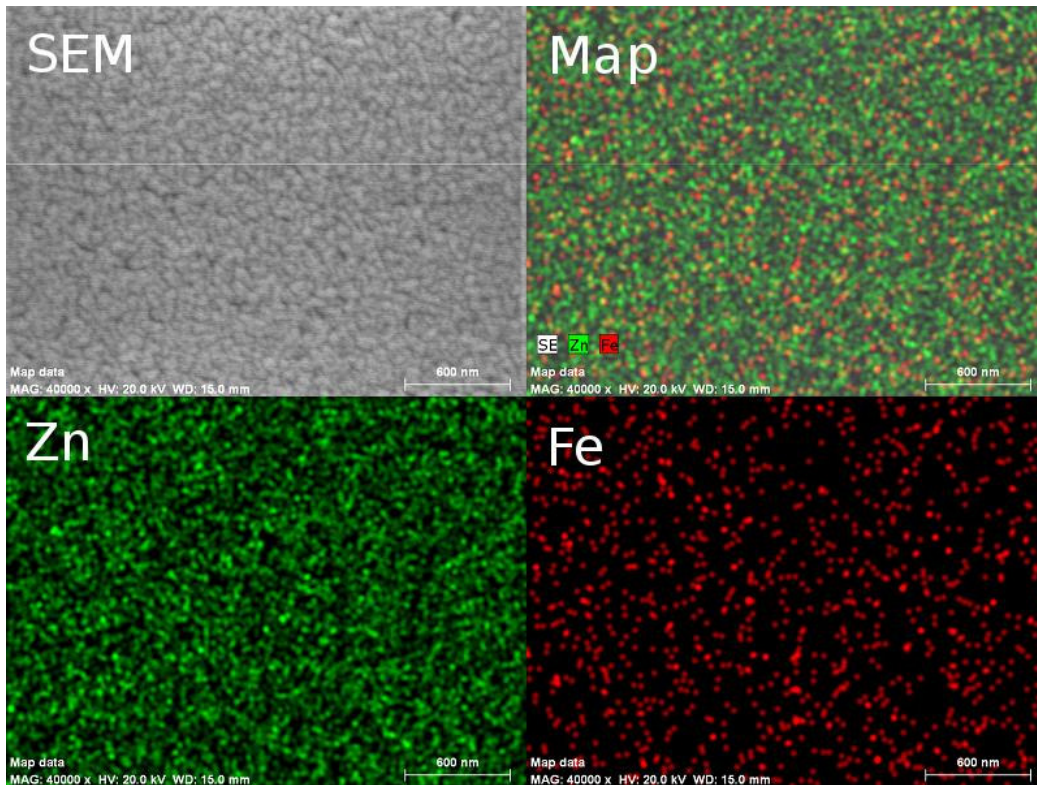
Fig 5.33: Element mapping of $Zn_{0.99}Fe_{0.01}O$ film.
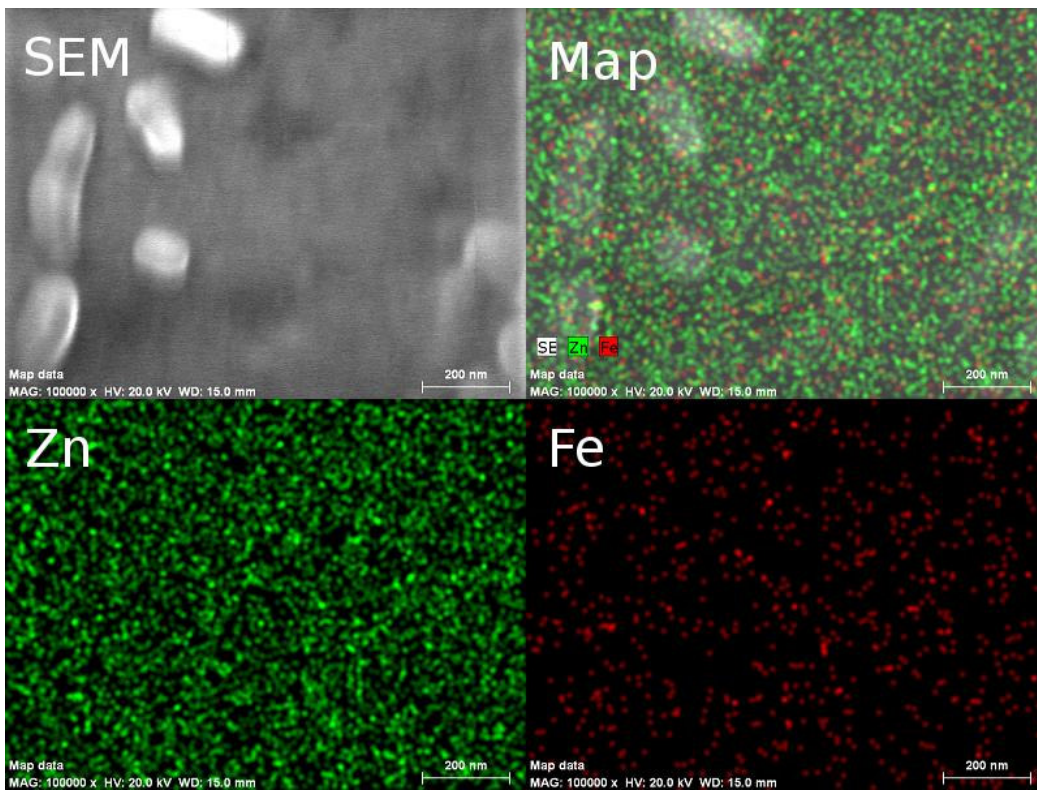
Fig 5.34: Element mapping of $Zn_{0.95}Fe_{0.05}O$ film.

In the case of $Zn_{1-x}Cu_xO$, the SEM images are shown in fig 5.35 at a magnification of 4×10^4. As in $Zn_{1-x}Fe_xO$, the film containing 1% Cu (0.6% by XRF) has a higher polycrystallinity than pure ZnO. The average crystallite dimensions are 150 ± 50 nm and a few small white (insulating) regions are visible. These could correspond to the Cu_2O secondary phase, which was detected by XRD at this concentration. This is not confirmed by the element mapping in fig 5.36, which shows a fairly uniform distribution of Cu and Zn atoms, and no results from other authors on the subject were readily available. The XRF results showed that the 5% film (3.3% by XRF) contains more Cu than the 2.5% film (3.9% by XRF) so the 5% film shall be considered first. In this image the surface is covered by the small white regions, so much so that it is not possible to determine the size of the crystallites below. If these regions are Cu_2O then, at this concentration, the average distance between Cu atoms (4.42 Å) is still too great for diffusion to occur. However, at the slightly higher concentration of the 2.5% film this appears not to be the case, as the white regions are significantly larger and the interconnections between them could be considered evidence of diffusion. At this concentration the average distance between Cu atoms would be 4.18 Å, compared to 3.02Å, which is the distance between neighbouring Cu atoms in Cu_2O. In the film with 10% Cu (9.5% by XRF), the white regions now have a size that is comparable to that of the crystallites, which are now visible and have a typical length of 110 ± 40 nm. Once again, the composition of the white regions from the element mapping in fig 5.37 is inconclusive, as the distribution of Cu and Zn is still appears to be uniform.
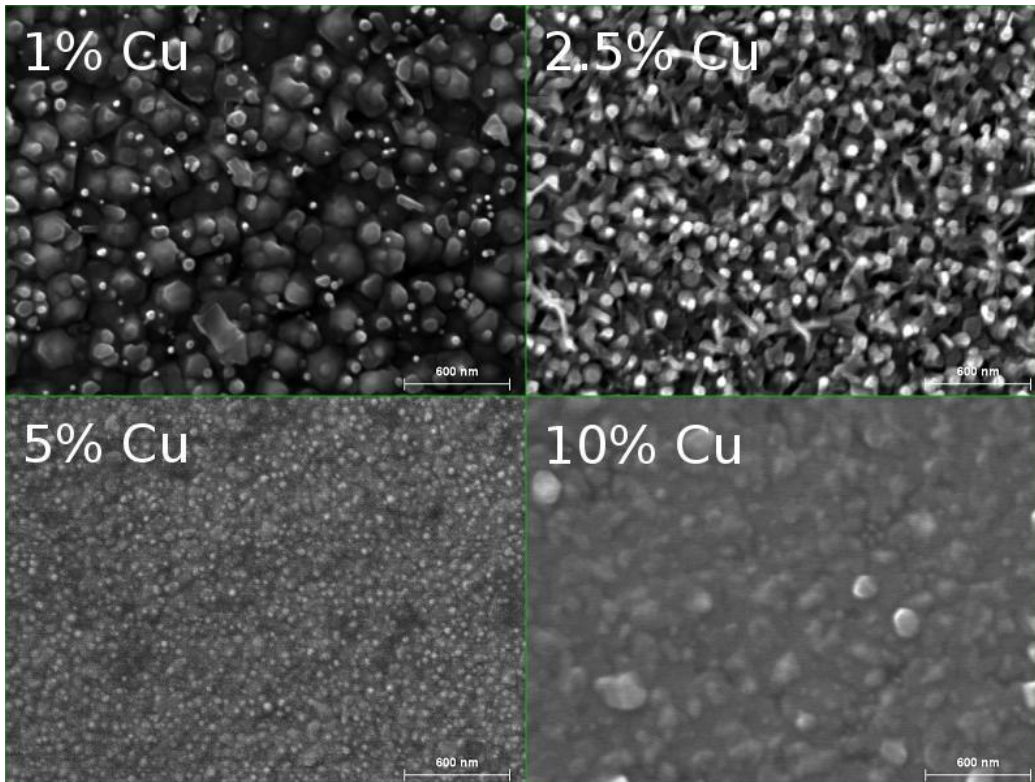
Fig 5.35: SEM images of $Zn_{1-x}Cu_xO$ film surfaces.
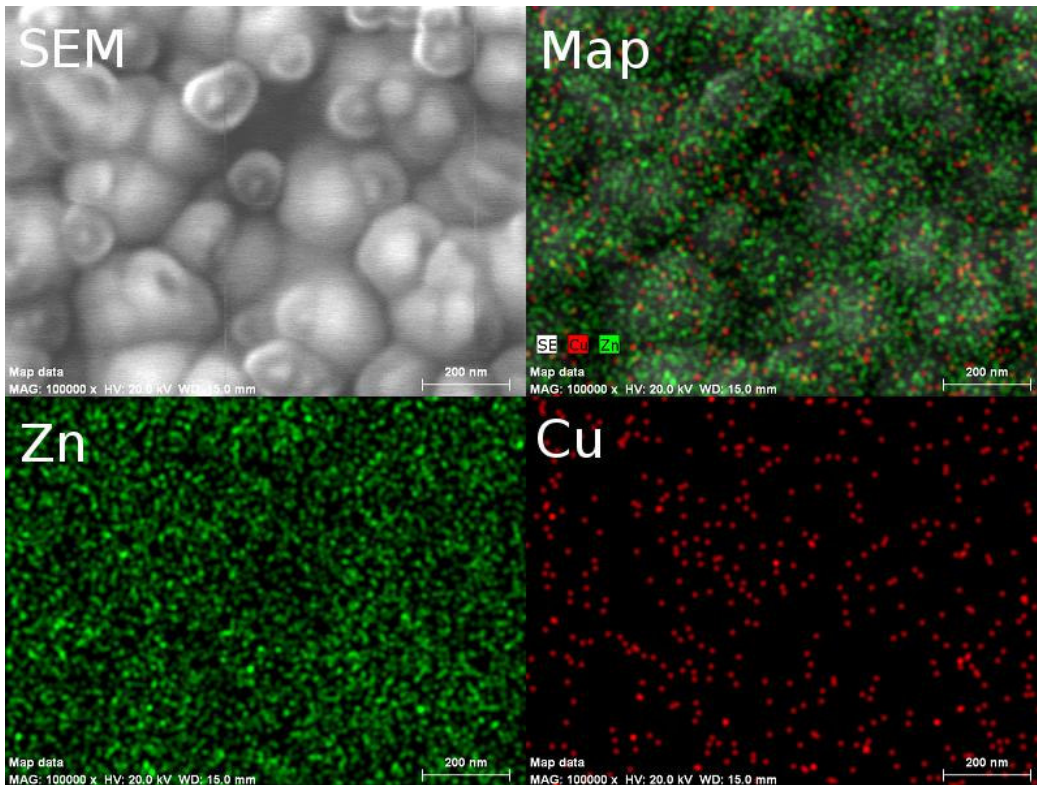
Fig 5.36: Element mapping of Zn$_{0.99}$Cu$_{0.01}$O film.
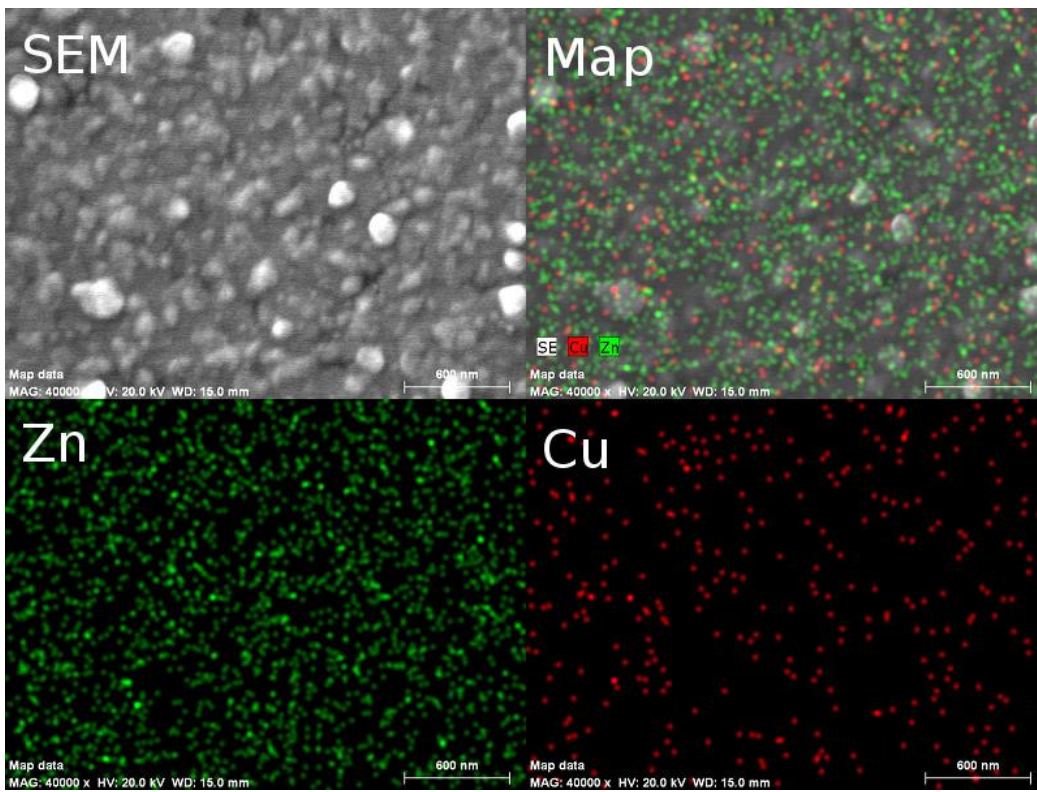
Fig 5.37: Element mapping of Zn$_{0.90}$Cu$_{0.10}$O film.

Finally, in the case of $Zn_{1-x}Ni_xO$, the SEM images at a magnification of 4×10^4 are shown in fig 5.38. In many ways they are similar to the $Zn_{1-x}Cu_xO$ results. The first image is taken at the slightly lower concentration of 0.5% (0.4% by XRF). Here the crystallites have average dimensions of 150 ± 50 nm, which is lower than that of pure ZnO. There is no evidence of a phase separation, in agreement with XRD results that do not detect NiO at this concentration. The element mapping in fig 5.39 shows the typical uniform distribution of Ni and Zn over the surface. On increasing the concentration to 1% (0.9% by XRF), the average crystallite dimensions were found to decrease to 110 ± 40 nm but the film was only 50 nm thick, which may have limited nucleation. A few small white regions are visible, which could be composed of NiO. Moving up to the 2.5% film (4.2% by XRF), the white regions are significantly larger, as are the crystallites which have average dimensions of 200 ± 70 nm. If the white regions are NiO, it is clear that, by this concentration, the average distance between Ni atoms (4.12Å) is sufficient for diffusion to occur. The distance between neighbouring Ni atoms in NiO is 2.95Å. Although these distances are similar to those found in $Zn_{1-x}Cu_xO$, diffusion could have started at lower Ni concentrations due to the increased stability of NiO compared to Cu_2O. In the final image (6% by XRF) the trend continues, with an enlargement of both the white regions and the crystallites, which now have average dimensions of 250 ± 80 nm. Unfortunately, the element mapping in fig 5.40 still does not give any clues about the composition of the white regions, continuing to show an even distribution of Ni and Zn.
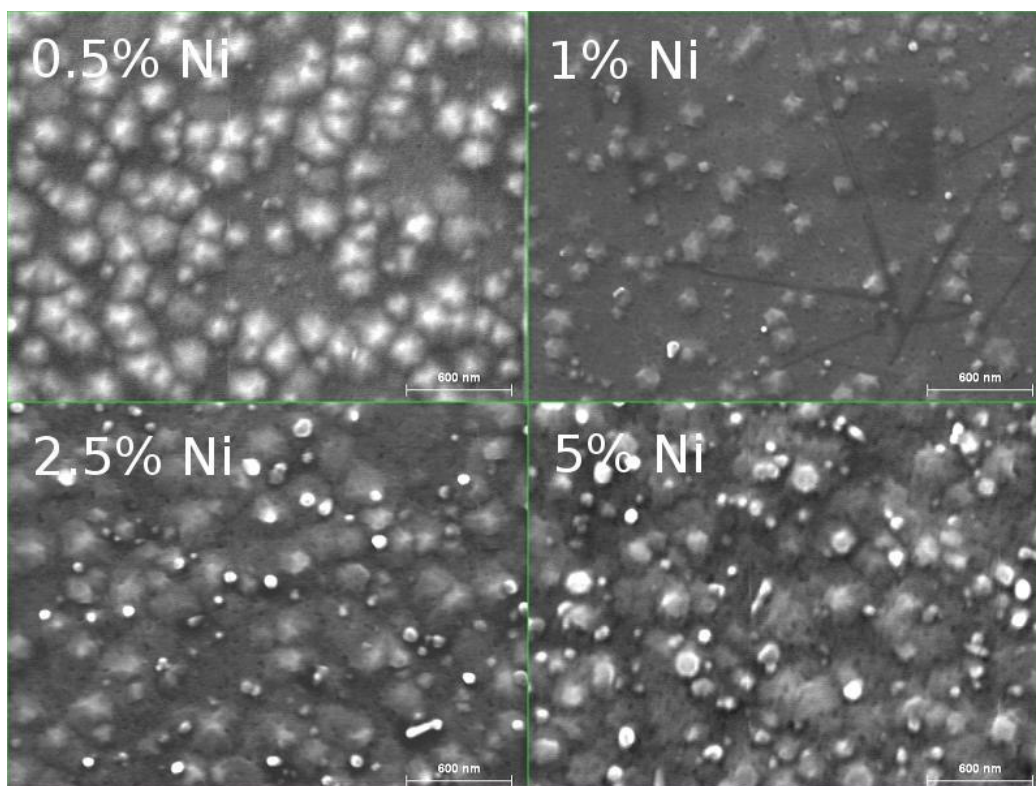
Fig 5.38: SEM images of $Zn_{1-x}Ni_xO$ film surfaces.
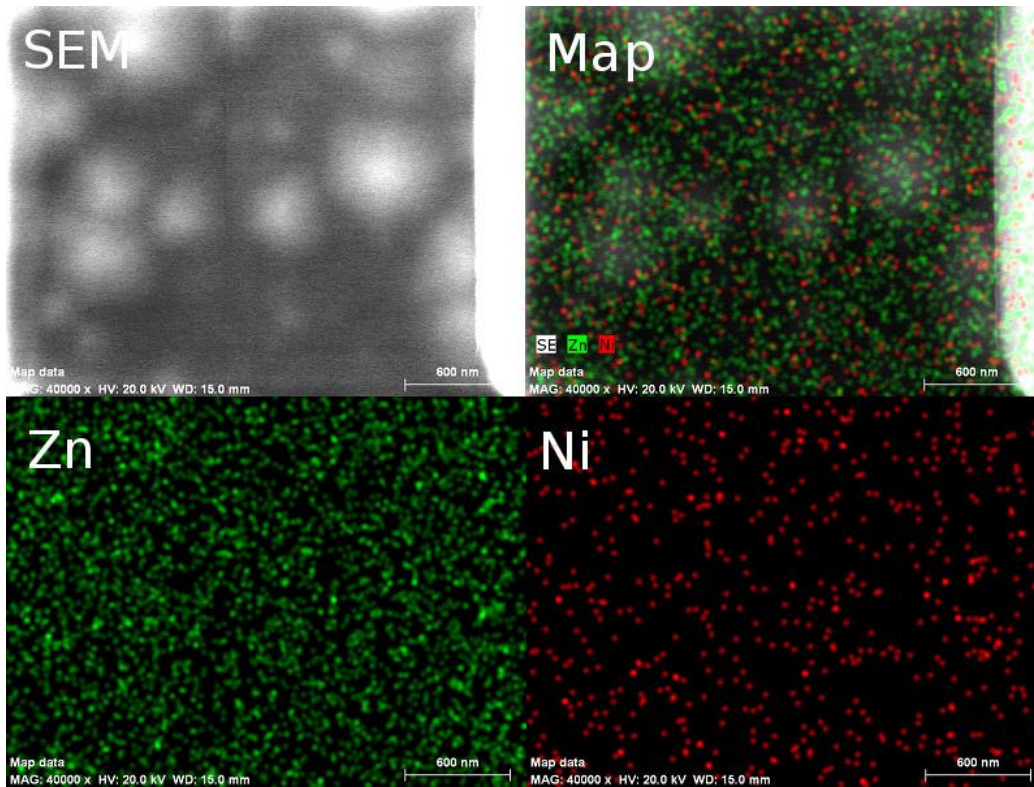
Fig 5.39: Element mapping of $Zn_{0.995}Ni_{0.005}O$ film.
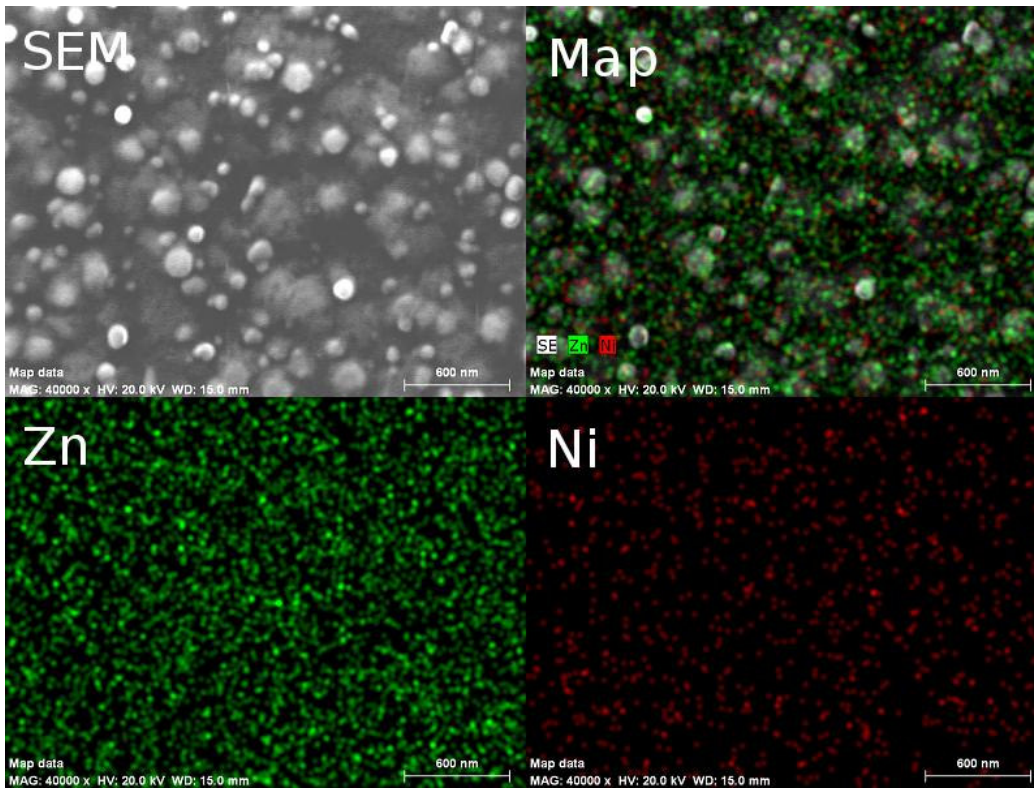
Fig 5.40: Element mapping of $Zn_{0.95}Ni_{0.05}O$ film.

5.3 Electronic properties

5.3.1 UPS

In this section the electronic states of the valence band shall be considered, making reference to the UPS spectra obtained by He-II excitation. Raw data was prepared for analysis by removing the baseline and scaling according to the integrated intensity of the Zn 3d peak in pure ZnO at around 10.3 eV. In the spectra acquired from the pure ZnO half of the heterojunction samples, the binding energy of the Zn 3d peak was determined by fitting with a Gaussian profile. As this energy is independent of the DMS deposited on the other half of the heterojunction, its average value was calculated across all samples and the relative shift caused by charging was determined in each case. The spectrum of the corresponding DMS was then shifted by the same energy to correct for this effect. A fitting using multiple Gaussian profiles was then performed to determine the binding energy, width and intensity of the principle peaks in the DMS spectra.
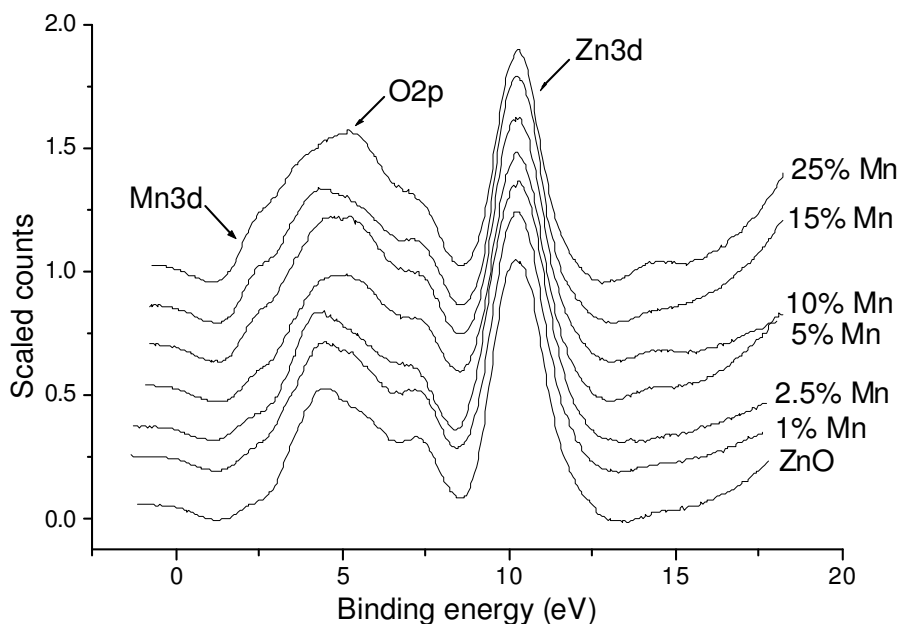
Fig 5.41: He-II UPS spectra of $Zn_xMn_{1-x}O$ films.

The He-II UPS spectra for $Zn_{1-x}Mn_xO$ are shown in fig 5.41. They have been vertically displaced relative to each other to allow comparison. The major features are the Zn 3d and O 2p levels, mentioned in the introduction. However, a peak on the low binding energy side of the O 2p levels is also observed. The Gaussian fitting reveals that the integrated intensity of this peak is directly proportional to Mn concentration, presented on the left hand side of fig 5.43. This strongly suggests that the peak corresponds to the Mn 3d levels. Fig 5.42 shows the Gaussian decomposition of spectra obtained for the films with Mn concentrations of 1% (left) and 25% (right). The dotted line indicates the experimental data, which shows good agreement with the sum of the Gaussians. Both of these graphs have been displaced vertically to allow the individual components to be seen. The right hand side of fig 5.43 shows the binding energy of the

119

Mn 3d peak in function of the concentration. At 1% Mn the energy is 2.58 ± 0.05 eV, which decreases by 0.36 eV to 2.22 ± 0.05 eV at 25%. An acceptable explanation for this shift would be p-d repulsion between the O 2p and Mn 3d levels. Conversely the O 2p levels are found to shift to higher binding energies in the same concentration range, with a similar change of 0.39 ± 0.07 eV, shown on the left hand graph of fig 5.44. The Zn 3d levels also influence this shift because, as the Mn concentration increases, the Zn concentration decreases, which reduces the p-d repulsion between the O 2p and Zn 3d levels. As the relative changes in Zn concentration are small, no significant shift is seen in the binding energy of the Zn 3d peak as the Mn concentration varies. However, the integrated intensity, shown on the right hand side of fig 5.44, decreases by 38 ± 5 %, which is around the expected value of 28 %. The conduction band minimum has Zn 4s character; therefore electric dipole transitions to these levels from the Mn 3d orbitals are not permitted. Consequently, the optical gap is determined by the next lowest energy transitions that are electric dipole permitted, which are from the O 2p orbitals. As these levels shift to higher binding energies with increasing Mn concentration, a corresponding increase in the optical gap would also be expected. This hypothesis will be investigated further in the optical properties section 5.4.1.
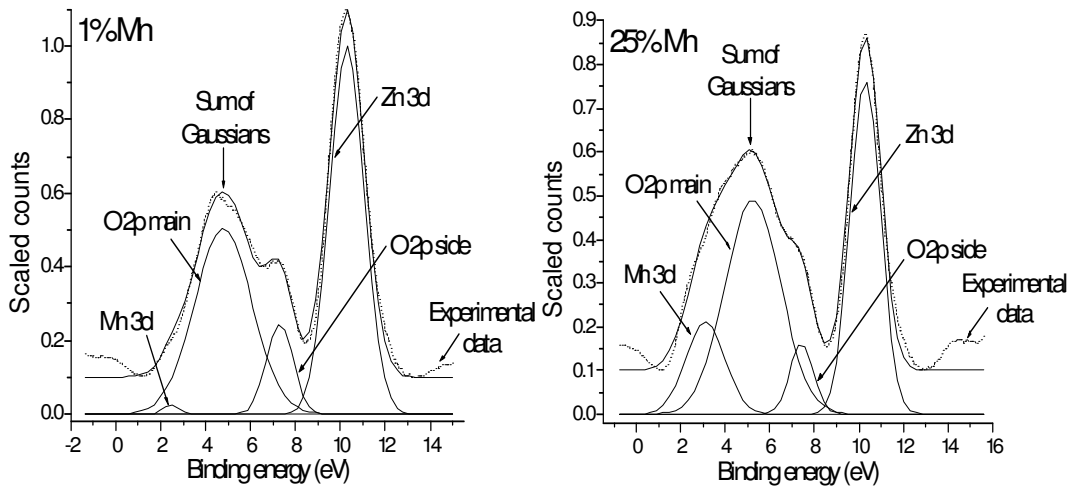
Fig 5.42: Gaussian decompositions of $Zn_{1-x}Mn_xO$ He-II UPS spectra.
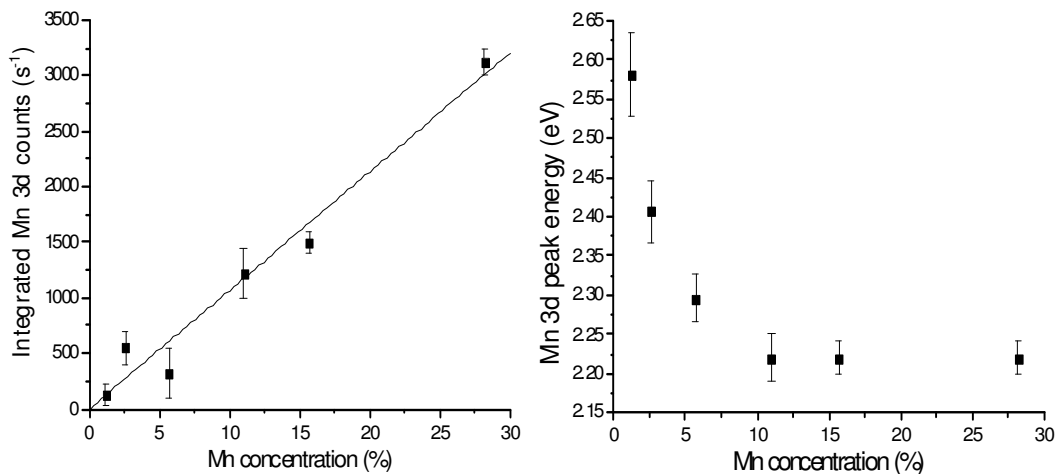
Fig 5.43: Intensity and binding energy of the Mn 3d peak in $Zn_{1-x}Mn_xO$ UPS results.
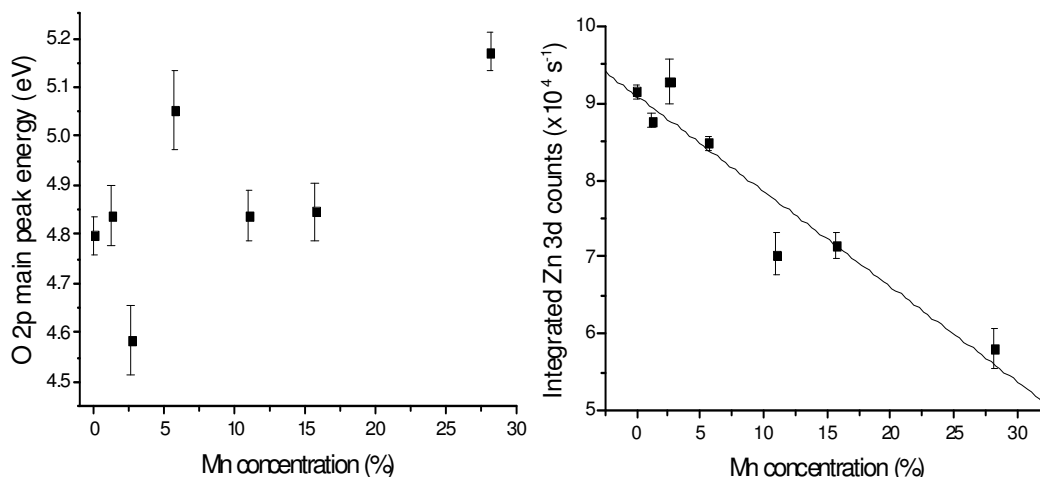
Fig 5.44: Variation in energy of O 2p main peak and intensity of Zn 3d peak.
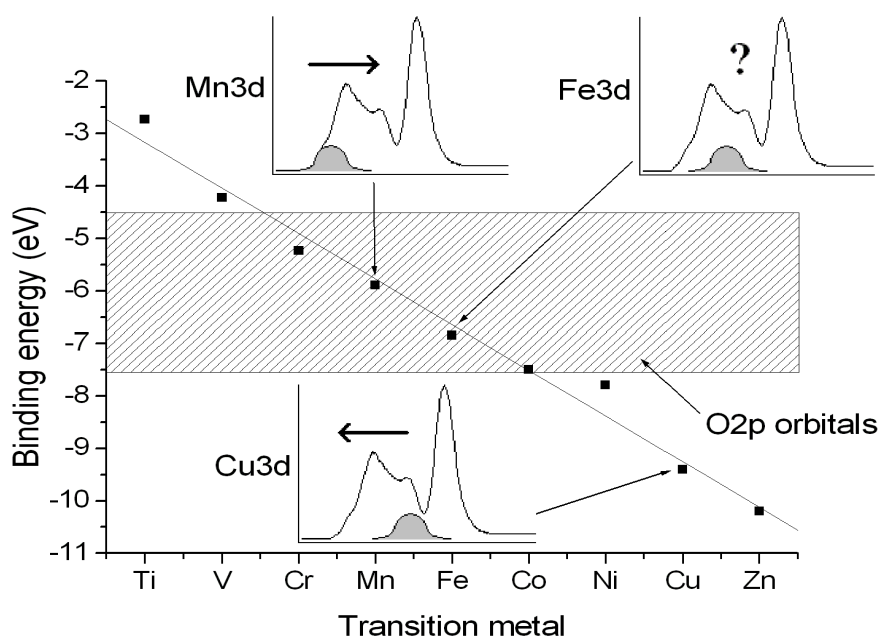
Fig 5.45: Theoretical 3d orbital energies of TMs [28].

Experimentally it is difficult to accurately determine the binding energy of the 3d orbitals of the period IV TMs. The excitation of a photoelectron in UPS leaves behind a hole, which perturbs the system and causes a shift in the measured binding energy. Other ionisation methods are only able to accurately determine the first ionisation potential, which would be a 4s orbital. However, theoretical values are readily available, such as those calculated by Kurihara et al. using the relativistic discrete-variational Dicac-Fock-Slater method [28]. These values are shown in fig 5.45 but are only, at best, approximate in the case of the DMS orbitals, as the influence of the O 2p orbitals is not accounted for. Nevertheless, they can help to explain the $Zn_{1-x}Mn_xO$ results and make predictions about the other DMSs. The theoretical values place the Mn 3d levels around the centre of the O 2p band, although it has been seen that they are probably closer to the top. The resulting p-d repulsion shifts the O 2p levels to higher

121

binding energies, as shown in the diagram. In the case of $Zn_{1-x}Cu_xO$, the theoretical binding energy of the Cu 3d orbitals is well below the O 2p band but still above the Zn 3d levels so p-d repulsion in the opposite direction would be expected. Although $Zn_{1-x}Ni_xO$ films could not be measured by UPS for technical reasons, a similar behaviour to $Zn_{1-x}Cu_xO$ would be predicted. In the case of $Zn_{1-x}Fe_xO$, the expected behaviour is not clear, as the theoretical values would place the Fe 3d levels right in the O 2p band. This could cause a broadening and intensifying of the O 2p levels as well as a shift in the binding energy, depending on the exact position of the Fe 3d orbitals.
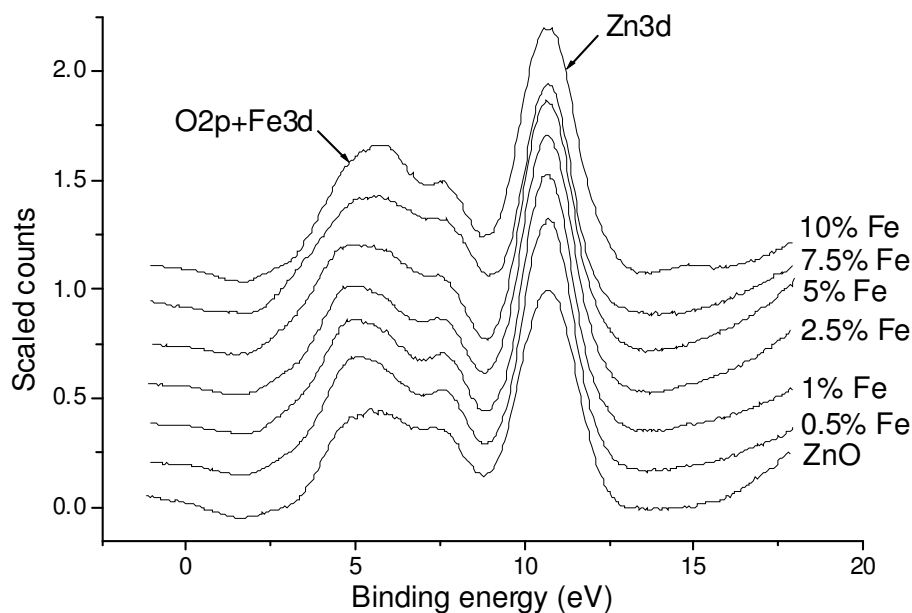
Fig 5.46: He-II UPS spectra of $Zn_xFe_{1-x}O$ films.

Fig 5.46 shows the vertically displaced He-II UPS spectra for $Zn_{1-x}Fe_xO$. Again, the Zn 3d and O 2p levels are clearly visible, although the position of the Fe 3d levels only becomes apparent after analysis. The Gaussian fitting was done in the same way as before and the decompositions are shown in fig 5.47 for the films with Fe concentrations of 1% (left) and 10% (right). In agreement with predictions, there is an intensifying and broadening of the O 2p levels, presented in fig 5.48. This is particularly apparent in the main peak, which shows a 24% increase in integrated intensity and broadens by 30% on increasing the Fe concentration from 0.5 to 10%. This is accompanied by a significant shift to higher binding energy of 0.29 ± 0.06 eV, shown in fig 5.49, on increasing the Fe concentration over the same range. The energy shift per percentage concentration increase of 25 meV seems too large to attribute solely to p-d repulsion, when compared to the 16meV observed in $Zn_{1-x}Mn_xO$. However, the energy distribution of the 3d levels could also affect the shift. It shall be shown in the XPS section (5.3.2) that the Mn is mainly in oxidation state II, whereas a significant proportion of the Fe has an oxidation state of III. This would produce a component to the Fe 3d peak at higher binding energies, especially at the larger Fe concentrations, which could increase the observed energy shift. Information on the optical gap will help to clarify this issue in section 5.4.1. Increasing the Fe concentration does not produce any noticeable changes in the binding energy or unscaled intensity of the Zn 3d peak.
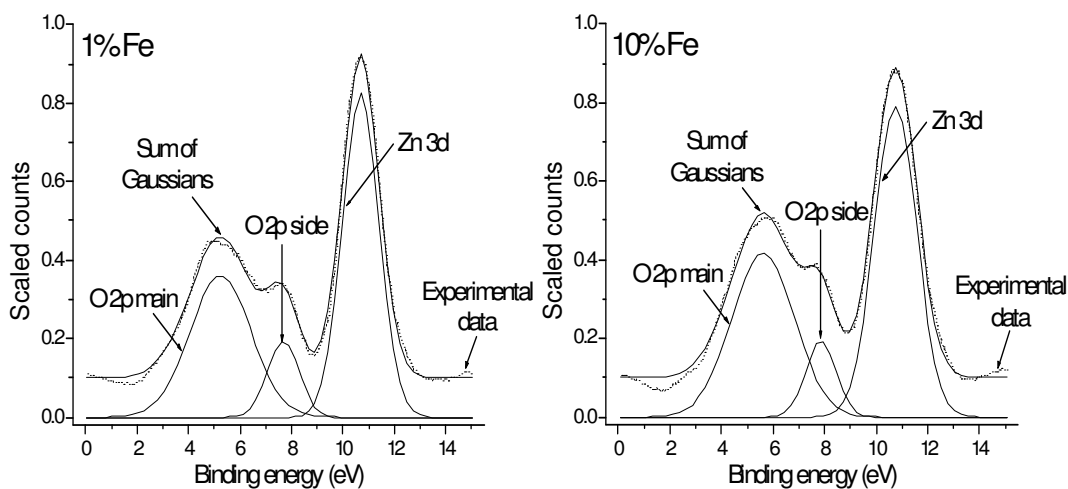
Fig 5.47: Gaussian decompositions of Zn₁₋ₓFeₓO He-II UPS spectra.
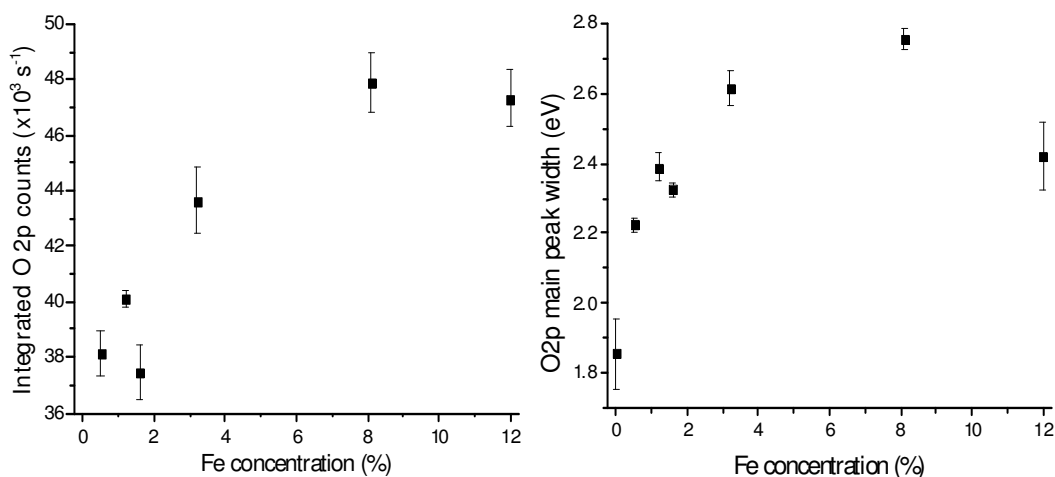
Fig 5.48: *Intensity and width of the O 2p main peak in Zn₁₋ₓFeₓO UPS results.*
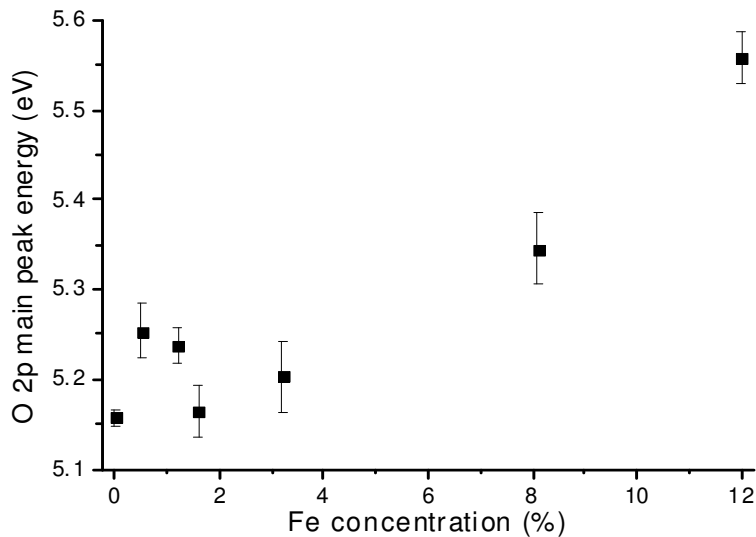
Fig 5.49: Binding energy of the O 2p main peak in Zn₁₋ₓFeₓO UPS results.

In the case of $Zn_{1-x}Cu_xO$, it was only possible to measure the He-II UPS spectrum of the sample containing 5% Cu. It is compared to the ZnO film on the other half of the heterojunction in fig 5.50. As in $Zn_{1-x}Fe_xO$, the position of the Cu 3d levels is not immediately apparent. Moreover there is no significant broadening or intensifying of either of the components of the O 2p peaks. However, they are shifted by an average binding energy of 0.12 ± 0.02 eV towards the Fermi level, corresponding to a decrease of 24 meV per percentage increase in Cu concentration. This agrees well with the theory that predicts a reversal in the direction of the p-d repulsion. Although the density of d-states with a higher binding energy than the O 2p orbitals is similar to pure ZnO, the Cu 3d levels are energetically closer to the O 2p states than the Zn 3d levels, so the p-d repulsion is greater. Such an effect should also cause the optical gap to decrease in energy. This will be investigated in section 5.3.1.
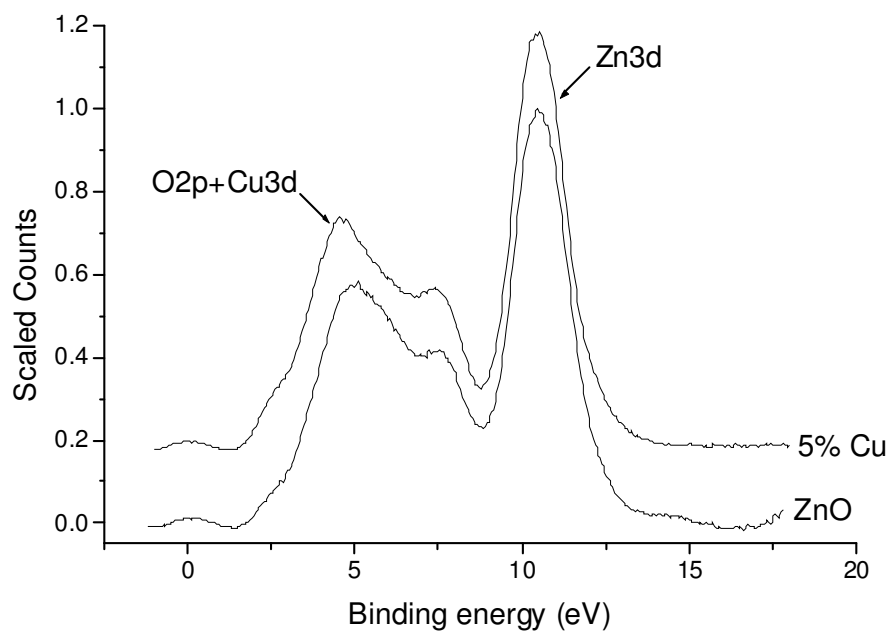
Fig 5.50: He-II UPS spectra of $Zn_{0.95}Cu_{0.05}O$ film.

5.3.2 XPS

This section reports on the core electronic levels identifiable from the Al K_α XPS spectra. A typical photoelectron spectrum does not only have peaks corresponding to the simple electronic transitions but also Auger transitions and a background generated by the emission of secondary electrons. Moreover, the peaks that do not come from s-states appear as doublets or multiplets due to the spin-orbit interaction. The full energy range XPS spectra of the DMS samples with the highest dilute cation concentrations are shown in figs 5.51 to 5.53. The overall form of the samples with lower concentrations was the same, so they are not shown. Photoemission peaks were identified according to standard electron binding energy tables [29] and have been labelled on the figures. For technical reasons it was not possible to measure the XPS spectra of the $Zn_{1-x}Ni_xO$ films.
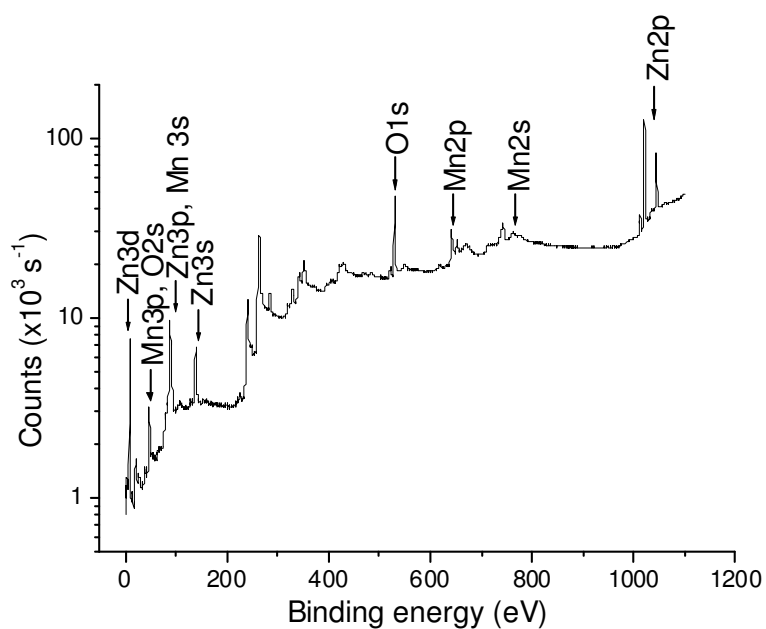
Fig 5.51: $Zn_{0.75}Mn_{0.25}O$ XPS spectrum in binding energy range 0-1100 eV.
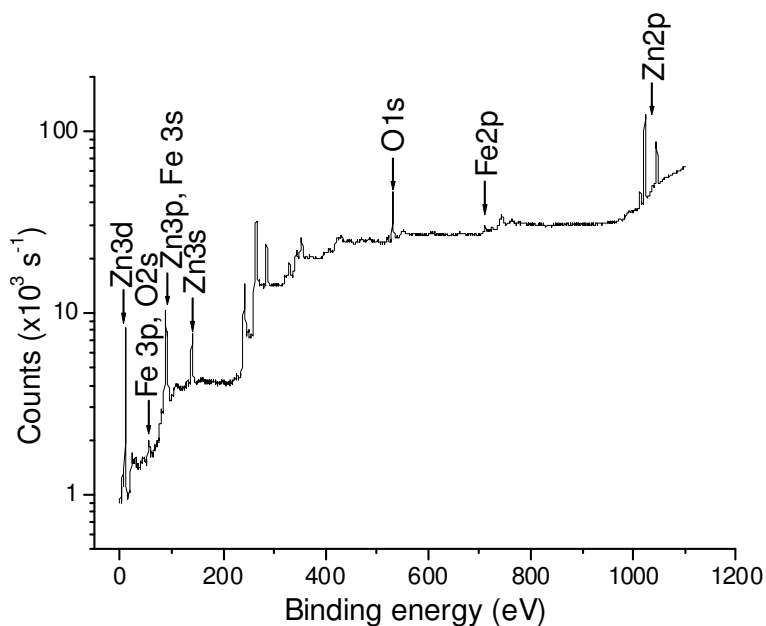
Fig 5.52: $Zn_{0.9}Fe_{0.1}O$ XPS spectrum in binding energy range 0-1100 eV.
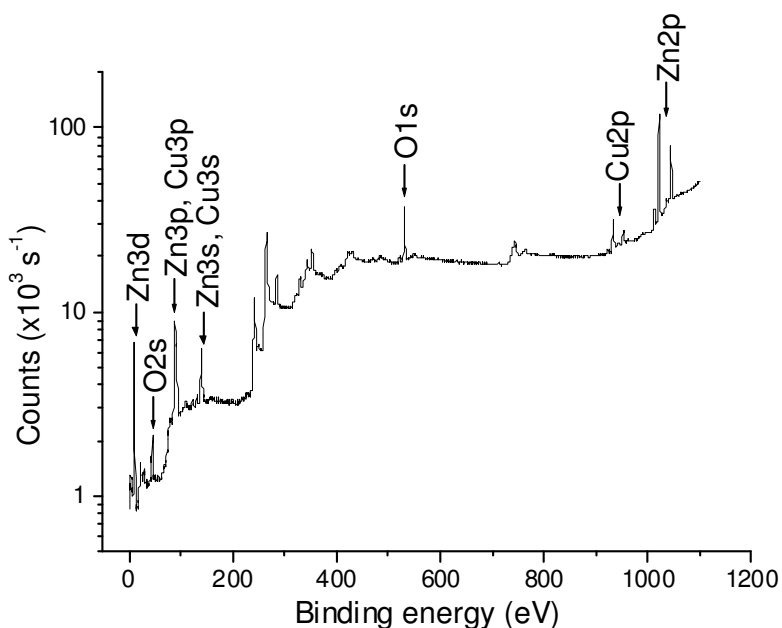
Fig 5.53: $Zn_{0.95}Cu_{0.05}O$ XPS spectrum in binding energy range 0-1100 eV.

After identification, the principal peaks, i.e. O 1s, Zn 2p and the 2p levels of the dilute cation, were isolated from the full spectral range. The background signals were removed and the intensities of the peaks were determined by Gaussian fitting. As the Zn $2p_{3/2}$ peak was the most intense, its amplitude was scaled to 1 and the other peaks were scaled relatively. Then the high resolution scans done in the region of the principal peaks were taken, fitted and scaled so that their maximum intensities would coincide with those determined from the full spectral range. Charging effects were corrected in a similar way to the UPS results by shifting the energy scales according to the binding energies of the Zn 2p levels in the pure ZnO halves of the heterojunctions.

Starting with $Zn_{1-x}Mn_xO$, the XPS spectra of the Mn 2p transitions are shown in fig 5.54. Due to the spin-orbit interaction, there are peaks corresponding to the Mn $2p_{3/2}$ and Mn $2p_{1/2}$ transitions. There is a clear increase in the intensity of the peaks as the Mn concentration increases. The actual values of the integrated intensities will be used towards the end of this section to verify the stoichiometry of the films. Apart from this, the Mn concentration has no other significant effect on the peaks. For example, the binding energy of the Mn $2p_{3/2}$ peak remains constant, with an average value of 641.3 ± 0.3 eV, corresponding to a Mn oxidation state of II [30]. This is confirmed by the presence of the satellite structure on the high binding energy side of the peaks [31], which occurs at an average energy of 644.7 ± 0.3 eV in the case of the Mn $2p_{3/2}$ levels. The reason why the satellite structure exists is that when a Mn 2p core electron is ionised, a hole is left in its place which causes the other Mn electrons to be more tightly bound. It can also make it energetically favourable for an electron from a neighbouring O ion to be transferred to the Mn ion, which effectively screens the hole potential. This reduces the charge imbalance after the photoelectron emission and, hence, reduces the measured binding energy of the Mn 2p level [32, 33]. Therefore, the main peaks in the XPS spectra correspond to transitions from screened Mn ions, whereas the satellite peaks are from unscreened ions.
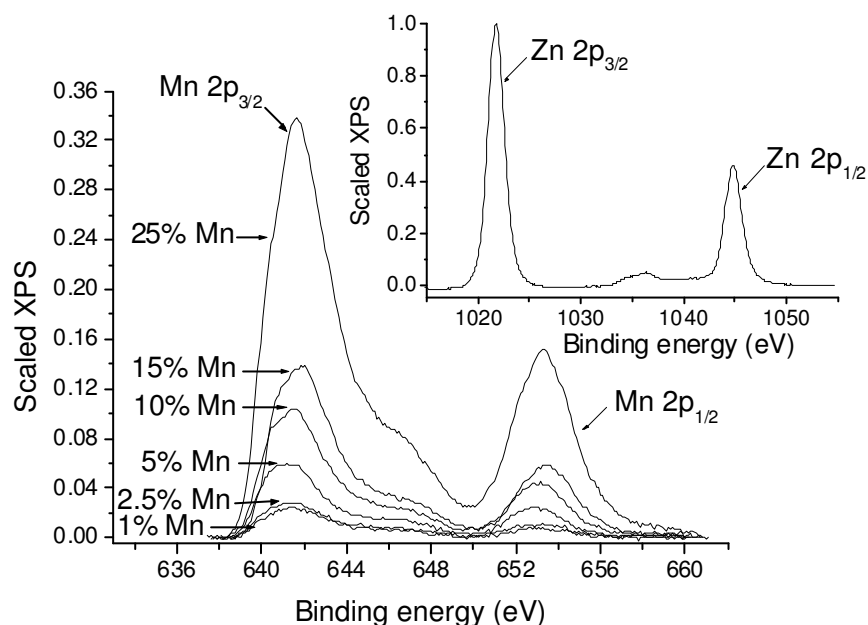
Fig 5.54: Mn 2p transitions in $Zn_{1-x}Mn_xO$ XPS spectra.

The XPS spectra of the Fe 2p transitions from the $Zn_{1-x}Fe_xO$ films are shown in fig 5.55. As in the case of the Mn 2p levels, the intensity of the peaks clearly increases with Fe concentration. Moreover, there is a slight shift towards higher binding energy, which is also seen in [34]. The Fe $2p_{3/2}$ peak shifts by 0.73 eV from 709.79 ± 0.03 to 710.52 ± 0.02 eV in the concentration range and a similar shift of 0.79 eV from 723.28 ± 0.04 to 724.07 ± 0.03 eV is observed in the Fe $2p_{1/2}$ peaks. The binding energies of the Fe 2p peaks in different oxidation states are given in [35]. In the II state, the $2p_{3/2}$ and $2p_{1/2}$ levels occur at 709.30 and 722.30 eV respectively, but they shift to 710.70 and 724.30 eV respectively in the III state. Therefore, it appears that there is a gradual oxidation of the Fe from II to III as the concentration increases. This agrees with the structural characterisation because Fe in the Zn substitutional position has an oxidation

state of II, which increases to III in Fe_2O_3. Hence, as the proportion of the Fe_2O_3 secondary phase increases, the resulting increase in oxidation is reflected in the binding energy of the Fe 2p levels. As in the case of the Mn 2p levels, the satellite structure resulting from transitions from unscreened Fe ions is observed on the high binding energy side of the main peaks, which occurs at an average energy of 714.4 ± 0.2 eV in the case of the Fe $2p_{3/2}$ levels, although this energy is also influenced by oxidation.
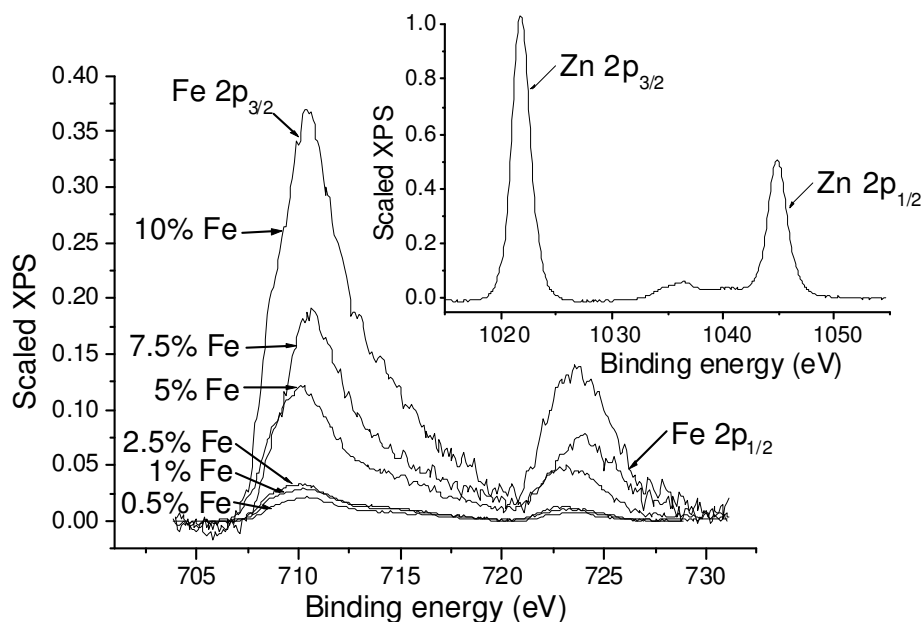
Fig 5.55: Fe 2p transitions in $Zn_{1-x}Fe_xO$ XPS spectra.

Fig 5.56 shows the XPS spectrum of the Cu 2p transitions for the $Zn_{0.95}Cu_{0.05}O$ film. The binding energy of the $2p_{3/2}$ peak is 932.56 ± 0.02 eV, which is slightly lower than the 933.7 eV that would be expected if the Cu were wholly in the II oxidation state [36]. Therefore, it appears that there is a significant contribution from Cu(I). In light of the structural characterisation, these results were to be expected, as a significant proportion of the Cu_2O secondary phase was detected in the 5% Cu film and the oxidation state of Cu in this compound is I. The $2p_{3/2}$ satellite peak is found at 944.2 ± 0.6 eV, so its separation from the main peak of 10.5 eV is much larger than in the Mn and Fe DMSs. Moreover, the satellite peak has a relatively low intensity. Both the binding energy and intensity effects mean that the core hole screening is particularly effective. Therefore, a high proportion of the O electrons must come from the local environment of the hole i.e.) the nearest neighbours [33]. Although $Zn_{1-x}Ni_xO$ films could not be measured by XPS, other authors already report these results [37, 38]. In [37] the binding energies of the $2p_{3/2}$ and $2p_{1/2}$ levels were 855.3 and 872.9 eV, respectively, with high energy satellites at 860.7 and 879.3 eV. These energies were found to be invariant with Ni concentration and the authors conclude that the Ni must be in the Zn substitutional position. However, Ni in both $Zn_{1-x}Ni_xO$ and NiO has the same oxidation state of II so no change would be expected on the appearance of the NiO secondary phase. Therefore, there is no contradiction with the structural characterisation.
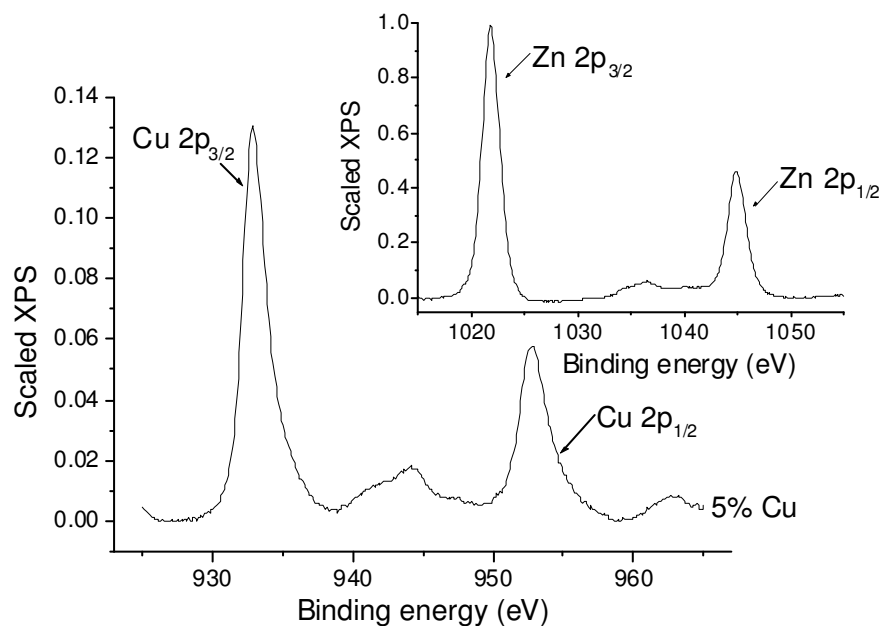
Fig 5.56: Cu 2p transitions in $Zn_{0.95}Cu_{0.05}O$ XPS spectrum.

Typical Zn 2p XPS spectra from the different DMSs are shown in the insets to figs 5.54 to 5.56. No significant changes were found between the spectra on changing the dilute cation element or its concentration. The average binding energy of the Zn $2p_{3/2}$ peak is 1022.1 ± 0.2 eV, identical to the average value found in the pure ZnO halves of the heterojunctions. This energy corresponds to the II oxidation state [39]. It appears that the core hole screening is even more effective in Zn than Cu, as the $2p_{3/2}$ satellite peak is separated from the main peak by a greater energy of 14.7 ± 0.3 eV and it also has a lower relative intensity.
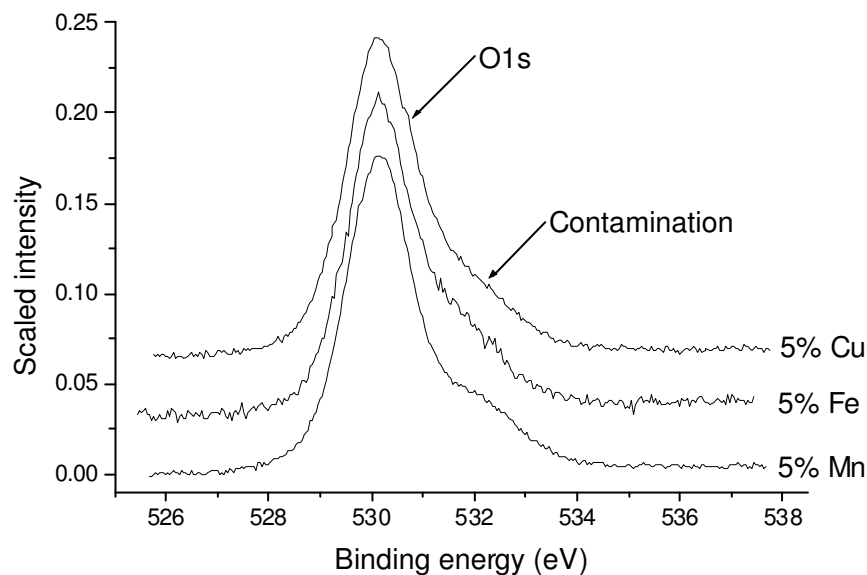
Fig 5.57: XPS spectra of the O1s peak in 5% DMS films.

Samuel John Gilliland

To complete the series of XPS spectra, the O 1s levels for the different DMSs are shown in fig 5.57. The spectra were fitted using two Gaussian profiles, although other authors use up to 4 [39]. The most intense peak, which occurs at an average binding energy of 530.10 ± 0.01 eV, corresponds to oxygen in the crystal lattice, whereas the side peak, at an average binding energy of 531.05 ± 0.02 eV is related to surface contamination. Sources of such contamination could be hydroxyl groups, water, $-CO_3$ and O_2. Although there are differences between certain O 1s spectra, there are no clear trends in function of dilute cation element or concentration. Therefore, the differences are probably of a random nature, depending on the cleanness of the surface of that particular film.

Finally, the XPS results were used to obtain a further set of results for the dilute cation concentrations in the films. The integrated intensity of the dilute cation 3d peaks (A_{DC}) were added and divided by the appropriate subshell photoionisation cross section (σ_{DC}), obtained from [40] and given in table 4.1 of section 4.2.4. This process was repeated for the Zn 3d peaks, with summed integrated intensity A_{Zn} and subshell photoionisation cross section σ_{Zn}. Using simple ratios, the dilute carrier proportion (x) could be calculated using the following equation:

$$x = \frac{1}{\left(\dfrac{A_{DC}\sigma_{Zn}}{A_{Zn}\sigma_{DC}}\right) + 1} \qquad (5.2)$$

Nominal Mn (%)	XPS Mn (%)	Nominal Fe (%)	XPS Fe (%)	Nominal Cu (%)	XPS Cu (%)
1	2.3 ± 0.2	0.5	0.68 ± 0.05	5	4.1 ± 0.1
2.5	2.8 ± 0.2	1	0.96 ± 0.07		
5	5.1 ± 0.3	2.5	1.11 ± 0.08		
10	9.2 ± 0.6	5	4.3 ± 0.3		
15	15.3 ± 0.9	7.5	6.8 ± 0.5		
25	30.4 ± 1.8	10	12.6 ± 0.9		

Table 5.2: DMS concentrations determined by XPS.

The results of the calculations are shown in table 5.2 and the majority are in agreement with those obtained by XRF in table 5.1, section 5.2.3. A few of the values are beyond the boundaries of the experimental errors but, in those cases, it is possible that there really was a significant difference in dilute cation concentration because the films characterised by XRF were deposited separately to the heterojunction films which were used in the XPS measurements. Therefore, any differences in growth conditions could have produced samples with different dilute cation concentrations.

5.4 Optical properties

5.4.1 Concentration effects

5.4.1.1 $Zn_{1-x}Mn_xO$

The optical transmission spectra of the films were converted to absorption coefficients using (3.47). A constant value of 2.0 was used for the refractive index of ZnO and all the DMSs. This is justified because ZnO shows a relatively low wavelength dependence in the region of interest [41]. Moreover, the refractive indices of MnO, FeO, CuO and NiO are 2.16, 2.32, 2.63 and 2.18 respectively [42]. Therefore, the maximum refractive index variation in the low concentration ranges used in this investigation would only be about 4%. Fig 5.58 shows the absorption coefficient of pure ZnO at room temperature and 20K. Low temperature absorption spectra are useful to evaluate the film quality through the features of the absorption edge which have been labelled in the figure. This is because, in samples with few defects, the low temperature width and intensity of the exciton is determined principally by phonon dispersion. The two peaks beyond the exciton have been identified as exciton + LO phonon resonances, as opposed to assigning them as B and C excitons, done by some authors [43]. This is because there is a constant energy difference between the peaks of 77 ± 3 meV, which is close to the LO phonon energy of 72 meV given in [44]. However, the B and C excitons would be separated by 15 and 40 meV, respectively [45], which is clearly not the case.
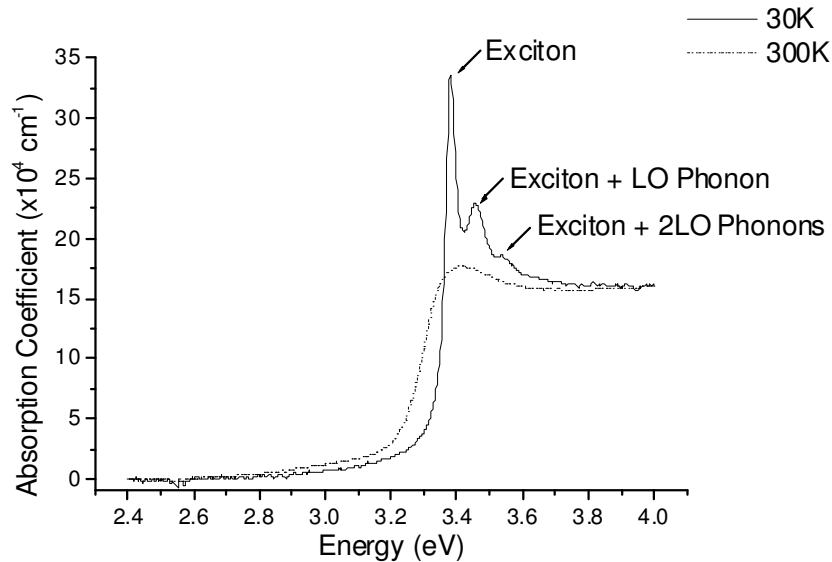
Fig 5.58: Absorption coefficient of pure ZnO at room temperature at 30K.

The low temperature absorption coefficient was fitted to a model based on the Elliot-Toyozawa equation (3.63). Since the excitonic edge is well defined, it was possible to determine the value of all the adjustable parameters. These may be divided into parameters related to the band-to-band absorption continuum: the gap (Eg) and continuum width (Γ_C) and those related to the discrete excitonic states: the Rydberg energy (R) and the exciton widths (Γ_m), where m is an integer. It was found that the

number of discrete excitonic states necessary for good agreement between theory and experiment was three. Gaussian additions were made to the model to take into account the exciton + LO phonon resonances with adjustable parameters corresponding to the LO phonon energy (E_p) and the width (Γ_p) of the contributions. In this case, two resonances were sufficient to reproduce the experimental results. The actual values of the parameters obtained for pure ZnO were Eg = 3.432 ± 0.002 eV, Γ_C = 0.189 ± 0.003 eV, R = 50.0 ± 0.5 meV, Γ_1 = 19.4 ± 0.2 meV, $\Gamma_2 = \Gamma_3$ = 0.20 ± 0.04 eV, E_p = 77 ± 3 meV and Γ_p = 26 ± 1 meV. These values were used as initial conditions for the fittings done with the DMSs.
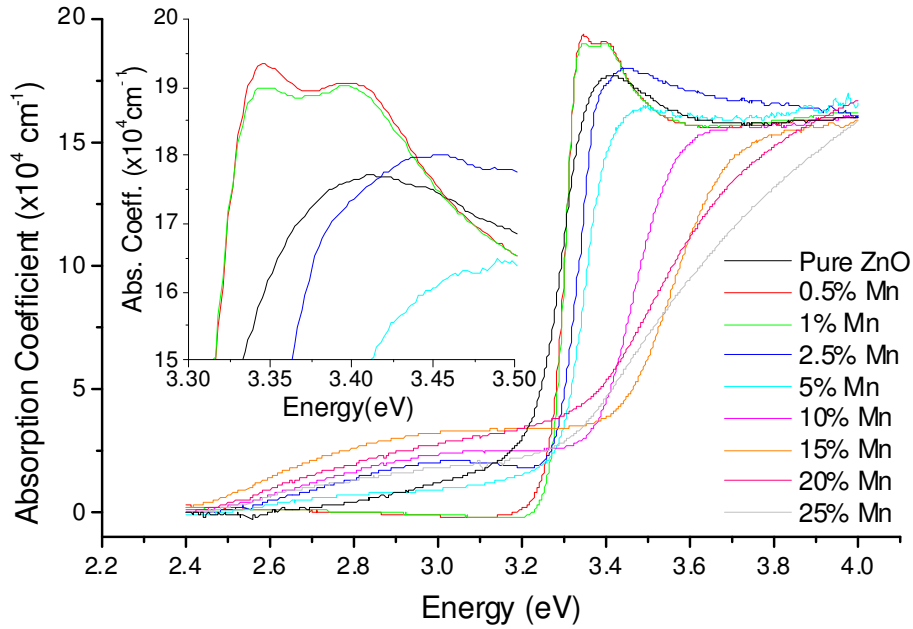
Fig 5.59: Absorption coefficients of $Zn_{1-x}Mn_xO$ films at room temperature.
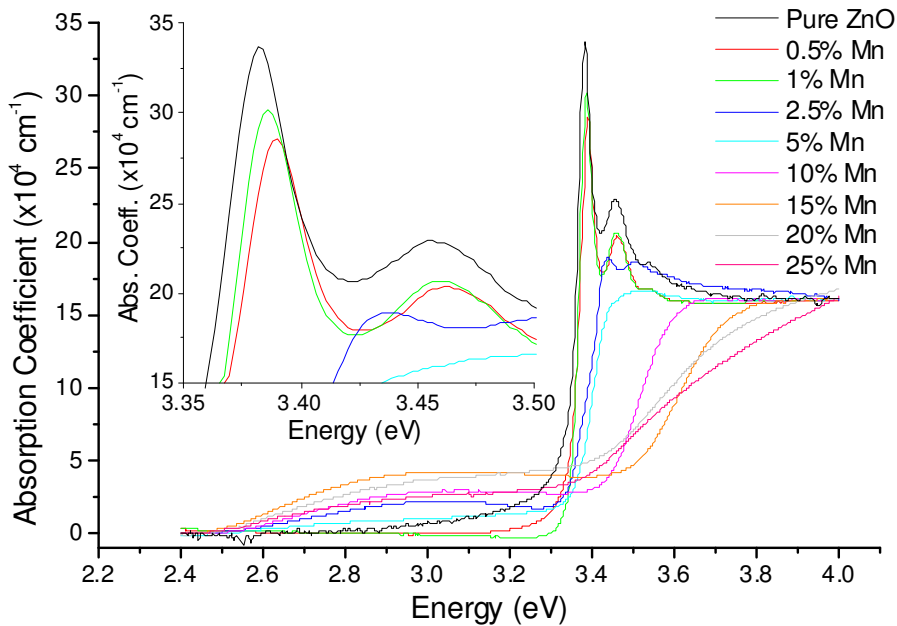
Fig 5.60: Absorption coefficients of $Zn_{1-x}Mn_xO$ films at 20K.

Figs 5.59 and 5.60 show the absorption coefficients of the $Zn_{1-x}Mn_xO$ films at room temperature and 30K respectively. The region around the excitonic peak has been amplified and shown in the inset to both figures to so that the effects of changing the DMS concentration may be more clearly seen. There are three main effects that may be observed as the dilute cation concentration is increased. Firstly, the excitonic peak and exciton + LO phonon resonances decrease in intensity and shift to higher energies. Secondly, the band-to-band absorption continuum also shifts to higher energies. Thirdly, a pre-edge absorption band emerges and intensifies. To quantify these effects, the model used for pure ZnO was applied with an additional Gaussian profile to model the intensity, energy and width of the pre-edge band. It is important to note that the use of a Gaussian profile in this situation is an approximation, since the energy of the peak maximum only corresponds indirectly to the energy of the transition responsible for the pre-edge band [46]. In order to simplify the fitting process and reduce the errors that could be introduced when a large number of fitting parameters are used, certain parameters were kept constant, maintaining the values obtained for pure ZnO. These parameters were the exciton Rydberg energy (R = 50 meV), the LO phonon energy (E_p = 77 meV) and the width of the less significant discrete excitonic contributions ($\Gamma_2 = \Gamma_3$ = 0.20 eV).
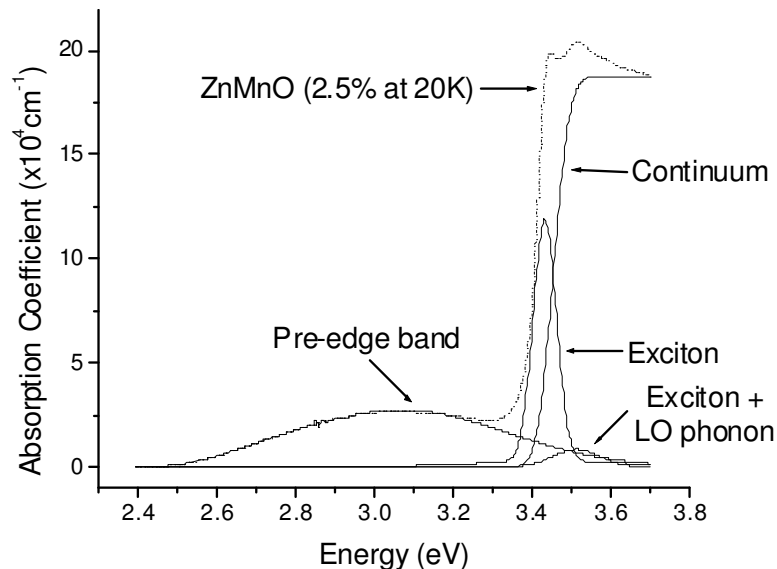
Fig 5.61: Decomposition of Elliot-Toyozawa fitting for $Zn_{0.975}Mn_{0.025}O$ film.

Fig 5.61 shows the different components of the fitting in the case of $Zn_{0.975}Mn_{0.025}O$. At low Mn concentrations, the exciton makes a particularly significant contribution to the form of the absorption edge. At higher concentrations the exciton is not directly observed, however it continues to influence the absorption coefficient, so it must remain in the model. The same is not true for the exciton + LO phonon resonances, which cannot be detected by the fitting at Mn concentrations beyond 5%. Conversely, the pre-edge band can only be detected at Mn concentrations starting from 2.5%. Figs 5.62a-d show graphs of the parameters determined by the fitting in function of Mn concentration at 20K.
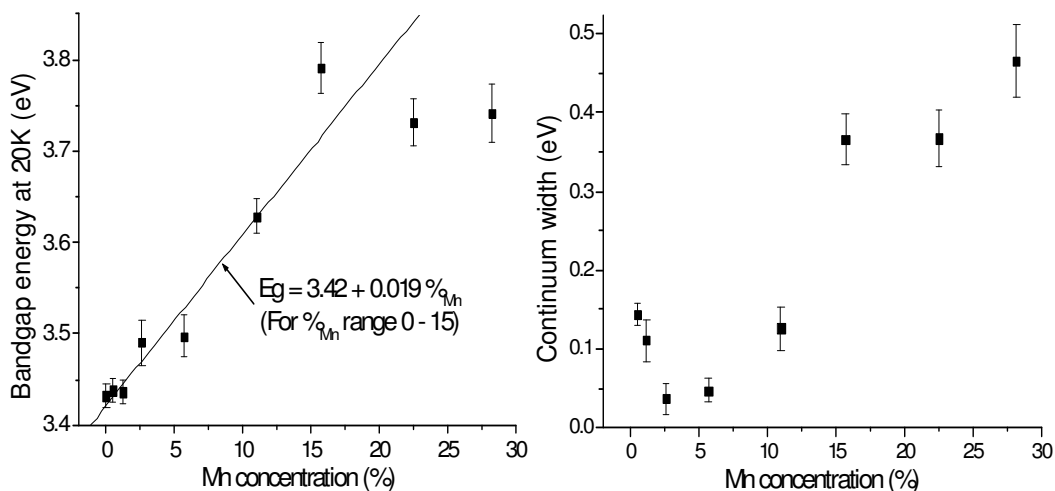
Fig 5.62a: Continuum parameters of $Zn_{1-x}Mn_xO$ films.
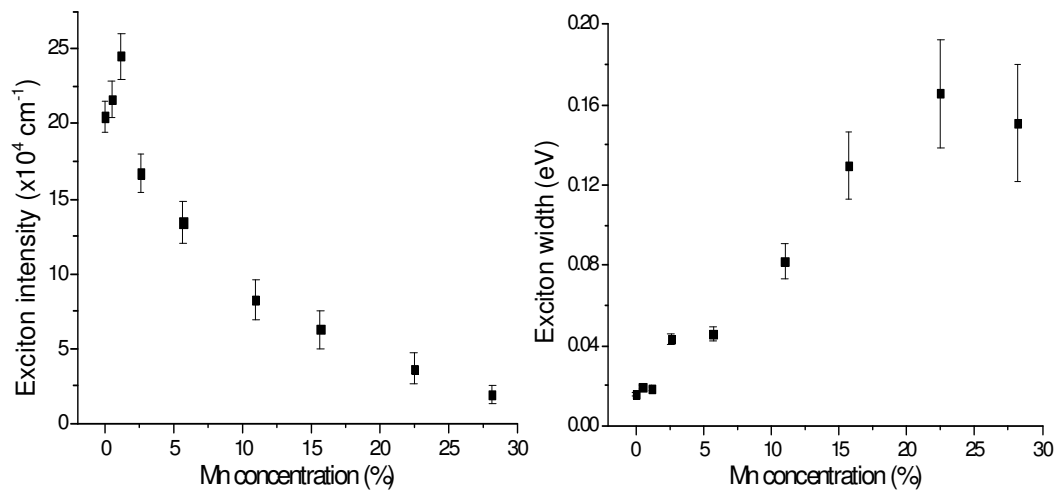
Fig 5.62b: Excitonic parameters of $Zn_{1-x}Mn_xO$ films.
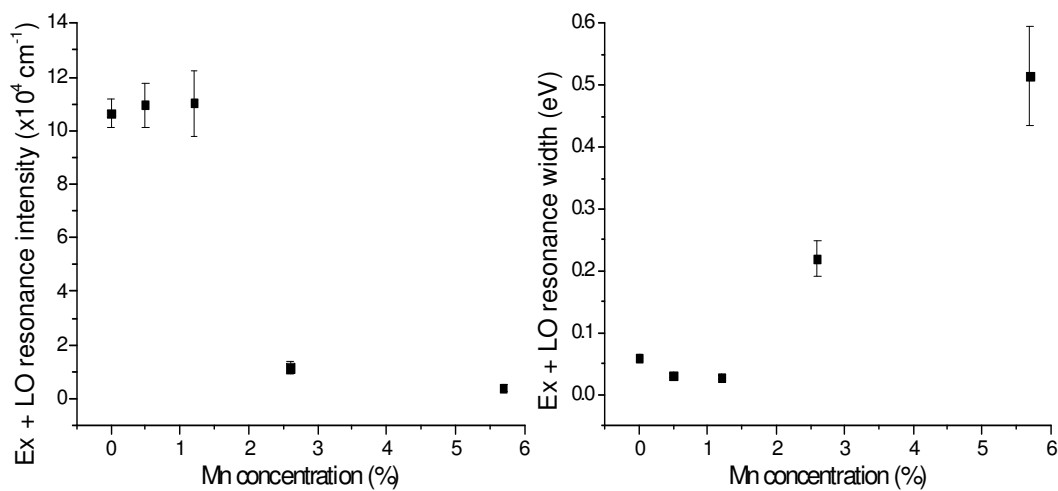
Fig 5.62c: Exciton + LO phonon resonance parameters of $Zn_{1-x}Mn_xO$ films.
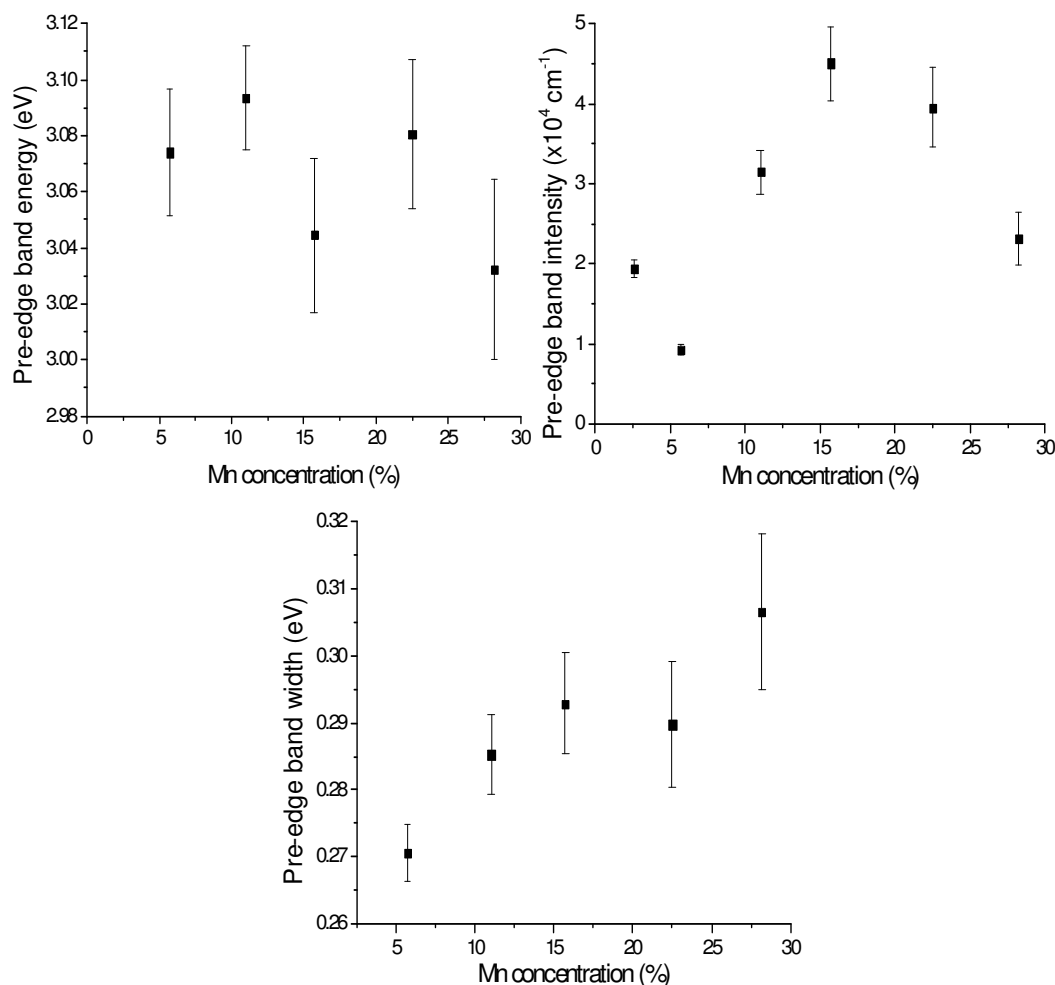
Fig 5.62d: Pre-edge band parameters of Zn$_{1-x}$Mn$_x$O films.

Starting with the continuum parameters in fig 5.62a, the bandgap increase in function of Mn concentration is approximately linear up to a concentration of 15%, with a coefficient of 19 ± 2 meV%$_{Mn}^{-1}$. We note that the direction and magnitude of the change is within errors of that of the O 2p levels determined by UPS in section 5.3.1, which shifted to higher binding energies at a rate of 13 ± 3 meV%$_{Mn}^{-1}$. Therefore, we conclude that the principal physical mechanism behind the behaviour of the optical gap is the modification of p-d repulsion as Zn is replaced by Mn. Beyond 15%, the variation flattens off, in agreement with DRX results in section 5.2.1, which suggest that the solubility limit of Mn in ZnO is reached at this point. Therefore, increasing the Mn concentration beyond this limit would be unlikely to cause a large change in bandgap energy. Although electron microscope images of the surface of the Zn$_{1-x}$Mn$_x$O films could not be taken, it would be expected that an increase in Mn concentration would cause more stress in the film, leading to defects and a greater degree of disorder. This is supported by the broadening of the continuum width observed in fig 5.62a (right), which increases by 0.43 ± 0.05 eV over the concentration range. The same mechanism is responsible for the trends observed in the exciton (fig 5.62b) and the exciton + LO phonon resonances (fig 5.62c), as defects increase the probability of an exciton being disassociated. Therefore, in both cases there is a decrease in intensity and an increase in width. In the case of the exciton, the decrease in intensity is 23 ± 6 ×10^{4}cm^{-1} and the

increase in width is 0.15 ± 0.03 eV over the concentration range. In the exciton + LO phonon resonances, the changes are $-11 \pm 1 \times 10^4 \text{cm}^{-1}$ and 0.49 ± 0.08 eV, respectively.

Before discussing results from the pre-edge band, it is important to distinguish between the different electronic transitions that could cause it. These are summarised in fig 5.63. Clearly it could not be a band-to-band (B-B) transition, as its energy is below that of the gap. This leaves internal transitions between Mn 3d levels (d-d*), transitions from the valence band to Mn 3d levels (VB-d*) and transitions from Mn 3d levels to the conduction band (d-CB). The latter two transitions produce charge transfer, as holes are transferred to the valence band or electrons to the conduction band. The fitting shows that energy of the pre-edge band, presented in fig 5.62d, decreases slightly or remains constant, with a value of 3.06 ± 0.03 eV over the whole Mn concentration range. This would lend itself particularly to d-d* transitions, as their relative energies would be unlikely to change significantly at different concentrations, although charge transfer transitions (CTTs) could behave in a similar way. As the UPS results in section 5.3.1 show, p-d repulsion causes the valence band minimum to decrease in energy, while the Mn 3d levels are shifted up. Therefore, the VB-d* CTT would increase in energy, making it an unlikely candidate for the pre-edge band. However, the d-CB CTT still remains a possibility. In order to elucidate the nature of the pre-edge transition, photoconductivity measurements were taken.
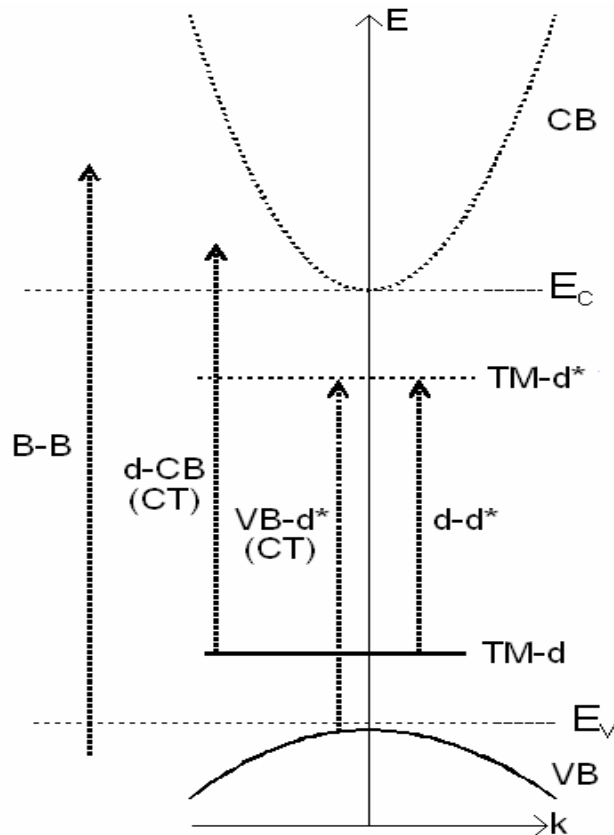
Fig 5.63: Candidates for pre-edge band transition.

Indium contacts were evaporated onto the surface of the $Zn_{0.85}Mn_{0.15}O$ film and the photocurrent was measured across it in the same wavelength range as the optical absorption measurements. The results are shown in fig 5.64, with the absorption

coefficient overlaid to assist interpretation. There is a clear photocurrent detected in the area of the pre-edge band, indicating the creation of photoexcited free carriers, which supports the assignment of this band as a CTT. Therefore, we conclude that the pre-edge band is produced by Mn 3d-CB CTTs with the additional possibility of some contribution of Mn 3d-d* internal transitions. This agrees with the conclusions of other authors [47] and shall be discussed further on the basis of the behaviour of the pre-edge band at high pressure in section 5.4.3. Returning to the results in fig 5.62d, the intensity of the pre-edge band increases to $4.5 \pm 0.5 \times 10^4 \text{cm}^{-1}$ at a concentration of 15%, the solubility limit. Beyond this point, the film consists of a mixture of phases containing Mn, which could explain the apparent decrease in intensity that occurs as the concentration is increased further. As with the other features of the $Zn_{1-x}Mn_xO$ absorption spectra, the width of the pre-edge band broadens with Mn concentration, due to the disorder effect. The observed broadening is 36 ± 12 meV over the concentration range.
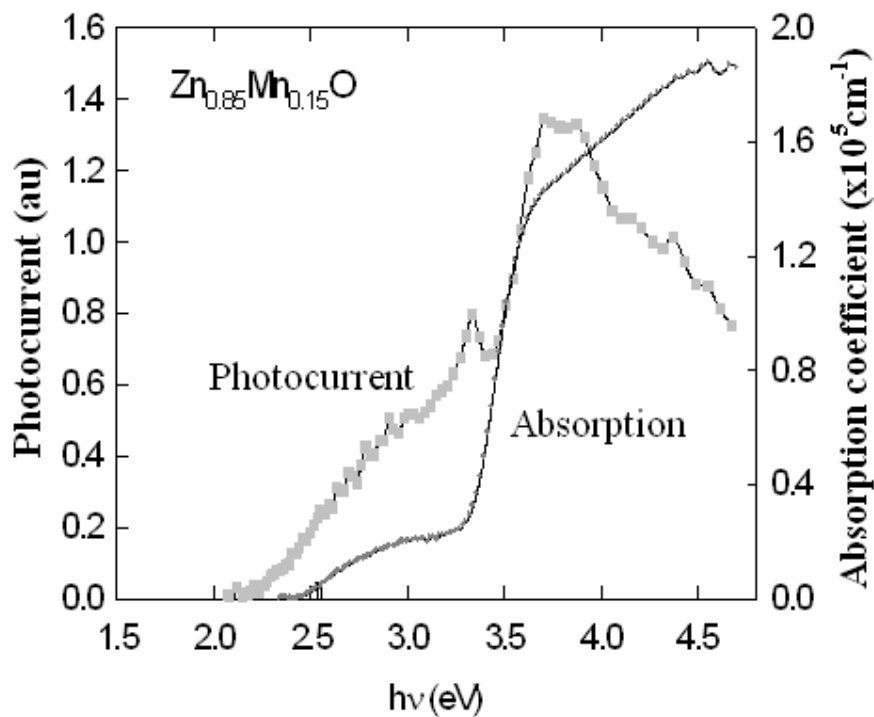
Fig 5.64: Photoconductivity measurements for $Zn_{0.85}Mn_{0.15}O$ film.

5.4.1.2 Zn$_{1-x}$Fe$_x$O
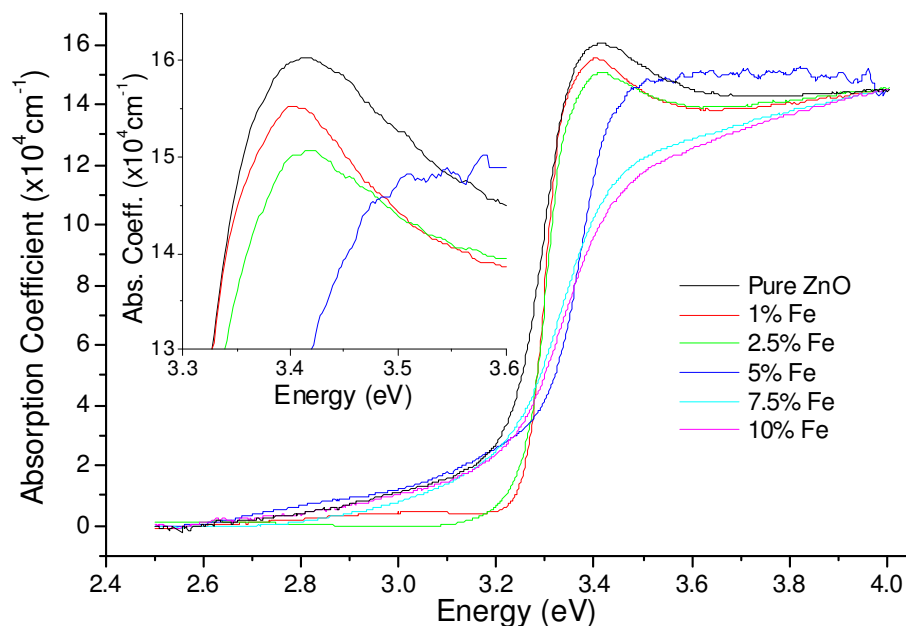
Fig 5.65: Absorption coefficients of Zn$_{1-x}$Fe$_x$O films at room temperature.
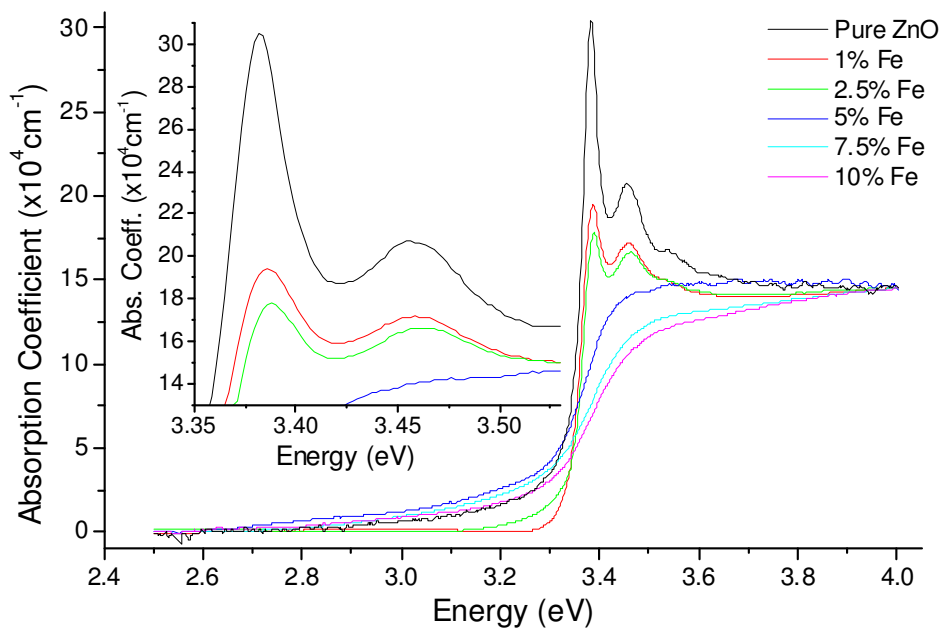
Fig 5.66: Absorption coefficients of Zn$_{1-x}$Fe$_x$O films at 20K.

In the case of Zn$_{1-x}$Fe$_x$O, the absorption coefficients at room temperature and 20K are shown in figs 5.65 and 5.66, respectively. As before, the region around the excitonic peak has been amplified and shown in the inset to both figures. The same general effects observed in the Zn$_{1-x}$Mn$_x$O films may be seen here, apart from the pre-edge band, which does not appear as well defined as in Zn$_{1-x}$Mn$_x$O, but rather as an absorption tail. This is because the Fe 3d orbitals are probably within the O 2p band, as

suggested by the UPS results in section 5.3.1. Therefore the CTTs would appear at energies above the bandgap. The fitting was applied in the same way as before and the results are shown in figs 5.67a-b.
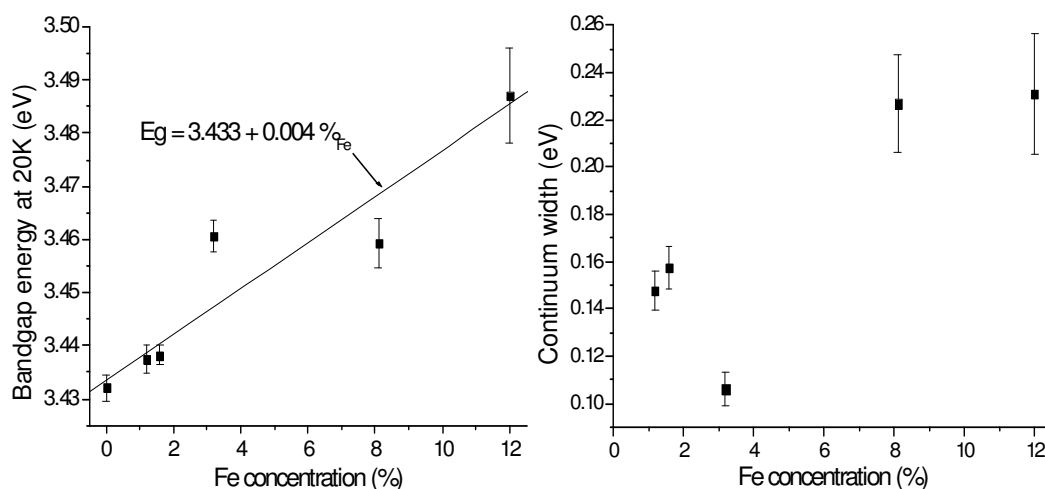
Fig 5.67a: Continuum parameters of Zn$_{1-x}$Fe$_x$O films.
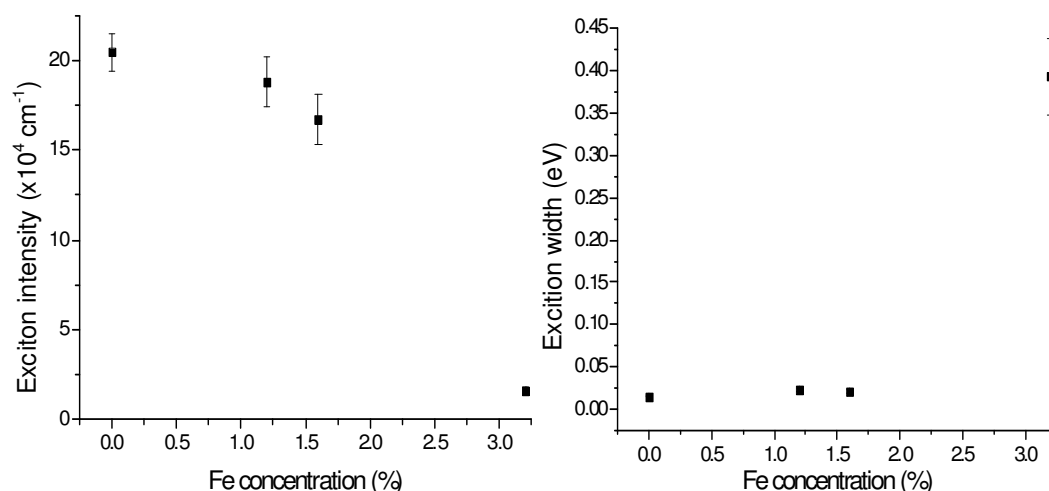
Fig 5.67b: Excitonic parameters of Zn$_{1-x}$Fe$_x$O films.

As in the case of the Mn DMS, the bandgap energy of Zn$_{1-x}$Fe$_x$O in fig 5.67a increases with concentration, but at a much lower average rate of 4 ± 1 meV%$_{Fe}^{-1}$. This is probably due to the position of the Fe 3d levels within the O 2p band. As the UPS results in section 5.3.1 show, p-d repulsion shifts the O 2p orbitals to lower energy in the case of Mn and higher energy in the case of Cu and Ni, leaving Fe somewhere in between. In the Mn DMS there was a direct link between the energy shift detected in the O 2p levels and the change in optical bandgap so it makes sense to assume this link would also apply in the other DMSs. Although an unusually large red shift of 25 ± 5 meV%$_{Fe}^{-1}$ was detected for the O 2p levels in the Fe DMS, it was not clear if it was really due to the change in p-d repulsion or if the presence of Fe III was responsible. In light of the optical results, it seems that it was mainly due to Fe III, however a small contribution from p-d repulsion must still occur to allow the change in bandgap energy. Moving on to the continuum width in fig 5.67a (right), a similar trend to the Mn DMS is

also observed with an increase of 0.13 ± 0.03 eV over the concentration range. As before, this is ascribed to the increase in disorder, confirmed by electron microscopy results in section 5.2.4. Related to this, the exciton intensity and width in fig 5.67b also show similar trends to the Mn DMS, with relatively large changes, over the concentration range, of $-19 \pm 2 \times 10^4 \text{cm}^{-1}$ and 0.38 ± 0.05 eV, respectively. The magnitude of the changes suggests that the rate of increase of disorder is greater in $Zn_{1-x}Fe_xO$ than $Zn_{1-x}Mn_xO$, probably due to the Fe_2O_3 secondary phase that appears from concentrations of 5% Fe. Results for the exciton + LO phonon resonances are not reported, as they were only measurable at the two lowest concentrations, making it difficult to determine any trends.

5.4.1.3 $Zn_{1-x}Cu_xO$

Figs 5.68 and 5.69 show the absorption coefficients of $Zn_{1-x}Cu_xO$ at room temperature and 20K, respectively. The general trends are not the same as in the previous two DMSs and only become apparent after applying the fitting. The results are shown in figs 5.70a-c. Naturally, there is no pre-edge band because the Cu 3d orbitals are well within the O 2p band. In certain films, particularly those containing 0.5 and 2.5% Cu, a weak absorption peak is seen at an energy of 3.415 ± 0.002 eV. This is probably due to excitonic absorption from a small proportion of $Zn_{1-x}Cu_xO$ that is not c-oriented. This was not taken into account in the fitting.
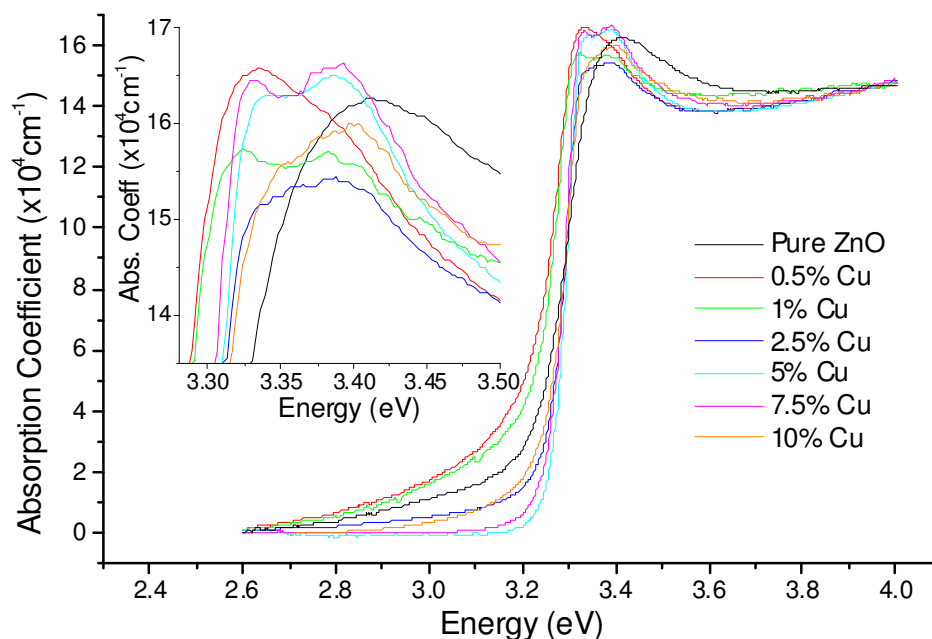
Fig 5.68: Absorption coefficients of $Zn_{1-x}Cu_xO$ films at room temperature.
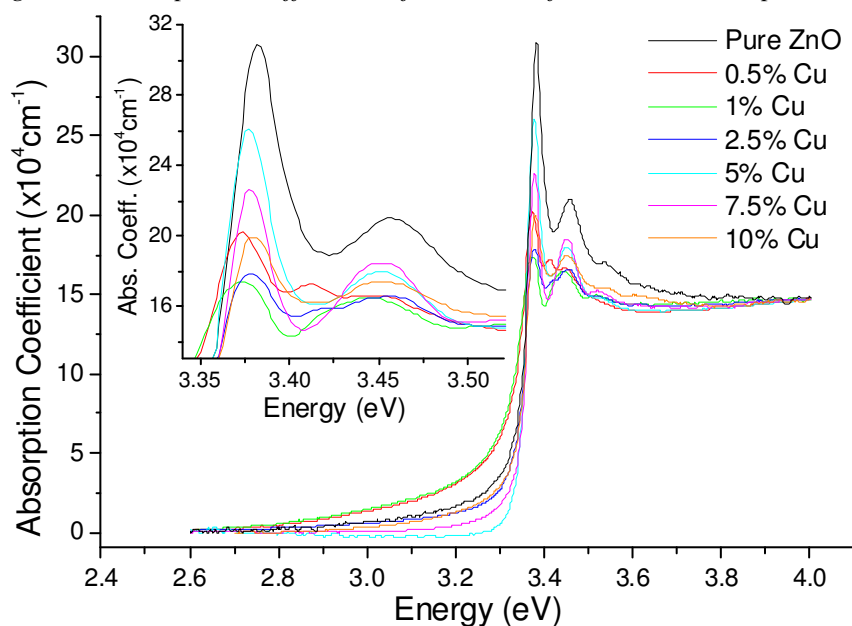
Fig 5.69: Absorption coefficients of $Zn_{1-x}Cu_xO$ films at 20K.
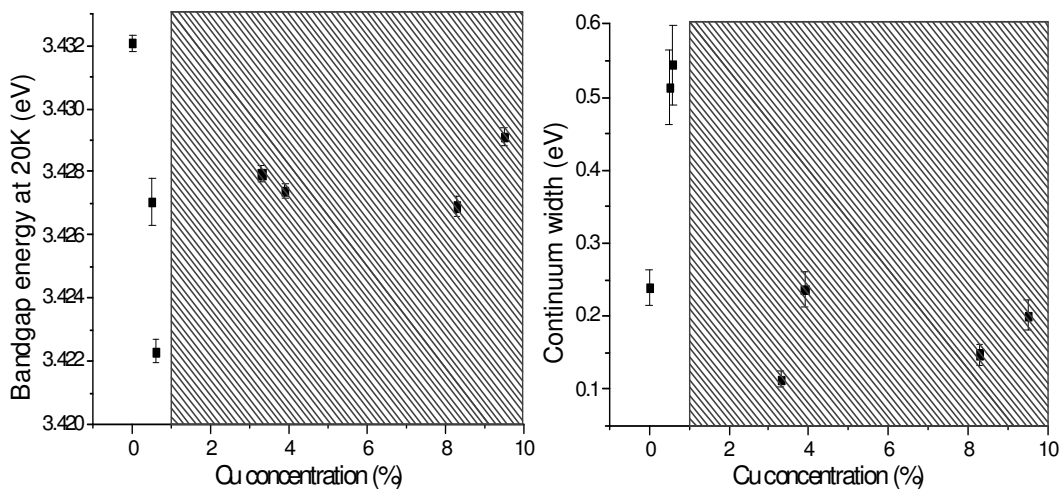
Fig 5.70a: Continuum parameters of $Zn_{1-x}Cu_xO$ films.
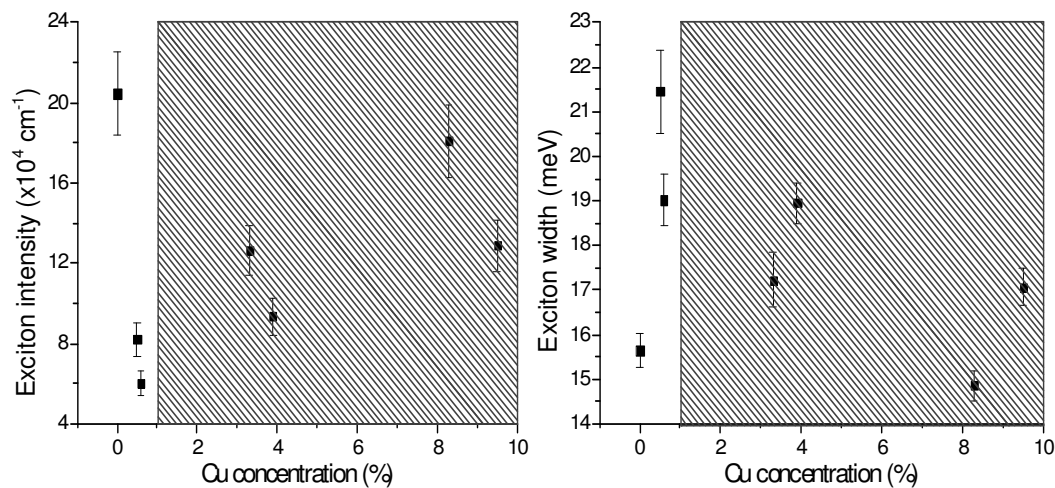
Fig 5.70b: Excitonic parameters of $Zn_{1-x}Cu_xO$ films.
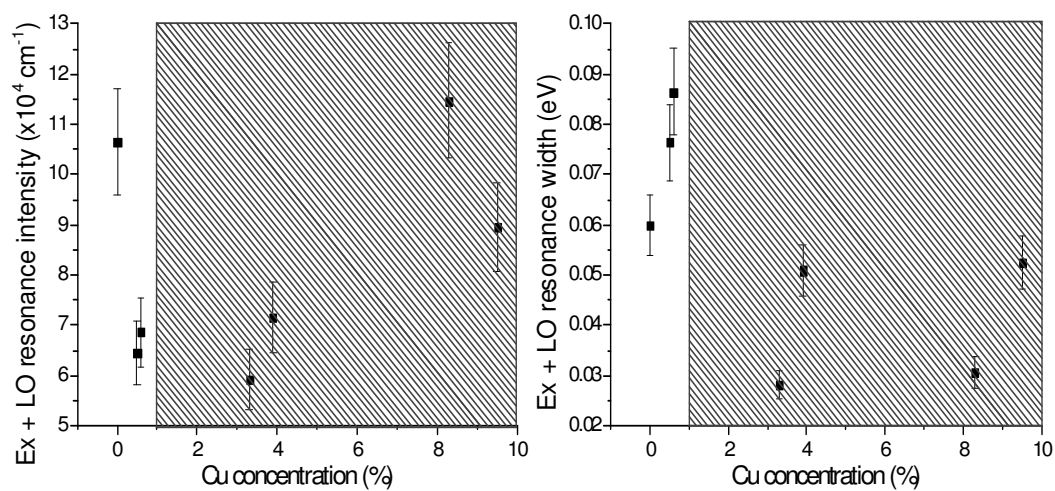
Fig 5.70c: Exciton + LO phonon resonance parameters of $Zn_{1-x}Cu_xO$ films.

On inspection of figs 5.70a-c, it appears than the points on the graphs follow a particular trend up to a concentration of about 1% and then follow the reverse trend at higher concentrations, corresponding to the hatched regions. The reason why the graphs have this form may be explained by referring to the structural characterisation in section 5.2. Up to a concentration of about 1%, it has been shown that the Cu ions mainly occupy the Zn substitutional position. However, as the Cu concentration increases and the average distance between Cu ions decreases, it becomes energetically favourable for them to diffuse so that they can form the more stable Cu_2O secondary phase. Initially there is a mixture of ZnO, $Zn_{1-x}Cu_xO$ and Cu_2O phases but the $Zn_{1-x}Cu_xO$ phase gradually disappears as Cu concentration rises and diffusion becomes increasingly likely. Therefore, as long as Cu_2O does not alter the optical properties of the films, the behaviour in the high concentration limit will be like that of pure ZnO. In light of this, it is only meaningful to study the effects of increasing the Cu concentration in the DMS up to the limiting concentration of around 1% (0.9 ± 0.1 %). Fig 5.70a (left) shows that the bandgap energy of $Zn_{1-x}Cu_xO$ decreases by 9.8 ± 0.5 meV between Cu concentration of 0 and 1%. This is in agreement with the UPS results in section 5.3.1 which predicted a decrease in optical gap energy due to the reversal of the direction of the p-d repulsion. As the film containing 1% Cu was not measured by UPS it is not possible to compare data quantitatively. Despite the change in direction of the bandgap energy trend, the remaining trends follow the same patterns as the previously mentioned DMSs because disorder still increases with concentration (up to the diffusion limit). Therefore, the continuum width in fig 5.70a (right) increases by 0.37 ± 0.06 eV between Cu concentrations of 0 and 1%. In a similar way, in fig 5.70b, the exciton intensity decreases by 14 ± 2 $\times 10^4 cm^{-1}$ and the width increases by 5.8 ± 0.9 meV. Likewise, in fig 5.70c, the exciton + LO phonon resonances decrease in intensity by 5 ± 1 $\times 10^4 cm^{-1}$ and increase in width by 41 ± 9 meV. We note that these values are comparable to those obtained in the Mn and Fe DMSs.

5.4.1.4 Zn$_{1-x}$Ni$_x$O

Finally, in the case of Zn$_{1-x}$Ni$_x$O, the absorption coefficients at room temperature and 20K are shown in figs 5.71 and 5.72, respectively. The general trends are the same as in Zn$_{1-x}$Cu$_x$O, however the changes are so small that only the bandgap energy, shown in fig 5.73, provides significant results. All the other parameters remain approximately constant, taking values which, within errors, are the same as those of pure ZnO mentioned at the start of this section.
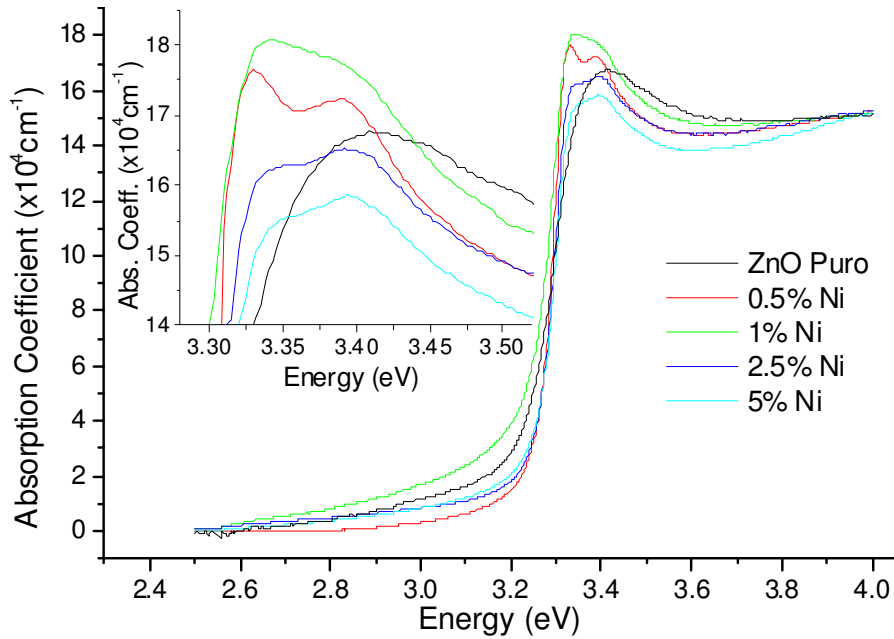
Fig 5.71: Absorption coefficients of Zn$_{1-x}$Ni$_x$O films at room temperature.
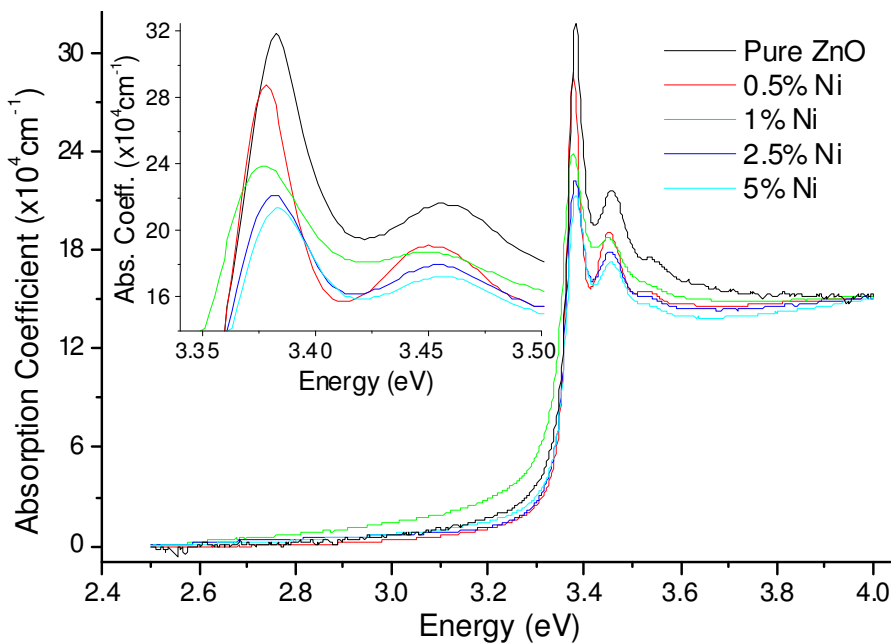
Fig 5.72: Absorption coefficients of Zn$_{1-x}$Ni$_x$O films at 20K.
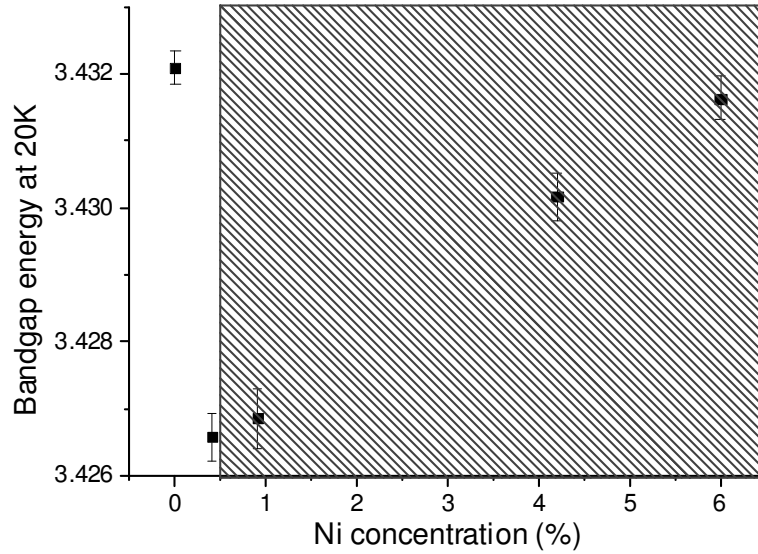
Fig 5.73: Continuum parameters of Zn$_{1-x}$Ni$_x$O films.

The form of fig 5.73 is similar to that of Zn$_{1-x}$Cu$_x$O in fig 5.70a (left), except that the diffusion limit occurs at the lower concentration of 0.60 ± 0.08 %. This is because the secondary phase NiO is more stable than Cu$_2$O, so Ni ions do not have to be as close together for diffusion to become energetically favourable, as mentioned in the electron microscopy results (section 5.2.4). The decrease in energy gap within this interval is 5.5 ± 0.4 meV, corresponding to a decrease per percent similar to that observed in the Cu DMS. Again, as Zn$_{1-x}$Ni$_x$O films were not measured by UPS it is not possible to compare data from the different methods.

Samuel John Gilliland

5.4.2 Low temperature effects

5.4.2.1 $Zn_{1-x}Mn_xO$

As in the previous section, the optical transmission data in the range 20-300 K was converted to absorption coefficients using (3.47). The same model, based on the Elliot-Toyozawa equation (3.63), was then applied to determine the evolution of the optical properties of the films in function of temperature. An important optical property is the bandgap energy, which is shown for pure ZnO in fig 5.74. In semiconductors there are two principal mechanisms that influence the temperature dependence of the bandgap energy: the electron-phonon interaction, explained in theory section 3.3.4, and the effect of disorder. In the case of the pure ZnO film, the disorder is very low, since the second exciton + LO phonon resonance can be clearly seen in the low temperature absorption spectrum shown in fig 5.58. Therefore, it is safe to assume that the electron-phonon interaction will be the dominant mechanism. The results show a clear decrease with increasing temperature, as predicted by the theory, and on fitting the data to the Bose-Einstein model (3.71) a good agreement is obtained, shown by the line on fig 5.74. The model provides a value for the energy of the phonon involved in the interaction, which, in this case, is 32 ± 4 meV.
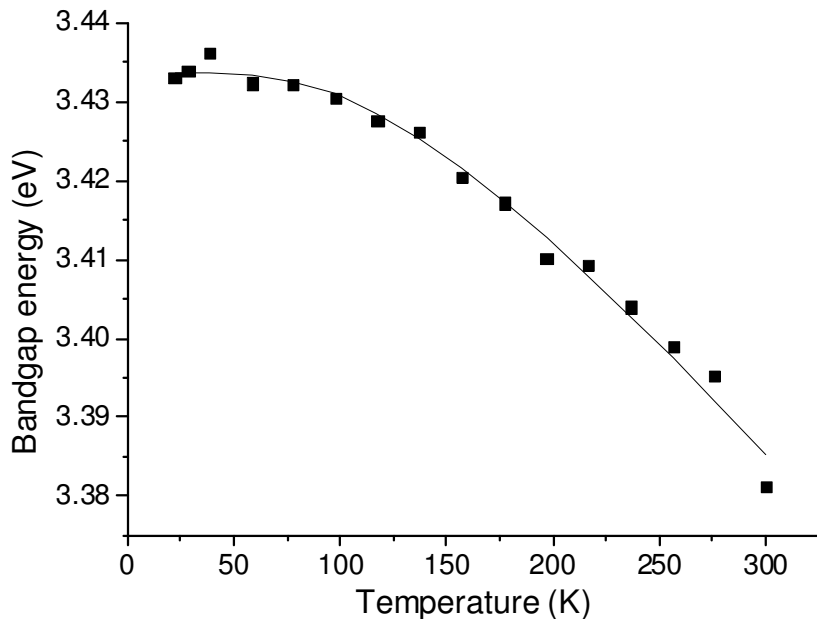
Fig 5.74: Temperature dependence of bandgap energy in pure ZnO.

146
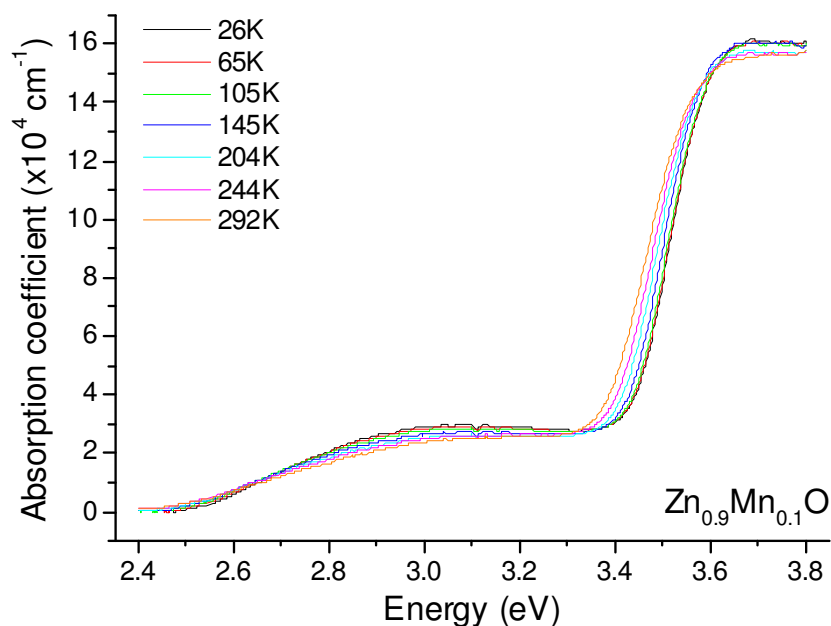
Fig 5.75: Absorption coefficient of $Zn_{0.9}Mn_{0.1}O$ in function of temperature.

Fig 5.75 shows the temperature variation in the absorption coefficient of the $Zn_{0.9}Mn_{0.1}O$ film in the range 26 - 292K. As in the case of concentration, there are also three main effects that may be observed as the temperature is increased. Firstly, the absorption front shifts towards lower energies. Secondly the excitonic peak, where visible, decreases in intensity and broadens. Thirdly the pre-edge band, which has been identified as a charge transfer transition (CTT), decreases in intensity. To quantify these effects, the fitting used for $Zn_{1-x}Mn_xO$ in the previous section was applied, with the additional Gaussian profile to model the intensity, energy and width of the CTT. The results of the fitting are shown in figs 5.76-5.79.
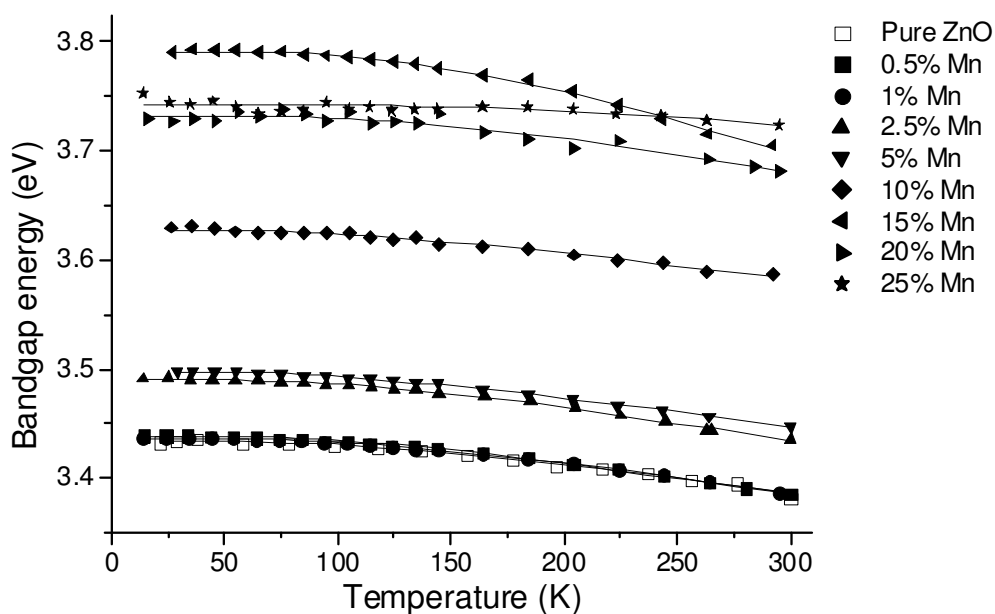
Fig 5.76: Temperature dependence of bandgap energy in $Zn_{1-x}Mn_xO$ films.

Samuel John Gilliland

Fig 5.76 shows the variation of bandgap energy in function of temperature for all the $Zn_{1-x}Mn_xO$ films. The vertical ordering of the curves reflects the increase in bandgap with Mn concentration discussed in the previous section. As mentioned earlier, there are two principal contributions that need to be taken into account: the electron-phonon interaction and the effect of disorder. With respect to the electron-phonon interaction, Gleize et al. [48] used Raman scattering to measure the energy of vibrational modes in $Zn_{1-x}Mn_xO$ thin films containing up to 22% Mn. They found that the E_2^L and E_2^H phonons showed a decrease in energy of less than 1 eV on increasing the Mn concentration over the full range. This is due to the weakening of the bond strength, which is probably a consequence of the contribution of the Mn 3d electrons to the bonds. We note that this more than compensates for the effect of the reduction in cation mass, which would be expected to increase the phonon energy. Besides this small effect observed in two phonons, the other phonon energies hardly varied. Therefore, it may be supposed that the effect of the electron-phonon interaction does not change significantly on increasing the Mn concentration. The same cannot be said for the static disorder introduced by forming an alloy, which increases notably with the proportion of Mn, so a deviation from the theory based purely on the electron-phonon interaction would be expected on increasing the Mn concentration.

This argument is supported by the experimental results, which allow the Bose-Einstein model (3.71) to be applied up to a concentration of 10% Mn without finding any appreciable variation in the phonon energy, obtaining an average value of 30±2 meV, within errors of the value found in pure ZnO. However, above this concentration, the phonon energies obtained from the model deviate from the predicted constant value. Therefore, it is not possible to use a general argument based on the phonon frequency to explain the temperature dependence of the gap on increasing the Mn concentration. Static disorder causes localised potentials to be introduced into the material which cause the scattering of electrons and holes and a decrease in the bandgap energy. This contribution increases with Mn concentration and is more effective at low temperature because localised potentials have an increased probability of scattering electrons or holes with low kinetic energies. This produces a partial compensation for the electron-phonon interaction, which also causes a decrease in the bandgap energy but at higher temperatures. This may be observed in fig 5.76 as the flattening of the energy variation that occurs at high concentrations, particularly in the film containing 25% Mn, which is almost horizontal.
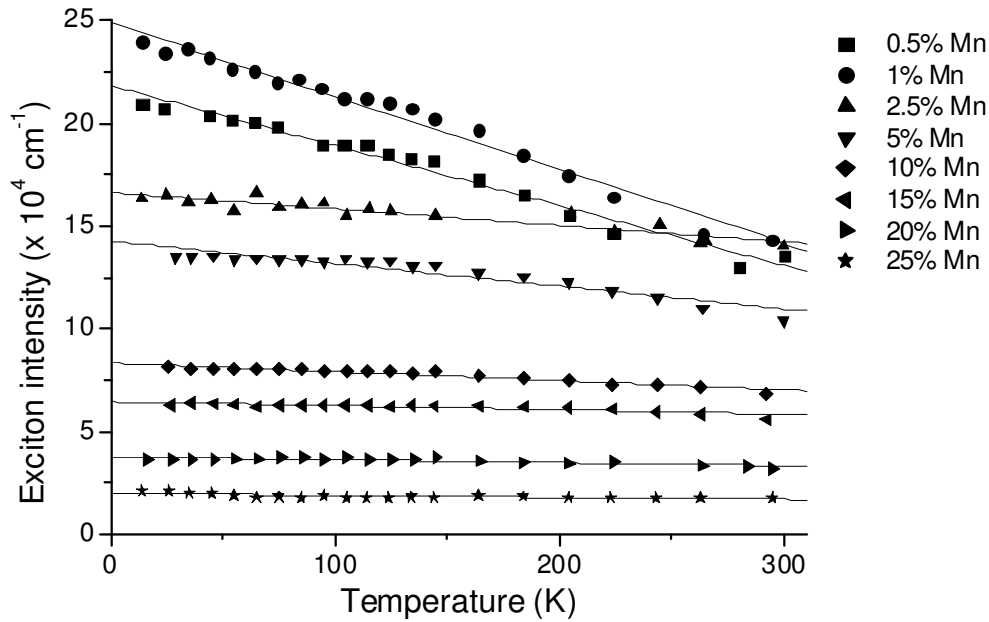
Fig 5.77: Temperature dependence of exciton intensity in $Zn_{1-x}Mn_xO$ films.

The temperature dependence of other factors shall now be considered, starting with the continuum width. Apart from at the lowest concentrations, this remains approximately constant with temperature, following the tendency shown in fig 5.62a (right). At the lowest concentrations there is a slight increase detected, for example, Γ_C in the sample containing 0.5% Mn increases by 30 ± 5 meV over the temperature range. This behaviour is similar to that of the exciton width, which occurs for the reasons which shall be described shortly. A related effect is reflected in the exciton peak intensity shown in fig 5.77. Excitons may be disassociated by phonons or defects but although the phonon density, which increases with temperature, does not vary much between films, the density of defects, which disassociate excitons more effective at low temperatures, increases with Mn concentration. Therefore, in the most dilute DMSs, disassociation by phonons is the dominant mechanism and the exciton intensity is seen to decrease with temperature, as the phonon density increases. However, at high Mn concentrations, this effect occurs in addition to the low temperature disassociation by defects, causing the variation to become more horizontal. The gradients of the linear fittings shown in the figure vary from $-310 \pm 20 \times 10^4 cm^{-1}K^{-1}$ at 0.5% Mn to $-9 \pm 3 \times 10^4 cm^{-1}K^{-1}$ at 25%.
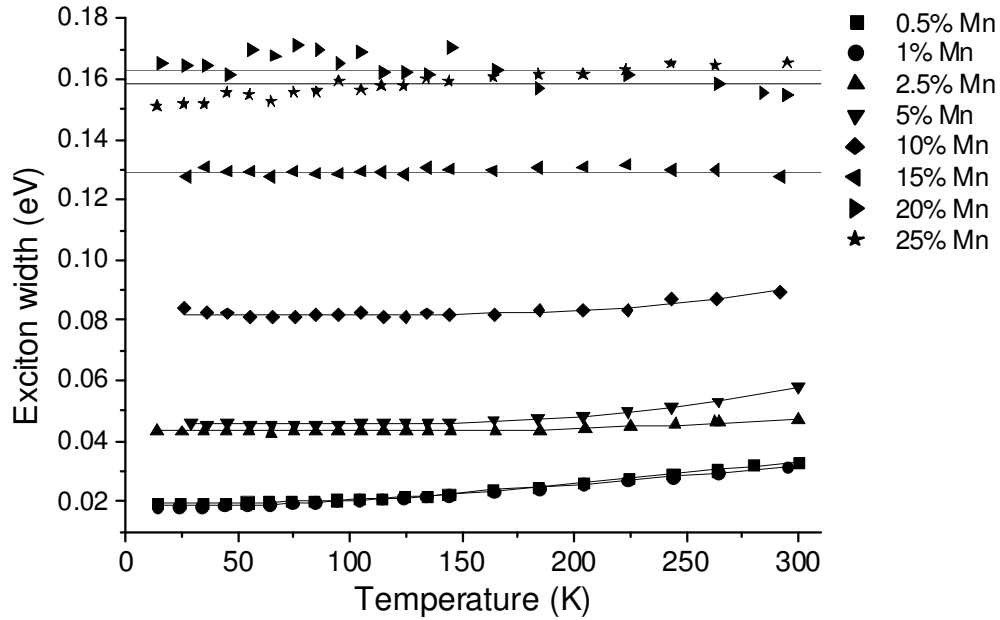
Fig 5.78: Temperature dependence of exciton width in $Zn_{1-x}Mn_xO$ films.

The exciton width variation in function of temperature is shown in fig 5.78. As in the case of the continuum width, the clearest effects are observed at low Mn concentration, were there is a significant temperature broadening. At higher concentration, the width remains practically constant. As with the previous optical properties, the reason for this behaviour can be qualitatively understood taking into account the combined effects of the electron-phonon interaction and static disorder. At low Mn concentrations, the dominant mechanism is the electron-phonon interaction, which causes phonon broadening of the exciton that increases with increasing phonon density and, hence, temperature. Equation (3.72) in theory section 3.3.4 shows how the Bose-Einstein model may be applied to the temperature dependence of the exciton width to obtain a value for the energy of the phonon responsible for the broadening. Both the phonons related to the change in bandgap energy and those that affect the exciton width interact with the hole in the valence band and the electron in the conduction band, although with different effects according to the parameter that they are influencing. On applying (3.72), a phonon energy of 29 ± 5 meV is obtained for the film containing 0.5% Mn, which is similar to that of the phonon involved in the change in bandgap energy, suggesting that both effects may be controlled by the same phonon. At higher Mn concentrations the effect of static disorder, which causes further exciton broadening, is also considerable. However, since it is more effective at low temperatures, the overall effect is to compensate for the electron-phonon interaction, causing the width to become more constant. This is clearly seen in the films in fig 5.78 with the highest Mn concentrations.

It was not possible to detect the peaks corresponding to the exciton + LO phonon resonances in the full temperature range except for at the lowest Mn concentrations (up to 5%). In these cases, the intensity and width were found to behave in the same general manner as those of the main excitonic peak. For example, at 0.5% Mn, the exciton + LO phonon resonance intensity decreased by $112 \pm 8 \times 10^4 cm^{-1}K^{-1}$ and the width increased by 14 ± 2 μeVK^{-1} over the full temperature range.
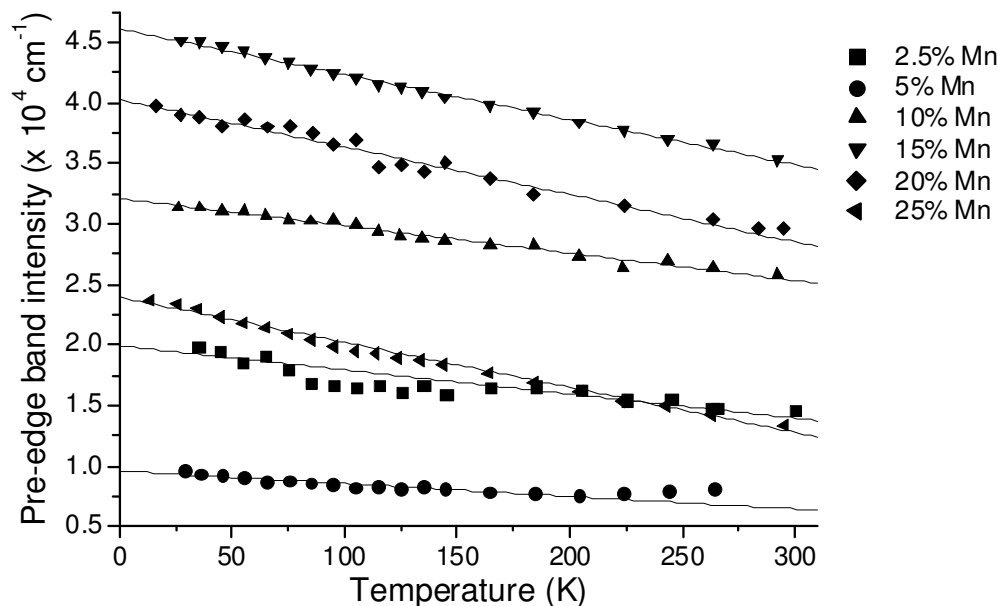
Fig 5.79: Temperature dependence of pre-edge band intensity in $Zn_{1-x}Mn_xO$ films.

Finally, the temperature variation of the pre-edge band shall be discussed. In fig 5.79, the intensity of the band is shown in function of temperature. As the temperature increases, there is a clear decrease in intensity at all concentrations. Moreover, the decrease is approximately linear, although the gradient increases with concentration. At 5% Mn, the decrease is 11 ± 3 cm^{-1}K^{-1}, whereas at 25% it grows to 37 ± 6 cm^{-1}K^{-1}. The exact mechanisms behind this behaviour are, at this stage, unclear but it could simply be an effect of statistical occupation. The previous assignment of this absorption band to a CTT from Mn 3d to the conduction band would imply that increasing the temperature should cause a decrease in the energy of its maximum as the conduction band redshifts. This appears to be the case, especially in the film containing 2.5% Mn, where the pre-edge band is particularly well defined. In this case a decrease of 61 ± 9 meV is observed, which is close to the bandgap energy shift of 55 ± 1 meV found in the same temperature range. The fact that the bandgap becomes more insensitive to temperature as the Mn concentration increases also seems to be consistent with the observed behaviour of the energy of the pre-band edge maximum. The width of the pre-edge band appears not to change with temperature, maintaining the low temperature values reported in section 5.4.1. This suggests that the electron-phonon interaction does not strongly influence the CTT.

5.4.2.2 $Zn_{1-x}Fe_xO$
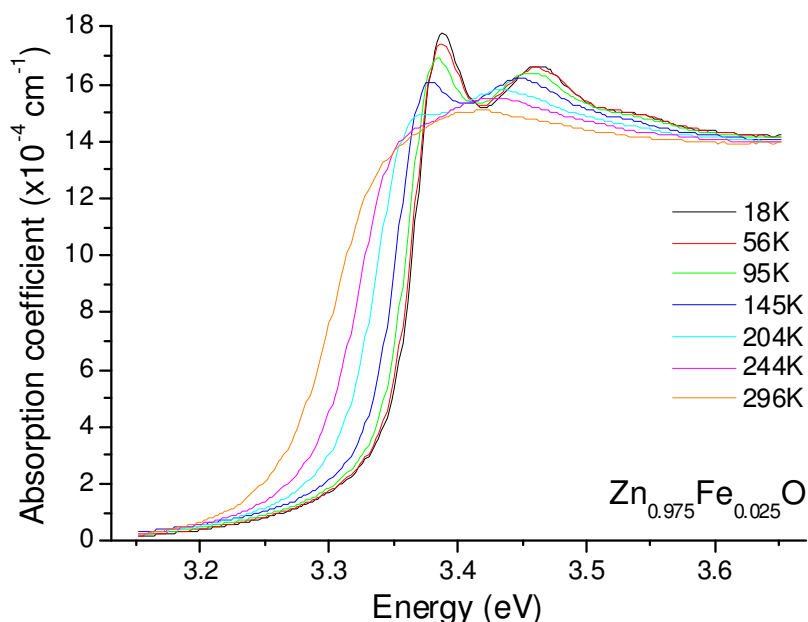
Fig 5.80: Absorption coefficient of $Zn_{0.975}Fe_{0.025}O$ in function of temperature.

In the case of $Zn_{1-x}Fe_xO$, the temperature evolution of the absorption coefficient for the $Zn_{0.975}Fe_{0.025}O$ film is shown in fig 5.80. The absorption curves were fitted in the same way as before to determine the optical properties of all the films. The bandgap energy in function of temperature is shown in fig 5.81. The behaviour appears similar to that of pure ZnO and the most dilute Mn DMSs, suggesting the electron-phonon interaction is the dominant mechanism. This was confirmed by fitting the experimental data to the Bose-Einstein model, where the phonon energy was not found to deviate from a constant value of 33 ± 2 meV, in contrast to the results from high concentration $Zn_{1-x}Mn_xO$ films. This is probably because the concentration range (limited by the solubility of Fe in the ZnO host) was not large enough for the effects caused by static disorder to become significant.

The other effects observed in the $Zn_{1-x}Fe_xO$ films were similar to those seen in low concentration $Zn_{1-x}Mn_xO$ films. The continuum was found to increase with temperature, especially at the lowest concentrations. For example, in the film containing 1% Fe, an increase of 34 ± 6 meV was measured over the range of temperatures. It was only possible to determine the intensity and width of the excitonic peak up to a Fe concentration of 5% but the exciton intensity was found to decrease with temperature in all cases, with a greater rate of decrease at lower concentrations. The rates of decrease varied from $280 \pm 10 \times 10^4 cm^{-1}K^{-1}$ at 1% Fe to $15 \pm 2 \times 10^4 cm^{-1}K^{-1}$ at 5%. The exciton width was found to increase in all cases, particularly at the lowest concentrations. On fitting the Bose-Einstein model for exciton width to the variation at the low Fe concentration of 1%, a phonon energy of 28 ± 2 meV was obtained. The exciton + LO phonon resonances could only be detected at Fe concentrations of 1% and 2.5%. At both these points, the intensity was found to decrease at a constant rate of $600 \pm 30 \times 10^4 cm^{-1}K^{-1}$ and the width increased at a constant rate of 36 ± 3 μeVK^{-1}.
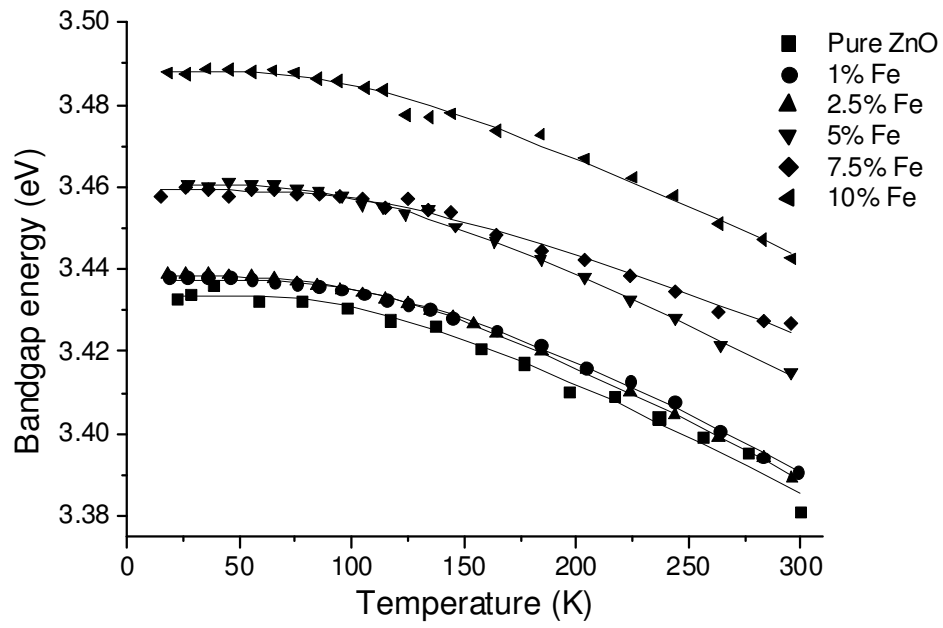
Fig 5.81: Temperature dependence of bandgap energy in Zn$_{1-x}$Fe$_x$O films.

5.4.2.3 Zn$_{1-x}$Cu$_x$O
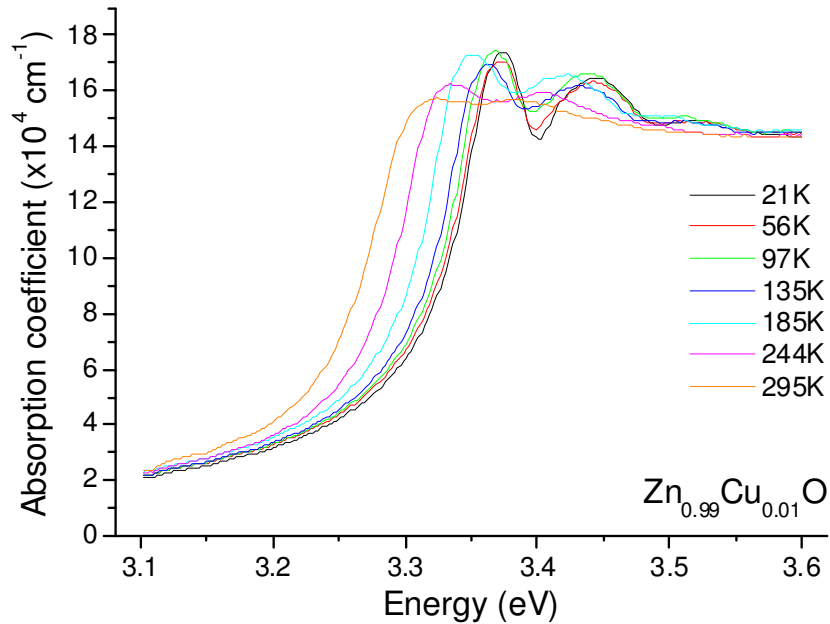
Fig 5.82: Absorption coefficient of Zn$_{0.99}$Cu$_{0.01}$O in function of temperature.

The temperature dependence of the optical properties of Zn$_{1-x}$Cu$_x$O shall now be considered, starting with the absorption coefficient of the Zn$_{0.99}$Cu$_{0.01}$O film shown in fig 5.82. This concentration is close to the maximum solubility of Cu in the ZnO host, beyond which the films begin to return to pure ZnO behaviour. The fitting was applied to the absorption data from the films containing 0.5% and 1% Cu and the resulting temperature variation of the bandgap energy is shown in fig 5.83. Despite the low Cu concentrations, fitting with the Bose-Einstein model was unsuccessful as the phonon frequencies obtained deviated from the expected constant values found in the other low concentration DMSs. This is probably due to experimental or analytical errors, since there is little physical basis to suggest that Cu would produce more static disorder than the other dilute cations.

With regards to the other optical properties, both of the films show the expected increase in continuum width with temperature. For example, there is an increase of 16 ± 4 eV in the film containing 1% Cu over the temperature range. The exciton intensity also decreases in both cases, with a rate of 106 ± 4 ×10^{4}cm^{-1}K^{-1} at a Cu concentration of 1%. The exciton width shows its characteristic behaviour at low cation concentrations, increasing by 24.0 ± 1.2 meV in the 1% Cu film. The exciton + LO phonon resonances decrease in intensity and increase in width in both cases. In the film containing 1% Cu the rate of decrease of intensity is 50 ± 4 ×10^{4}cm^{-1}K^{-1} and the rate of increase of width is 84 ± 4 μeVK^{-1}.
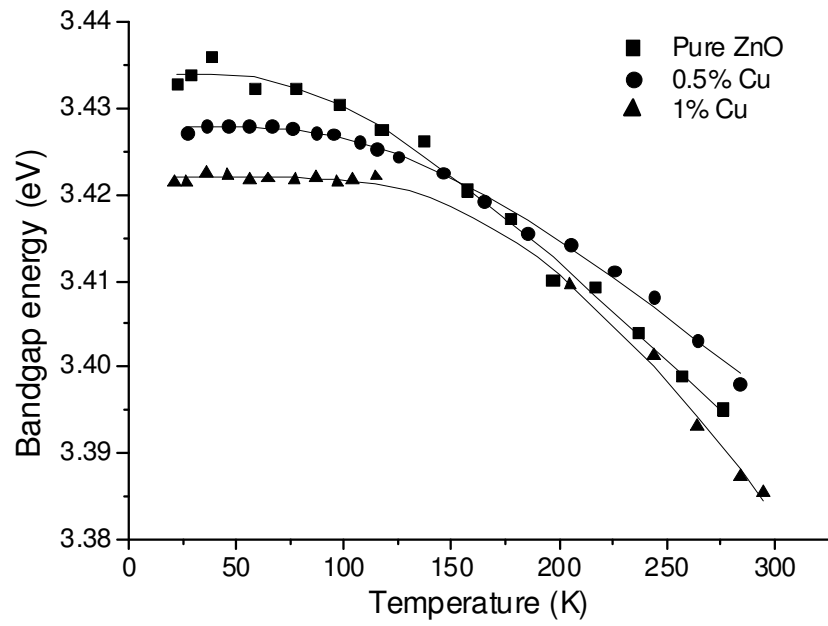
Fig 5.83: Temperature dependence of bandgap energy in Zn$_{1-x}$Cu$_x$O films.

5.4.2.4 $Zn_{1-x}Ni_xO$
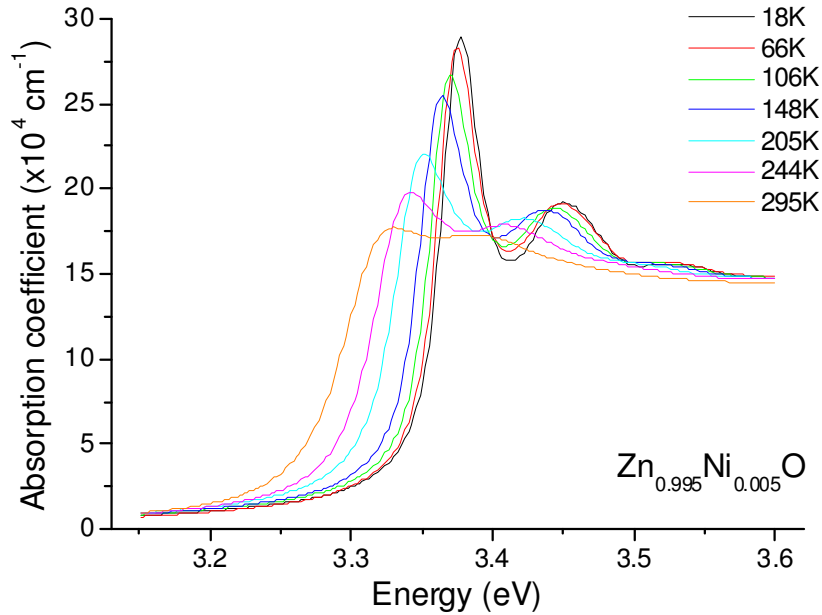
Fig 5.84: Absorption coefficient of $Zn_{0.995}Ni_{0.005}O$ in function of temperature.

Finally, in the case of $Zn_{1-x}Ni_xO$, the temperature evolution of the absorption coefficient of the $Zn_{0.995}Ni_{0.005}O$ film is shown in fig 5.84. This concentration is close to the maximum solubility of Ni in ZnO, as determined by the structural characterisation. On applying the fitting, the bandgap energy in function of temperature is shown in fig 5.85. Despite the slight change in bandgap energy on going from pure ZnO to a Ni concentration of 0.5%, the Bose-Einstein model reveals no significant change in phonon frequency, obtaining a value of 31 ± 1 meV. This shows that the electron-phonon interaction is the dominant mechanism, as expected at small dilute cation concentrations. The continuum width in $Zn_{0.995}Ni_{0.005}O$, which would be expected to increase slightly, remains approximately constant at 183 ± 3 meV but the rest of the optical properties in this film behave as predicted on increasing the temperature. The exciton intensity decreases at a rate of $430 \pm 20 \times 10^4 cm^{-1}K^{-1}$ and its width increases by 14.9 ± 0.6 meV. The exciton + LO phonon resonances decrease in intensity at a rate of $100 \pm 10 \times 10^4 cm^{-1}K^{-1}$ and increase in width at a rate of 39 ± 5 μeVK^{-1}.
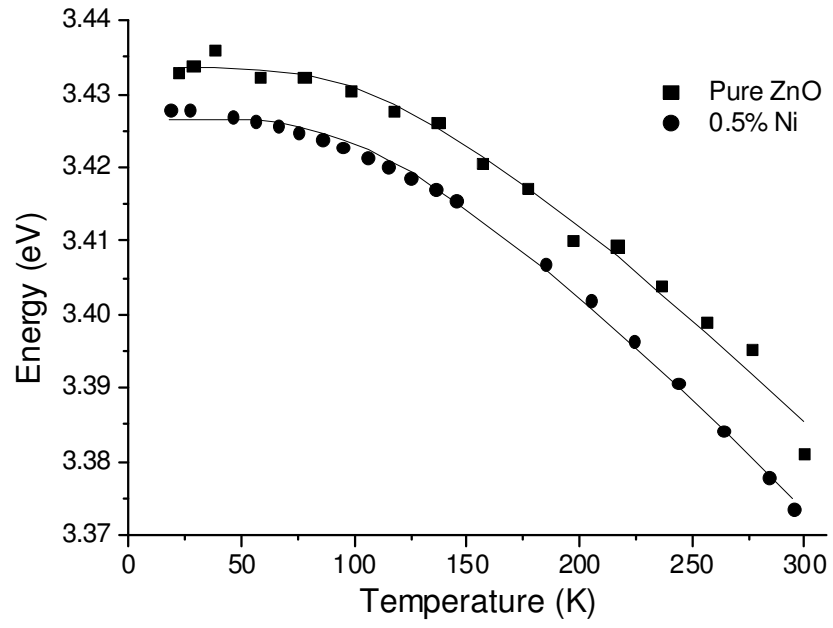
Fig 5.85: Temperature dependence of bandgap energy in Zn$_{1-x}$Ni$_x$O films.

5.4.3 High pressure effects

5.4.3.1 Zn$_{1-x}$Mn$_x$O
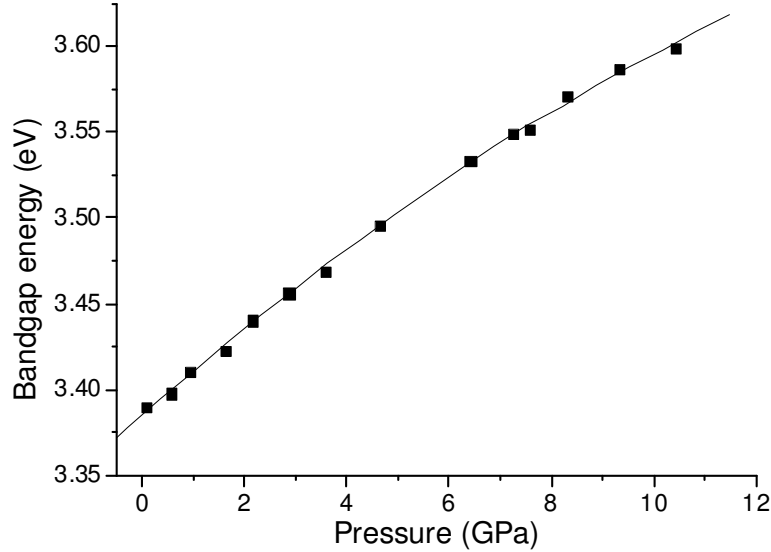
Fig 5.86: Pressure dependence of bandgap energy in pure ZnO.

As in previous sections, the optical transmission data taken in the pressure range 0-15 GPa was converted to absorption coefficients using (3.47) and the Elliot-Toyozawa model (3.63) was applied to determine the evolution of the optical properties of the films in function of pressure. The bandgap energy of pure ZnO, shown in function of pressure in fig 5.86, clearly increases in agreement with the theory described in section 3.3.5 for a covalently bonded semiconductor. When choosing a suitable model to fit this dependence, publications often treat the bandgap as being linear with P or lnV. Equations (3.75) and (3.88) imply that neither of these models are completely correct because the bulk modulus increases with decreasing volume. For this reason, it is preferable to use a quadratic fitting of the form:

$$E_g(P) = E_g(0) + \alpha P + \beta P^2 \quad (5.3)$$

This model can be used up to moderately high pressures without deviating significantly from the experimental points, as seen in the figure. In this case the values of α and β are 24.4 ± 0.3 meVGPa^{-1} and -0.44 ± 0.05 meVGPa^{-1} respectively. These values are comparable to those reported by Mang et al. of α = 25.3 ± 0.1 meVGPa^{-1} and β = -0.28 ± 0.01 meVGPa^{-1} [49]. If a simple linear fitting is done, a pressure coefficient of 21.0 ± 0.4 meVGPa^{-1} is obtained, in agreement the theoretical value of Zhang et al. [50] mentioned in theory section 3.3.5.

Fig 5.87 shows the pressure variation of the absorption coefficient of the Zn$_{0.9}$Mn$_{0.1}$O film in the wurtzite phase. As the pressure increases there are several effects that may be observed. Firstly the direct absorption edge shifts to higher energies. The same is true for the CTT, which also becomes less intense and broadens slightly. Although the excitonic peak is not visible in this figure, it may be observed up to a Mn

concentration of 1%, where it is seen to intensify in function of pressure. As in the previous analysis, the model based on the Elliot-Toyozawa equation (3.63) was applied to quantify these effects and the results shall now be discussed.
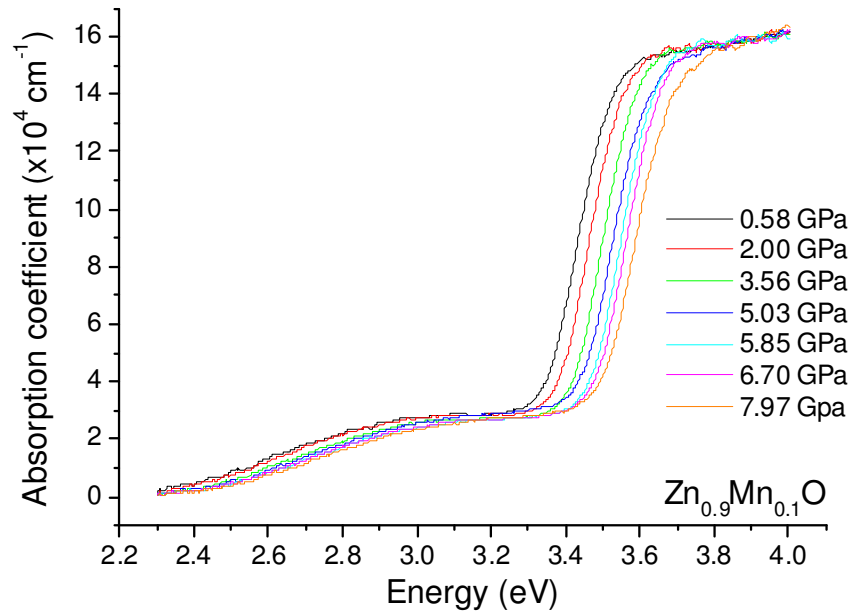
Fig 5.87: Absorption coefficient of wurtzite $Zn_{0.9}Mn_{0.1}O$ in function of pressure.
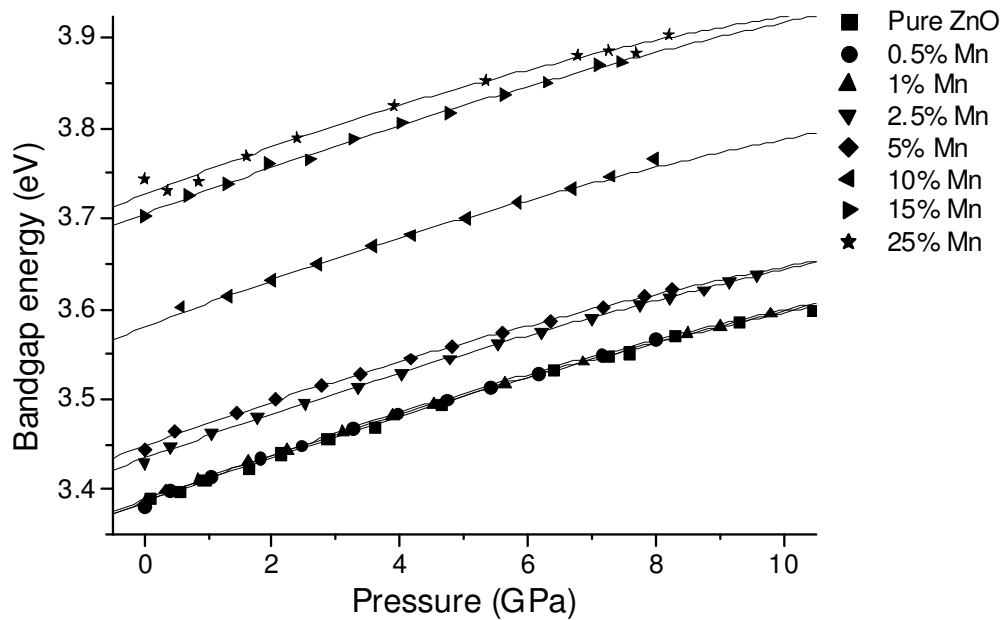
Fig 5.88: Pressure dependence of bandgap energy in $Zn_{1-x}Mn_xO$ films.

Fig 5.88 shows the bandgap energy in function of pressure. There is a clear increase at all concentrations, in agreement with theory. The experimental data was used to fit the parameters of (5.3) but it was found that there was no significant change in α or β as the concentration varied. The average values of these coefficients were $\alpha = 26.5 \pm 0.9$ meVGPa^{-1} and $\beta = -0.58 \pm 0.12$ meVGPa^{-1}. Therefore, it would only be possible to test the theory discussed in section 3.3.5 if the experimental errors could be reduced. If a

simple linear fitting is done to the experimental data, a constant pressure coefficient of 21.4 ± 0.7 meVGPa^{-1} is obtained, which is within the error limits of the value obtained for pure ZnO. With regards to the continuum width, it was found that pressure did not cause the values at each Mn concentration to vary significantly from those given at ambient pressure.
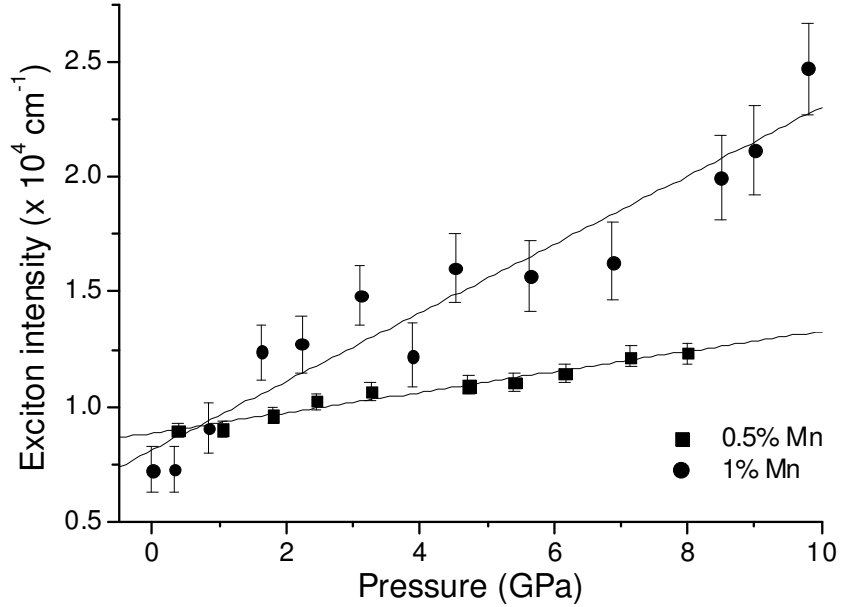
Fig 5.89: Pressure dependence of exciton intensity in $Zn_{1-x}Mn_xO$ films.

Preparing samples to be charged in the DAC involves separating them from the mica substrate, which introduces more defects in the samples. As measurements were taken at room temperature, the excitonic peak could only be detected up to a Mn concentration of 1%, whereas the exciton + LO phonon resonances could not be detected at all. The pressure dependence of the exciton peak intensity is shown in fig 5.89. In both cases an increase is observed with increasing pressure, although the rates vary considerably between 440 ± 30 cm^{-1}%GPa^{-1} at 0.5% Mn and 1500 ± 100 cm^{-1}GPa^{-1} at 1% Mn. This difference could just be due to different concentrations of defects in the two films so, to be able to draw any meaningful conclusions, it would be necessary to measure more samples. However, the general trend can be explained by following the reasoning of Le Toullec et al. [51] who show that the Elliot-Toyozawa equation may be used to obtain the following approximate expression for the integrated intensity of the first excitonic peak at constant temperature and defect concentration:

$$I_X = \Gamma_X \alpha_1 \approx \frac{4R\alpha_0}{\pi} \quad (5.4)$$

where α_1 is the absorption coefficient at the maximum of the excitonic peak, R is the exciton Rydberg energy and α_0 is the absorption coefficient above the gap where it becomes constant. As α_0 does not vary significantly with pressure, the increase in exciton intensity must be due to an increase in the Rydberg energy. This stands to reason because, as the bandgap energy increases, so do the electron and hole effective masses. This increases the exciton effective mass, which has been shown to be directly proportional to the Rydberg energy in (3.60). The increase in Rydberg energy also

implies a longer lifetime, so one would expect the exciton width to decrease. Although this effect is not clearly observed in all the films, it is in reasonable agreement with the experimental data. For example, the exciton width in the film containing 0.5% Mn decreases by 41 ± 6 meVGPa^{-1} in the pressure range up to the rocksalt phase transition.
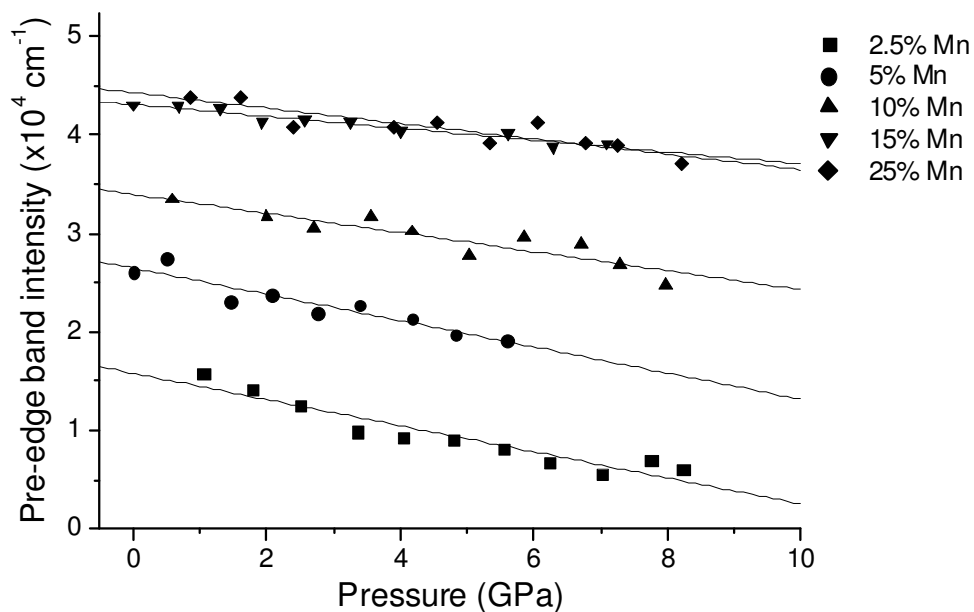
Fig 5.90: Pressure dependence of CTT intensity in $Zn_{1-x}Mn_xO$ films.
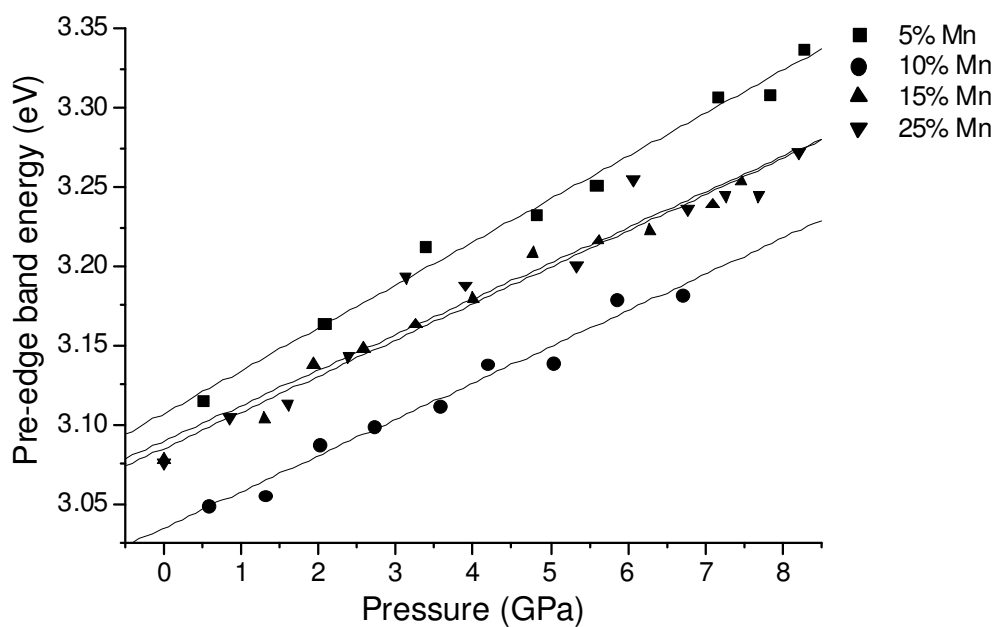
Fig 5.91: Pressure dependence of CTT energy in $Zn_{1-x}Mn_xO$ films.
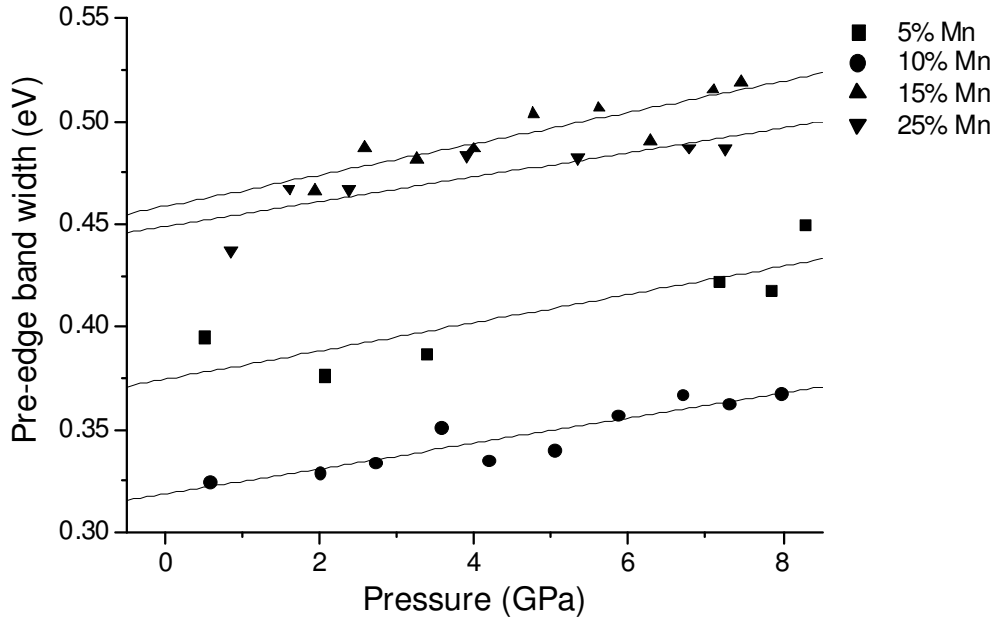
Fig 5.92: Pressure dependence of CTT width in $Zn_{1-x}Mn_xO$ films.

The effect of pressure on the CTT is shown in figs 5.90-5.92. On increasing the pressure, three main trends are observed. Firstly, in fig 5.90, the intensity decreases at an approximately constant rate of 1000 ± 300 cm^{-1}GPa^{-1}. Secondly, in fig 5.91, the energy increases at an average rate of 24 ± 2 meVGPa^{-1}, significantly larger than that of the bandgap. Thirdly, in fig 5.92, the width increases by 6.7 ± 0.8 meVGPa^{-1}. All these effects appear to be independent of the Mn concentration. To understand their physical origin, the notation in fig. 5.63 shall be used. It has been mentioned in the theory section 3.3.5 that high pressure usually produces an energy increase at both the CBM and VBM. However, the CBM energy increases at a greater rate than the VBM so the resulting band to band (B-B) pressure coefficient is positive. That is:

$$\frac{dE}{dP}(B-B) > 0 \qquad (5.5)$$

Although no publications appear to exist on the pressure dependence of the energies of the Mn d-d* transitions, a similar investigation into $Zn_{1-x}Co_xO$ showed the Co d-d* transition energies to be practically insensitive to pressure [52]. As there is no reason to suggest that the Mn d-d* transitions should behave differently, it is safe to assume that:

$$\frac{dE}{dP}(d-d*) \approx 0 \qquad (5.6)$$

Therefore, if the VBM is increasing in energy and the Mn 3d levels are remaining at the same energy, the CT transition from Mn d levels to the conduction band (d-CB) must have a greater pressure coefficient than the band to band transition, in agreement with the experimental results:

$$\frac{dE}{dP}(d-CB) > \frac{dE}{dP}(B-B) \qquad (5.7)$$

Note that the results are incompatible with the other CT transition from the valence band to the Mn d* levels (VB-d*) because, through a similar reasoning, this would have a pressure coefficient less than that of the band to band transition:

$$\frac{dE}{dP}(VB - d^*) < \frac{dE}{dP}(B - B) \quad (5.8)$$

This confirms that the nature of the CT transition responsible for the pre-edge band is of the d-CB type. This result not only explains the change in CTT energy at high pressure but also its intensity and width. As the pressure increases, there is an increasing overlap between the CTT and the absorption of the exciton and direct bandgap. The resulting resonance causes a gradual decrease in the measured intensity of the CTT. As for the width, it was mentioned earlier that the CTT could also contain a component from Mn d-d* internal transitions. As the energies of these transitions do not change under pressure but the CT transition energies do, the result would be a broadening of the band, in agreement with results. Therefore, it is likely that these internal transitions do form part of the CTT.
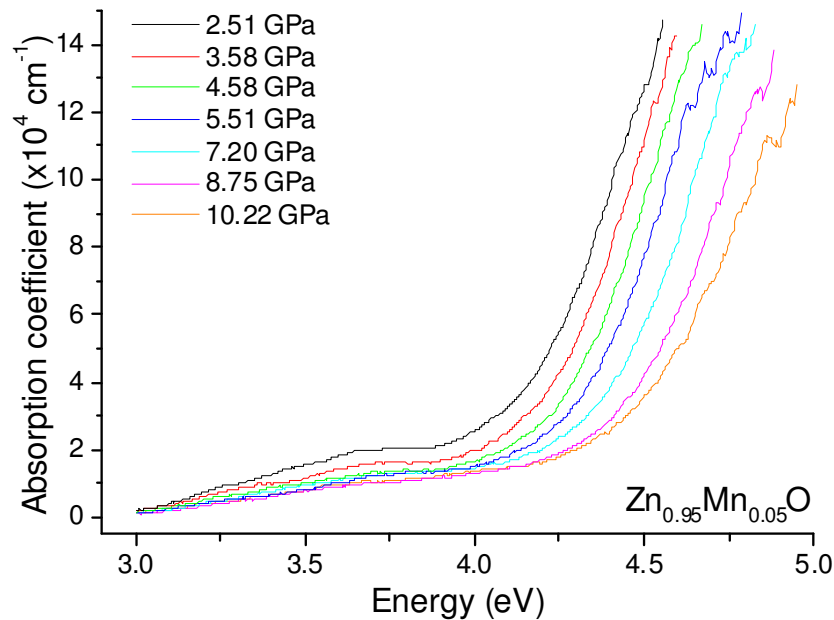
Fig 5.93: Absorption coefficient of rock salt Zn$_{0.95}$Mn$_{0.05}$O in function of pressure.

On reaching the pressure of the phase transition to the rocksalt structure, the absorption edges of ZnO and its DMSs change form. Fig 5.93 shows the absorption coefficient of rocksalt Zn$_{0.95}$Mn$_{0.05}$O at different pressures. The strong absorption seen at high energies is the tail of the direct transition at Γ that occurs at a higher energy than in the wurtzite phase. However, this is not the fundamental transition, as there is an indirect gap between L and Γ at around 2.45 eV, mentioned in the introduction. As thin films were used, the absorption was too weak to measure the energy of this gap or determine its pressure coefficients. At around 3.7 eV a knee is sometimes seen in the absorption coefficient, as in the case of fig 5.93. This is due to an incomplete transition from the wurtzite to rocksalt phase, which could have been eliminated by increasing the maximum pressure in the experiment. As pressure decreases, the tail of the direct

transition shifts towards lower energies. It was not possible to determine the energy of the direct gap because not enough of the absorption edge was present to be able to use the Elliot-Toyozawa model. However, it was noted that the curves are approximately parallel at high absorption coefficients, so relative shifts of the direct edge at a constant absorption coefficient could be calculated to provide an estimate for the direct gap pressure coefficient. This was done at the absorption coefficients indicated next to the results in fig 5.94. All the relative shifts were approximately linear with pressure and, as in the case of the wurtzite phase, no significant change in pressure coefficient was observed on changing the Mn concentration. The average value of this coefficient was 40 ± 5 meVGPa^{-1}, which is within the error limits of the value of 35 ± 2 meVGPa^{-1} found in pure ZnO [46]. It is important to note that the order of the linear fittings and the points at which they cross the energy axis provide no additional information about the rocksalt phase bandgap, since these factors depend mainly on the thickness of the films. At Mn concentrations of 10% and beyond, the films were significantly thicker than those containing smaller concentrations. In these cases it was necessary to take the data points at lower absorption coefficients, which caused a reduction in their energies.
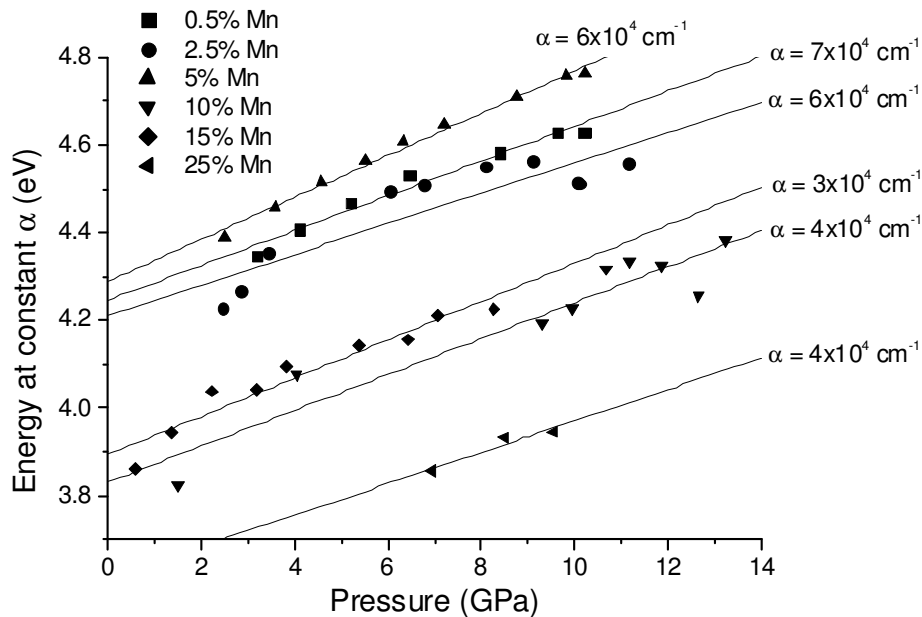
Fig 5.94: Pressure dependence of absorption edge shift in rock salt $Zn_{1-x}Mn_xO$ films.

The pressure at which the transition to the rocksalt phase occurs shall now be discussed. LDA calculations by Maouche et al. provide a theoretical transition pressure of 6.77 GPa in pure ZnO [53]. However, this result is significantly below the experimentally determined value of 9.7 GPa, reported by Sans et al. [45]. The phase transition pressures in $Zn_{1-x}Mn_xO$ are shown in function of Mn concentration in fig 5.95. Both the upstroke and downstroke show negative trends, which are approximately linear. The gradients of the lines for the upstroke and downstroke are -0.04 ± 0.02 and -0.13 ± 0.01 GPa%$_{Mn}$$^{-1}$ respectively. The reason for the negative trends is related to the "chemical pressure" effect. When Zn is substituted for a cation with a larger atomic radius it produces stress within the material, meaning that less stress needs to be applied externally to produce the upstroke phase transition. On the downstroke, the internal stress must be recovered so it is necessary to decrease the externally applied pressure further to produce the phase transition. The y-intercept of the upstroke line is 9.4 ± 0.4

GPa, in agreement with the experimental value for pure ZnO. In the downstroke line the value is 2.4 ± 0.2 GPa, hence the hysteresis is 7.0 ± 0.4 GPa. Hysteresis occurs because during phase transitions energy is required to overcome the potential barrier between the two different atomic configurations. Therefore, it is energetically favourable for ZnO and its DMSs to remain in the rocksalt structure until the pressure decrease avails enough potential energy to be able to produce the reverse transition. For Mn concentrations of above 19 ± 3 % this potential energy is not reached and metastable rocksalt films are recovered.

Fig 5.95: Phase transition pressure in $Zn_{1-x}Mn_xO$ films.

5.4.3.2 Zn$_{1-x}$Fe$_x$O

Fig 5.96: Absorption coefficient of wurtzite Zn$_{0.975}$Fe$_{0.025}$O in function of pressure.

Regarding the Fe DMS, the pressure variation of the absorption coefficient of the wurtzite Zn$_{0.975}$Fe$_{0.025}$O film is shown in fig 5.96. The general appearance is similar to that of Zn$_{1-x}$Mn$_x$O without the CTT. Experimental data was fitted to the Elliot-Toyozawa model and the results are shown in fig 5.97.

Fig 5.97: Pressure dependence of bandgap energy in Zn$_{1-x}$Fe$_x$O films.

Fig 5.97 shows the bandgap energy in function of pressure. As the effect of the dilute cation concentration on the bandgap is much smaller than in $Zn_{1-x}Mn_xO$, the points from the different films are much closer together. For this reason, the order of the data sets at 6 GPa has been added to the graph. The experimental data was fitted to (5.3) and, as in the case of $Zn_{1-x}Mn_xO$, α and β were approximately constant for all Fe concentrations. The average values were $\alpha = 25.5 \pm 0.8$ meVGPa^{-1} and $\beta = -0.50 \pm 0.06$ meVGPa^{-1}, within errors of those obtained for pure ZnO and the Mn DMS. The same is true if a simple linear fitting is performed and, in this case, an average pressure coefficient of 19.9 ± 1.4 meVGPa^{-1} is obtained. As for the other continuum parameter, the continuum width, it was found that pressure did not cause the values at each Fe concentration to vary significantly from those obtained at room pressure. The excitonic peak could be fitted up to a Fe concentration of 2.5%, although the exciton + LO phonon resonances were too weak to be fitted at any concentration. The pressure dependence of the exciton peak intensity gave mixed results, showing an increase of 450 ± 50 cm^{-1}%GPa^{-1} in the 2.5% Fe film, whereas the intensity remained constant in the 1% Fe film. This is probably due to a particularly high concentration of defects in the 1% Fe film. The exciton widths were also found to remain approximately constant in both films.

Fig 5.98: Absorption coefficient of rock salt Zn$_{0.975}$Fe$_{0.025}$O in function of pressure.

The pressure dependence of the absorption coefficient of rocksalt $Zn_{0.975}Fe_{0.025}O$ is shown in fig 5.98. The explanation of the form is the same as that given for $Zn_{1-x}Mn_xO$. As before, the relative shifts of the direct edge were found and the results are shown in fig 5.99 along with the absorption coefficients at which the data points were taken. Again, all the relative shifts were approximately linear with pressure and no significant change in pressure coefficient was observed on changing the Fe concentration. The average value of the coefficient was 30 ± 4 meVGPa^{-1}, which is also within the error limits of the value obtained for pure ZnO.

Fig 5.99: Pressure dependence of absorption edge shift in rock salt $Zn_{1-x}Fe_xO$ films.

Fig 5.100: Phase transition pressure in $Zn_{1-x}Fe_xO$ films.

The phase transition pressures are shown in fig 5.100 and linear fittings have been done. The y-intercepts of the lines are 9.8 ± 0.2 and 1.7 ± 0.3 GPa for the upstroke and downstroke respectively, in good agreement with previous results. Moreover, the gradient of the downstroke line is -0.13 ± 0.01 GPa%$_{Fe}^{-1}$, the same as in $Zn_{1-x}Mn_xO$. However, the hysteresis of 8.1 ± 0.4 GPa is slightly larger and the gradient of the upstroke line is positive, with a value of 0.36 ± 0.04 GPa%$_{Fe}^{-1}$. Although these effects could be due to substitutional Fe or its secondary phases, a simpler explanation would be the influence of the mica substrate. Although care was taken to remove the maximum quantity of substrate from the film while charging the cell, it was not possible to remove

all of it. Therefore, to produce the phase transitions, particularly in the case of the upstroke, additional pressure would need to be applied (or released on the downstroke) to provide the potential energy necessary to break the bonds in the mica, increasing the hysteresis. Due to technical reasons, the $Zn_{1-x}Fe_xO$ films measured at high pressure were considerably thinner than those of $Zn_{1-x}Mn_xO$. Therefore, the influence of the substrate would be stronger, providing an acceptable explanation for the differences.

5.4.3.3 Zn$_{1-x}$Cu$_x$O

Fig 5.101: Absorption coefficient of wurtzite Zn$_{0.99}$Cu$_{0.01}$O in function of pressure.

The pressure variation of the absorption coefficient of wurtzite Zn$_{0.99}$Cu$_{0.01}$O is shown in fig 5.101. Once again, the spectra show the expected shift to higher energies as pressure increases. They were fitted to the Elliot-Toyozawa model and the results shall now be discussed. Fig 5.102 shows the bandgap energy in function of pressure. Since only the film containing 1% Cu was within the DMS solubility range, only the results from this sample shall be discussed. However, results from the other films have also been shown in this and several other figures for comparison purposes. The experimental data for Zn$_{0.99}$Cu$_{0.01}$O was fitted to (5.3) and values of α = 24.4 ± 0.3 meVGPa^{-1} and β = -0.31 ± 0.03 meV were obtained. When a simple linear fitting was done and the resulting pressure coefficient was 21.2 ± 0.3 meVGPa^{-1}. These values agree with those obtained for pure ZnO so we conclude that forming a Cu DMS has no significant effect on the bandgap pressure coefficient within the achieved solubility range. The continuum width was also not found to vary significantly from its room pressure values. The excitonic properties could be determined in the Zn$_{0.99}$Cu$_{0.01}$O film but not the exciton + LO phonon resonances. The pressure dependence of the exciton peak intensity was in agreement with previous results showing a clear increase at a rate of 310 ± 30 GPa^{-1}. However, the exciton width was practically unaffected by pressure.

Fig 5.102: Pressure dependence of bandgap energy in $Zn_{1-x}Cu_xO$ films.

Fig 5.103: Absorption coefficient of rock salt $Zn_{0.99}Cu_{0.01}O$ in function of pressure.

Fig 5.103 shows the pressure dependence of the absorption coefficient of rocksalt $Zn_{0.99}Cu_{0.01}O$. Evidently, the maximum pressure was too low to produce a complete phase transition so there is still a relatively high proportion of the wurtzite phase, shown by the knee at around 3.5 eV. The relative shift of the direct edge was found at the indicated absorption coefficient and the results are shown in fig 5.104. As in the other DMSs, the relative shift observed in $Zn_{0.99}Cu_{0.01}O$ follows a linear trend and the pressure coefficient of 32 ± 3 meVGPa^{-1} is within error limits of the value obtained in pure ZnO.

Fig 5.104: Pressure dependence of absorption edge shift in rock salt $Zn_{1-x}Cu_xO$ films.

Fig 5.105: Phase transition pressure in $Zn_{1-x}Cu_xO$ films.

Finally, the phase transition pressures are shown in fig 5.105. The upstroke and downstroke pressures in the $Zn_{0.99}Cu_{0.01}$ film are 10.4 ± 0.6 and 2.0 ± 0.5 GPa respectively. These values are within errors of those obtained for pure ZnO because, with such a low dilute cation concentration, the affect produced by Cu is less than the experimental error introduced by the mica substrate. Therefore, none of the results obtained for the $Zn_{0.99}Cu_{0.01}O$ film at high pressure showed any significant deviation from the behaviour of pure ZnO. For this reason, high pressure measurements were not taken for the $Zn_{1-x}Ni_xO$ films because, with an even lower solubility limit (about 0.5%), it was almost certain that the same conclusion would be reached.

5.5 Magnetic properties

The results obtained from the magnetic characterisation described in the method (section 4.4) were firstly corrected in order to remove the background signal from the substrates, the plastic straw and the Kapton tape. Fig 5.106 shows the magnetic moment in function of temperature of two sapphire substrates and the plastic straw with Kapton tape. The difference between the two substrates is that the treated sapphire had a 100nm thick layer of ZnO deposited over it at a temperature of 600ºC. It is unclear whether the ZnO layer, thermal treatment, differences in substrate composition or experimental conditions are responsible for the difference between the substrate responses. However, we note that the signals, of the order of -1 μAm^2, are much smaller than that of a typical DMS film, such as $Zn_{0.95}Mn_{0.05}O$ shown in fig 5.107, which has a magnetic moment of around 0.1 mAm^2 in the low temperature limit. For this reason, relatively small differences between substrate responses do not significantly affect the overall signal when measuring the magnetization of the DMS films grown over sapphire until temperatures of around 50K. This is not the case with films grown over mica because the magnetic moment of just 1mg of mica substrate thermally treated at 600ºC for 6 hours, shown in fig 5.107, is almost ten times greater than a typical film response. Therefore relatively small changes between substrates can lead to large variations in the overall signal at all temperatures when measuring the DMS films grown over mica. This makes it extremely difficult to separate the contributions from sample and substrate and, therefore, only results from films grown over sapphire shall be discussed in this section.

Fig 5.106: Magnetic moments of sapphire substrates and a plastic straw.

Fig 5.107: Magnetic moments of mica and a typical film.

The magnetic moment of each film was extracted from the total measured magnetic moment by subtracting the magnetic moment of 1mg of treated sapphire multiplied by the mass of the film plus substrate, shown in fig 5.108. This assumes that the mass of the film is negligible compared to that of the substrate, which is a valid assumption, as a 100nm thick ZnO film with a surface area of $1cm^2$ has a mass of only $56\mu g$, compared to a typical substrate mass of 20mg. The magnetic moment of the plastic straw and Kapton tape was also subtracted to leave only the response of the film. The volume of each film was then calculated by multiplying the thickness, found in the optical characterisation, by the surface area, estimated from enlarged digital photographs of the samples placed on squared paper. The magnetic moment of each film was finally divided by its volume to find the magnetisation (M) in Am^{-1}.

Fig 5.108: Magnetic moments of mica and a typical sample.

5.5.1 Field dependence of magnetisation

5.5.1.1 $Zn_{1-x}Mn_xO$

Figure 5.109a shows the magnetisation loops at a temperature of 1.8K for $Zn_{1-x}Mn_xO$, where x = 0.05, 0.10, 0.15, 0.20 and 0.25. The region around zero-field has been enlarged and is shown in fig 5.109b. The first thing noted is the absence of hysteresis, which would have been indicative of ferromagnetic behaviour, in all films except the one containing 25% Mn, where a coercive field of 5mT is observed. A common explanation for apparent ferromagnetism is the inclusion of ferromagnetic or ferrimagnetic phases or clusters in the sample. In this case, a ferrimagnetic secondary phase could be (Zn, Mn) Mn_2O_4 [54], a possibility within the interpretation of the XRD results in section 5.2.1. In all other films, the small differences that exist between the magnetising and demagnetising cycles are within the limits of experimental error. These results are in disagreement with the numerous publications which report that $Zn_{1-x}Mn_xO$ is ferromagnetic, including [55-57]. Besides ferromagnetic secondary phases, another explanation for the erroneous detection of ferromagnetism is the failure to recognise ferromagnetism in the substrate. Many authors that claim that $Zn_{1-x}Mn_xO$ is ferromagnetic deposit their samples over sapphire substrates, as in this investigation. However, sapphire presents a relatively strong ferromagnetic response which must be corrected for. Fig 5.110 shows the magnetisation loop at 1.8K for treated sapphire. The coercive field is 42mT which, if uncorrected, would be sufficient to give a positive result. These findings are in agreement with the conclusions of Che Mofor et al. [58].

Fig 5.109a: M(B) loops at 1.8K for Mn DMSs.

Fig 5.109b: Zero field region in M(B) loops at 1.8K for Mn DMSs.

Fig 5.110: M(B) loop at 1.8K for treated sapphire.

The magnetisation loops were modelled by the Brillouin function (3.96), introduced in section 3.4.2. The outer unfilled shell of Mn is the 3d orbital, which contains 5 unpaired electrons, so the value of S was fixed at 5/2. Firstly the Landé g factor was calculated, which is defined as:

$$g = g_L \frac{J(J+1) - S(S+1) + L(L+1)}{2J(J+1)} + g_S \frac{J(J+1) + S(S+1) - L(L+1)}{2J(J+1)} \quad (5.9)$$

where L and J are the orbital and total electronic angular momenta respectively. g_L and g_S are other electron g-factors which, to a good approximation, take the values of 1 and 2 respectively. Bearing in mind that J = L + S and a $3d^5$ level has a ^{6}S

configuration in the Russell-Saunders coupling scheme [59], L=0 and (5.9) simplifies to g = 2. This value for g was substituted into (3.98). It is noted that the maximum value of the function $B_J(y)$ in (3.97) is 1 so $Ng\mu_BJ$ in (3.96) corresponds to the saturation magnetisation, M_{sat}. Therefore, this parameter could be determined by defining it as a variable and performing a fitting with the Brillouin function. The results are shown in fig 5.111 and the agreement with experimental data is reasonable, although there are two particular areas where deviation is observed. One is the region close to zero-field, which is particularly prone to errors, especially those introduced in the correction for the substrate response and the other is in the high field region, suggesting that the films do not reach magnetic saturation.

Fig 5.111: Brillouin function fitting with $Zn_{1-x}Mn_xO$.

It is customary to express M_{sat} in terms of Bohr magnetons (μ_B) per Mn ion, where:

$$\mu_B = \frac{e\hbar}{2m_e} \qquad (5.10)$$
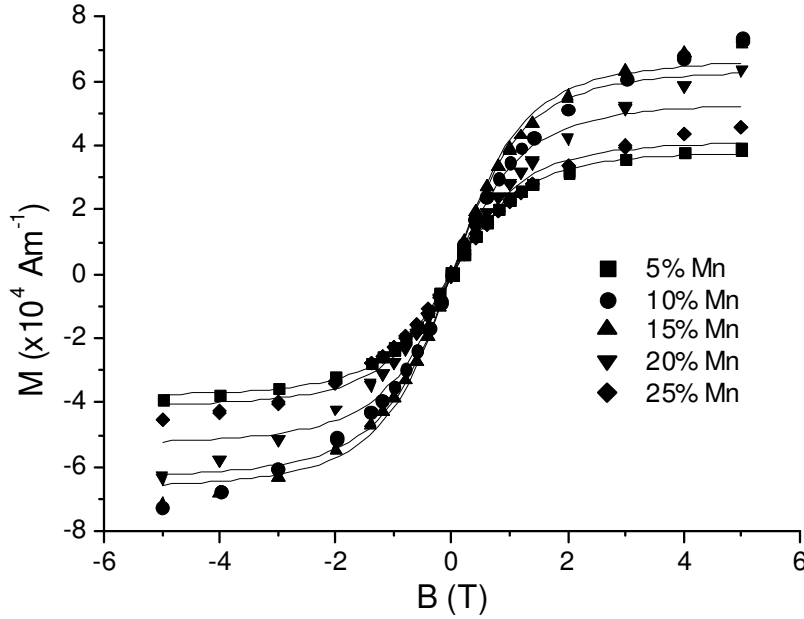
and corresponds to the electron magnetic dipole moment in a hydrogen atom. The results are shown in fig 5.112. There is a clear decrease in M_{sat} as Mn concentration increases, an effect which has also been observed by other authors, such as Masuko et al. [60], who obtain a downwards trend in M_{sat} in $Zn_{1-x}Mn_xO$ films with Mn concentrations between 5% and 10% at 1.85K. The reason given for this trend is the antiferromagnetic superexchange interaction between neighbouring Mn ions observed in $Zn_{1-x}Mn_xTe$ by Barilero et al. [61]. Further evidence for the occurrence of this interaction shall be presented in section 5.5.2, where the results in function of temperature are considered. We note that in the absence of antiferromagnetic interactions, the saturation magnetism per Mn ion should be $5\mu_B$, which seem large in comparison with experimental values, especially at low Mn concentrations. This adds support to the suggestion that the films do not reach magnetic saturation. Therefore, it

would be convenient to repeat the experiment at a future date over a wider range of magnetic fields.
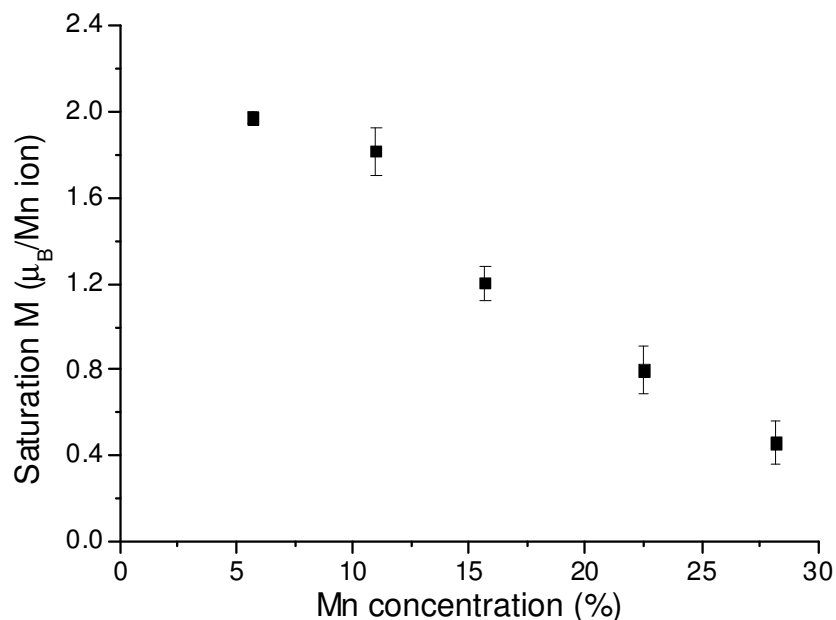
Fig 5.112: Saturation magnetisation in function of Mn concentration.

Magnetisation loops were also measured at a temperature of 300K. However, it was not possible to extract meaningful conclusions from this data due to the difficulty in separating the magnetic moments of the film and substrate. In the high temperature limit of fig 5.108, the contribution of the film to the measured magnetic moment is so small that it cannot be accurately separated from that of the substrates. Therefore, relatively small changes in magnetic moment due to differences in the composition of each substrate produce large errors in the calculated magnetic moments of the films, making comparison difficult. As a final remark, we would like to stress that, in spite of the fact that the magnetic response of the thin films deposited over mica could not be accurately separated from that of the substrate (due to the paramagnetic behaviour of natural mica), no ferromagnetic behaviour was observed in $Zn_{1-x}Mn_xO$ films deposited over mica.

5.1.1.2 $Zn_{1-x}Fe_xO$

The field dependence of the magnetisation of films containing Fe shall now be discussed. Fig 5.113a shows the magnetisation loops in function of B at a temperature of 1.8K for $Zn_{1-x}Fe_xO$, where x = 0.025 and 0.05. An enlargement of the zero-field region is shown in fig 5.113b. Once again, we note little evidence of ferromagnetism in the film containing 2.5% Fe, but a coercive field of 32mT is detected when the concentration is increased to 5%. It is highly unlikely that this ferromagnetic response comes from the DMS, despite the claims of several authors, including Mandal et al. who observed a coercive field of 19mT in $Zn_{0.9}Fe_{0.1}O$ nanoparticles [62]. A more plausible explanation of the results, in the light of the structural characterisation, would be to attribute the ferromagnetism to the secondary phase γ-Fe_2O_3, which was found by XRD in section 5.2.1 (fig 5.12), especially in the film containing 5% Fe. γ-Fe_2O_3 is known to be ferrimagnetic [63], therefore its expected response would be like that of a weak ferromagnet, in agreement with the results.
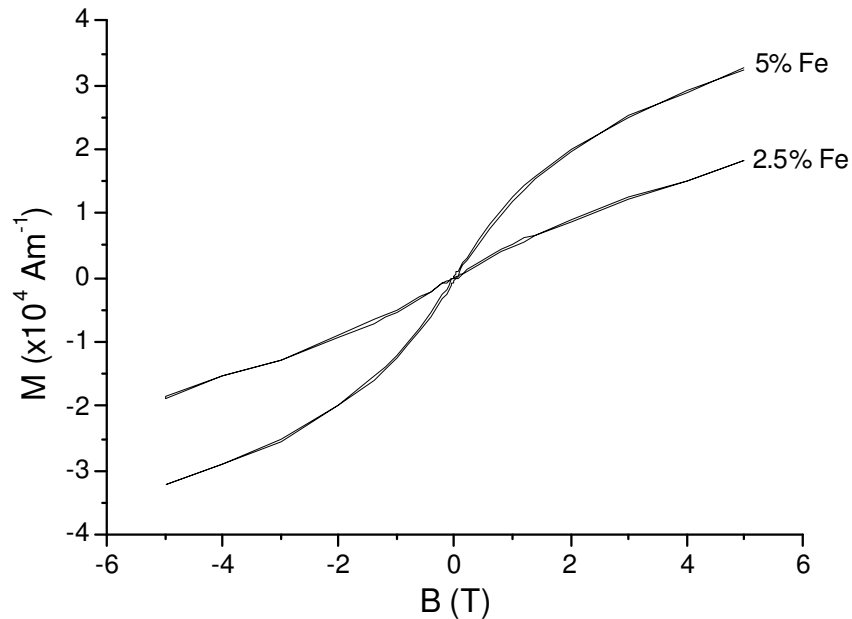
Fig 5.113a: M(B) loops at 1.8K for Fe DMSs.
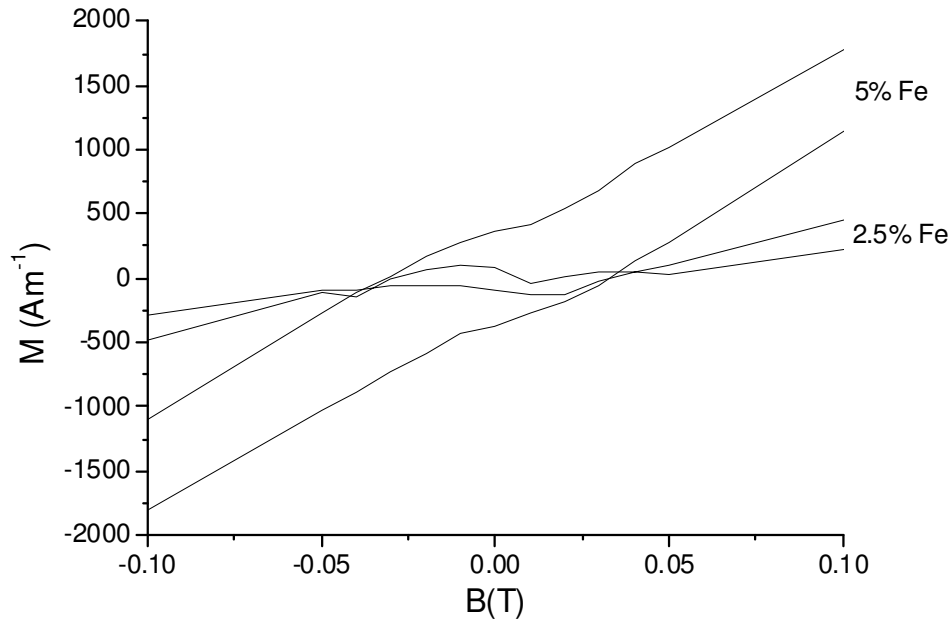
Fig 5.113b: Zero field region in M(B) loops at 1.8K for Fe DMSs.

As in the case of the $Zn_{1-x}Mn_xO$ films, the magnetisation loops were modelled by the Brillouin function (3.96). The outer shell of Fe contains 6 electrons but only 4 are unpaired so the value of S is 2. In the Russell-Sunders coupling scheme, the $3d^6$ level has a ^5D configuration so, in a free Fe atom, L=2 and J=4. However, this is not what is experimentally observed in solids with dilute transition element ions of the Fe period, for which the measured value of J turns out to be very close to S, with g values very close to 2. The orbital contribution, L, is said to be quenched, which is attributed to the crystal field splitting of 3d levels that breaks their degeneracy along with the L-S coupling, diminishing the contribution of the orbital magnetic moment [64]. Substituting g=2 into (3.98) the results obtained are shown in fig 5.114, which also show reasonable agreement with the experimental data. As expected, this fitting deviates somewhat from the experimental points in the high field region, especially in the case of $Zn_{0.975}Fe_{0.025}O$. However, we note that the magnetisation of this film clearly does not reach saturation, which complicates the fitting process. The values of M_{sat} obtained were 2.3 ± 0.3 and 1.7 ± 0.1 μ_B per Fe ion for the films containing 2.5% and 5% Fe respectively. As in the $Zn_{1-x}Mn_xO$ films, there appears to be a downward trend, which could be taken as evidence of an antiferromagnetic superexchange interaction in this DMS too. In absence of antiferromagnetic interactions, the magnetisation should be $4\mu_B$ so the experimental values still seem rather small. As before, it was not possible to draw conclusions from the magnetisation loops at 300K.
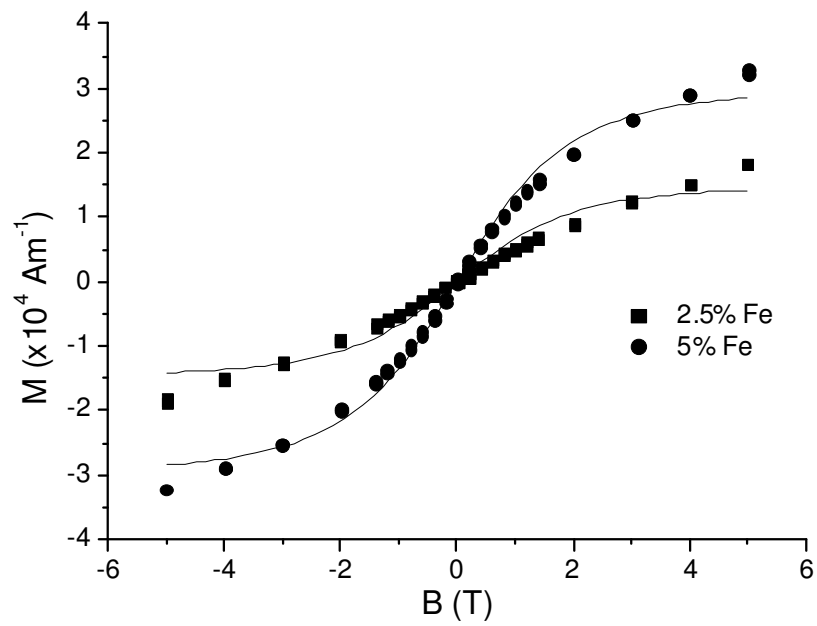
Fig 5.114: Brillouin function fitting for $Zn_{1-x}Fe_xO$.

5.5.2 Temperature dependence of magnetisation

5.5.2.1 $Zn_{1-x}Mn_xO$

Figure 5.115 shows the magnetisation of the $Zn_{1-x}Mn_xO$ films in function of temperature at an applied field of 0.5T. As the temperature increases, the magnetic force responsible for the magnetisation is more easily overcome by the thermal energy of the unpaired electrons, explaining the general form of the curves.
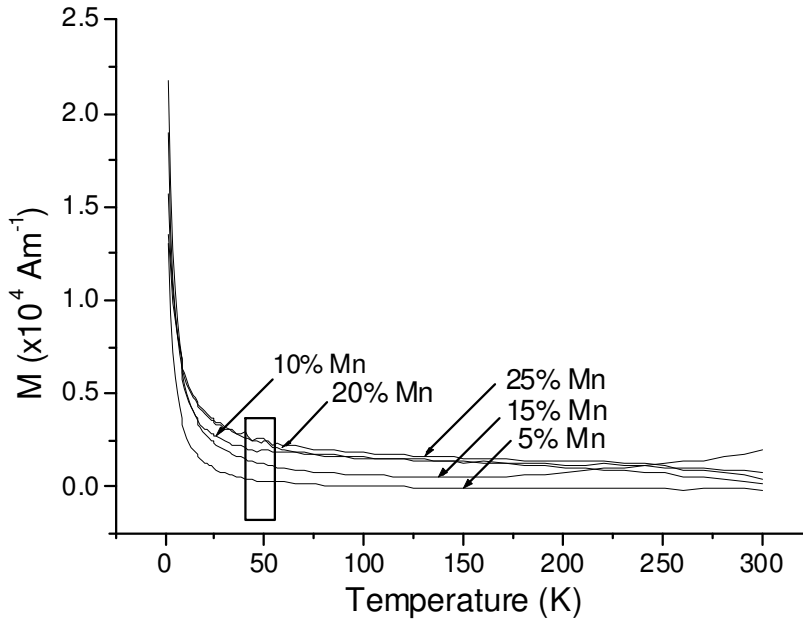
Fig 5.115: M(T) curves for Mn DMSs.

An unusual feature of the curves is an anomaly observed around 47 K, in the boxed region of fig 5.115. Moreover, several authors have published papers where the anomaly appears, although it is often ignored. Lee et al. [65] suggest that it is due to a secondary phase or the Fermi temperature of the film, in the case of it being ferromagnetic. A more likely explanation becomes evident when the response of both sapphire and mica substrates without any samples deposited are considered. Fig 5.116 shows the magnetisation of the samples and substrates in the region of the anomaly. The curves have been scaled and shifted vertically relative to each other to allow comparison. Clearly, the anomaly originates in the substrate and either the films are not completely corrected for it or they respond in such a way as to compensate for it. We note that the samples of Lee et al. were also grown over sapphire substrates, so it seems almost certain that this is the correct explanation.
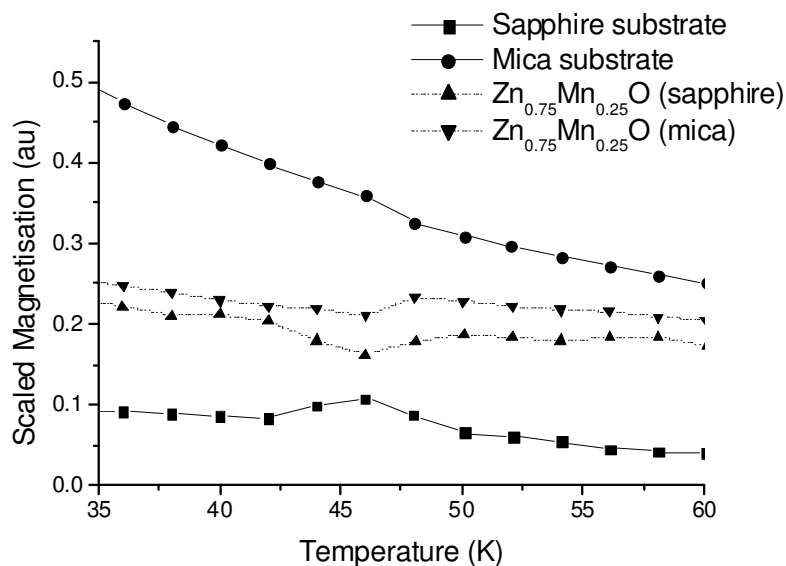
Fig 5.116: Relationship between anomaly and substrates.

As pure mica and sapphire should be diamagnetic, the physical origin of the anomaly in the substrates is most probably due to the presence of similar impurities in both kinds of substrates, as the singularity occurs at the same temperature. Natural mica is an alumino-silicate with an Al content close to 15% in which Al atoms can be in local configurations similar to those in Al_2O_3 [66]. Therefore, the presence of impurities with similar local configurations in both substrates seems to be a reasonable hypothesis. The temperature response of the sapphire substrate with no deposited film is shown in fig 5.117. In the region above 65K, the substrate is clearly diamagnetic, as the magnetisation is negative and temperature independent. Below 65K this behaviour changes and the M^{-1}-T plot in the inset shows that the substrate starts to become ferromagnetic, in agreement with [58]. At 2K, the ferromagnetism was strong enough to be detected in the M(B) loop in fig 5.110. Therefore, the anomaly appears to be related to the ferromagnetic contribution of some unidentified impurities in Al_2O_3. We performed some X-ray fluorescence analysis of the substrates and found traces of period V transition metals and lanthanides, adding weight to this argument.
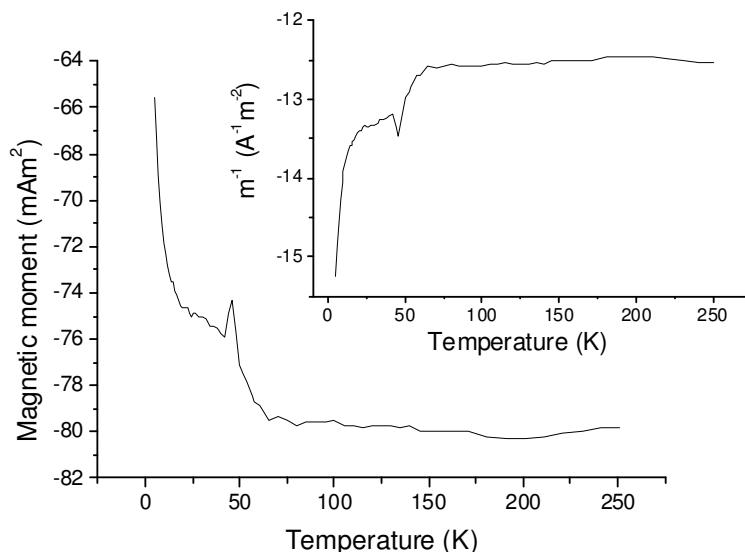
Fig 5.117: Temperature dependence of sapphire substrate with no deposited film.

In order to determine the type of magnetism produced in the $Zn_{1-x}Mn_xO$ films, the inverse of the magnetisation was plotted against the temperature. Up to a temperature of around 50K, all the samples produced an approximately linear trend. However, the trend often deviated from the line at above this temperature. This is most probably due to the failure to correct completely for the substrate contribution. As the substrate has an approximately constant magnetic moment in this region, the range at which the trend was linear could be extended by applying a relatively small offset to the experimental data. The results corrected by this method are shown in fig 5.118. When compared with the initial results in fig 5.115, the main difference is that the graphs converge more in the high temperature limit, which is what would be expected in materials with similar magnetic properties.
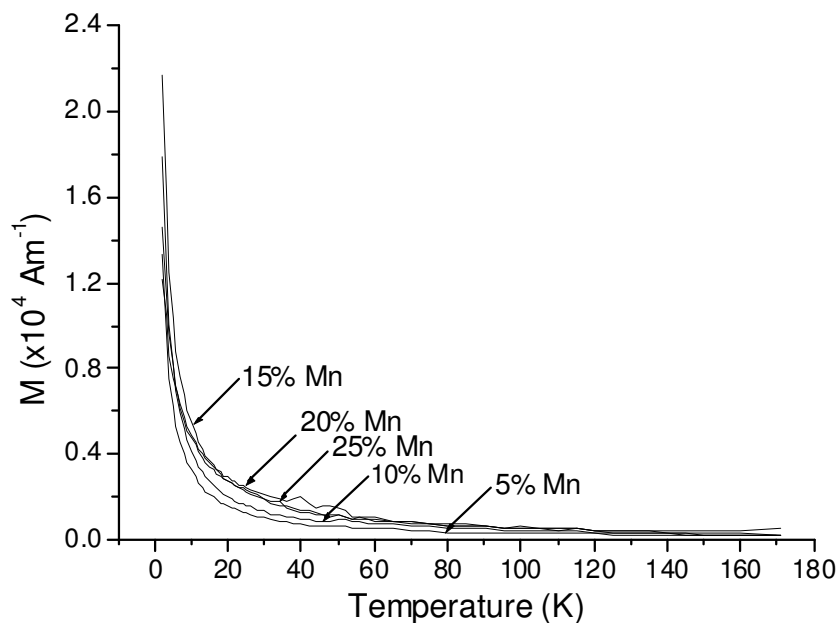
Fig 5.118: Corrected M(T) curves for Mn DMSs.

The inverse magnetisation plots are shown in fig 5.119a. Even after correcting, the effect of the substrate still becomes significant at above 150K, especially in the $Zn_{0.9}Mn0_{0.1}O$ film. The linear trends show the films to be clearly paramagnetic. However, to investigate the extent of the paramagnetism in the low temperature regime, the temperature dependence of the magnetisation multiplied by the temperature (MT) was plotted in fig 5.120. While a material is paramagnetic, it would be expected to give a constant MT value. This appears not to be the case in $Zn_{1-x}Mn_xO$ at low temperature, as the experimental data clearly dips below the average values, shown as lines on the graph. This appears to correspond to the onset of the aforementioned antiferromagnetic behaviour. This is supported by the enlargement of the low temperature region of the inverse magnetisation plots, shown in fig 5.119b. All the linear fittings cross the temperature axis at negative values, which is a typical characteristic of antiferromagnetic behaviour.
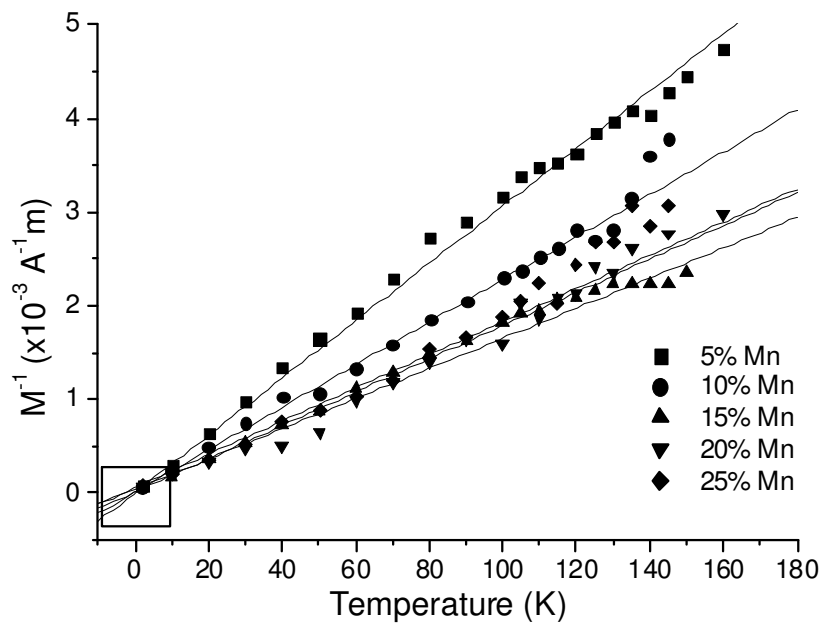
Fig 5.119a: M^{-1} plots for Mn DMSs.
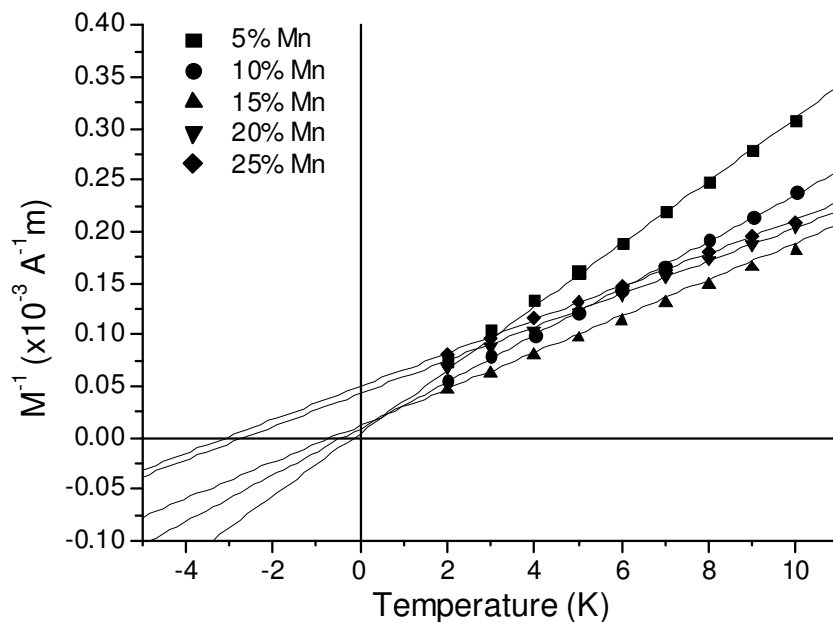
Fig 5.119b: Enlarged low temperature region of M^{-1} plots for Mn DMSs.
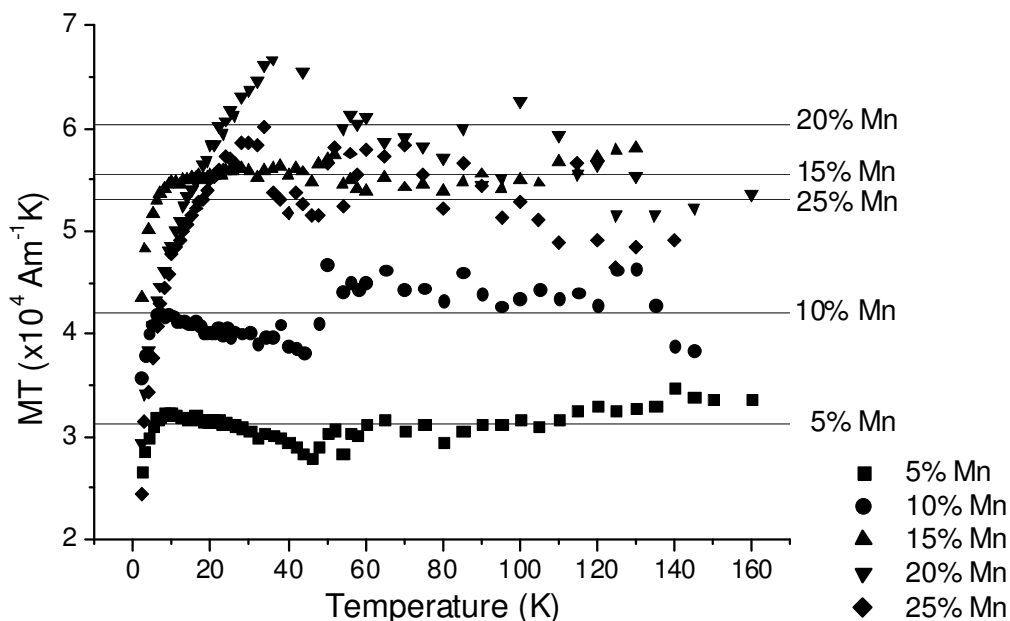
Fig 5.120: MT plots for Mn DMSs.

To gain a more quantitative understanding of the magnetic behaviour of the films, the inverse magnetisation plots in fig 5.119a were fitted to the Curie-Weiss law (3.99). In order to do this fitting, the magnetisation needed to be converted to molar susceptibility (χ_m) by dividing by the field (0.5T) and the number of moles per cubic metre (69667). The Curie constant in function of Mn concentration is shown on the left hand side of fig 5.121 and an increasing trend is observed which becomes horizontal as the Mn concentration reaches the DMS saturation limit. This makes physical sense because the Curie constant is an indication of the strength of the paramagnetism. Therefore, as the concentration of paramagnetic ions increases, the

magnetic response increases accordingly. The Weiss constant, also obtained in the fitting, is shown on the right hand side of fig 5.121. It is always small and negative, corresponding to a weak antiferromagnetic interaction, in agreement with the MT plots in fig 5.120. Its absolute value increases as the Mn concentration increases, which also makes physical sense because the higher the concentration of Mn ions, the greater the chance that a Mn ion will have other Mn ions as second nearest neighbours. This strengthens the antiferromagnetic superexchange interaction so a greater temperature is needed to prevent the spins from being anti-aligned. The particular values obtained for the Weis constants indicate that the Néel temperature should be even lower, as it is normally the case [64]. This is probably the reason that a transition to the AF state was not observed. Our results are in agreement with those of Tomaszewska-Grzeda et al. who obtained Weiss constants of less than 1K in $Zn_{1-x}Mn_xO$ nanopowders with Mn concentrations of 2.6 and 7.6% [67].
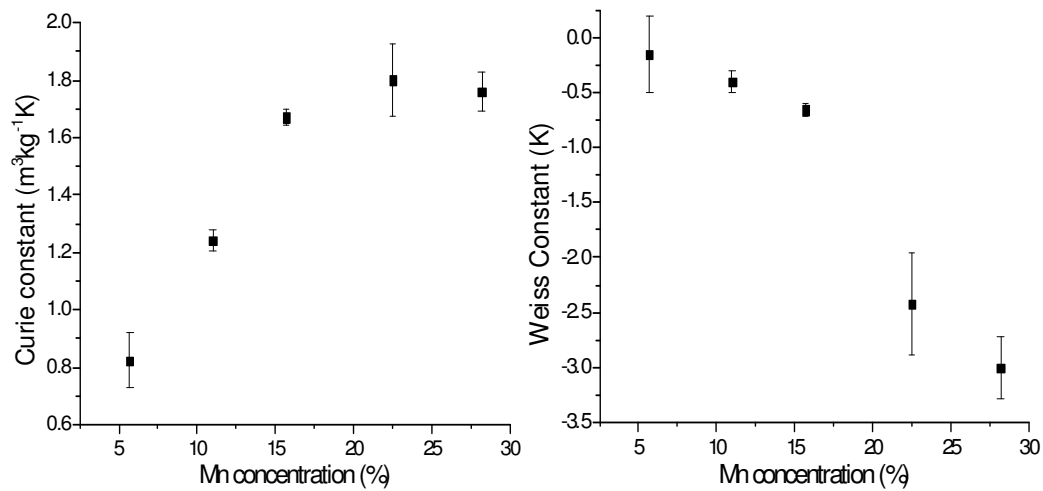
Fig 5.121: Curie constants and Weiss constants for Mn DMSs.

Samuel John Gilliland

5.5.2.2 $Zn_{1-x}Fe_xO$

In the Fe DMS, the experimental data was also offset to reduce the remaining contribution from the substrate. The corrected curves are shown in fig 5.122. The inverse magnetisation was then plotted in fig 5.123a and the resulting linear trends show that these films are also paramagnetic. Moreover, on observing the MT plot in fig 5.124, it is noted that the experimental points also lie significantly below the average lines in the low temperature limit. This supports the notion that an antiferromagnetic superexchange interaction similar to that proposed in $Zn_{1-x}Mn_xO$ is operative in $Zn_{1-x}Fe_xO$ at these temperatures. The negative temperature intercepts in the enlarged low temperature region of the inverse magnetisation plots shown in fig 5.123b add weight to this argument. Although no publications from other authors were readily available to support this hypothesis, we note that these interactions have also been observed in $Zn_{1-x}Co_xO$ films [68]. The inverse magnetisation plots in fig 5.123a were fitted to the Curie-Weiss law and the Curie constants obtained were 0.33 $\pm$ 0.12 $m^3kg^{-1}K$ at a Fe concentration of 2.5%, increasing to 0.96 $\pm$ 0.09 $m^3kg^{-1}K$ at 5% Fe. The rate of increase appears to be greater than that of the Mn DMS. This could be due to contamination from the ferrimagnetic γ-Fe_2O_3 phase, although justification is difficult with the results from only two films. Finally, Weiss constants of -3.0 $\pm$ 0.3 and -3.37 $\pm$ 0.08 K were obtained in the films with Fe concentrations of 2.5 and 5 respectively. These negative values are further evidence for the low temperature antiferromagnetic superexchange interaction.
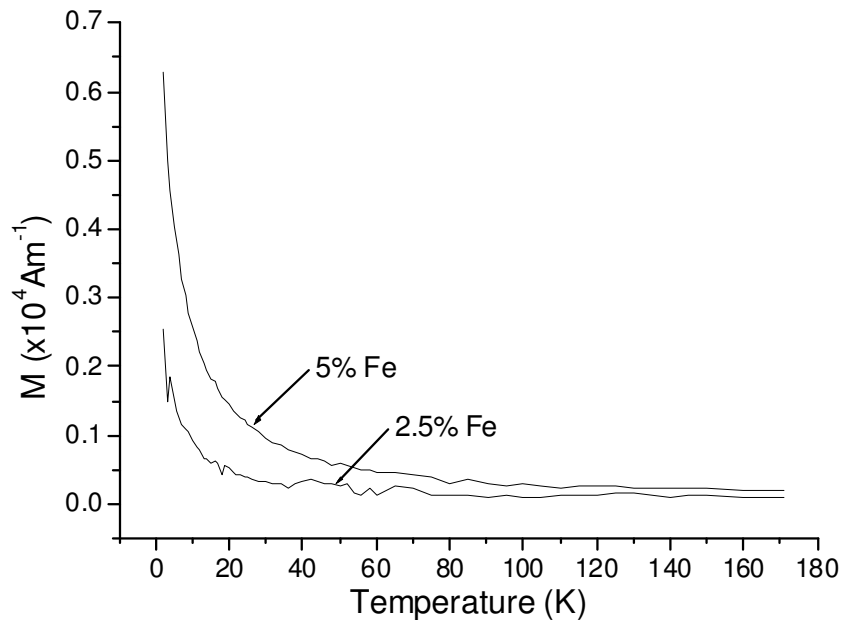
Fig 5.122: Corrected M(T) curves for Fe DMSs.
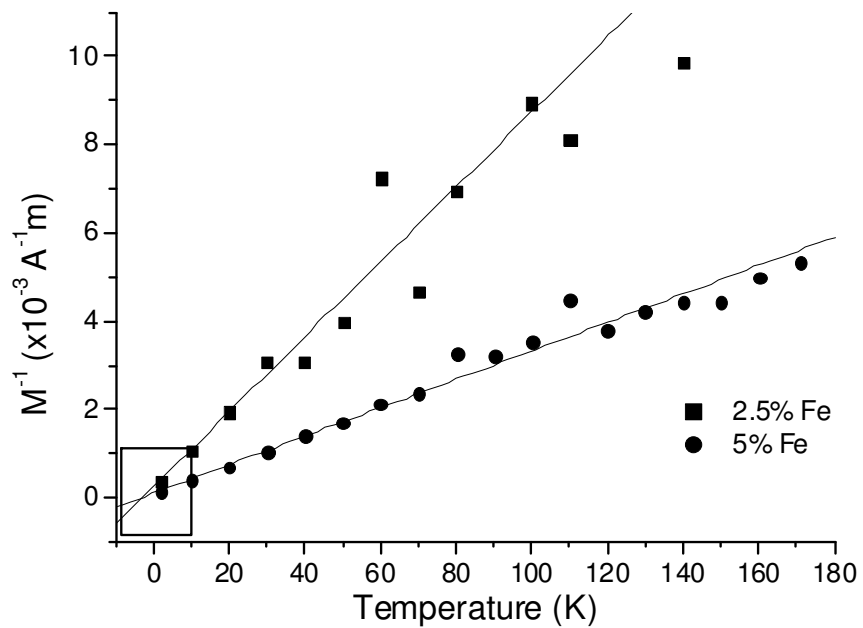
Fig 5.123a: M^{-1} plots for Fe DMSs.
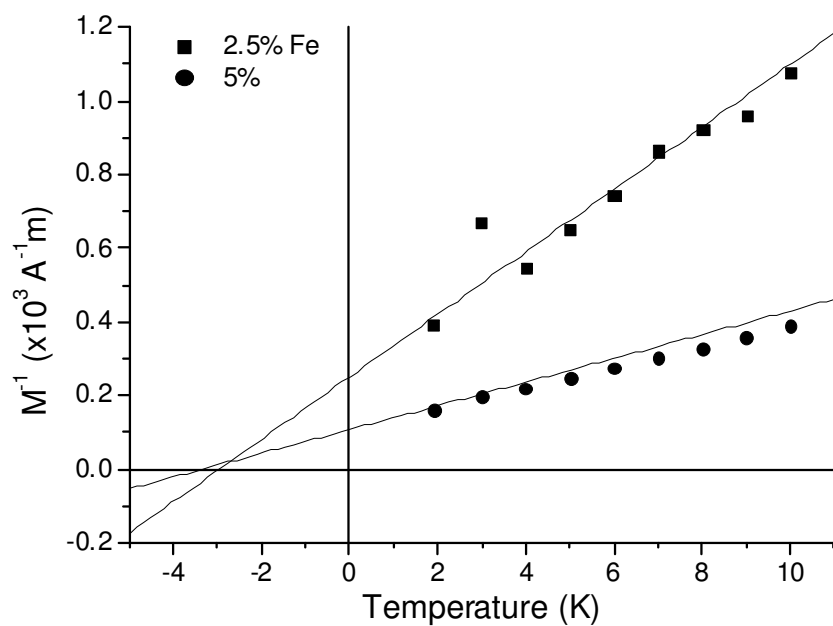
Fig 5.123b: Enlarged low temperature region of M^{-1} plots for Mn DMSs.
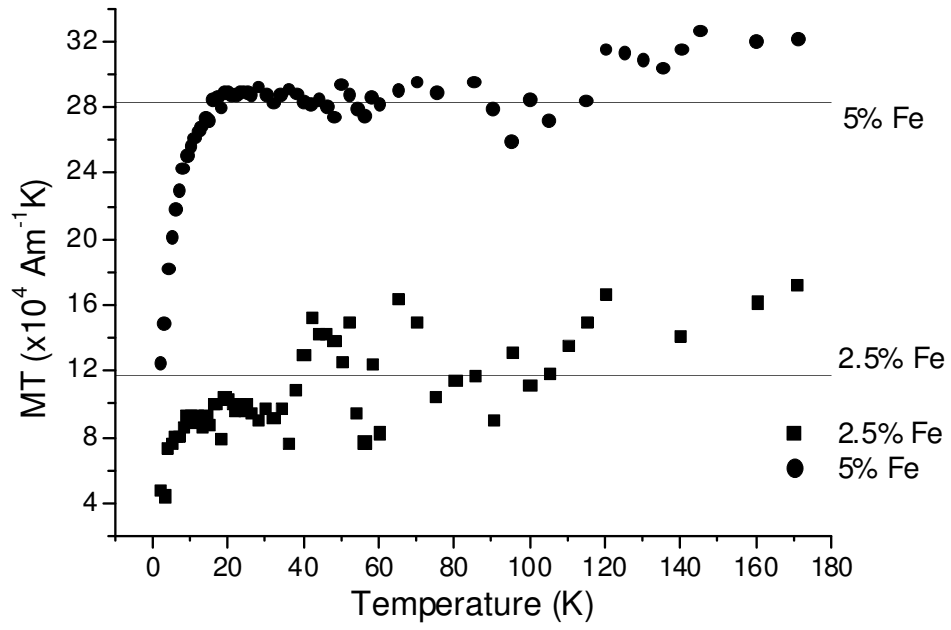
Fig 5.124: MT plots for Fe DMSs.

5.6 Bibliography

[1] A. Kilni, A. Manousaki, D. Anglos and C. Fotakis. J. Appl. Phys. **98**, 123301 (2005).

[2] F. Claeyssens, A. Cheesman, S. Henley and M. Ashfold. J. Appl. Phys. **92**, 6886 (2002).

[3] S. Djenize, S. Bukvic, A. Sreckovic and Z. Nikolic. New Astron. **11**, 256 (2006).

[4] S. Acquaviva and M.L. De Giorgi. Appl. Surf. Sci. **208**, 620 (2003).

[5] N. Harris. "Modern Vacuum Practice", Self-Published (2005).

[6] http://www.aip.org/avsguide/refguide/opticalele.html

[7] Natl. Bur. Stand. (U.S.) Circ. **539**, 3 (1960).

[8] O. Garcia-Martinez, R. Rojas, E. Vila and J. Martin de Vidales. Solid State Ionics **63**, 442 (1993).

[9] R. Heller, J. McGannon and A. Weber. J. Appl. Phys. **21**, 1283 (1950).

[10] K. Ando, H. Saito, T. Sekiguchi, Y. Zoo, M. Murakami, Y. Matsumoto, T. Hasegawa and H. Koinuma. Appl. Phys. Lett. **78**, 3824 (2001).

[11] Natl. Bur. Stand. (U.S.) Monogr. **25**, 61 (1972).

[12] A. Patterson. Phys. Rev. **56**, 978 (1939).

[13] G. Brown "X-ray Identification and Crystal Structures of Clay", London Mineralogical Society (1961).

[14] Natl. Bur. Stand. (U.S.) Circ. **539**, 23 (1953).

[15] S. Wiles and W. Eysel. Mineral. Petrograph. Institut der Universitaet Heidelberg, Germany (1992).

[16] G. Pei, C. Xia, L. Wang, X. Li, X. Jiao and J. Xu. Scr. Mater. **56**, 967 (2007).

[17] B. Ravel. J. Synchrotron Radiat. **8**, 314 (2001).

[18] B. Li, X. Xiu, R. Zhang, Z. Tao, L. Chen, Z. Xie, Y, Zheng and Z. Xie. Mater. Sci. Semicond. Process. **9**, 141 (2006).

[19] M. Krause. J. Phys. Chem. Ref. Data **8**, 307 (1979).

[20] J. Pellicer-Porres, A. Segura, J. Sánchez-Royo, J. A. Sans, J. P. Itié, A. M. Flank, P. Lagarde and A. Polian. Appl. Phys. Lett. **89**, 231904 (2006).

[21] A.L. Ankudinov, B. Ravel, J.J. Rehr, and S.D. Conradson. Phys. Rev. B **58**, 7565 (1998).

[22] T, Eto, S. Endo, M. Imai, Y. Katayama and T. Kikegawa. Phys. Rev. B **61**, 14984 (2000).

[23] H. Ohzono, M. Kouno, H. Miyake and H. Ohyama. Anal. Sci. **17**, i135 (2001).

[24] Y. Kim, M. Yoon, I. Park, Y. Park and J. Lyou. Solid State Commun. **129**, 175 (2004).

[25] D. Look, G. Farlow, P. Reunchan, S. Limpijumnong, S. Zhang and K. Nordlund. Phys. Rev. Lett. **95**, 225502 (1995).

[26] Z. Chen, L. Zhuge, X. Wu and D. Meng. Thin Solid Films **515**, 5462 (2007).

[27] U. Alver, T. Kilinç, E. Bacaksiz and S. Nezir. Mater. Sci. Eng. B **138**, 74 (2007).

[28] M. Kurihara, M. Hirata, R. Sekine, J. Onoe and H. Nakamatsu. J. Nucl. Mater. **326**, 75 (2004).

[29] J. Bearden and A. Burr. Rev. Mod. Phys. **39**, 125 (1967).

[30] Y. Lin, J. Xu, W. Zou, L. Lv, Z. Lu, F. Zhang, Y. Du, Z. Huang and J. Zheng. J. Phys. D: Appl. Phys. **40**, 3674 (2007).

[31] D. Hou, X. Ye, H. Meng, H. Zhou, X. Li, C. Zhen and G. Tang. Mater. Sci. Eng., B **138**, 184 (2007).

[32] S. Hüfner. "Photoelectron Spectroscopy", Springer (2003).

[33] M. Johnson, H. Starnberg and H. Hughes. J. Phys. C: Solid State Phys. **20**, 4385 (1987).

[34] X. Wei, C. Song, K. Geng, F. Zeng, B. He and F. Pan. J. Phys.: Condens. Matter **18**, 7471 (2006).

[35] A. Chen, X. Wu, Z. Sha, L. Zhuge and Y. Meng. J. Phys. D: Appl. Phys. **39**, 4762 (2006).

[36] X. Wang, C. Song, D. Li, K. Geng, F. Zeng and F. Pan. Appl. Surf. Sci. **253**, 1639 (2006).

[37] Z. Yin, N. Chen, F. Yang, S. Song, C. Chai, J. Zhong, H. Qian and K. Ibrahim. Solid State Commun. **135**, 430 (2005).

[38] G. Pei, F. Wu, C. Xia, J. Zhang, X. Li and J. Xu. Curr. Appl. Phys. **8**, 18 (2008).

[39] J. Li, D. Shen, J. Zhang, D. Zhao, B. Li, Y. Lu, Y. Liu and X. Fan. J. Magn. Magn. Mat. **302**, 118 (2006).

[40] J. Yeh and I. Lindau. At. Data Nucl. Data Tables **32**, 1 (1985).

[41] Ü. Özgür, Ya. I. Alivov, C. Liu, A. Teke, M. Reshchikov, S. Dogan, V.Avrutin, S. J. Cho and H. Morkoc. J. Appl. Phys. **98**, 041301 (2005).

[42] R. Weast, "Handbook of Chemistry and Physics 67th Edition", CRC Press (1987).

[43] J. Muth, R. Kolbas, A. Sharma, S. Oktyabrsky and J. Narayan. J. Appl. Phys. **85**, 7884 (1999).

[44] W. Lijun and N. Giles. J. Appl. Phys. **94**, 973 (2003).

[45] J. Sans, A. Segura, F. Manjón, B. Marí, A. Muñoz and M. Herrera-Cabrera. Microelectron. J. **36**, 928 (2005).

[46] J. A. Sans Tresserras doctoral thesis, "Electronic structure of ZnO-based wide band gap semiconductors: Growth and characterisation of the transparent conducting oxide ZnO:Ga and the semimagnetic alloy Zn1-xCoxO and their high pressure phases". Universitat de València (2007).

[47] T. Fukumura, Z. Jin, A. Ohtomo, H. Koinuma, and M. Kawasaki. Appl. Phys. Lett. **75**, 3366 (1999).

[48] J. Gleize, E. Chikoidze, Y. Dumont, E. Rzepka and O. Gorochov. Supperlattices Microstruct. **42**, 242 (2007).

[49] A. Mang, K. Reimann and S. Rubenacke. Solid State Commun. **94**, 251 (1995).

[50] X. Zhang, Z. Chen, Y. Qi, Y. Feng, L. Zhao, M. Ma, R. Liu and W. Wang. Chin. Phys. Lett. **24**, 1032 (2007).

[51] R. Le Toullec, N. Piccioli and J. Chervin. Phys. Rev. B **22**, 6162 (1980).

[52] J. Sans, A. Segura, J. Sánchez-Royo, C. Ferrer-Roca and E. Guillotel. Phys. Stat. Sol. (b) **244**, 407 (2006).

[53] D. Maouche, F. Saad Saoud and L. Louail. Mater. Chem. and Phys. **106**, 11 (2007).

[54] H. Zhang, E. Shi, Z. Chen, X. Liu and B. Xiao. J. Phys.: Condens. Matter **18**, L477 (2006).

[55] W. Xu, Y. Zhou, X. Zhang, D. Chen, Y. Xie, T. Liu, W. Yan and S. Wei. Solid State Commun. **141**, 374 (2007).

[56] A. Pradhan, D. Hunter, B. Lasley-Hunter, J. Dadson, K. Zhang and R. Rakhimov. J. Appl. Phys. **99**, 08M108 (2006).

[57] H. Schmidt, M. Diaconu, H. Hochmuth, M. Lorenz, A. Setzer, P. Esquinazi, A. Pöppl, D. Spemann, K. Nielsen, R. Gross, G. Wagner and M. Grundmann. Superlattices Microstruct. **39**, 334 (2006).

[58] A. Che Mofor, A. El-Shaer, A. Bakin, A. Waag, H. Ahlers, U. Siegner, S. Sievers, M. Albrecht, W. Schoch, N. Izyumskaya, V. Avrutin, S. Sorokin, S. Ivanov and J. Stoemenos. Appl. Phys. Lett. **87**, 062501 (2005).

[59] F. Cotton. "Chemical Applications of Group Theory", Wiley (1990).

[60] K. Masuko, A. Ashida, T. Yoshimura and N. Fujimura. J. Magn. Magn. Mater. **310**, e711 (2007).

[61] G. Barilero, C. Rigaux, M. Menant, N. Hy Hau and W. Giriat. Phys. Rev. B **32**, 5144 (1985).

[62] S. Mandal, T. Nath and A. Das. J. Appl. Phys. **101**, 123920 (2007).

[63] C. Cannas, D. Gatteschi, A. Musinu, G. Piccaluga and C. Sangregorio. J. Phys. Chem. B **1998**, 7721 (1998).

[64] C. Kittel "Introduction to Solid State Physics", Wiley (2005).

[65] S. Lee, T. Won Kang and D. Young Kim. J. Crystal Growth **284**, 6 (2005).

[66] N. Scarth and T. Evitt. European Patent EP19990302169 (1999).

[67] A. Tomaszewska-Grzeda, A. Opalińska, E. Grzanka, W. Łojkowski, A. Gedanken, M. Godlewski, S. Yatsunenko, V. Osinniy and T. Story. Appl. Phys. Lett. **89**, 242102 (2006).

[68] P. Sati, C. Deparis, C. Morhain, S. Schäfer, and A. Stepanov. Phys. Rev. Lett. **98**, 137204 (2007).

Samuel John Gilliland

6 Conclusions

$Zn_{1-x}M_xO$ (M = Mn, Fe, Ni, Cu) films were deposited at optimal conditions over mica and sapphire substrates by laser ablation of polycrystalline targets containing stoichiometric mixtures of chemical compounds. These films were then characterised structurally, electronically, optically and magnetically.

Structural characterisation:

A detailed structural characterisation was done including plume emission spectroscopy, XRD, XAS, XRF, electron microscopy and microanalysis to ensure that the expected films had been correctly deposited.

Plume emission spectroscopy was done to analyse the growth conditions during deposition. Emission lines related to neutral and singly ionised TMs (both Zn and the dilute cations) were identified. The expected lines were usually observed, except in the Ni DMS, as Ni has a particularly low vapour pressure. The intensity of the lines did not change over time, indicating a constant chemical composition of the plasma and, consequently, growth conditions. During $Zn_{1-x}Mn_xO$ deposition, the intensity of the Mn emission lines was proportional to the Mn concentration in the targets.

XRD measurements were taken to investigate the crystal structure of the films. Results show that the films grown over sapphire have preferred c-orientation. This reduces strain in the films due to lattice mismatch. $Zn_{1-x}Mn_xO$ films are single phase until a Mn concentration of at least 15%. In this range, increased ionic radius causes a linear increase in the c lattice parameter of $1.69 \pm 0.04 \times 10^{-3}$ $Å\%_{Mn}^{-1}$. $Zn_{1-x}Fe_xO$ is single phase up to a Fe concentration of 2.5%, above which Fe_2O_3 is found. Up to this concentration, an increase in Fe causes a proportional increase in the c lattice parameter of $5.2 \pm 0.2 \times 10^{-4}$ $Å\%_{Fe}^{-1}$. $Zn_{1-x}Cu_xO$ is single phase up to a concentration of 1%, after which Cu_2O is found. In this range, increasing the Cu concentration causes a linear decrease in the c lattice parameter of $2.13 \pm 0.08 \times 10^{-4}$ $Å\%_{Cu}^{-1}$. This is because the ionic radius is smaller than that of Zn. In $Zn_{1-x}Ni_xO$ the situation is unclear because the NiO diffraction peaks are not seen. Moreover, no significant change in c is detected.

XAS was measured to determine the dilute cation coordination environment. In order to do this XANES spectra were compared to theoretical simulations and references. In $Zn_{1-x}Mn_xO$, the form of the XANES remained constant in function of Mn concentration, implying that the Mn is always in the wurtzite configuration. In $Zn_{1-x}Fe_xO$ a mixture of two phases is found, with the proportion of Fe_2O_3 increasing with the Fe concentration. In $Zn_{1-x}Cu_xO$ a gradual transition from wurtzite to Cu_2O configurations is observed. In Ni DMS a similar transition occurs but over a lower concentration range so that by 5% Ni, the XANES is almost identical to that of NiO. XRF measurements were used to determine the dilute cation concentration in the films. In most cases a good agreement with nominal concentrations was found.

Scanning electron microscopy was used to examine the film surfaces, which were found to be polycrystalline. The average crystallite size in pure ZnO was 300 ±

100 nm. $Zn_{1-x}Mn_xO$ films were not conducting and attempts to observe the metalised surfaces were not successful. In $Zn_{1-x}Fe_xO$ films, the crystallite size decreased with Fe concentration. From 5% Fe onwards (3.2% by XRF), edge-like encrustations were observed which could correspond to the Fe_2O_3 secondary phase. In $Zn_{1-x}Cu_xO$ films, insulating regions were observed that could correspond to Cu_2O. As the Cu concentration increased, more of these regions appeared and cross-links occurred when the separation between Cu atoms reached 4.18 Å, which could be a sign of diffusion. Above this concentration, insulating regions were larger and more separated. In $Zn_{1-x}Ni_xO$ films, images suggest that a similar process occurs but at lower concentrations. No phase separation was observed at 0.5% Ni (0.4% by XRF) but separated insulating regions were already observed by 1% Ni (0.9% by XRF). This may be because NiO is more structurally stable than Cu_2O. Element mapping microanalysis at the maximum resolution of 5nm did not reveal any large clusters of metallic atoms and could not provide any additional information about the chemical composition of the structures observed in the SEM images.

Electronic characterisation:

Photoelectron spectroscopy measurements were taken to investigate the electronic properties of the films. He-II UPS and Mg K_α XPS were done to investigate the electronic states of the valence band and core electronic levels respectively.

O 2p and Zn 3d levels were identified in the UPS spectra of all films. In $Zn_{1-x}Mn_xO$ a peak was observed on the low binding energy side of the O 2p levels, whose intensity was directly proportional to Mn concentration. It is likely that this peak corresponds to the Mn 3d levels. Its binding energy decreases by 0.36 ± 0.07 eV over the concentration range, whereas the energy of the O 2p peaks increases by 0.39 ± 0.07 eV. An acceptable explanation for this would be an increase in p-d repulsion. In $Zn_{1-x}Fe_xO$ films the O 2p levels intensify by 24% and broaden by 30% over the concentration range, consistent with the explanation that the Fe 3d levels are located within the O 2p band. The energy of the O 2p levels increases by 0.29 ± 0.06 eV due to p-d repulsion and a skewing of the energy spectrum caused by Fe(III). In the $Zn_{0.95}Cu_{0.05}O$ film, the position of the Cu 3d levels is not apparent. The O 2p levels decrease in binding energy by 0.12 ± 0.02 eV, in agreement with theory that predicts a reversal in the direction of the p-d repulsion. It appears that the Cu 3d levels have a greater binding energy than the O 2p states but, as they are energetically closer than the Zn 3d levels, the p-d repulsion is greater. $Zn_{1-x}Ni_xO$ films were not measured but a similar effect to the Cu DMS would be expected.

In XPS measurements, peaks corresponding to the O 1s and Zn 2p core levels were identified in all films and the oxidation states of the dilute cations were determined by the positions of their 2p peaks and satellites. $Zn_{1-x}Mn_xO$ films were in oxidation state II over the whole concentration range. In $Zn_{1-x}Fe_xO$ films it appears that there was a gradual oxidation of the Fe from state II to III as the concentration increased, consistent with the structural characterisation. In the $Zn_{0.95}Cu_{0.05}O$ film there was a significant contribution from Cu(I), also in agreement with the structural characterisation. $Zn_{1-x}Ni_xO$ films were not measured by XPS but a constant oxidation state of II would be expected, as in the case of Zn, which was always found to be in this state. The integrated intensities of the dilute cation 2p peaks were used to obtain a

second set of data on the stoichiometry of the films, which was in good agreement with XRF results.

Optical characterisation:

Optical absorption measurements were taken to investigate the changes in the absorption edge caused by the dilute cation type and concentration at low temperature and high pressure. Results were fitted to a model based on the Elliot-Toyozawa equation to determine the optical properties.

In $Zn_{1-x}Mn_xO$ films, the bandgap increase in function of Mn concentration is approximately linear, with a coefficient of 19 ± 2 meV$\%_{Mn}^{-1}$ up to a concentration of 15%, due to p-d repulsion. In this concentration range the continuum width broadens by 0.43 ± 0.05 eV due to the increase in disorder. This effect is also responsible for the decrease in excitonic intensity and the broadening of its width by 0.15 ± 0.03 eV. The exciton + LO phonon resonance also decreases in intensity and broadens by 0.49 ± 0.08 eV. A pre-edge band is observed that remains at a constant energy of 3.04 ± 0.05 eV but increases in intensity and broadens by 36 ± 12 meV. Photoconductivity measurements show a clear increase in photocurrent in this region, leading to conclusion that it is principally due to a CTT from Mn 3d levels to the conduction band. In $Zn_{1-x}Fe_xO$ films, the bandgap increase is approximately linear in the whole concentration range, with a rate of 4 ± 1 meV$\%_{Fe}^{-1}$. The continuum width broadens by 0.13 ± 0.03 eV and the exciton decreases in intensity and broadens by 0.38 ± 0.05 eV due to the increase in disorder. There is insufficient data to comment on the exciton + LO phonon resonance. In $Zn_{1-x}Cu_xO$ films up to the solubility limit of 0.9 ± 0.1 %, the bandgap energy decreases by 9.8 ± 0.5 meV, confirming the reversal of the p-d repulsion. However, disorder still increases so the continuum width increases by 0.37 ± 0.06 eV and the exciton intensity decreases and its width increases by 5.8 ± 0.9 meV. The exciton + LO phonon resonance also decreases in intensity and its width increases by 41 ± 9 meV. Beyond the solubility limit, Cu begins to diffuse out of the Zn substitutional position to form the Cu_2O secondary phase, an effect which increases with Cu concentration. As Cu_2O appears not to affect the measured optical properties in this concentration range, they revert to those of pure ZnO. In $Zn_{1-x}Ni_xO$ films, a similar trend to the Cu DMS is observed but the solubility limit of 0.60 ± 0.08 % is lower because NiO is more stable than Cu_2O. Up to the solubility limit, the decrease in bandgap energy is 5.5 ± 0.4 meV.

In all films, low temperature produces a blue-shift of the absorption edge, although the magnitude of the shift depends on the combined effect of the electron-phonon interaction and static disorder. In $Zn_{1-x}Mn_xO$ films the electron-phonon interaction dominates at low concentrations. Therefore, the Bose-Einstein model may be used to confirm that the bandgap phonon energy of 30 ± 2 meV does not vary significantly from that of pure ZnO. However, this model breaks down beyond a Mn concentration of 10% due to the effect of static disorder, which partially compensates for the electron-phonon interaction by causing a reduction in the bandgap energy at low temperatures, where it is particularly effective. These effects can also be used to explain other optical properties of the films. At low Mn concentrations both the continuum and exciton widths show considerable temperature broadening due to the electron-phonon interaction but this is partially compensated by the low temperature broadening caused by static disorder at high concentrations. Likewise, the exciton

intensity decreases with temperature at low Mn concentrations due to disassociation caused by phonons, which is balanced by low temperature disassociation caused by static disorder at high concentrations. The exciton + LO phonon resonances follow similar trends to the aforementioned excitonic properties. The temperature dependence of the energy of the pre-edge band appears to follow that of the bandgap, consistent with its assignation as a CTT. Its intensity decreases with temperature in all films and its width remains approximately constant. In $Zn_{1-x}Fe_xO$, the electron-phonon interaction controls the temperature dependence of the optical properties in all films, since the greatest Fe concentration is only 10%. For this reason, the general trends are similar to those of the low concentration Mn DMSs. In $Zn_{1-x}Cu_xO$ films up to the solubility limit, the Bose-Einstein model can not confirm that the dominant mechanism is the electron-phonon interaction. However, the remaining optical properties are similar to those of the other low concentration DMSs. Beyond the solubility limit, the behaviour gradually returns to that of pure ZnO. In $Zn_{1-x}Ni_xO$ films, apart from an approximately constant continuum width, no significant changes in optical properties from those observed in pure ZnO are found at any Ni concentration due to the low saturation limit.

In the wurtzite phase, high pressure produces a blue-shift in the absorption edge, in agreement with the theory for covalently bonded semiconductors. The bandgap energy variation was fitted to a quadratic model but no significant change was detected from the behaviour of pure ZnO, which had linear and quadratic pressure coefficients of $\alpha = 25.3 \pm 0.1$ meVGPa^{-1} and $\beta = -0.28 \pm 0.01$ meVGPa^{-1} respectively. As high pressure does not significantly affect disorder, the continuum width did not change significantly in any of the films. The exciton could only be observed at low dilute cation concentrations and the exciton + LO phonon resonance could not be detected at all because measurements were taken at room temperature. In function of pressure, exciton intensities normally increased due to an increase in the Rydberg energy and their widths decreased due to the related increase in lifetime. The rates appeared to vary arbitrarily between samples so it is likely that they are dependent on defect concentrations introduced on charging the cell. In the $Zn_{1-x}Mn_xO$ films, high pressure caused the CTT to diminish in intensity and increase in energy by 24 ± 2 meVGPa^{-1} and width by 6.7 ± 0.8 meVGPa^{-1}. All these effects were independent of Mn concentration and occur because high pressure causes the CBM and VBM to increase in energy, whereas the energy of the Mn 3d levels is pressure insensitive. This confirms that the CTT is between the Mn 3d levels and the conduction band.

In the rocksalt phase a pronounced change was observed in the form of the absorption coefficient. As films were thin, it was not possible to measure the energy of the indirect gap. However, the tail of the direct gap at Γ could be studied, which also blueshifted with increasing pressure. Although it was not possible to determine the energy of this direct gap, its pressure coefficient could be estimated and, in all cases, the coefficient was not significantly different from that of 35 ± 2 meVGPa^{-1}, obtained for pure ZnO. In this material the phase transition occurs at 9.7 GPa on the upstroke and 2.0 GPa on the downstroke, in agreement with results from DMSs with low dilute cation concentrations. At higher concentrations the $Zn_{1-x}Mn_xO$ films showed a linear decrease in both upstroke and downstroke transition pressures due to the "chemical pressure" effect. The rates of decrease for the upstroke and downstroke were 0.04 ± 0.02 and 0.13 ± 0.01 GPa%$_{Mn}^{-1}$ respectively. Hence, metastable rocksalt

films were recovered for Mn concentrations of above 19 ± 3 %. In $Zn_{1-x}Fe_xO$ films the downstroke phase transition pressure decreased at a rate of 0.13 ± 0.01 GPa%$_{Fe}^{-1}$. However, the upstroke phase transition pressure apparently increased with Fe concentration, probably due to the effect of the mica substrate. The phase transition pressures of $Zn_{1-x}Cu_xO$ films were constant due to the low solubility limit, taking values of 10 ± 2 and 2.1 ± 0.1 GPa for the upstroke and downstroke respectively. Due to the even lower solubility limit in $Zn_{1-x}Ni_xO$, these films were not characterised at high pressure.

Magnetic characterisation:

The purpose of this characterisation was to determine the magnetisation of the DMS films in function of applied magnetic field and temperature. Results from films grown over mica proved difficult to analyse due to the large substrate magnetic response, so only results from films grown over sapphire are reported.

In M(H) loops at 1.8K, after the substrate contribution was subtracted, the only $Zn_{1-x}Mn_xO$ film that showed any evidence of ferromagnetism was the highest concentration film (25% Mn), where a coercive field of 5mT was observed, probably due to ferrimagnetic (Zn, Mn) Mn_2O_4 secondary phases. Experimental results were modelled successfully by the Brillouin function and the saturation magnetisation was found to decrease by 1.5 ± 0.1 μ_B per Mn ion over the concentration range between 5% and 25%. This could be caused by an antiferromagnetic superexchange interaction between neighbouring Mn ions. In $Zn_{1-x}Fe_xO$ films, the DMS with 2.5% Fe showed no ferromagnetism but at 5% Fe a small coercive field of 32mT was detected, probably due to the ferrimagnetic γ-Fe_2O_3 secondary phase detected by XRD. On modelling with the Brillouin function, the saturation magnetisation was also found to decrease by 0.6 ± 0.3 μ_B per Fe ion between the two films. Magnetisation loops at 300K could not be analysed due to an incomplete removal of the substrate magnetic moment.

In M(T) curves, an unusual feature at around 47 K, mentioned by some authors, was found to be a substrate effect related to the ferromagnetic contribution of some unidentified impurities in Al_2O_3. $Zn_{1-x}Mn_xO$ films showed typical paramagnetic behaviour, except in the low temperature limit where signs of the onset of antiferromagnetism were observed. On applying the Curie-Weiss law, the Curie constant, which indicates the strength of the paramagnetism, increased by 0.9 ± 0.1 $m^3kg^{-1}K$ over the concentration range. The Weiss constant was always found to be small and negative, providing further evidence for low temperature antiferromagnetism. Its value was found to decrease by 2.8 ± 0.3 K over the same range. The $Zn_{1-x}Fe_xO$ films were also paramagnetic with similar signs of low temperature antiferromagnetism. The value of the Curie constant increased by 0.6 ± 0.2 $m^3kg^{-1}K$ between the films and the Weiss constant, which was also always small and negative, decreased slightly by 0.4 ± 0.3 K.

Future developments:

The results obtained in this work provide considerable scope for future investigation. Some developments could be:

- Completion of the photoelectronic study of $Zn_{1-x}Cu_xO$ and $Zn_{1-x}Ni_xO$ films. UPS measurements would provide further information about the p-d repulsion reversal observed with these dilute cations and predicted oxidation states could be confirmed by XPS.
- Further magnetic measurements over a wider range of fields, especially with $Zn_{1-x}Fe_xO$ films, as these were only measured up to a Fe concentration of 5%. This would allow saturation magnetism values to be determined more precisely and the effect of ferrimagnetic secondary phases to be quantified. $Zn_{1-x}Cu_xO$ and $Zn_{1-x}Ni_xO$ films could also be measured, although it is unclear whether the low solubility limits would prevent any significant magnetisation from being detected.
- Additional measurements on the $Zn_{1-x}Mn_xO$ CTT to study the change in photoconductivity in function of the Mn concentration.
- High pressure measurements on bulk DMS monocrystals to study the energy and pressure dependence of the indirect gap in the rocksalt phase. Also by measuring the DMS films up to higher energies, the energy of the rocksalt phase direct gap could be found.
- Low temperature high pressure measurements to allow a more precise determination of the optical properties, especially those relating to excitonic effects.
- Infrared measurements on wurtzite and rocksalt DMSs to investigate the dilute cation d-d* internal transitions. It would probably be necessary to use thicker films or monocrystals to obtain sufficient absorption.
- Transport measurements to determine the carrier concentrations and mobilities of the DMSs. $Zn_{1-x}Mn_xO$ samples would need to be doped with Ga in order to increase the carrier concentration.
- Raman scattering measurements to provide complimentary results about the vibrational properties of the films at the Γ point.
- Photoluminescence measurements to provide additional information about the excitonic properties and impurities in the films.
- Ab-initio calculations of bandgap energies in function of dilute cation concentration to strengthen the theoretical basis behind conclusions made about p-d repulsion.
- The study of ZnO alloyed with two or more dilute cations. For example, Han et al. [1] report that doping $Zn_{1-x}Fe_xO$ with Cu is a "key to room-temperature ferromagnetism".
- The integration of the results found in this study with those obtained from ZnO alloyed with other TMs, such as Co. In this way a general description of the behaviour of ZnO DMSs could be constructed.

Bibliography:

[1] S. Han, J. Song, C. Yang, S. Park, J. Park, Y. Jeong, K. Rhie. Appl. Phys. Lett. **81**, 4212 (2002).

7 Resumen en Castellano

7.1 Introducción

El ZnO es un semiconductor II-VI de gap ancho con una energía de gap de 3,37 eV a temperatura ambiente [1]. Aunque los mono-cristales masivos sin dopar muestran normalmente una baja conductividad tipo n o un comportamiento resistivo [2], puede dotárseles de una alta conductividad eléctrica tipo n al dopar con varios elementos del grupo III, tales como Al [3], Ga [4] o In [5]. Estos elementos contribuyen con un electrón libre cuando ocupan la posición substitucional para Zn, lo cual produce un óxido transparente conductor (TCO). La red de citas ISI "Web of knowledge™" hace referencia a más que 30.000 artículos sobre el ZnO, con publicaciones desde el año 1900 [6], lo cual significa que es un material relativamente bien estudiado. Este hecho esta relacionado, sin duda, con las numerosas aplicaciones industriales que se han encontrado en campos tan diversos como la agricultura, la química, las cerámicas, los lubricantes, la medicina, los cosméticos y las gomas. De interés particular son las aplicaciones optoelectrónicas como los LEDs [7] y láseres [8] ultravioletas y los detectores fotoconductivos [9]. Su energía de gap es parecida a la de GaN, 3,44 eV [1], por tanto podría servir como substituto en ciertas aplicaciones. Además, su mayor energía de enlace del excitón de 59 meV [10], comparado con 22 meV en el GaN [11], mejora, en principio, su capacidad para emitir luz.

El ZnO sin dopar es diamagnético [12] pero se pueden alterar sus propiedades magnéticas al formar una aleación con un elemento magnético como Mn [13], Fe [14] o Co [15] para producir un semiconductor magnético diluido (DMS). Aunque se han estudiado los DMS durante más que 30 años, han atraído más interés recientemente tras la publicación de un artículo de Dietl et al. [16], el cual predice ferromagnetismo a temperatura ambiente en aleaciones DMS de gap ancho, como el $Ga_{1-x}Mn_xN$ y el $Zn_{1-x}Co_xO$. Las propiedades semiconductoras y ferromagnéticas coexisten en semiconductores magnéticos como los chalcogenuros de Eu y Mn [17, 18] y las espinelas de Cr, pero la estructura cristalina de tales materiales es muy diferente de la de los semiconductores tradiciones que se usan en la industria como el Si y el GaAs. Además, sus temperaturas de Curie son bastante bajas y su crecimiento cristalino es difícil. Por tanto, los semiconductores magnéticos basados en semiconductores no magnéticos serían más convenientes. Tales materiales podrían tener aplicaciones en la magnetoóptica y la espintrónica [20], como memorias no volátiles, informática cuántica y dispositivos novedosos de comunicación. Por tanto, es de interés particular estudiar los DMS de gap ancho basados en ZnO aleado con óxidos de metales de transición (TM) como Mn, Fe, Ni y Cu.

Se han publicado muchos artículos sobre el $Zn_{1-x}Mn_xO$, la mayoría de los cuales tratan de sus propiedades magnéticas. La polémica aparente sobre si el material es ferromagnético ha aumentado la publicación e, informes que suelen ser contradictorios encuentran antiferromagnetismo [21], diamagnetismo [22] y paramagnetismo [23]. Aún cuando se encuentra el ferromagnetismo, no hay un acuerdo sobre la temperatura de Curie, con valores citados tan bajos como 45K [24] hasta por encima de 420K [25]. Se han publicado bastante menos artículos sobre el $Zn_{1-x}Fe_xO$, el $Zn_{1-x}Cu_xO$ y el $Zn_{1-x}Ni_xO$ pero la gran mayoría de ellos tratan de las

propiedades magnéticas, con ferromagnetismo a temperatura ambiente citado normalmente en las tres aleaciones [26-28], aunque la polémica también existe [29]. Está claro que hace falta un entendimiento más comprensivo de los materiales, haciendo hincapié en la preparación y la aplicación correcta de las técnicas experimentales para evitar resultados erróneos causados por sustratos o conjuntos de átomos magnéticos.

Casi tan enigmático como las propiedades magnéticas en si es el origen de tales propiedades. En el artículo de Dietl mencionado anteriormente [16], el mecanismo propuesto para explicar el ferromagnetismo es una interacción de intercambio entre los huecos libres y los espines localizados. No obstante, para que esto ocurra, los materiales tendrían que ser dopados fuertemente tipo p. Esto es problemático, ya que los materiales normalmente son dopados tipo n, debido a dadores procedentes de intersticiales de Zn o vacantes de O. Además, Zhang et al. [30] mostraron que un dopado tipo p intrínseco en ZnO es teóricamente imposible, ya que existe una baja entalpía de formación de defectos compensadores. No obstante, Kim et al. informan que se puede obtener cierto nivel de conductividad tipo p al dopar con los elementos del grupo V: N [31] y As [32]. En este caso hay una posible explicación para el ferromagnetismo observado; sin embargo otros grupos de investigación reclaman que aún existe el ferromagnetismo en muestras de $Zn_{1-x}Mn_xO$ dopadas tipo n [33, 34]. En este caso se requeriría otra explicación, como el intercambio mediado por electrones en una banda desdoblada por espín, propuesta por Coey et al. [35].

En cuanto a las propiedades ópticas, algunas publicaciones ya mencionan la absorción óptica de $Zn_{1-x}Mn_xO$ [36, 37], aunque ninguna de ellas informa sobre medidas a altas presiones. Esta técnica es particularmente apropiada para entender la relación entre propiedades estructurales y electrónicas, ya que la "presión química", que se produce al sustituir una especie atómica por otra de un tamaño diferente, suele ser análoga a la presión física aplicada externamente. Además, se puede obtener y caracterizar las fases de alta presión. La situación con los otros DMS bajo investigación es parecida, aunque se han publicado menos artículos. Existen algunas publicaciones sobre las propiedades ópticas de los DMS basados en ZnO aleado con Fe [38], Cu [39] y Ni [40] pero ninguna de ellas hace uso de la técnica de altas presiones. Por tanto, este estudio es científicamente interesante.

Como introducción a los materiales, se presentarán la estructura cristalina e electrónica de ZnO y sus DMS mencionados anteriormente.

7.1.1 Estructura cristalina

A temperatura y presión ambiente (RTP), ZnO tiene la estructura cristalina de wurzita. La wurzita tiene una red de Bravais hexagonal, que se muestra en la figura 7.1. Los vectores primitivos de la red se definen en el espacio cartesiano por las relaciones siguientes:

$$\vec{A}_1 = \frac{1}{2}a\vec{x} - \frac{\sqrt{3}}{2}a\vec{y}$$

$$\vec{A}_2 = \frac{1}{2}a\vec{x} + \frac{\sqrt{3}}{2}a\vec{y} \quad (7.1)$$

$$\vec{A}_3 = c\vec{z}$$
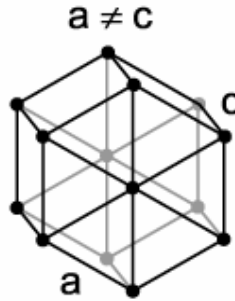
Fig 7.1: Red de Bravais hexagonal.

Donde a y c son las constantes de red. En el caso del ZnO a RTP, estas constantes toman los valores de a = 3,2495 Å y c = 5,2069 Å [41]. En cada punto de la red se repite la base, que consiste en dos átomos de Zn y dos de O. Se puede expresar la posición de estos átomos en términos de los vectores primitivos de la red (7.2), tal como se muestra en la estructura de la figura 7.2.

$$\vec{Z}_1 = \frac{1}{3}\vec{A}_1 + \frac{2}{3}\vec{A}_2$$

$$\vec{Z}_2 = \frac{2}{3}\vec{A}_1 + \frac{1}{3}\vec{A}_2 + \frac{1}{2}\vec{A}_3$$

$$\vec{O}_1 = \frac{1}{3}\vec{A}_1 + \frac{2}{3}\vec{A}_2 + u\vec{A}_3 \quad (7.2)\ [42]$$

$$\vec{O}_2 = \frac{2}{3}\vec{A}_1 + \frac{1}{3}\vec{A}_2 + \left(\frac{1}{2}+u\right)\vec{A}_3$$
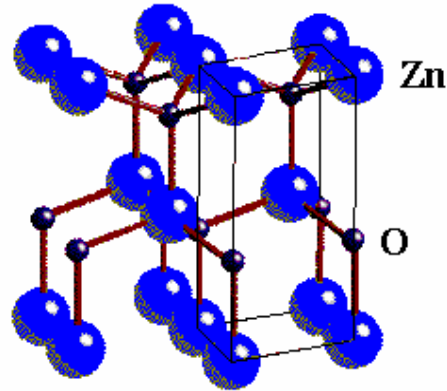
Fig 7.2:Estructura wurzita de ZnO.

Donde $\vec{Z}$ y $\vec{O}$ representan las posiciones respectivas de los átomos de Zn y O. u es la fracción entre la distancia catión-anión a lo largo del eje c y la constante de red c, que toma el valor de 0,380 en ZnO a RTP [43]. Por tanto, la estructura consiste en átomos de Zn y O coordinados tetraédricamente y apilados con un patrón ABAB. El grupo espacial de esta estructura es P6$_3$mc. En un tetraedro regular el valor de u sería 0,375, lo cual significa que existe una pequeña compresión uniaxial en la dirección c. Esto es debido a la atracción entre los planos de aniones y cationes, por tanto los enlaces químicos no son completamente del tipo covalente sp^3 sino que tienen una componente iónica también. Se puede separar los efectos de la contribución iónica de la covalente mediante el modelo Philips-Van Vechten y se halla que la contribución covalente sp^3 es la más fuerte, como en la mayoría de los materiales con coordinación tetraédrica. En este tipo de enlace se suben los electrones de 2s^2 a la capa p, lo cual cambia su configuración a 2p^6. Estos electrones hibridan con la capa exterior 4s^2 del Zn para producir dos enlaces covalentes sp^3.

Al formar un DMS, las constantes de red cambian conforme con la concentración y tipo del ion TM que substituye al Zn. Es importante notar que por encima de cierto límite, aumentar la concentración del TM suele formar fases secundarias y no sirve la descripción sencilla que se ha usado hasta ahora. En el $Zn_{1-x}Mn_xO$, por ejemplo, el limite de solubilidad del Mn es normalmente entre un 15% [44] y un 35% [45]. Se pueden alcanzar las mayores concentraciones solamente cuando se realiza el crecimiento del material en condiciones fuera del equilibrio. Por encima de esta concentración aparecen picos adicionales en difractogramas de rayos X que corresponden a las fases secundarias, como $ZnMnO_3$. En el caso de los otros TM, Ando et al. determinaron los límites de solubilidad para el crecimiento por epitaxia por haz molecular y se los muestran en la figura 7.3 [46].
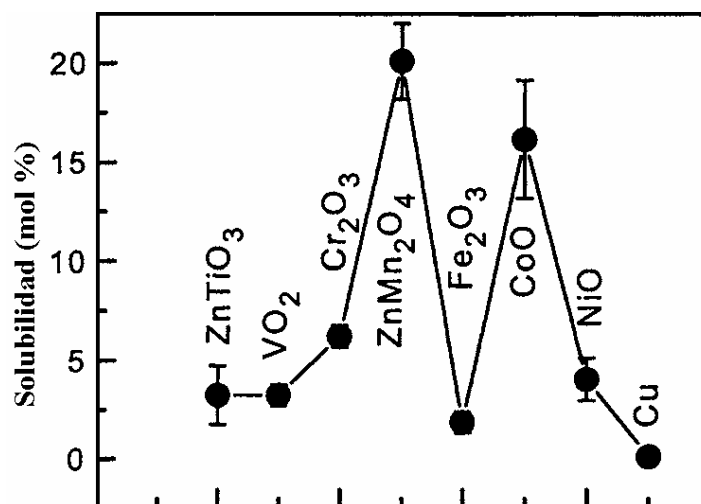
Fig 7.3: Límites de solubilidad de iones TM en ZnO.

Suponiendo la ausencia de fases secundarias, el factor que tiene más influencia sobre el cambio en las constantes de red al formar un DMS es el radio iónico del TM. El radio iónico de Mn^{2+} en coordinación tetraédrica es 0,66 Å [44], el cual es más grande que el de Zn^{2+}, 0,60 Å. Por esta razón, ambas constantes de red a y c aumentan con la concentración de Mn. Tomaszewska et al. informan de cambios de $\delta a = 0,007$ y $\delta c = 0,014$ Å con respecto al ZnO puro al formar una aleación con un 5% de Mn [47]. Se observa un aumento parecido en las constantes de red al formar una aleación con Fe, el cual tiene un radio iónico de 0,63 Å [48]. No obstante se ve una disminución en las constantes de red del $Zn_{1-x}Cu_xO$ [39] y el $Zn_{1-x}Ni_xO$ [44] al aumentar la concentración del TM, ya que los radios iónicos respetivos de Cu^{2+} y Ni^{2+} son 0,57 y 0,55Å, más pequeños que Zn^{2+}.

Al aplicar altas presiones al ZnO, se produce una disminución en el volumen de la celda de unidad. Recio et al. [49] confirmaron este resultado por XRD a altas presiones. A una presión de sobre 10 GPa, se hace energéticamente favorable producir una transición de fase a la estructura NaCl, acompañada por una disminución de volumen de un 17% [50]. La fase NaCl tiene una red de Bravais cúbica centrada en cara (FCC) (figura 7.4) con los siguientes vectores primitivos de la red:

$$\vec{A}_1 = \frac{a}{2}(\vec{x} + \vec{y})$$

$$\vec{A}_2 = \frac{a}{2}(\vec{y} + \vec{z}) \qquad (7.3)$$

$$\vec{A}_3 = \frac{a}{2}(\vec{z} + \vec{x})$$
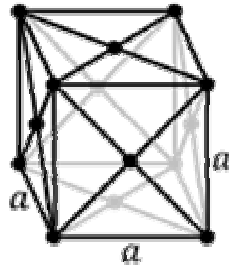
Fig 7.4: Red de Bravais FCC.

El valor de la constante de red a en condiciones RTP es 4,275 ± 0,004 Å. Se sabe esto porque se observa una histéresis grande al disminuir la presión. Aunque normalmente se encuentra la transición inversa a la fase wurzita a una presión sobre 2 GPa [51], excepcionalmente se puede recuperar ZnO en la fase NaCl metaestable [49]. La base consiste en un átomo de Zn y otro de O separados por $\vec{A}/2$, donde $\vec{A}$ es cualquier vector primitivo de la red. Por tanto, se puede considerar la estructura como dos redes FCC desplazados por $\vec{A}/2$, una con respeto a otra, como muestra la figura 7.5. La coordinación de cada átomo es octaédrica y el grupo espacial correspondiente es Fm3m.
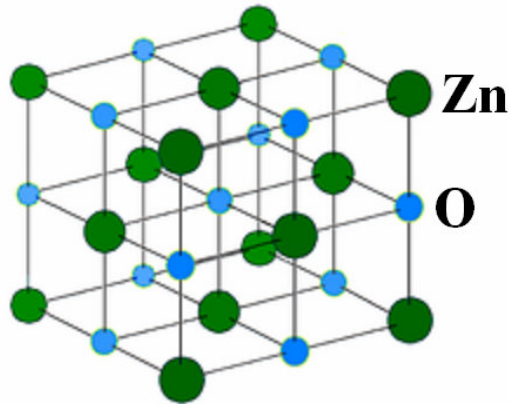
Fig 7.5: Estructura NaCl de ZnO.

En la siguiente sección es necesario referir a las fases wurzita y NaCl en el espacio recíproco. Por tanto se muestran las zonas de Brillouin de las estructuras hexagonal y FCC en la figura 7.6.
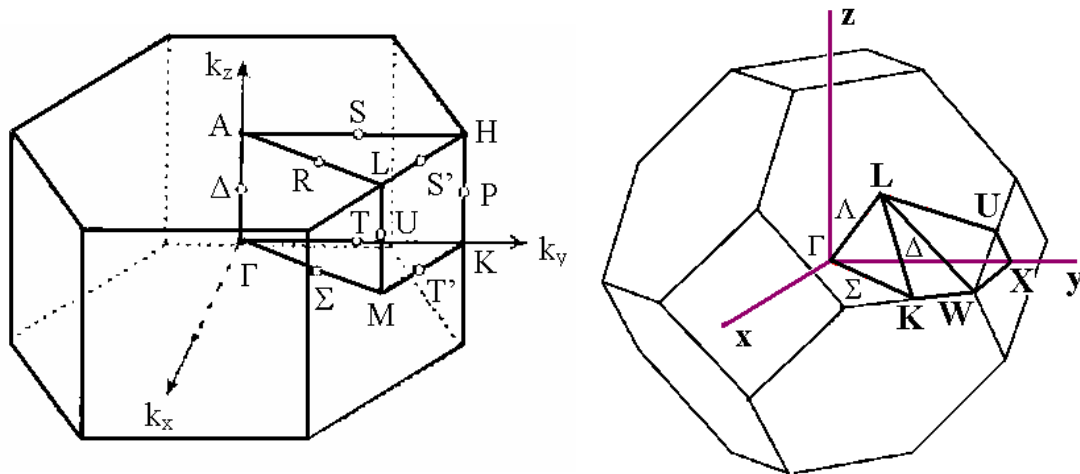
Fig 7.6: Zonas de Brillouin para a) (izquierda) red de Bravais hexagonal y b) (derecha) red de Bravais FCC.

7.1.2 Estructura electrónica

La figura 7.7 muestra la estructura de bandas electrónicas de la fase wurzita de ZnO a RTP [52], calculado por el método ab initio pseudopotencial con una base de ondas planas en el marco de la teoría de densidad funcional (DFT) dentro de la aproximación de densidad local (LDA). Los puntos de alta simetría en el eje horizontal corresponden con los que se ven en la zona de Brillouin hexagonal de la figura 7.6a.
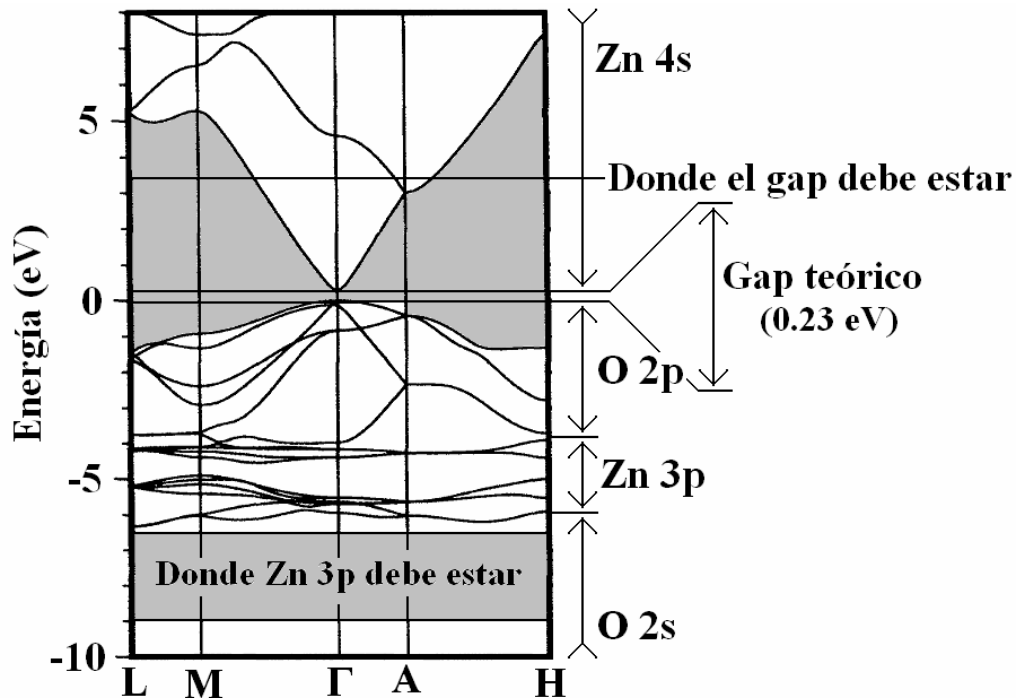
Fig 7.7: Estructura de bandas electrónicas de la fase wurtzita de ZnO.

La estructura electrónica consiste en tres regiones: la banda de conducción de niveles Zn 4s, la banda de valencia superior de niveles O 2p y la banda de valencia inferior de niveles Zn 3d. Hay bastante hibridación entre los niveles O 2p y Zn 3d, debido a su cercanía. Se nota que el gap ocurre en el punto Γ y es una transición directa. Un fallo típico de la LDA es que frecuentemente subestima la energía del gap, observado claramente en este caso. La subestimación es particularmente grande debido a que es necesario incluir los niveles Zn 3d en la banda de valencia. No obstante, la sobreestimación de la energía de estos niveles aumenta la repulsión de los niveles O 2p por el efecto de repulsión p-d. Este efecto cierra el gap y allana la dispersión de las bandas, alejando las masas efectivas del electrón y hueco de sus valores experimentales respetivos de $m_e = 0,19 \, m_0$ y $m_h = 1,21 \, m_0$ [54].

Cuando se forma un DMS, se introducen niveles del catión diluido (Mn, Fe, Cu o Ni) en la estructura de bandas. Los niveles que más influyen en la estructura cercano al gap son los 3d, que también deben ser incluidos en la banda de valencia. Como en el caso de los niveles Zn 3d, los niveles 3d del catión diluido se hibridan con los niveles O 2p y producen la repulsión p-d. La teoría del campo cristalino demuestra que en los complejos con coordinación tetraédrica, como el ZnO de la fase wurzita, donde cuatro ligandos forman un tetraedro alrededor del ion metal, es energéticamente favorable

colocar un simple electrón en cada uno de los 5 orbitales d antes de emparejar electrones. El complejo resultante es de "alto espín", ya que las configuraciones electrónicas favorecen una alta proporción de electrones d no emparejados, sobre todo en el caso de Mn y Fe. El espín produce acoplamiento espín-espín y espín-orbita así que es necesario tomar en cuenta estos efectos al calcular la estructura de bandas. Chien et al. [55] publicaron la estructura de bandas de $Zn_{1-x}Mn_xO$, $Zn_{1-x}Fe_xO$ y $Zn_{1-x}Cu_xO$ en configuraciones espín arriba y espín abajo. La figura 7.8 muestra el resultado de sus cálculos en el caso del $Zn_{1-x}Mn_xO$ de espín arriba.
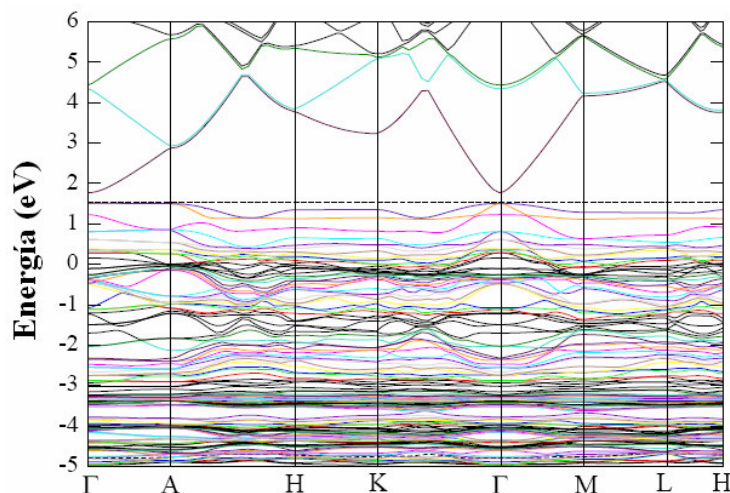
Fig 7.8: Estructura de bandas de $Zn_{1-x}Mn_xO$ de espín arriba.

Al comparar directamente con la figura 7.7, está claro que la inclusión de los niveles Mn 3d produce cambios grandes en la banda de valencia superior. Otra forma de apreciar el efecto de estos niveles es considerar la densidad de estados (DOS). En la figura 7.4 se muestra la DOS LDA del ZnO puro de la fase wurzita [55], que se comparará con las DOS de los otros DMS (figura 7.10). Toyoda et al. [56] calcularon la DOS para los DMS de Mn, Fe y Ni y Xiong et al [57] hicieron lo mismo para el DMS de Cu. En la figura, se han coloreado de gris las bandas que corresponden con los niveles 3d de los cationes diluidos y se han mostrado las DOS para configuraciones de espín mayoritario y minoritario.
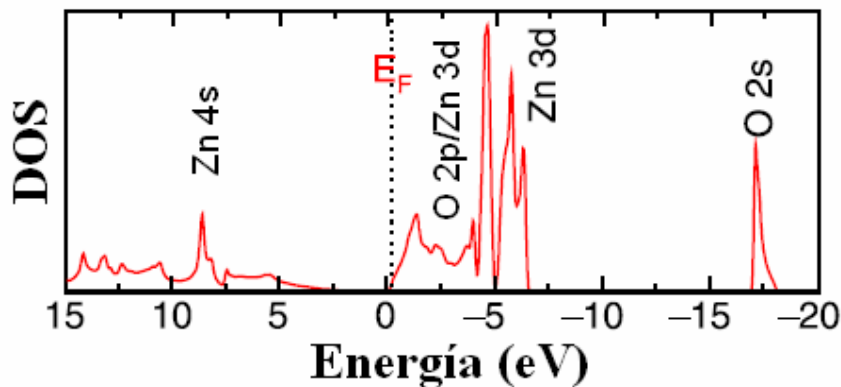
Fig 7.9: DOS teórico del ZnO de la fase wurzita.
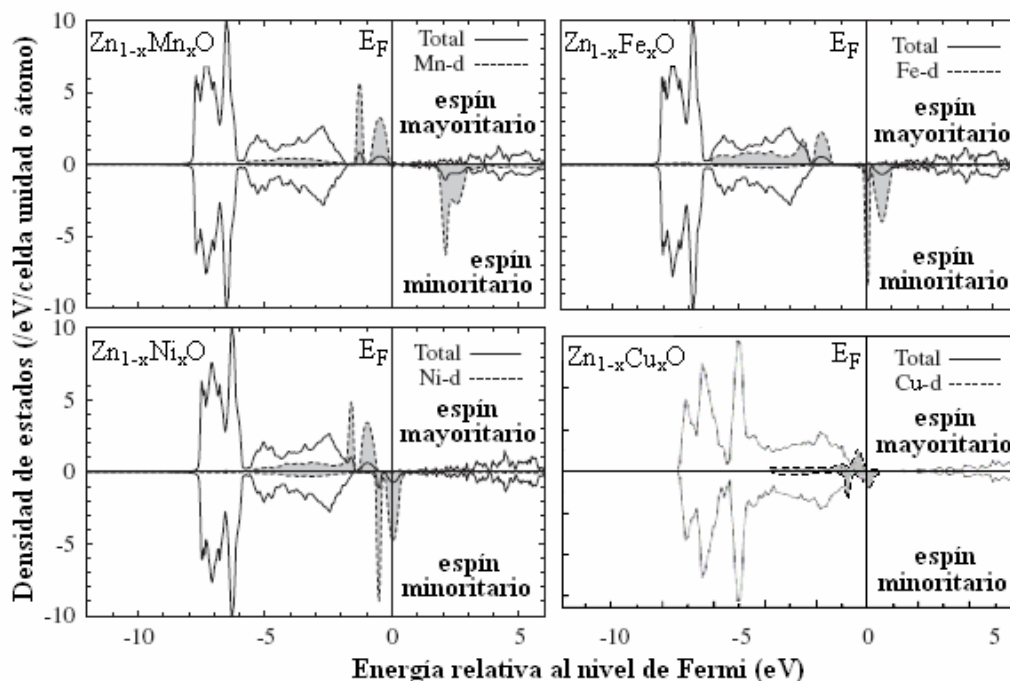
Fig 7.10: DOS teórico de los DMS del ZnO.

En el $Zn_{1-x}Mn_xO$ (espín mayoritario), se puede apreciar que los niveles Mn 3d caen principalmente dentro de 2eV del VBM, por tanto se esperaría que la inclusión del Mn afectaría fuertemente las propiedades ópticas cerca del gap, incluso su energía. El papel grande que el espín juega en la DOS también sugeriría propiedades magnéticas fuertes. En el $Zn_{1-x}Fe_xO$, los niveles Fe 3d están un poco más lejos del VBM, en el rango energético sobre -1,5 a 6 eV, mientras los niveles Ni 3d en el $Zn_{1-x}Ni_xO$ caen entre los de Mn y Fe, a una energía de entre -1 y -5 eV. Por último, se observa que los niveles Cu 3d en el $Zn_{1-x}Cu_xO$ están muy cercas del VBM, como en el $Zn_{1-x}Mn_xO$, con la mayoría de los niveles dentro de solamente 1 eV de la energía de Fermi (E_F). No obstante, los cálculos teóricos aproximan una realidad que se puede comprobar experimentalmente con medidas fotoelectrónicas.

La figura 7.11 muestra la evolución de la DOS, calculada por Jaffe et al. [58], al someter la fase wurzita del ZnO a altas presiones hidrostáticas. De nuevo, para la fase wurzita, se observa que los tres cambios mayores que producen la presión son un desdoblamiento de los niveles Zn 3d, un ensanchamiento ligero de los niveles O 2s y Zn 3d y una disminución en la intensidad y energía del primer pico por debajo de E_F. Al alcanzar la transición a la fase NaCl a una presión p_t, se observa una disminución repentina de la intensidad del primer pico por debajo de E_F, acompañada por un estrechamiento de los picos Zn 3d y una reducción de la energía de los estados O 2s. En la figura 7.12, se muestra la estructura de bandas de la fase NaCl a p_t. En ésta se nota que la transición interbanda que menos energía tiene ya no es un gap directo en el punto Γ, sino un gap indirecto entre L y Γ. La energía calculada del gap es justamente por debajo del valor determinado experimentalmente de $E_{gi} = 2,45 \pm 0,15$ eV [59]. La razón para la transición desde un semiconductor directo hasta un indirecto se basa en el cambio de coordinación de tetraédrica a octaédrica. En coordinación tetraédrica, los orbitales p y d pueden mezclarse en el punto Γ pero en coordinación octaédrica hay

simetría de inversión en este punto, así que las reglas de selección de Laporte prohíben la mezcla allí. No obstante, la mezcla todavía puede ocurrir alejado de Γ, así que la falta de repulsión p-d reduce la energía en el punto Γ pero su presencia aumenta la energía en el punto L, lo cual forma un nuevo gap.
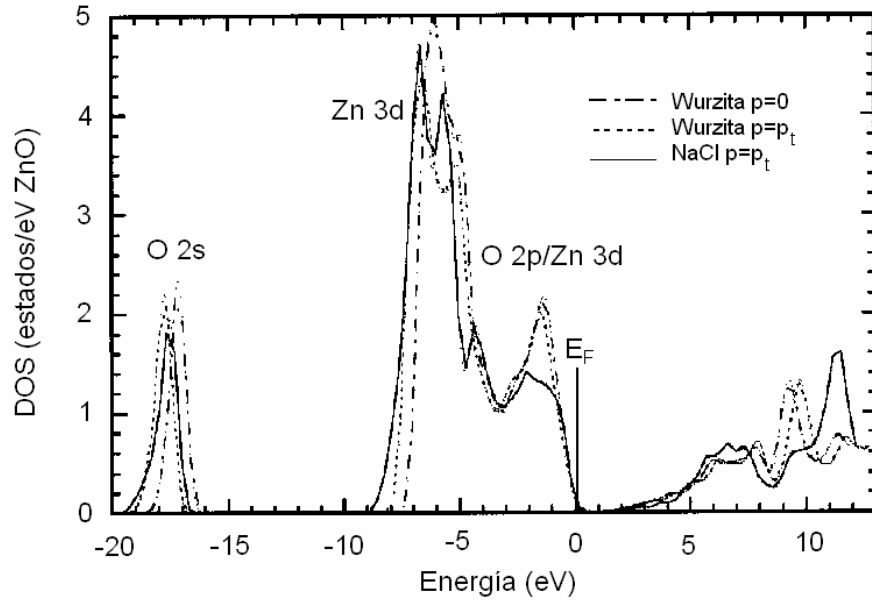
Fig 7.11: Evolución de la DOS del ZnO a altas presiónes.
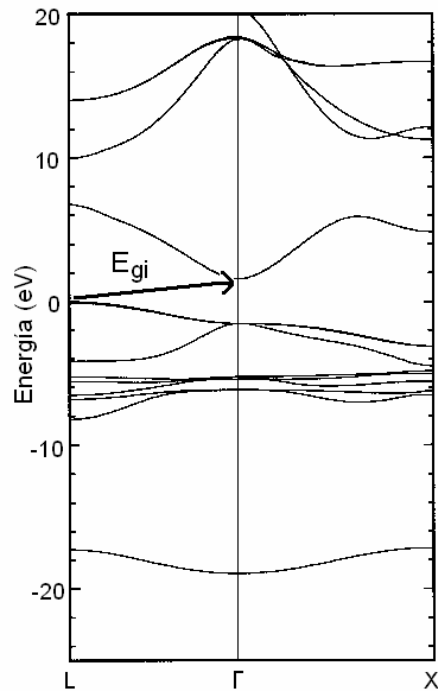
Fig 7.12: Estructura de bandas del ZnO de la fase NaCl a p_t.

7.2 Conclusiones

Se depositaron capas de $Zn_{1-x}M_xO$ (M = Mn, Fe, Ni, Cu) en condiciones óptimas sobre sustratos de mica y zafiro por ablación láser de blancos policristalinos compuestos de mezclas estequiométricas de compuestos químicos. Se caracterizaron las capas estructuralmente, electrónicamente, ópticamente y magnéticamente.

Caracterización estructural:

Se hizo una caracterización estructural detallada incluyendo espectroscopia de emisión de la pluma, XRD, XAS, XRF, microscopia electrónica y microanálisis para asegurarse de que se hubieran depositado las capas esperadas.

Se hizo espectroscopia de emisión de la pluma para analizar las condiciones de crecimiento durante la deposición. Se identificaron las líneas de emisión relacionadas con los TM neutros y simplemente ionizados. En general, se observa las líneas esperadas, excepto en el caso del DMS del Ni, ya que el Ni tiene una presión de vapor particularmente baja. La intensidad de las líneas no cambió a lo largo del tiempo, lo cual indica una composición química constante del plasma y, por tanto, de las condiciones de crecimiento. Durante la deposición del $Zn_{1-x}Mn_xO$, la intensidad de las líneas de emisión del Zn fue proporcional a la concentración de Mn en los blancos.

Se tomaron medidas de XRD para investigar la estructura cristalina de las capas. Los resultados muestran que las capas sobre zafiro tienen una orientación preferente en la dirección c. Esto reduce la tensión en las capas debida al desajuste entre las redes del DMS y del sustrato. Las capas del $Zn_{1-x}Mn_xO$ tienen una sola fase hasta una concentración de Mn de, por lo menos, un 15%. En este rango, el aumento en el radio iónico causa un aumento lineal en la constante de red c de $1,69 \pm 0,04 \times 10^{-3}$ Å$\%_{Mn}^{-1}$. El $Zn_{1-x}Fe_xO$ tiene una sola fase hasta una concentración de Fe de un 2,5%, por encima del cual se encuentra el Fe_2O_3. Hasta esta concentración, un aumento de Fe produce un aumento proporcional de la constante de red c de $5,2 \pm 0,2 \times 10^{-4}$ Å$\%_{Fe}^{-1}$. $Zn_{1-x}Cu_xO$ tiene una sola fase hasta una concentración de un 1% y después se encuentra el Cu_2O. En este rango, aumentar la concentración de Cu causa una disminución lineal de la constante de red c de $2,13 \pm 0,08 \times 10^{-4}$ Å$\%_{Cu}^{-1}$. Esto es porque el radio iónico es más pequeño que el del Zn. En el $Zn_{1-x}Ni_xO$ la situación no está clara, ya que los picos de difracción del NiO no se observan. Además, no se detecta un cambio apreciable en c.

Se midió XAS para determinar el entorno de coordinación del catión diluido. Para hacer esto, se compararon espectros de XANES con simulaciones teóricas y referencias. En el $Zn_{1-x}Mn_xO$, la forma de la XANES fue constante en función de la concentración de Mn, lo cual significa que el Mn siempre está en la configuración wurzita. En el $Zn_{1-x}Fe_xO$, se encuentra una mezcla de dos fases y un aumento en la proporción de Fe_2O_3 al aumentar la concentración de Fe. En el $Zn_{1-x}Cu_xO$, se observa una transición gradual desde wurzita hasta el Cu_2O. En el DMS de Ni, una transición parecida ocurre pero a lo largo de un menor rango de concentración, ya que al llegar a un 5% de Ni, el espectro XANES es casi idéntico a la de NiO. Se usó medidas de XRF para determinar la concentración de cationes diluidos en las capas. En la mayoría de los casos se encontró un buen acuerdo con las concentraciones nominales.

Se empleó microscopia electrónica de barrido para examinar las superficies de las capas, las cuales eran policristalinas. El tamaño promedio de un cristalito de ZnO puro era 300 ± 100 nm. Las capas de $Zn_{1-x}Mn_xO$ no mostraron conductividad eléctrica y los intentos para formar imágenes de las superficies metalizadas no tuvieron éxito. En las capas de $Zn_{1-x}Fe_xO$, el tamaño de los cristalitos disminuyó en función de concentración de Fe. Desde un 5% de Fe (3,2% por XRF), se observaron incrustaciones afiladas que podrían corresponder con la fase secundaria de Fe_2O_3. En las capas de $Zn_{1-x}Cu_xO$, se observaron regiones aislantes que podrían corresponder con el Cu_2O. Al aumentar la concentración de Cu, aparecieron más de estas regiones y se observaron enlaces entre las regiones cuando la separación entre átomos de Cu bajó hasta 4,18 Å, una posible señal de la difusión. Por encima de esta concentración, las regiones aislantes eran más grandes y separadas. En las capas de $Zn_{1-x}Ni_xO$, las imágenes sugieren que un proceso parecido ocurre pero a concentraciones más bajas. No se observó ninguna separación de fases a un 0,5% de Ni (0,4% por XRF) pero ya se vieron regiones aislantes separadas al llegar a un 1% de Ni (0,9% por XRF), tal vez sea porque el NiO es más estable estructuralmente que el Cu_2O. Mapas de elementos por microanálisis a la resolución máxima de 5 nm no revelaron conjuntos grandes de átomos metálicos grandes ni podían proveer información adicional sobre la composición química de las estructuras observadas en las imágenes SEM.

Caracterización electrónica:

Se tomaron medidas de espectroscopia fotoelectrónica para investigar las propiedades electrónicas de las capas. Se hizo UPS con la línea He-II y XPS con la línea K_α del Mg, para investigar los estados electrónicos de la banda de valencia y los estados profundos respectivamente.

Se identificaron los niveles O 2p y Zn 3d en los espectros UPS de todas las capas. En el $Zn_{1-x}Mn_xO$ se observó un pico en el lado de baja energía de ligadura de los niveles O 2p, cuya intensidad era directamente proporcional a la concentración de Mn. Es probable que este pico corresponde con los niveles Mn 3d. Su energía de ligadura disminuye un $0,36 \pm 0,07$ eV a lo largo del rango de concentración, mientras la energía de los picos O 2p aumenta un $0,39 \pm 0,07$ eV. Una explicación aceptable sería un aumento en la repulsión p-d. En las capas de $Zn_{1-x}Fe_xO$ los niveles O 2p se intensifican un 24% y se ensanchan un 30% en el rango de concentración, lo cual es consecuente con la explicación que los niveles Fe 3d se encuentran dentro de la banda O 2p. La energía de los niveles O 2p aumenta un $0,29 \pm 0,06$ eV debido a la repulsión p-d y una redistribución del espectro de energía causado por Fe(III). En la capa de $Zn_{0,95}Cu_{0,05}O$, la posición de los niveles Cu 3p no está clara. La energía de ligadura de los niveles O 2p disminuye un $0,12 \pm 0,02$ eV, de acuerdo con la teoría que predice una inversión en la dirección de la repulsión p-d. Parece que los niveles Cu 3d tienen mayor energía de ligadura que los estados O 2p pero, ya que están energéticamente más cercanos que los niveles Zn 3d, la repulsión p-d es mayor. No se midieron las capas de $Zn_{1-x}Ni_xO$ pero se esperaría un efecto parecido al DMS del Cu.

En las medidas XPS, se identificaron los picos correspondientes a los niveles profundos O 1s y Zn 2p en todas las capas y se determinaron los estados de oxidación de los cationes diluidos por las posiciones de sus picos 2p y satélites. Las capas de $Zn_{1-x}Mn_xO$ el Mn está en un estado de oxidación II en todo el rango de concentraciones. En las capas de $Zn_{1-x}Fe_xO$ parece que hubo una oxidación gradual del Fe desde el estado

II al III al aumentar la concentración, lo cual es consistente con la caracterización estructural. En la capa de $Zn_{0,95}Cu_{0,05}O$ hubo una contribución importante de Cu(I), también de acuerdo con la caracterización estructural. No se midieron las capas de $Zn_{1-x}Ni_xO$ pero se esperaría un estado de oxidación constante de II, como en el caso del Zn, el cual siempre se encontró en este estado. Se usaron las intensidades integradas de los picos 2p de los cationes diluidos para obtener una segunda serie de datos sobre la estequiometría de las capas, los cuales estaban de acuerdo con los resultados XRF.

Caracterización óptica:

Se tomaron medidas de absorción óptica para investigar los cambios en el frente de absorción causados por el tipo y la concentración del catión diluido a baja temperatura y alta presión. Se ajustaron los resultados a un modelo basado en la ecuación Elliot-Toyozawa para determinar las propiedades ópticas.

En las capas de $Zn_{1-x}Mn_xO$, el aumento del gap en función de la concentración de Mn es aproximadamente lineal, con un coeficiente de 19 ± 2 meV$\%_{Mn}^{-1}$ hasta una concentración de un 15%, debido a la repulsión p-d. En este rango de concentración la anchura del continuo se ensancha $0,43 \pm 0,05$ eV a causa del aumento del desorden. También este efecto es responsable de la disminución en la intensidad del excitón y su ensanchamiento de $0,15 \pm 0,03$ eV. La resonancia excitón + fonón LO también disminuye en intensidad y se ensancha $0,49 \pm 0,08$ eV. Se observa una banda con una energía inferior al frente de absorción directo con una energía constante de $3,04 \pm 0,05$ eV que se intensifica y se ensancha 36 ± 12 meV. Medidas de fotoconductividad demuestran un aumento claro de fotocorriente en esta región así que se concluye que es principalmente debido a una transición de transferencia de carga (CTT) desde los niveles Mn 3d hasta la banda de conducción. En las capas de $Zn_{1-x}Fe_xO$, el aumento del gap es aproximadamente lineal en todo el rango de concentración, con una pendiente de 4 ± 1 meV$\%_{Fe}^{-1}$. La anchura del continuo se ensancha $0,13 \pm 0,03$ eV y la intensidad del pico excitónico disminuye y se ensancha $0,38 \pm 0,05$ eV debido al aumento en desorden. Hay datos insuficientes para comentar sobre el excitón + resonancia fonón LO. En las capas de $Zn_{1-x}Cu_xO$, hasta el límite de solubilidad de $0,9 \pm 0,1$ %, la energía del gap disminuye $9,8 \pm 0,5$ meV, confirmando la inversión de la repulsión p-d. No obstante, el desorden todavía aumenta así que la anchura del continuo aumenta $0,37 \pm 0,06$ eV y la intensidad del pico excitónico disminuye y se ensancha 5.8 ± 0.9 meV. También la resonancia excitón + fonón LO disminuye en intensidad y se ensancha 41 ± 9 meV. Por encima del límite de solubilidad, el Cu empieza a difundirse de la posición substitucional del Zn para formar la fase secundaria de Cu_2O, un efecto que aumenta con la concentración de Cu. Ya que parece que el Cu_2O no afecta las propiedades ópticas que se han medido en el rango de concentración, vuelven a las de ZnO puro. En las capas de $Zn_{1-x}Ni_xO$, se observa una tendencia parecida a la del DMS de Cu pero el límite de solubilidad de $0,60 \pm 0,08$ % es más bajo porque el NiO es más estable que el Cu_2O. Hasta el límite de solubilidad, la disminución en la energía del gap es 5.5 ± 0.4 meV.

En todas las capas, la baja temperatura produce un corrimiento del frente de absorción hacia energías mayores, aunque la magnitud del corrimiento depende del efecto combinado de la interacción electrón fonón y el desorden estático. En las capas de $Zn_{1-x}Mn_xO$, la interacción electrón fonón domina a concentraciones bajas. Por tanto, se puede usar el modelo Bose-Einstein para confirmar que la energía del fonón del gap

de 30 ± 2 meV no varia apreciablemente de la del ZnO puro. No obstante, este modelo fracasa por encima de una concentración de Mn de un 10% debido al efecto del desorden estático que parcialmente compensa la interacción electrón fonón, disminuyendo la energía del gap a bajas temperaturas donde es particularmente eficaz. También se puede usar estos efectos para explicar las otras propiedades ópticas de las capas. A bajas concentraciones de Mn, las anchuras del continuo y el excitón muestran un ensanchamiento considerable con la temperatura a causa de la interacción electrón fonón pero el ensanchamiento por el desorden estático a bajas temperaturas compensa parcialmente a altas concentraciones. En la misma manera la intensidad del excitón disminuye con la temperatura a bajas concentraciones de Mn debido a la desasociación por fonones pero la desasociación por el desorden estático a bajas temperaturas compensa a altas concentraciones. La resonancia excitón + fonón LO sigue una tendencia parecida a la del excitón mencionada anteriormente. La energía de la banda antes del frente de absorción directo parece seguir el mismo comportamiento en función de la temperatura que el gap, de acuerdo con su asignación como CTT. Su intensidad disminuye con la temperatura en todas las capas y su anchura permanece aproximadamente constante. En el $Zn_{1-x}Fe_xO$ la interacción electrón fonón controla el comportamiento de las propiedades ópticas en todas las capas, ya que la mayor concentración es solamente un 10%. Por esta razón, las tendencias generales son parecidas a las de los DMS de Mn de baja concentración. En las capas de $Zn_{1-x}Cu_xO$ hasta el límite de solubilidad, el modelo Bose-Einstein no puede verificar que el mecanismo dominante es la interacción electrón fonón. No obstante, las propiedades ópticas restantes son parecidas a las de los otros DMS de baja concentración. Por encima del límite de solubilidad, las propiedades ópticas vuelven gradualmente a las del ZnO puro. En las capas de $Zn_{1-x}Ni_xO$ no hay cambios importantes en las propiedades ópticas con respeto a las del ZnO puro para ninguna concentración de Ni debido al bajo límite de saturación, excepto una anchura del continuo aproximadamente constante.

En la fase wurzita, la alta presión produce un corrimiento del frente de absorción hacia energías mayores, de acuerdo con la teoría para semiconductores covalentes. Se ajustó la energía del gap a un modelo cuadrático pero no se detectó ningún cambio importante con respeto al comportamiento de ZnO puro, que tenía los coeficientes de presión lineal y cuadrático de $\alpha = 25,3 \pm 0,1$ meVGPa^{-1} y $\beta = -0,28 \pm 0,01$ meVGPa^{-1} respectivamente. Puesto que las altas presiones no afectan el desorden de una manera considerable, la anchura del continuo no cambió apreciablemente en ninguna capa. Solamente se observó el excitón a bajas concentraciones de catión diluido y no se pudo detectar la resonancia excitón + fonón LO, ya que se tomaron las medidas a temperatura ambiente. En función de la presión, la intensidad del excitón solía aumentar, debido a un aumento en la energía de Rydberg y su anchura disminuyó a causa del aumento resultante en tiempo de vida. Las pendientes variaron de manera arbitraria entre las muestras, así que es probable que dependan de la concentración de defectos introducidos al cargar la celda. En las capas de $Zn_{1-x}Mn_xO$, la alta presión causó una disminución en la intensidad de la CTT y un aumento en su energía de 24±2 meVGPa^{-1} y su anchura de $6,7 \pm 0,8$ meVGPa^{-1}. Todos estos efectos son independientes de la concentración de Mn y ocurren porque la alta presión causa un aumento en la energía del CBM y VBM, mientras la energía de los niveles Mn 3d apenas cambian con la presión. Esto confirma que la CTT se produce entre los niveles Mn 3d y la banda de conducción.

En la fase NaCl, se observó un cambio marcado en la forma del coeficiente de absorción. Al tratarse de capas delgadas, no fue posible medir la energía del gap indirecto. No obstante, se pudo estudiar la cola del gap directo en el punto Γ, que tambián se corrió hacia energías mayores al aumentar la presión. Aunque no fue posible determinar la energía de este gap directo, se pudo estimar su coeficiente de presión y, en todos los casos, el coeficiente no varió considerablemente de 35 ± 2 meVGPa^{-1}, el valor encontrado en el ZnO puro. En este material la transición de fase ocurre a 9,7 GPa al subir la presión y 2,0 GPa al bajarla, de acuerdo con resultados de los DMS con bajas concentraciones de catión diluido. A concentraciones mayores, las capas de $Zn_{1-x}Mn_xO$ mostraron una disminución lineal en las presiones de la transición de fase al subir y bajar la presión, debido al efecto de la "presión química". Las pendientes de la disminución eran $0,04 \pm 0,02$ y $0,13 \pm 0,01$ GPa%$_{Mn}^{-1}$ al subir y bajar la presión respectivamente, recuperándose capas en la fase NaCl metaestable para concentraciones de Mn por encima de 19 ± 3 %. En las capas de $Zn_{1-x}Fe_xO$, la presión de la transición de fase al bajar la presión disminuyó con una pendiente de $0,13 \pm 0,01$ GPa%$_{Fe}^{-1}$. No obstante, la presión de la transición de fase al subir la presión pareció aumentar con la concentración de Fe, probablemente a causa del efecto del sustrato de mica. Las presiones de las transiciones de fase en las capas de $Zn_{1-x}Cu_xO$ se mantuvieron constantes, debido al bajo límite de solubilidad, tomando valores de 10 ± 2 y $2,1 \pm 0,1$ GPa al subir y bajar la presión respectivamente. Puesto que las capas de $Zn_{1-x}Ni_xO$ tenían un límite de solubilidad aún más bajo, no se caracterizaron a alta presión.

Caracterización magnética:

El propósito de esta caracterización fue determinar la magnetización de las capas DMS en función del campo magnético aplicado y la temperatura. No se pudieron analizar los resultados de las capas depositadas sobre mica a causa de la gran respuesta magnética del sustrato, así que solamente se presentan los resultados de las capas depositadas sobre zafiro.

En los ciclos M(H) a 1,8K, después de restar la contribución del sustrato, la única capa de $Zn_{1-x}Mn_xO$ que mostró evidencia del ferromagnetismo era la que más concentración de Mn tenía (25%), donde se observó un campo coercitivo de 5mT, probablemente debido a las fases secundarias ferrimagnéticas (Zn, Mn) $Mn_2O_{4.}$ Se interpretaron los resultados experimentales con éxito con la función de Brillouin y se encontró una disminución de la imanación de saturación de 1.5 ± 0.1 μ_B por ion de Mn a lo largo del rango de concentración entre un 5% y un 25%. Esto podría ser la consecuencia de una interacción de superintercambio antiferromagnético entre iones Mn vecinos. En las capas de $Zn_{1-x}Fe_xO$, en el DMS con un 2,5% de Fe no se observó ferromagnetismo pero para un 5% de Fe, se detectó un pequeño campo coercitivo de 32mT, probablemente debido a que γ-Fe_2O_3 es una fase secundaria ferrimagnética, detectada por XRD. Al modelar con la función de Brillouin, se encontró una disminución de la imanación de saturación de 0.6 ± 0.3 μ_B por ion de Fe entre las dos capas. No se pudieron analizar los ciclos de magnetización a 300K a causa de una corrección incompleta del momento magnético del sustrato.

En las curvas M(T), se encontró que una anomalía a 47K, mencionada por algunos autores resultó ser un efecto del sustrato relacionado con la contribución ferromagnética de impurezas desconocidas en el Al_2O_3. Las capas de $Zn_{1-x}Mn_xO$ demostraron un comportamiento paramagnético típico, excepto en el límite de baja

temperatura donde se vieron señales del comienzo del antiferromagnetismo. Al aplicar la ley de Curie-Weiss, la constante de Curie, que indica la fuerza del paramagnetismo, aumentó 0.9 ± 0.1 m^{3}kg^{-1}K a lo largo del rango de concentración. La constante de Weiss resultó ser pequeña y negativa en todos los casos, lo cual aporta más evidencia para el antiferromagnetismo a baja temperatura. Su valor disminuyó 2.8 ± 0.3 K en el mismo rango de concentración. Las capas de $Zn_{1-x}Fe_xO$ también resultaron ser paramagnéticas con señales parecidas del antiferromagnetismo a baja temperatura. El valor de la constante de Curio aumentó 0.6 ± 0.2 m^{3}kg^{-1}K entre las capas de más baja y las de más alta concentración mientras que la constante de Weiss, que también era siempre pequeña y negativa, diminuyó 0.4 ± 0.3 K.

Desarrollo para el futuro:

Los resultados obtenidos en este trabajo permiten la posibilidad de continuar la investigación en el futuro. Algunos desarrollos podrían ser:

- Finalización del estudio fotoelectrónico de las capas de $Zn_{1-x}Cu_xO$ y $Zn_{1-x}Ni_xO$. Las medidas de UPS suministrarían más información sobre la inversión de la repulsión p-d predicha con estos cationes diluidos y medidas XPS podrían confirmar los estados de oxidación.
- Medidas magnéticas adicionales con un rango más amplio de campos, sobre todo con capas de $Zn_{1-x}Fe_xO$, ya que solamente de midió hasta un 5% de Fe. Esto permitiría la medida más precisa de las imanaciones de saturación y la cuantificación del efecto de las fases secundaria ferrimagnéticas. También se podría medir capas de $Zn_{1-x}Cu_xO$ y $Zn_{1-x}Ni_xO$, aunque no está claro si los bajos límites de solubilidad evitarían la detección de diferencias en la magnetización.
- Medidas adicionales sobre la CTT del $Zn_{1-x}Mn_xO$ para estudiar el cambio de fotoconductividad en función de la concentración de Mn.
- Medidas a alta presión con monocristales en volumen de los DMS para estudiar la energía y comportamiento del gap indirecto en función de la presión en la fase NaCl. También, al medir las capas hasta energías más altas, se podría encontrar la energía del gap directo en la fase NaCl.
- Medidas a alta presión y baja temperatura simultáneamente para permitir una determinación más precisa de las propiedades ópticas, sobre todo las que están relacionadas con los efectos excitónicos.
- Medidas infrarrojas sobre los DMS de las fases wurzita y NaCl para investigar las transiciones internas d-d* del catión diluido. Probablemente sería necesario usar capas más espesas o monocristales para obtener suficiente absorción.
- Medidas de transporte para determinar las concentraciones y movilidades de los DMS. Sería necesario dopar las capas de $Zn_{1-x}Mn_xO$ con Ga para aumentar la concentración de portadores.
- Medidas de dispersión Raman para proveer resultados complementarios sobre las propiedades vibracionales de las capas en el punto Γ.
- Medidas de fotoluminiscencia para suministrar información adicional sobre las propiedades excitónicas y las impurezas en las capas.
- Calculos ab-initio de la energía del gap en función de la concentración de cationes diluidos para fortalecer la base teórica detrás de las conclusiones hechas sobre la repulsión p-d.

- El estudio del ZnO aleado con dos o más cationes diluidos. Por ejemplo, Han et al. [60] informan que dopar el $Zn_{1-x}Fe_xO$ con Cu es "una clave al ferromagnetismo a temperatura ambiente".
- La integración de los resultados encontrados en este estudio con los del ZnO aleado con otros TM, como el Co. De esta manera se podría realizar una descripción general del comportamiento de los DMS del ZnO.

Bibliografía:

[1] – [59] Igual a la bibliografía en la sección 1.3.
[60] S. Han, J. Song, C. Yang, S. Park, J. Park, Y. Jeong, K. Rhie. Appl. Phys. Lett. **81**, 4212 (2002).